Author:
Russell-Pavier, Freddie

Title:
'Hi-Fi Nanoscience'

Exploring the nanoscale with optical pickup units

'Hi-Fi Nanoscience' | Exploring the nanoscale with optical pickup units

Frederick S. Russell-Pavier

Interface Analysis Centre, School of Physics

A thesis submitted to the University of Bristol in accordance with the requirements for award of the degree of Doctor of Philosophy in the Department of Physics, Faculty of Science

January 2020   Word Count: 63,280 words

Abstract

In this work, an optical pickup (OPU) (Model: HD85/650, Sanyo, Japan) is adapted for several developments in surface microscopy techniques. A principle investigation studies the application of OPUs into high-speed atomic force microscopy (HS-AFM), a technique for measuring 3D topographical maps on the nanoscale. OPUs contain a high-fidelity linear displacement detection system of ~6 µm range, a narrow laser spot size (~1 µm) and a high measurement bandwidth of (~45 MSs^{-1}), making the device well suited to nanoscale displacement sensing at high-speeds. An OPU-based HS-AFM is developed in this work that can image large areas (millimetres) at high rates of 2 megapixels/s, high tip velocity (10 mms^{-1}) with area imaging rate of 25 µm^{2}s^{-1}. It is compared against an existing commercial instrument to show sub-nanometre displacement sensitivity via the detection of the primary and secondary modes of a free (MSNL) HS-AFM cantilever in air with amplitudes equal to 0.838 ± 0.24 nm and 0.125 ± 0.04 nm, respectively.

The OPU HS-AFM developed in this work was applied in a study, which imaged CRISPR-Cas9 molecules, used as a programmable nanoparticle for DNA mapping. It was shown that the OPU HS-AFM could be applied in a genomics application by identifying the spacing of the CRISPR-Cas9 molecule on a TERT gene (expected: 46.9 nm; measured: 47.7 ± 8.1 nm) and HER2 gene (expected: 114.1 nm; measured: 108.2 ± 17.1 nm) within the measurement uncertainty. The abundancy of these genes can be used for clinical purposes as the over expression of the HER2 gene can be an indication of breast cancer. A pair of OPUs were later incorporated into an HS-AFM to monitor and assist in developing a high-speed sample scanner, which was manufactured via stereography 3D-printing. Whilst the dual axis parallel flexure scanner had typically been operated in 'open-loop' mode while conducting HS-AFM, the monitoring of the true motion of the scanner in real-time with the OPUs was shown to reduce the lateral imaging error by up to a mean of 19 nm per pixel (i.e. 40 % reduction in lateral error).

Subsequently, the OPU was adapted for high-speed optical profilometry (HS-OP) as a non-contact technique to help 'bridge the gap' between the HS-AFM lateral imaging scale (~10^{-9} m) and other optical lateral imaging scales (>10^{-6} m) under ambient conditions. It is shown that the HS-OP is capable of imaging an area of 100x that of the HS-AFM in the same time. Presented applications of this instrument include topography mapping of a UO$_2$ thin film, real-time capture of the evaporation of a saline solution microdroplet on a metal surface and imaging of the surface features of a Tilia Cordata leaf. Throughout the development and research in this thesis, several image processing techniques were implemented to enable successful study and scalability of the captured surface microscopy images. Principally, a method is presented for automatic feature correlation and stitching of composite surface microscopy images to help link the techniques developed here to large length scales. In each instance, the algorithm used is presented and a case study undertaken to evaluate their significance.

ii

Acknowledgments

Author's declaration

I declare that the work in this dissertation was carried out in accordance with the requirements of the University's Regulations and Code of Practice for Research Degree Programmes and that it has not been submitted for any other academic award. Except where indicated by specific reference in the text, the work is the candidate's own work. Work done in collaboration with, or with the assistance of, others is indicated as such. Any views expressed in the dissertation are those of the author.

Frederick S. Russell-Pavier   January 2020

Contents

Figures

xviii

Nomenclature

Acronym/ Initialism/ Shortening	Definition
ADS	Astigmatic detection system
AFM	Atomic force microscopy
AMF	Adaptive median milter
APC	Automatic power control
AC	Alternating current
BR	Blu-ray
CD	Compact disc
CRISPR	Clustered regularly interspaced short palindromic repeats
DAQ	Data acquisition
DC	Direct current
DNA	Deoxyribonucleic acid
DVD	Digital versatile disc
EM	Electromagnetic
.exe	Executable
FFT	Fast fourier transform
FPS	Frames per second
GNU	GNU's not unix
HOPG	Highly oriented pyrolytic graphite
HS-AFM	High-speed atomic force microscopy
HS-OP	High-speed optical profilometry
ICE	Image composite editor
LASER	Light amplification by stimulated emission of electromagnetic radiation
LDV	LASER doppler Shift Vibrometer
MLL	Mean line levelling
NA	Numerical aperture
NCC	Normalised cross-correlation

NI	National instruments
OP	Optical profilometry
OPU	Optical pickup
PID	Proportional integral derivative
PNR	Phosphorene nanoribbon
QPD	Quadrant photodiode
RMS	Root mean squared
SNR	Signal-to-noise ratio
SPM	Scanning probe microscopy
USB	Universal serial bus
VI	Virtual instrument
ZIRLO	Zirconium low oxidation

Research outputs

Talks:

Nanoscale material characterisation: the use of a modified dvd pickup in high-speed atomic force microscopy, Nanotech, France (2017)

Nanoscale material characterisation: the use of a modified dvd pickup in high-speed atomic force microscopy, INASCON, Bristol (2017)

DVD optical pick-ups for traceable high-bandwidth nanoscale sensing: applications in high-speed atomic force microscopy and more, NPL PGI Conference, UK (2016)

Posters:

A functional and real-time scanning probe microscope made with LEGO® bricks for educational STEM outreach in the UK, ISPM Conference, Belgium (2019)

Nanoscale material characterisation: high-speed AFM with DVD optical pickups, NPL PGI Conference, UK (2017)

DVD optical pickups for traceable high-bandwidth nanoscale sensing: applications in high-speed atomic force microscopy and more, NPL PGI Conference, UK (2016)

Submissions to Journals (Author):

Sample Preparation Methods for Optimal HS-AFM Analysis: Duplex Stainless Steel for Ultramicroscopy, Ultramicroscopy, *Submitted,* (March 2020)

Bringing real-time traceability to high-speed atomic force microscopy, Meas. Sci. Technol., vol. 31, 074005 (2020)

Production of phosphorous nanoribbons, *Nature,* vol. 568, pp. 216–220 (2019)

'Hi-Fi AFM': high-speed contact mode atomic force microscopy with optical pickups, Meas. Sci. Technol., vol. 29, 105902 (2018)

DNA nanomapping using CRISPR-Cas9 as a programmable nanoparticle, Nature Communications, vol. 8, Article number: 1665 (2017)

Single crystal, luminescent carbon nitride nanosheets formed by spontaneous dissolution, Nano letters 17.10, pp. 5891-5896 (2017)

Patents:

System, method, computer-accessible medium and apparatus for DNA mapping, WO2018129226A1 (2018)

Outreach and public engagement:

National finalist in the IoM^3 Young Person's Lecture Competition (2020) [Final postponed]

Developed an AFM made with Lego bricks and handout for stand in the School of Physics, on University of Bristol Open Days (2018-2019).

Developed an AFM made with Lego bricks and performed a workshop with other members of the HS-AFM team at Hanham Woods Academy, Bristol. (2018)

Presented a talk at Southville School, Bristol describing the work mechanism of a mechanical microscope, with a live demonstration using an AFM made with Lego bricks. (2018)

Teaching:

First Year Laboratory Demonstrator, School of Physics, University of Bristol (2015-2019).

Assisted in the supervision of numerous (~10) final year BSc and MSci Final Year Projects.

Additional Funding:

Secured three months of funding from the National Productive Fund incentivised industrial placement for Engineering Physical Sciences Research Council Students to work with Bristol Nanodynamics. (2019)

Awarded a travel bursary from funds donated by an alumni Peter Bye to the School of Physics, Universiy of Bristol (2017)

Chapter 1: Introduction

1.1 Background

  The research carried out in this thesis builds upon a wide variety of successful scientific endeavours (e.g. creation of a compact room temperature low power laser) and the mass production of miniaturised consumer technology (e.g. the compact disc (CD) player) that have further evolved over recent decades. Historical and technological breakthroughs in the fields of optics, magnetism, electronics, computer science and engineering have enabled highly capable consumer electronics to be distributed on a worldwide scale for low-cost. Furthermore, a high demand for worldwide distribution of the formats of CD, digital versatile disc (DVD), and Blu-ray could have been spawned, in part, due to the creativity of the artists and performers who generated such widely-desired content. The combination of technological advances, to allow the creation of optical media discs and pickups, coupled with the global demand for high-fidelity digital multimedia formats have all been major underpinning factors that have facilitated the research carried out in this thesis.

  In this thesis, the development and production of a 'single' component, the optical pickup unit (OPU), is applied in scientific practice to enable cutting-edge research primarily focussed on assaying the nanoscale, with other applications investigated too. As part of this process, a broad and detailed set of considerations for the control and function of the OPU must be understood. In order to translate the application of this device from its typical use case, embedded in an integrated commercial product for reading and writing to optical discs, to a bespoke scientific measurement tool, the characterisation, control and operational consistency of the device need be obtained. In turn, when applying this technology to a scientific field, validation must be carried out against existing techniques that are commonplace within that field. In addition, and where possible, demonstrating the capabilities of a newly-validated technique by collaborating with other cutting-edge researchers allows for the purpose of the ongoing development to be understood and justified.

  The scientific applications of the OPU investigated in this thesis have been broad, with studies residing in several distinct research fields including atomic force microscopy (AFM), nanopositioning, optical profilometry and image processing. In each case, the technique may then be used in tandem with a secondary research field such as genomics, biology or metallurgy. As such, a review of prior research and literature is concentrated into the introduction section of each chapter, rather than structuring the thesis in a more conventional format with a unified literature review at the beginning of the thesis. The motivation for this structure is for each chapter to be comprehended or referenced in isolation, whereas this introduction chapter looks to outline the structure and contents of the thesis.

  Following the Introduction, in Chapter 2 this thesis goes on to describe the background, functionality and control of the OPU. Subsequently, a specific commercially-available OPU

(HD-SF65/850, Sanyo, Japan) is selected and the electronics that were created in this work to make use of the features onboard this OPU are described and evaluated. In turn, Chapter 3, builds upon the control and sensing achieved from the development work carried out in Chapter 2. The OPU is integrated into a detection head within a custom-built high-speed atomic force microscope (HS-AFM), using contact mode and achieving sub-nanometre (i.e. < 1 nm) height resolution and nanometre (e.g. 2-4 nm) lateral resolution. The performance of this bespoke, OPU-based, HS-AFM is then validated against a commercially-available HS-AFM. Applications of this OPU-based system in research, including for genomic and metallurgy studies, are presented in turn. Thereafter, Chapter 4 builds upon the successful application of OPUs to surface microscopy by implementing the pickup in several optical profilometer configurations. Images captured by these OPU-based optical profilometers demonstrate the benefits to research applications via the presentation of studies of a uranium dioxide thin film, in one instance. A second significant application of the optical profilometer demonstrates the imaging of stomata structures on the surface of a leaf and compares these against equivalent datasets collected on a scanning electron microscope (SEM).

In Chapter 5, an in-depth study into configurations that provide multi-axis positioning and sensing with OPUs is undertaken. It is shown how the OPU can be widely used in several positioning configurations as both a performant actuator and sensor. Within this body of experimentation, it is shown how 3D-printed flexure stages can be used with OPU sensing to create a performant high-speed nanoscale scanner that can be used within a commercial AFM operating with reduced error compared to an open-loop version of this scanner previously reported on in both Chapter 3 and literature (1,2).

Thereafter, Chapter 6 details the digital image processing algorithms that were implemented in software written to control and process the data from the OPU-based microscopes developed in this work. Initially, the methods which have been implemented to enhance the data by reducing the presence of imaging artefacts and sources of sensor noise are detailed. In the latter part of Chapter 6, a description of a method developed in this work for combining surface microscopy images (i.e. 'image stitching') taken from multiple locations on the sample is presented and evaluated using a test dataset with simulated image artefacts.

The remainder of this introduction chapter looks to give a brief background to each of the chapters presented in this thesis. The purpose for doing this is to, in short, highlight the background and motivation for each avenue of research that has been undertaken.

1.2. The optical pickup unit (OPU)

Owing to the large amount of international research and development preceding James Russell's 1966 patent (3), outlining the technology that led to the modern day optical media disc formats (i.e. CDs, DVDs and Blu-rays), OPUs have been produced in their millions (4). These devices have been integrated into portable, industrial and domestic applications existing in day-to-day environments

for decades. To perform consistently in such a wide range of applications, OPUs have several embedded control systems within them, including a astigmatic detection system (ADS), multi-axis voice coil motors (VCM) and high-bandwidth (i.e. 10-100s MHz) quadrant photodiodes (QPD) (5). The objective lens typically has a high numerical aperture (NA), resulting in a very small laser spot (0.5-1.5 µm) (5). Due to these advanced systems being made available at the low price point of ~£5, OPUs give tremendous potential for bespoke, one-off or prototype design of instrumentation requiring millimetre to sub-nanometre measurement or actuation (6–9) .
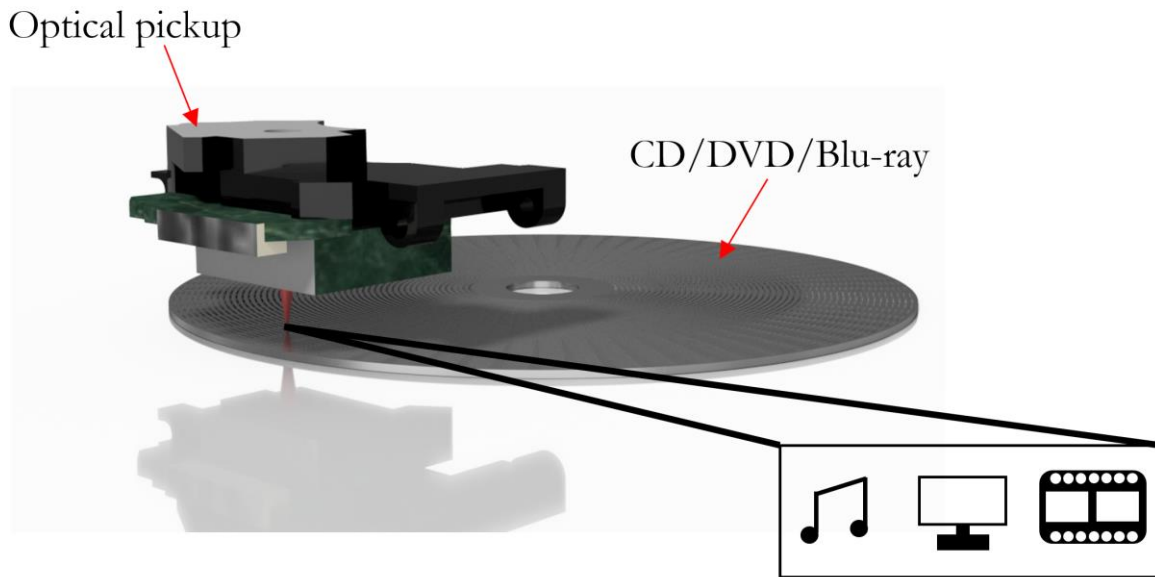
Figure 1: A conceptual image representing the typical commercial function of the Sanyo HD65/850 optical pickup, used throughout this thesis, and an optical media disc (not to scale).

Translating commercial OPUs to research applications has been carried out for several decades and within a variety of research fields, including sensing for biological, material science, seismological, gravity measurements, accelerometery, microscopy applications and more. Whilst the measurement properties of the optical pickups are well suited to many applications, the main 'barrier to entry' which prevents the widespread implementation of these devices for scientific research occurs due to the lack of available information (e.g. technical specification sheet) and the peripheral hardware typically available to evaluate and control these devices. Historically, it is rare that an optical pickup can be used in a standalone way for measurement outside an optical disc media player, as an 'off-the-shelf' and 'plug-and-play' solution. In recent years, including in this thesis, efforts have been made to 'democratise OPU technology' such as by Edwin Hwu (10), to enable researchers to attempt novel measurement configurations without having to first overcome the technical barrier to entry by providing knowledge and electronics schematics that have enabled prior scientific investigations.

In this work, OPUs are applied to the scientific instrumentation fields of AFM, nanopositioing and 3D optical profilometry, following successes of prior integration of these devices for measurements in microscopy (11–13). The sensing configurations developed here have been focussed on making use of the high-bandwidth capabilities (i.e. megasamples per second) of the OPUs, which enable much higher imaging rates than are achievable with the sensors typically used in these instruments. In addition, this work demonstrates successful implementation of the OPUs in several actuation and displacement sensing configurations to allow for high-rate sample scanning with high-repeatability and minimal error across the nano-to-millimetre scale.

1.3 Atomic force microscopy (AFM)

In the drive to 'shed the light' on Richard Feynman's widely cited 'Plenty of room at the bottom' (14) (i.e. the nanometre length scale and below) a large number of tools have been developed for tasks such as assaying (15) and manipulating materials (16) at the nanoscale using scanning probes. Whilst many of the techniques interact with the surface via a source of electromagnetic radiation, it has also been shown that force-based measurements using scanning probe microscopy (SPM) techniques also yield highly-detailed results and in some cases, e.g. scanning tunnelling microscopy (STM) and AFM, give lateral resolutions higher than achievable with electromagnetic-based sample interaction (17).

Within the wide field of SPM techniques, AFM is a widely-used and well-known technique that can be performed in a number of modes. Conventional AFM is categorised into three major types: non-contact, intermittent contact and contact modes, where the name refers to the contact between a micro-mechanical beam, the cantilever and the sample surface. The degree of contact is better understood by looking at the tip-sample interaction force regime described by the Leonard-Jones model:

$$V_{LJ}(r) = 4\varepsilon \left[\left(\frac{\sigma}{r^6} \right)^6 + \left(\frac{\sigma}{r^{12}} \right)^{12} \right] \qquad (1)$$

where V_{LJ} is the potential, ε is the depth of the potential well, σ is the distance at which the potential between two interacting particles is minimum and r is the distance between the particles.
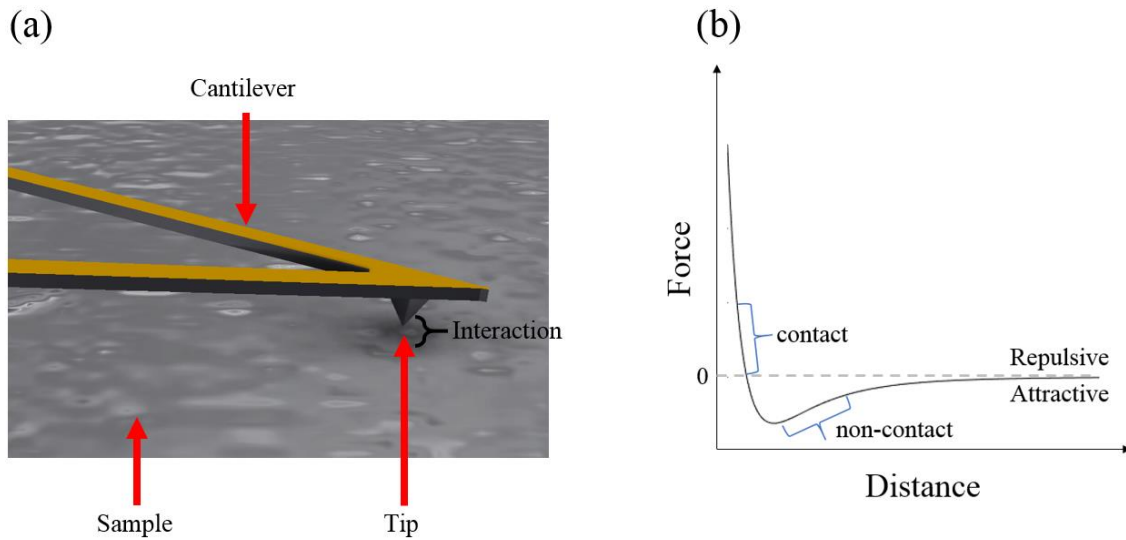
Figure 2: 3D schematic of the probe-sample interface in atomic force microscopy (AFM) (a) and a graph showing the Leonard-Jones model with two distinct AFM modes labelled (b) (not to scale) where intermittent contact mode falls in between these regions.

A large amount of research and development into AFM has been carried out at the University of Bristol (18–21). As part of this development, an HS-AFM became commercially-available from Bristol Nano Dynamics (Bristol, UK) and installed as part of a University of Bristol facility which is available for both academic and industrial use (an EPSRC TRAC Facility) that has led to a number of recent notable publications (1,22–24). The methodology that is implemented in the commercial AFM (Bristol Nano Dynamics, Bristol, UK), underpins the work done here in investigating the potential for OPUs to be used in a high-speed, contact mode, atomic force microscopy detection head. Figure 3 shows the principle functional components of the LDV based HS-AFM (Bristol Nano Dynamics, UK).
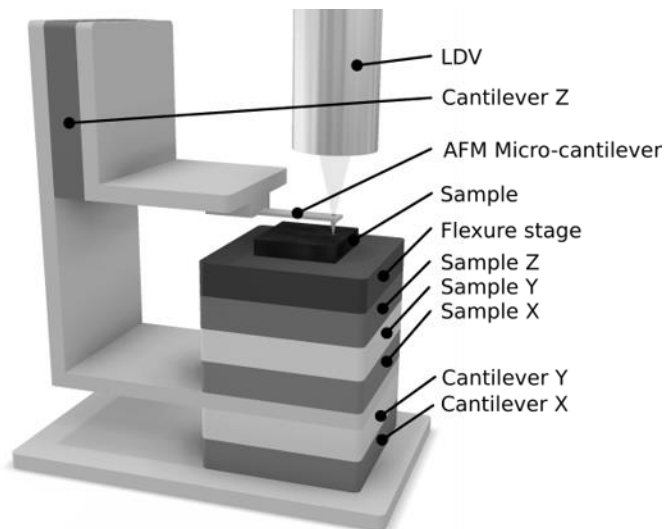
Figure 3: 3D schematic of the laser doppler vibrometer (LDV) high-speed contact mode atomic force microscope, showing a number of stacked actuators, each moving either sample or cantilever in the axis x, y or z (not to scale). *(Reproduced with the permission of O. Payton)*

In this work, a focus is put upon integrating an OPU in place of the LDV, within a bespoke HS-AFM used in contact mode. This instrument is constructed to incorporate a similar methodology and set of design considerations to that shown in Figure 3, for not only the detection of the cantilever but also to measure the location of the sample whilst it is actuated at high line-scan rates (i.e. a fast scan (x-axis) of kHz rates and a slow scan (y-axis) of Hz) over several micrometres by the flexure stage.

The novel implementation of OPU technologies to AFM has been a research objective of a number of notable works since the initial reporting of this method by Quercioli (1999) (2,6,25–30) each offering exciting opportunities for new measurement and discovery. Prior studies show OPU-based AFM measurements have been validated via calibration grids (2,27,29,31). Other published research shows how these tools can, in turn, be used for nanoscale studies such as the analysis of DNA (1,32,33) or 2D materials (28,34,35), demonstrating how these novel configurations can yield immediate impact in modern emerging research fields.

1.4 Optical profilometry

As mentioned in the previous section, AFM provides high lateral and height resolution. However, as AFM is a force-based measurement, it can be very sensitive to surface properties such as sample stiffness, high-aspect topography and loose surface debris leading to tip contamination, for example (36). In addition, the high lateral resolution (e.g. <5-20 nm) means it requires a lot of measurements to be taken to extend the imaging area up to 10-100s of micrometres (37) with high pixel density. By contrast, optical profilometry, a surface imaging technique described is this section, is a non-force-dependent surface microscopy technique. The lateral resolution of optical profilometry

8

outlined in Chapter 4 is much wider than is seen in AFM by a factor of 100-500 times, owing to the lateral resolution being limited by the laser spot size (i.e. ~1 μm).

The working principle of an optical profilometer to collect surface microscopy data is displayed in Figure 4. One benefit of using an optical pickup in the optical profilometer head is to make use of the inbuilt multisegmented photodiode, as the reflection of the focussed laser beam from the surface is made incident on a quadrant photodiode and the signal is read out independently. Several type of measurements can then be derived from this sensor input, such as total reflected light from the sample, a measure of displacement using a calculation of the focus of the laser beam and angular variations on the sample due to the centre of the returning laser beam being offset from the centre on the sensor.
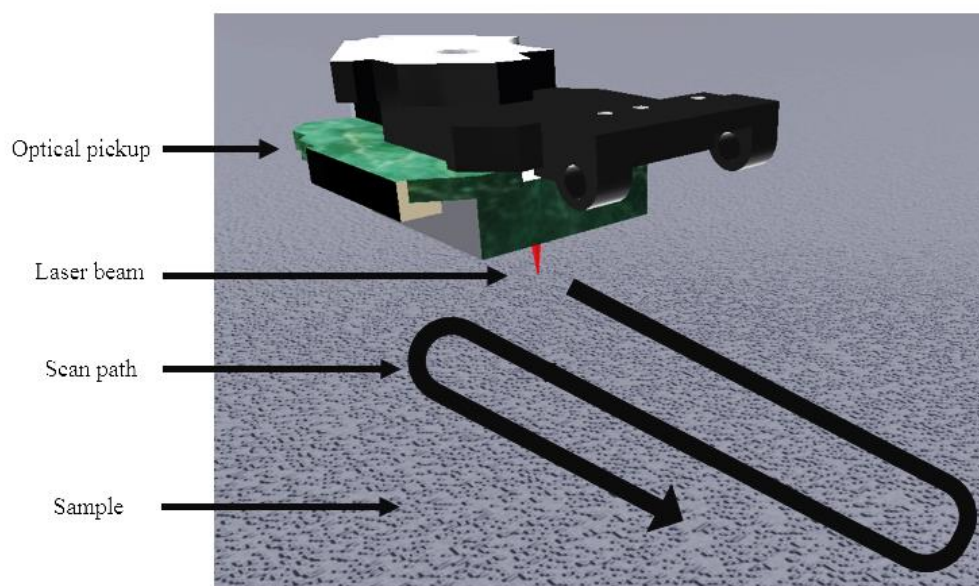
Figure 4: 3D schematic demonstrating how a 3D optical profilometer collects surface topography measurements (not to scale).

This thesis looks at several novel configurations of OPU-based optical profilometry for large-area topography mapping, real-time surface dynamics and as a tool to exist within an AFM detection head for cantilever alignment. The areas of study described in Chapter 4 include surface inspection of synthesised thin films of uranium dioxide within the field of material science, surface inspection of a leaf (species: Tilia Cortada) surface for biological studies, evaporation of microdroplets for dynamic metal corrosion studies and dimensional measurement of a cantilever for AFM alignment.

A number of related works into OPU-based profilometry have been conducted previously, with a focus on biological samples such as cells and molecules (33,38,39), dimensional measurement (13,40) and surface inspection (41,42). Whilst the measurement properties of OPU-based optical profilometry are not as unique as AFM, as many other sensors could do an equivalent role as the OPU in this method, the technique is very complementary to OPU-based AFM. OPU-based profilometry not only offers a different scale of measurement, allowing imaging of a wider field-of-view in the same time but also a

non-contact alternative to AFM that can be used to inspect a sample surface prior to making contact with it. Crucially, the technique is also available with little modification within the OPU-based AFM detection head mentioned in the previous section, as little additional hardware is needed beyond that already required for an AFM detection head. Using multiple surface inspection techniques in a single detection head gives great opportunity to use correlative microscopy to show how AFM measurements on the nanoscale relate to higher-scale phenomena on the sample, reinforcing the scalability of the surface studies and increasing the numbers of scale lengths an OPU-based instrument can operate over.

1.5 Positioning: actuation and sensing

Whereas the previous two chapter outlines have concentrated on studying an entire instrument and their application, Chapter 5 focusses specifically on positioning applications (i.e. both sensing and actuation) of the OPUs. In part, this chapter reveals further information about the positioning performance of the OPU-based HS-AFM and optical profilometer. In addition, studies go on to demonstrate how novel configurations can both reduce the error in existing commercial instruments and give rise to a prototype tuning fork based high-speed scanner that could make use of the higher bandwidth provided by the optical pickups in future work.

The body of experimentation carried out in this chapter focusses on the custom-built actuators that were made in this work to perform HS-AFM and optical profilometry. To generate the motion, four types of actuators were implemented: piezoelectric actuators; voice coil motors; tuning fork oscillators and reduction mechanics. To evaluate the actuators' performance, three types of optical sensors were then used, including a laser Doppler vibrometer, multi-axis fibre interferometer and multiple optical pickups.

In Figure 5, a standard arrangement of these actuators and sensors in a 2D scanner are shown in relation to the sample. Arranging them in this way allows for the comparison on the drive signal waveform to be compared to the sensor waveform and the determination of sources of error in the motion due to effects such as non-linearity, electronic noise and mechanical vibration. In Chapter 5, different cases show how the sample and detection head are moved with respect to one another to facilitate a 2D scan path and enable imaging.
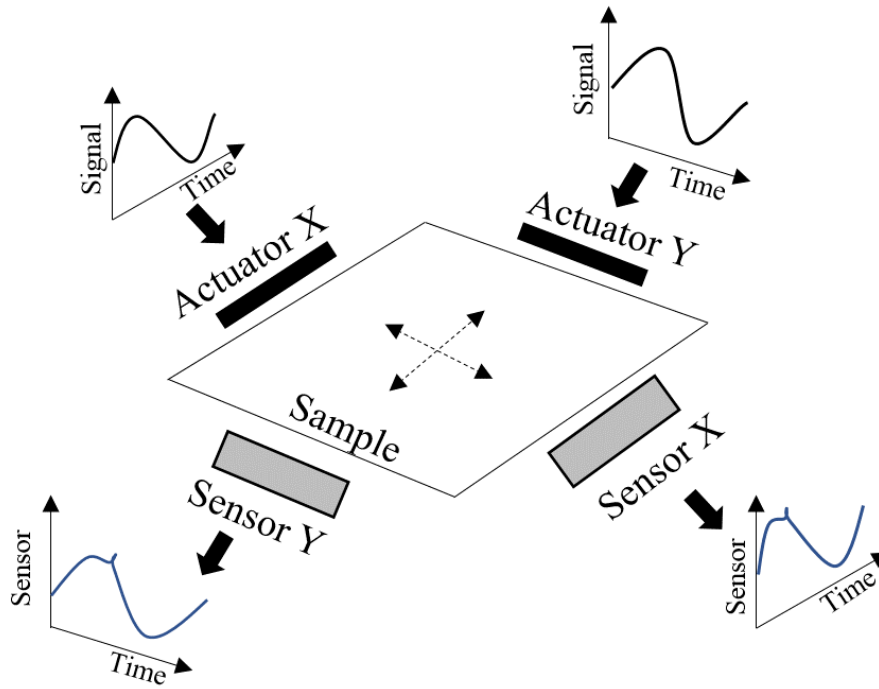
Figure 5: Simplified schematic of the principal components of multi-axis scanning for surface microscopy (not to scale), where graphs are displayed in arbitrary units.

Positioning at the nanoscale is a large research field as it underpins a wide variety of tools and techniques used for measurement and alignment at this scale. Optical pickups are well-suited, compact, low-cost and high-bandwidth optical sensors which can also operate as nano-to-millimetre scale actuators. This combination offers tremendous application potential in a variety of positioning applications. Implementation of optical pickups in bespoke positioning configurations is less widely reported than some of the previously-mentioned implementations of optical pickups. Some previous studies have looked at them as nanoscale actuators (27), motion sensors (43) and scanning lens microscopes (44).

1.6 Digital image processing

Chapter 6 focusses on the algorithms that were developed and implemented to process the sensor data, which had been collected by OPU-based microscopes developed in this work, once the digital images had been constructed. The purpose of these algorithms was in part to improve the imaging capabilities of the microscopes in real-time, allowing for reduction in sensor noise and imaging artefacts. An additional purpose of this work was to extend the field-of-view of the instruments via planar motion of the imaging window over the sample and the use of image combination (i.e. image stitching like in a panoramic photograph) using a normalised cross-correlation-based algorithm created for the instruments developed in this thesis.

In Figure 6 a simplification of the steps taken to construct a digital image from a scanning microscope, such as the ones developed in Chapter 3 and Chapter 4 is presented, where Figure 6 (a) shows how the unique measurement area (grey circle) might be translated to the first five locations of a simplified path. Figure 6 (b) shows a typical waveform response from the sensors at each of these locations over time, where a changing velocity of the scan path has resulted in a different amount of time being attributed to each position on the sample. Figure 6 (c) shows how these unique measurement locations can then be attributed to unique pixels in a 2D array or image or the first row.
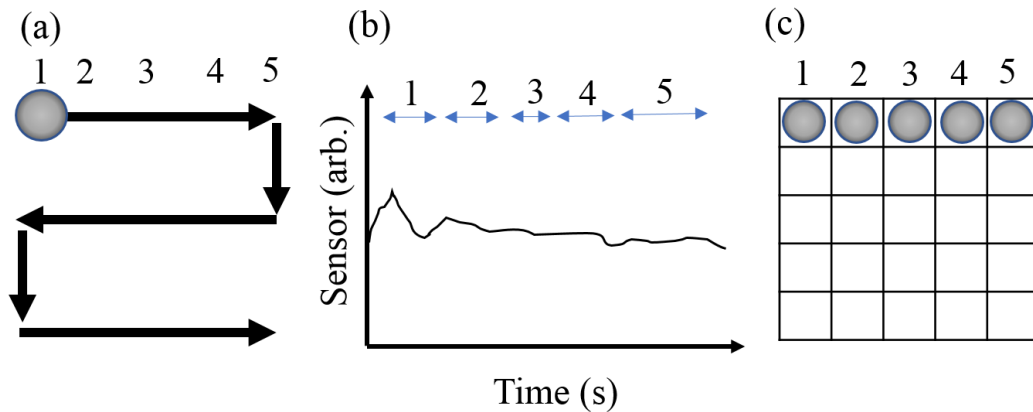
Figure 6: Construction of a digital image from a scanning microscope path (a), sampled with sensor waveforms (b) and then binned in accordance to location (c).

Whilst a wide variety of commercial image processing tools and software exist for post-processing, these environments cannot typically be immediately implemented for real-time processing on instrument data. As such, this chapter presents a program written in National Instrument's (NI) (USA) Labview and in places benefitting from tools from NI's Vision environment, to create routines, programs and executables which allow for traceable manipulation of the raw data collected by the instruments. For each routine, case studies using data from an HS-AFM, optical profiler or 'stock' images akin to surface microscopy data with synthesised noise have been used to validate the methods that have been implemented.

Extensive research, prior to this thesis, has gone into creating programs for the post-processing of surface probe measurements, for example Gwyddion (45) is ubiquitously used. Much of the available software has vast capability, such as found in ImageJ (46), an open source program to post-process microscopy images, that provides plugins that offer scripting to allow for processing of data on bulk. Equally, in surface microscopy the application of custom Labview routines, such as the ones provided by NI's Vision, have also been shown to be effective with AFM images (47). As a result, Chapter 6 does not have scope to seek to explain or evaluate all routines that could be implemented. Instead, the chapter covers those methods that were implemented in-real time or in immediate post-processing and which, in turn, had a consequence of significantly benefitting the studies carried out by the surface microscopy instruments developed in this work.

1.7 Summary

Having described the background of optical pickups, the development and characterisation of custom-built hardware to control optical pickups (Chapter 2) carried out in this thesis go on to permit the development of multiple configurations described in Chapters 3-5, which have notable applications in surface microscopy. As well as giving a detailed description as to the instrumentation and methods developed in this work, efforts have been undertaken to build software environments that control these instruments, which can process the data in real-time, thus improving the scope for observation using these measurement tools. Where appropriate, additional executables and example data can be found in an external media storage. Further details relating to this can be found at the back of the thesis.

Chapter 2. Optical pickups: function and control

The focus of this chapter is to give detailed insight into the motivation, properties and requirements of optical pickups (OPU) used to read and write to optical media disc storage formats. As part of a review of the operational requirements of an OPU in general terms, the key measurement systems fundamental to their functionality are described in detail. The properties and requirements of a specific OPU (SF-HD65/850, Sanyo, Japan), for combined use with both CD and DVD, are then explored with the view to building bespoke electronics to integrate with the device and to make use of it's inbuilt emission, actuation and measurement systems. Building upon understanding of the typical properties for optical pickups and the detailed specification for the SF-HD65/850, this chapter then focuses on the novel electronics that were developed to allow for user operation of this OPU for experimental purposes.

2.1 An overview of optical pickups

Modern optical pickup heads, such as those commonly found in CD, DVD and Blu-ray players, are designed to read from and in some cases, write data to a disc using a method that stems from a technique originally documented in a patent granted in 1970 to J. T. Russell entitled 'Analogue to Digital to Photographic Recording and Playback System' (48). A key factor that led to the long-running success of this portable digital storage medium was the high density of data storage of 10^6 bits per square inch (48). Other factors for success over the following years include the low-cost of reproduction and the longevity of the stored information. These outstanding properties resulted in optical media discs becoming more popular than other storage mediums for media, such as magnetic tape or phonograph records in popular consumer electronics by the early 21st century. Several distinct types of discs were developed thereafter, significantly driven by the global demand to have high quality, compact and portable media players for a low cost.

The first and well established optical media disc, the compact disc or CD, was to be used ubiquitously over the coming decades and sold over 200 billion units by its 25th anniversary (4). The compact disc is made up of four distinct layers: a polycarbonate layer; an aluminium reflection layer (40-80 nm); a protective lacquer 10-20 µm; and an artwork layer (49). The digital data are encoded onto the polycarbonate layer. The bits (i.e. 0 or 1) are encoded onto the optical disc with the use of two different physical 'states', otherwise referred to as 'channel bits'. The first physical state consists of a

low area of the disc that has been engraved away to a depth equal to a quarter of the wavelength of the laser light; this is referred to as a 'pit'. The second physical state consists of a high area of the disc without engraving; this area is referred to as a 'land'. The information is encoded to the disc in such a way that a '1' bit corresponds to a state changing (e.g. from pit to land) and a zero bit corresponds to a state not changing (i.e. remaining as a pit or a land). Additionally, for every eight bits (or one byte) of information, eight-to-fourteen modulation (EFM) (50) is used to write eight bits of information into 14 physical channel bits on the disc. This process, later extended to EFMPlus (51), is also found in DVD formats. Crucially, it ensures that there is a minimum of two consecutive channel bits of the same type (i.e. land or pit) and no more than a maximum of 10 consecutive channel bits of the same type in a row. This helps to avoid situations where a large number of pits could be written in a row, which could result in sustained periods without a change of state and, therefore, no measure of angular velocity of the disc. Such constraints mean that every pit and land correspond to at least three clock ticks in the system. As such, it reduces the demands on the reading/writing to the disc and makes the disc more resilient against surface defects, dust and handling damage.

To detect for land or pits on a compact disc format, a near-infrared laser with wavelength 780 nm is used in tandem with a multi-segment photodiode. As the pits have a depth of a quarter of the wavelength of the laser light, should the laser beam be part incident on a pit and part on a land, the pit-reflected laser will be 180º out-of-phase with the laser beam incident on a non-pitted area and, thus, destructively interfere and cause a drop in laser light intensity incident on the photodiode (52). Consequently, the compact disc has the physical properties as labelled in Figure 7.

Compact Disc (CD)

State length:	850 nm
State width:	500 nm
Track pitch:	1.6 μm
Spot size:	1.7 μm
Wavelength:	780 nm
NA:	0.4-0.45
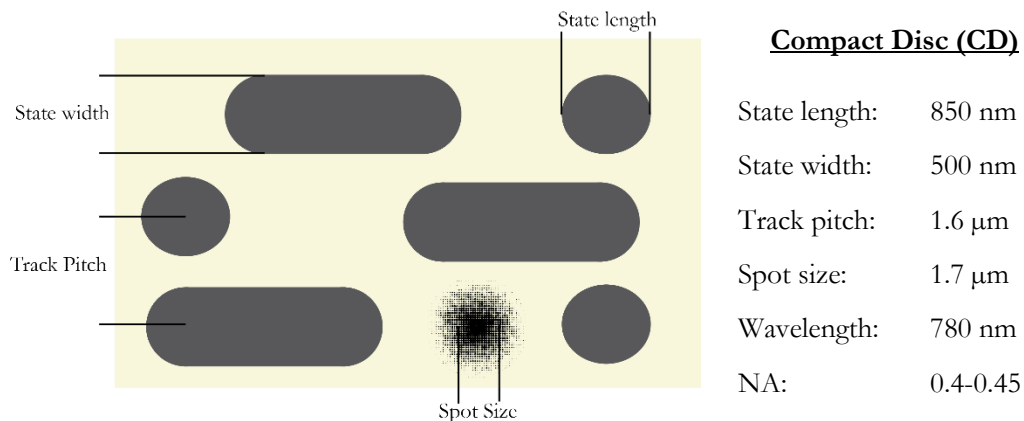
Figure 7: Identifying important physical dimensions of an optical disc and dimensions. (51)

The track on a CD spirals out from the centre of the optical disc, with a track pitch of 1.6 μm (Figure 7) resulting in a total spiral track length of 5.38 km on the disc, able to contain up to 650 MB of digital information.

The external dimensions of the optical disc are typically common between CDs, DVDs and Blu-ray discs. However, a key distinction between the three formats is the wavelength of the laser diode

used in the pick-up unit; DVD pickups use a 650 nm laser and Blu-ray pickups use 405 nm wavelength lasers. The impetus for using these shorter wavelengths of light, compared to that used for CD, is that it is possible to achieve narrower spot radius thus smaller track pitches, state length and state pitches, resulting in a higher data storage density on the disc. The physical dimensions can be found in Figure 8. From 1991 to 2006, the development of this technology increased the data density of the digital information from 0.1 Gbits/in^2 to 500 Gbits/in^2 (51). With such improvements a typical single-layered DVD is able to store 4.7 GB and a single-layer Blu-ray discs 25 GB.

Digital Versatile Disc (DVD)		Blu-ray	
State length:	400 nm	State length:	150 nm
State width:	320 nm	State width:	130 nm
Track pitch:	740 μm	Track pitch:	320 μm
Spot size:	1.1 μm	Spot size:	480 nm
Wavelength:	650 nm	Wavelength:	405 nm
NA:	0.6-0.65	NA:	0.85

Figure 8: Physical dimensions in DVD and Blu-ray format optical media discs (51)**.**

2.1.1 Embedded optical and electromechanical systems

In Figure 9 a 3D exploded diagram of a typical arrangement (53) of optical, electrical and mechanical components found in an optical pickup is presented. From this schematic, it is possible to see the path the laser light takes after being emitted from the laser diode, reflecting off the optical media disc and falling on a quadrant photodiode. While the laser diode, beam splitters and objective lens are in a standard configuration common to a simple microscope, the addition of the voice coil motors around the objective, an astigmatic lens and a quadrant photodiode into the system can only be understood by considering the calculations of the focus and tracking errors that are made whilst the optical pickup is in typical operation. Further explanation of these detection systems is outlined in the following sections.
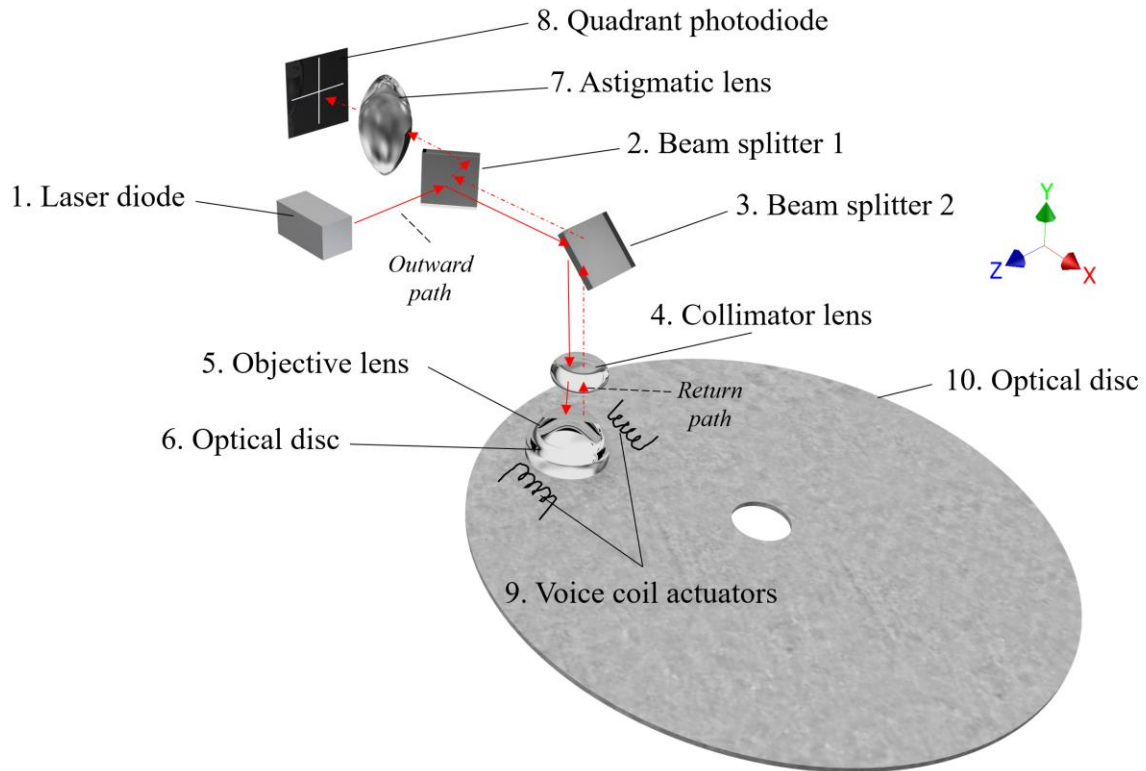
Figure 9: Simplified 3D schematic showing how the optical and electromechanical systems in an optical pickup are placed with respect to one another (not to scale) (54)**.**

2.1.2 Focus error detection

A key measurement system found in optical pickups is the focus error (FE) detection mechanism (53), which is used whilst the OPU is in operation to ensure the laser spot is in focus on the disc and can successfully read the pits and lands. A typical method for detecting the FE signal makes use of an astigmatic detection system (ADS).

"Within the ADS, a quadrant photodiode (QPD) generates a measure of the FE of the laser relative to the disc surface. The FE measurement is taken by focusing the returning laser beam through an astigmatic lens onto the QPD. When focussed through a lens, the astigmatic beam has two orthogonal focal planes: the sagittal and tangential. These focal planes are offset in space by a fixed distance that is a property of the emission laser. The laser is deemed in-focus when the reflected beam falls symmetrically about the centre point of the two focal planes" (2). Figure 10 looks to demonstrate how a change in physical displacement of a reflective surface results in a different laser profile being incident on the quadrant photodiode.
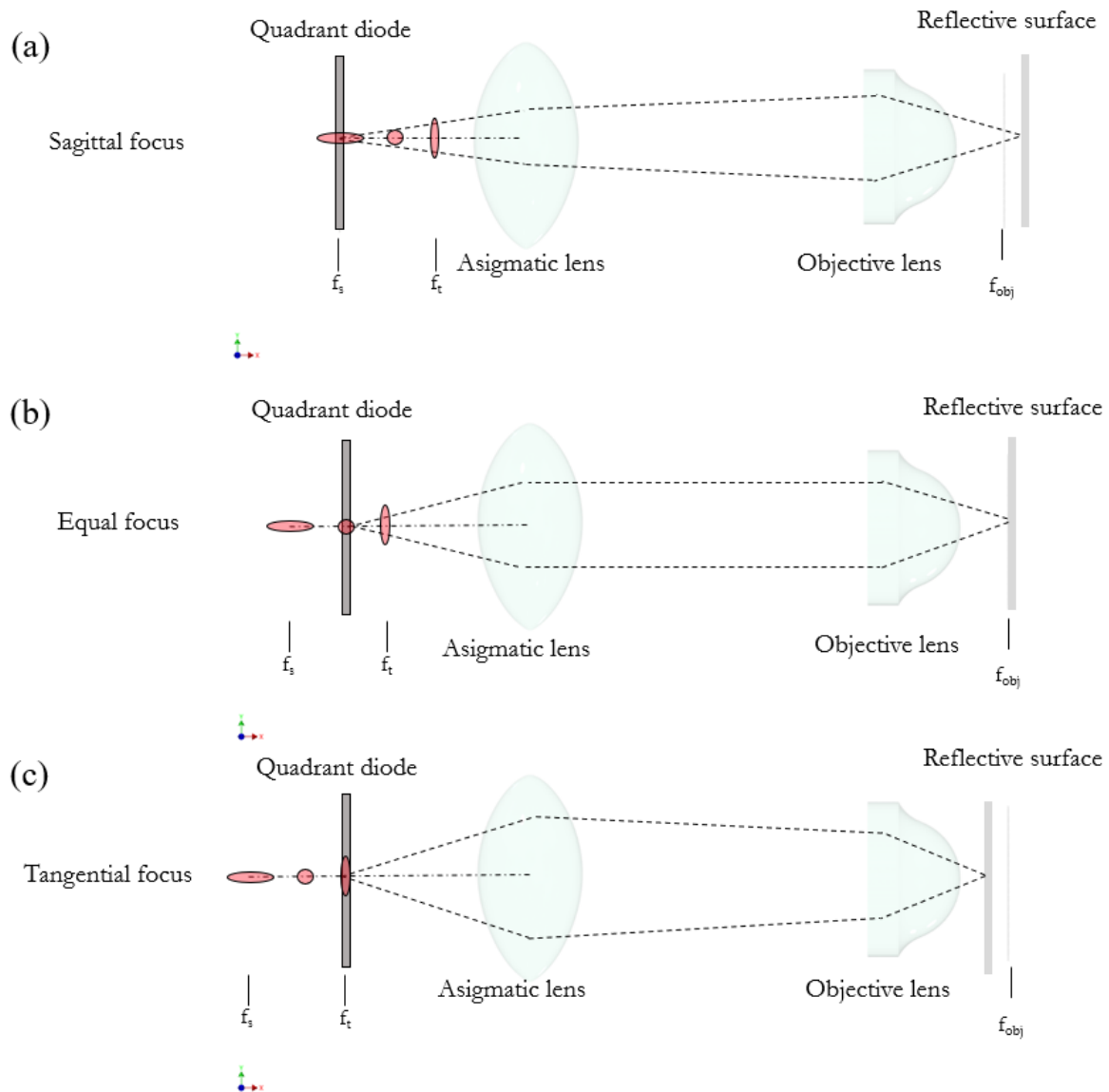
Figure 10: Simplified version of an astigmatic detection system that is typically found in an optical pickup to measure the focus of the system. In this instance, the sagittal focus is achieved if the reflective surface is slightly too close to the objective (a), the laser is deemed in focus (b) if it is in the transition between the sagittal focus (a) and the tangential focus (c).

In Figure 11 it is shown how the different laser profiles fall incident on the photodiode (i.e. quadrant A, B, C & D). By taking signals from the four quadrants it is possible to then make a measurement of focus error using Equation 2 (p. 20). Additionally, to normalise against fluctuations in laser intensity incident on the photodiode, the normalised focus error (NFE) can be calculated using Equation 3 (p. 20).
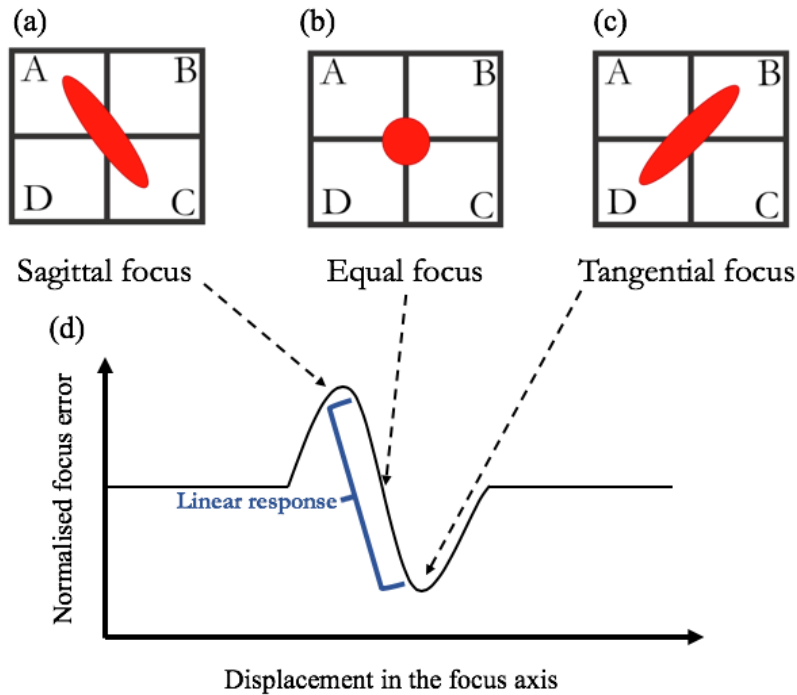
Figure 11: A QPD with the quadrants labelled (A-D). The three most distinct focal regimes of the astigmatic detection system are shown ((a)-(c)). The beam profile incident on the QPD is shown in each case. An idealised response curve is then plotted in (d) showing how the significant features correspond to the different focal regimes.

$$FE = (A + C) - (B + D) \tag{2}$$

$$NFE = \frac{(A+C)-(B+D)}{A+B+C+D} \tag{3}$$

The idealised response graph, commonly referred to as the s-curve, is plotted in Figure 11 (d), showing how the NFE output is predominantly linear when the ADS is in focus between the sagittal and tangential focal planes. This part of the response curve is known as the linear region and is used to ensure that the laser remains in the middle of this, where equal focus is achieved and there is an equal contribution from A, B, C and D, throughout operation. In each type of optical media disc the linear region of the astigmatic detection system varies as follows: ~9 µm (CD); ~6 µm (DVD); and ~3 µm (Blu-Ray) (55).

2.1.3 Tracking error detection

Another principle measurement system built into the optical pickup measures the tracking error (TE). This ensures that the laser spot tracks the spiral of pits and lands that extends out from the centre of the optical disc. This detection is measured using either the three-beam method (5), differential push-pull (DPP) (5) or differential phase detection (DPD) (5,56) depending on the optical media disc type. For the first two methods, the integrated photodiode requires addition segments names E-H, and arranged as shown in Figure 12.
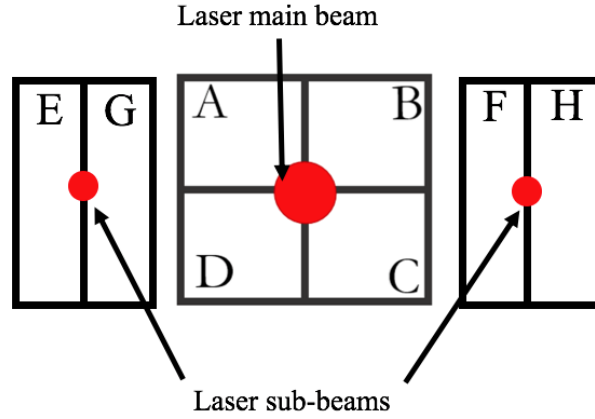
Figure 12: Schematic supporting the explanation of calculating the tracking error in an optical pickup with the use of addition sub-beams, photodiodes and methods including three-beam, differential push-pull and differential phase detection.

The TE can then be calculated in the following way for each method:

Three-beam method devised for CD-ROM,

$$TE = E - F \tag{4}$$

Differential push-pull (DPP) method devised for CD-R and CD-RW,

$$TE_{PP} = (A + D) - (B + C) \tag{5}$$

$$TE_{SPP} = (E + F) - (G + H) \tag{6}$$

$$TE_{DPP} = TE_{PP} - TE_{SPP} \tag{7}$$

Whilst the DPP could be applied to the land-pit structured DVD-R and DVD-RW optical disc structures, it is not appropriate for DVD-ROM as it doesn't use a land-pit structure (5). Therefore, a third generation of tracking error calculation was developed called the differential phase detection (DPD) method. The DPD method is calculated by looking at the phase difference between the four photodiode quadrants (A-D). To perform this measurement electronics are used in the configuration as outlined in Figure 13.

A single method of calculating the tracking error is typically attributed to a given CD, DVD or Blu-ray laser pathway. However, within a single multifunctional OPU multiple techniques can be present, such as the OPU described later in this chapter which contains the three-beam method for the CD laser pathway and the DPD method for the DVD laser pathway.
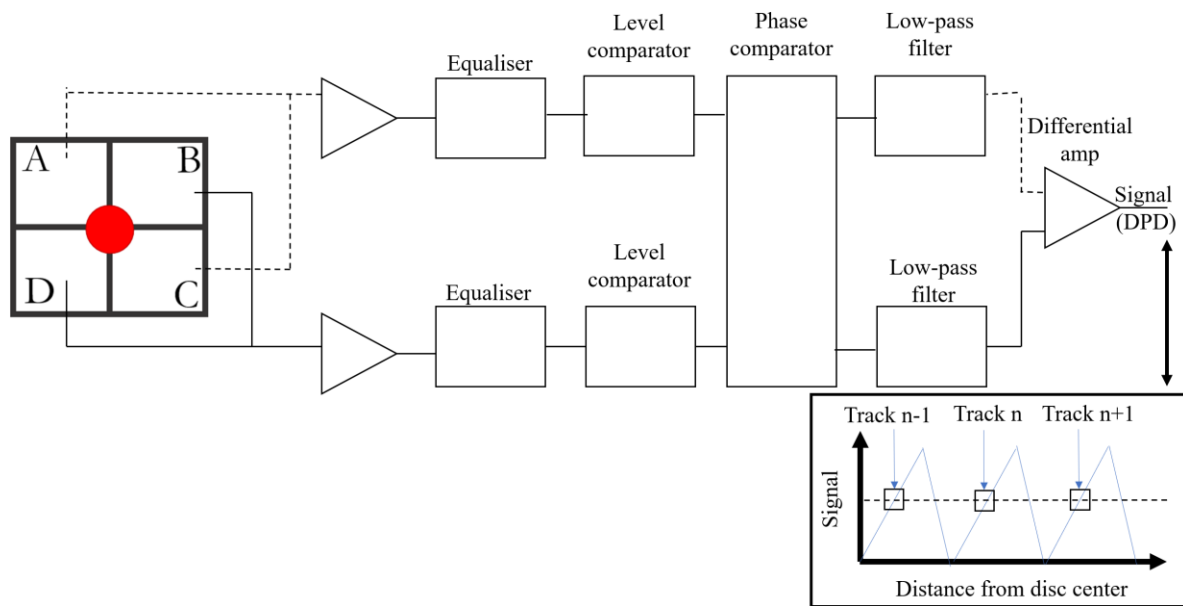
Figure 13: System schematic of the electronics used to calculate the differential phase detection (DPD) tracking error signal in optical pickup units (5,57)**.**

2.1.4 Focus and tracking actuators in optical pickups

Whilst the scheme described in 2.1.2 and 2.1.3 perform the measurement of focus error and tracking error in each case, the systems do not inherently attempt to reduce the error. This function is left to a positioning system surrounding the objective lens of the OPU. The positioning system is a multi-axis system that implements the use of the focus and tracking actuators, whilst additional degrees of freedom, such as angular actuation, tip or tilt are also implemented in some cases (e.g. OPU66.50 D, Phillips, Netherlands). It is typical, as shown earlier in Figure 9, for the multi-axis positioning system to be based on a voice coil motor (VCM) to allow for a control loop to reposition the lens in response to measured errors. By passing a current through either coil of wire attached to the objective lens, which is between two permanent magnets, the lens is displaced along the focus axis. In Figure 14, a schematic is presented to outline the orientation of the voice coil motors with respect to the optical media disc.
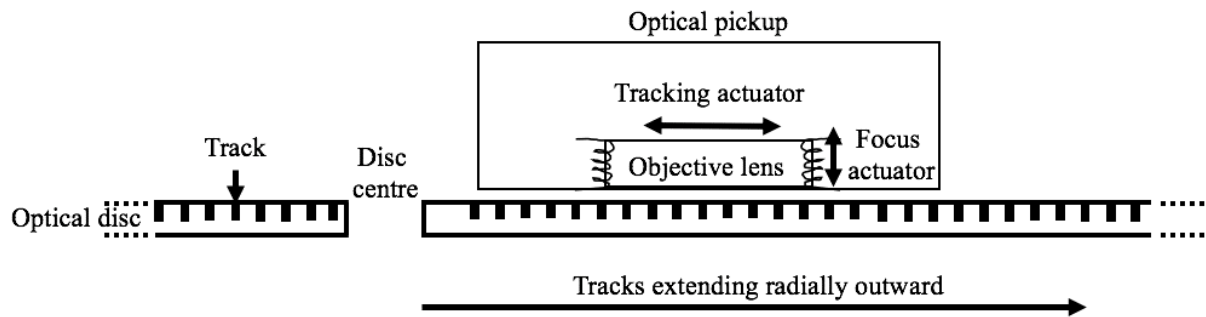
Figure 14: Schematic representing how the voice coils surrounding the lens are oriented to allow for correction of the focus and tracking errors measured by the focus error and tracking error detection systems in an optical pickup (not to scale).

2.1.5 Overview of an optical pickup: conclusions

In this section an overview of the background, hardware and methods of optical pickups found in CD, DVD and Blu-ray drives has been outlined. With such high commercial demand for these devices globally to be integrated into domestic media players, computers and portable music players (e.g. Discman, Sony) the unit cost has been driven down dramatically, with units being made available for <£5. Having given an overview of the key principle capabilities found in optical pickups in this section, the next looks in further detail at a specific example, the Sanyo SF-HD65/850, a commercially-available optical pickup for which a specification datasheet has been made widely available by retailers (e.g. RS Components, UK) when purchasing a replacement pickup. Typically the OPU can be used out of the box, however in this work the small modification of removing the diffraction grating (see Figure 15 for further details) is carried out to increase the laser intensity through the objective and reduce the amount of scatter light caused by the addition optical interface.

2.2 Sanyo SF-HD65/850 operational overview

For the research carried out in this thesis, a Sanyo SF-HD65, or the model variant, Sanyo SF-HD850, optical pickup has been used. The production of these optical pickups dates from 2006 for the SF-HD65 and 2007 for the SF-HD850. This optical pickup has the capability of reading both CD and DVD optical media discs and, therefore, contains a dual wavelength (i.e. CD: 790 nm and DVD: 650 nm) laser diode. As well as the dual-wavelength laser diode, a dual-axis (i.e. focus and tracking) voice coil motor surrounds the objective lens. This optical pickup also has an inbuilt high-frequency modulator, which helps reduce relative intensity noise of the laser and reduces the amount of current needed to drive it. Another key advantage is that the QPD quadrants (A-D), based on an embedded integrated chip, output pre-amplified voltage signals from the optical pickup. This minimises the signal path length and, therefore, minimises the opportunity for the current outputs from the QPD quadrants to pick up noise prior to subsequent additional amplification. A labelled diagram of this optical pickup is seen in Figure 15.

23
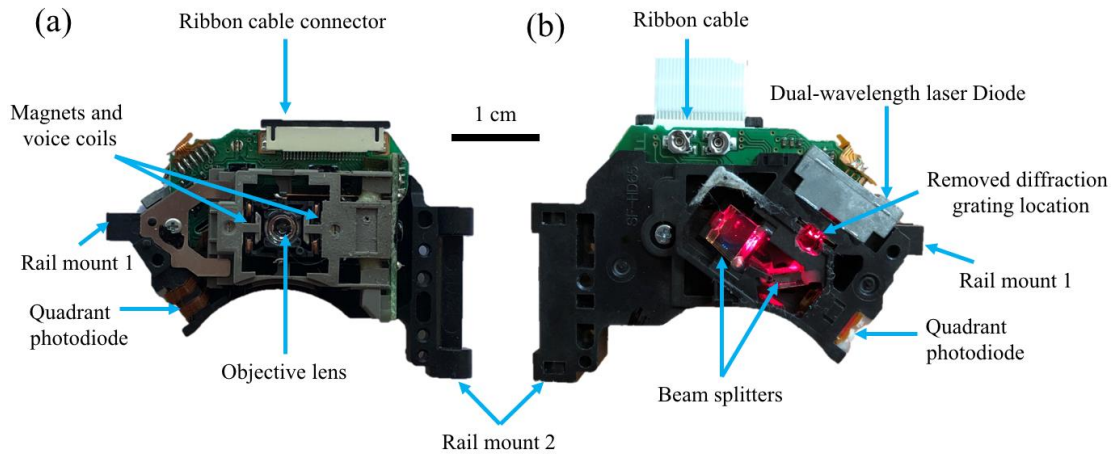
Figure 15: External photos (emission side (a) and reverse side (b)) of the Sanyo-HD65 OPU, with visible components labelled next to a 1 cm marker for scale.

2.2.1 Sanyo SF-HD65 pin allocation

Whilst common themes between the pin allocation on OPUs can be seen, each OPU tends to have a unique multi-pin interface that can typically have between 10-100 uniquely addressable pins. The mapping of these pins is rarely readily available or accessible, as they are often written with the intention of only expert use and internal work within a company.

To access the control and sensing channels on the Sanyo SF-HD65/850 a 24-pin flexible printed cable (FPC) or 'ribbon cable' is used. The pins on the optical pickup are then grouped in accordance to the three key functions of the optical pickup namely: emission (laser diode); actuation (dual-axis voice coils); and sensing (quadrant photodiode). An itemisation of the relevant pins is shown in Figure 16.

Whilst the table of pins acts as a guide in accessing the principled systems onboard the optical pickup, careful consideration for the electronics that interfaces with some of them is needed. A more detailed description of the groupings of pins is then further explained in the following sections.

	PIN No.	PIN 名前 PIN name	機能区分 Functional unit	Added context:
'Actuation'	1	F−	アクチュエーター Actuator	The negative direction in the focus voice coil actuator
	2	F+		The positive direction in the focus voice coil actuator
	3	T+		The positive direction in the tracking voice coil actuator
	4	T−		The negative direction in the tracking voice coil actuator
'Sensing'	5	C/c	受光素子部 Photo detector	The C quadrant of the quadrant photodiode (capitals=CD lowercase=DVD)
	6	D/d		The D quadrant of the quadrant photodiode (capitals=CD lowercase=DVD)
	7	CD/DVD SW		Logic pin for switching between the CD and DVD laser (see logic later)
	8	RF		Onboard summation of A/a, B/b, C/c & D/d
	9	A/a		The A quadrant of the quadrant photodiode (capitals=CD lowercase=DVD)
	10	B/b		The B quadrant of the quadrant photodiode (capitals=CD lowercase=DVD)
	11	F		The F quadrant of the quadrant photodiode (capitals=CD)
	12	GND−PD		Ground pin for the quadrant photodiode
	13	Vc(Vref)		Reference voltage for the quadrant photodiode
	14	Vcc		Power for the photodiode (5V)
	15	E		The E quadrant of the quadrant photodiode (capitals=CD)
	16	(N.C.)		Not connected
'Emission'	17	VR−CD	レーザー部 Laser diode	Variable resistor for CD (see logic later)
	18	VR−DVD		Variable resistor for DVD (see logic later)
	19	CD−LD		Monitoring diode inside the laser
	20	MD		Monitoring diode inside the laser
	21	HFM		Logic for turning on the high-frequency module
	22	(N.C.)		Not connected
	23	DVD−LD		Input voltage for the laser diode (5V)
	24	GND−LD		Ground for the Laser diode

Figure 16: Pin-out allocation on the Sanyo 65/850 DVD optical pickup (taken from the SF-HD65 specification sheet by Sanyo, Japan) with a table of additional description for reference.

2.2.2 SF-HD65/850: emission – dual-wavelength laser diode

Previously in Figure 9, it was shown how the compact dual-wavelength laser diode is positioned in relation to the optical components. The SF-HD65/850 OPUs are specified to have a maximum laser output power of 7 mW (as seen in Figure 17(a)). However, having travelled through the optical components in typical operation, the laser spot emitted from the objective lens typically has a power of 0.23 mW (CD) and 0.30 mW (DVD) for this optical pickup. The specification states that the optical pickup doesn't have an onboard automatic power control circuit (APC) and this has to be supplied externally. The specification sheet for this OPU suggests an APC circuit to use with the pickup, as outlined later in section 2.3.1. As previously mentioned, the SF-HD65/850 does have an onboard high-frequency module which is specified to oscillate at 390 MHz and is enabled by sending 5 V to pin 21 on the FPC connector (Figure 16). In Figure 17(b) and Figure 17(c) further details about the beam divergence and the presence of a monitor photodiode internal to the laser diode are described. The electrical schematic in Figure 17(c), reveals that the monitoring photodiode (MD) (pin 20, Figure 16) is of the common cathode laser diode type, as the cathodes of the two laser diodes and photodiode are all connected to pin 2 (in Figure 17(b)). This is an important consideration when powering the laser diode with an external laser driver (e.g. WLD3343, Wavelength Electronics).

(a)

5. 電気性能／ELECTRICAL PERFORMANCE

5.1 レーザーダイオード／Laser Diode

項目 Item			規格 Specifications		特記事項 Remarks
			DVD	CD	
レーザーダイオード (LD) Laser diode					TOLD2000MDA (東芝) or TOLD2000FDA (東芝) (TOSHIBA CORPORATION)
最大定格 Maximum ratings	逆電圧 [VRL] Reverse voltage		2.0 V	2.0 V	
	光出力 Laser power		7 mW	7 mW	
	動作温度 Operating temperature		−10〜+70 ℃	−10〜+70 ℃	レーザーダイオードケース温度 (Tc) Temperature on the housing case of laser diode.
電気特性 Electrical characteristics	しきい値電流 [Ith] Threshold current		25 mA (標準) (Typ.)	20 mA (標準) (Typ.)	高周波重畳オフ時 With high frequency module turned off
			45 mA (最大) (Max.)	40 mA (最大) (Max.)	
	動作電流 [Iop] Operating current		35 mA (標準) (Typ.)	35 mA (標準) (Typ.)	Po (LD unit) = 5 mW Tc=25℃
			90 mA (最大) (Max.)	70 mA (最大) (Max.)	Po (LD unit) = 5 mW Tc=70℃
APC 回路 APC circuit			無し Without APC		APC 回路基準電圧：180 mV APC circuit reference voltage
高周波重畳回路 (HFM) High frequency module	駆動電圧 [Vcc] Drive voltage		4.5 V 〜 5.5 V		推奨電源電圧：Vcc 5 V Recommended voltage power supply
	発振周波数 Oscillation frequency		390 MHz ±25%		

(b)

Product No.	Max Ratings		Lasing Wave-length (nm)	Threshold Current (mA)	Operation Current (mA)	Beam Divergence		Operation Voltage (V)	Monitor Current (mA)	Marking
	Po (mW)	Case Temperature (℃)				θ∥ (°)	θ⊥ (°)			
TOLD2000MDA	7	−10 〜 70	650/790	25/20	35/35	9/10	28/32	2.2/2.2	0.15/0.35	AN
TOLD2000SDA										B

(c)

1. Laser diode (650 nm) anode
2. Laser diode (650 nm / 780 nm) cathode / Photodiode cathode
3. Laser diode (780 nm) anode
4. Photodiode anode
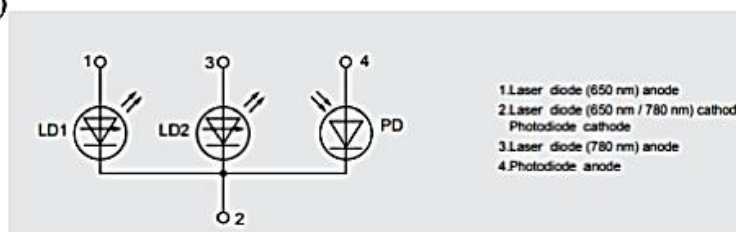
Figure 17: Detailed information regarding the emission properties of the dual wavelength (i.e. 650 nm and 790 nm) laser diode in the Sanyo SF-HD65, where (a) shows the summary electrical properties of the laser (taken from the SF-HD65 specification sheet by Sanyo, Japan) revealing a TOLD2000MDA (Toshiba, Japan) laser is used, (b) further electrical and optical properties (taken from a Toshiba-produced manual) and (c) a circuit diagram for the internal arrangement of the TOLD2000MDA (taken from a Toshiba-produced manual).

Further information surrounding the benefits of the high-frequency module can be found in Figure 18. Here, a plot taken from the specification sheet of the laser diode (TOLD2000MDA, Toshiba, Japan) is presented showing how the relative intensity noise is reduced with the activation of the high-frequency modulation, a broadening of the emitted wavelengths is observed compared to the

high-frequency modulation of the laser. In some alternative applications of the optical pickup, such as interferometry or doppler-velocimetry, this is an important consideration.
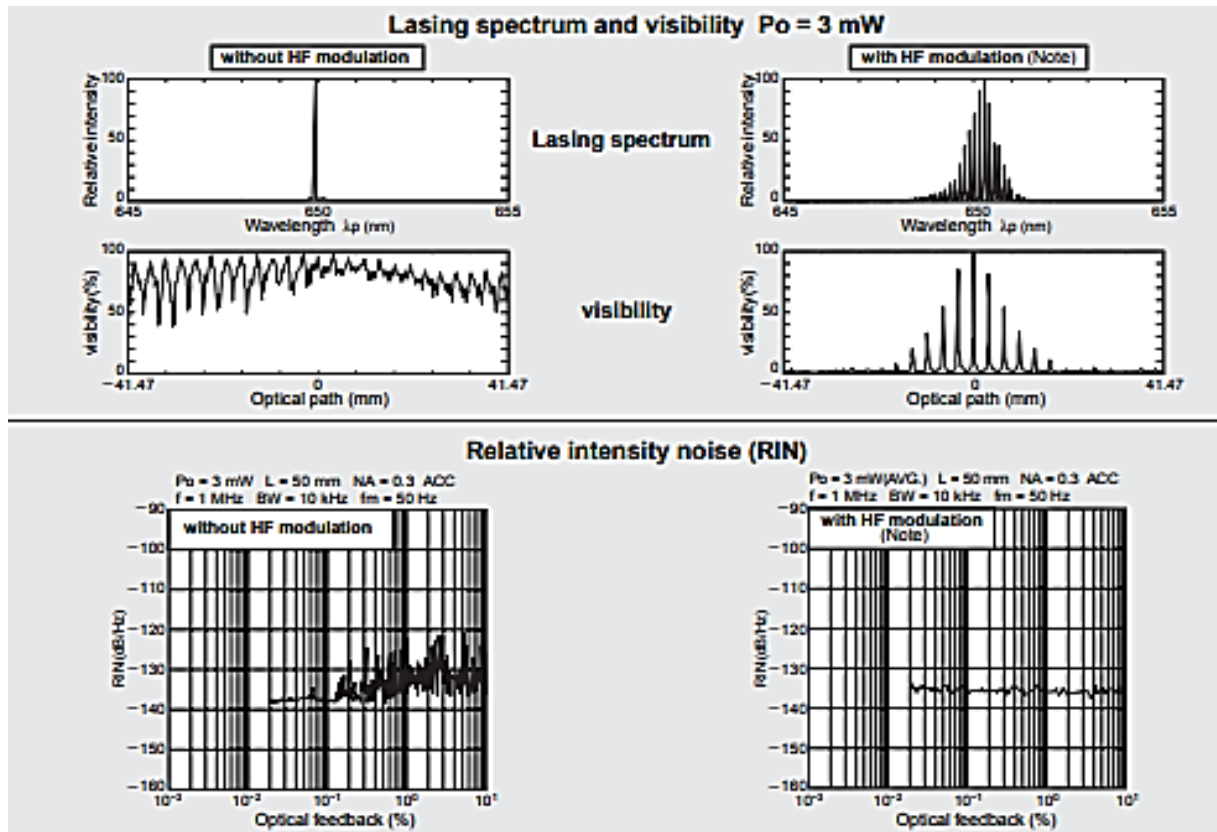
Figure 18: Comparison of the emission properties of the DVD (650 nm) Toshiba TOLD2000MDA laser diode (taken from a Toshiba-produced manual) found onboard the Sanyo SF-HD65/850 optical pickup with the high-frequency (HF) modulator switched off (left) or on (right).

2.2.3 SF-HD65/850: actuation – dual axis voice coil motors

By looking closer at an external photograph of the optical pickup (Figure 19) we can see where the integrated tracking and focusing actuators are housed within the objective lens cavity in the OPU. In the orientation the OPU is presented in Figure 19, the tracking (T) actuator acts up (T+) and down (T-) on the page and the focusing (F) actuator acts in (F-) and out (F+) of the page using the equivalent co-ordinate system, as described in the specification sheet.
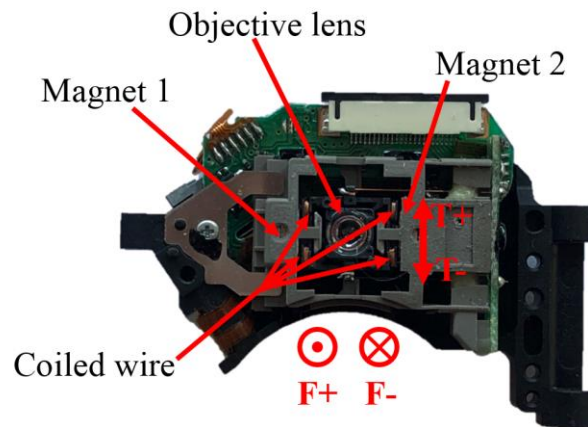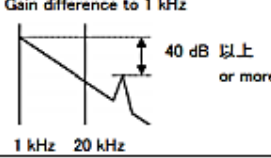
Figure 19: Sanyo SF-HD65/850 optical pickup with the focus (F) and tracking (T) axis voice coils surrounding the OPU labelled.

Looking at the summary specification for the voice coil motors (Figure 20(a) and Figure 20(b)) they require a relatively high amount of current 220 mA (continuous) per axis. The travel range of focus actuator is +1.1 mm (i.e. in the positive direction) and -0.7 mm (i.e. in the negative direction). The equivalent range for the tracking actuator is ±0.4 mm.

From looking at the physical properties of the system such as the linear range of the astigmatic detection system (e.g. typically: CD: 9 μm, DVD: 6 μm, Blu-ray: 3 μm (55)) and track width (e.g. typically: CD: 500 nm, DVD: 320 nm and Blu-ray: 130 nm (5)) it is revealed that the stability and positioning capability must be on the order of 10-100s of nanometres. An evaluation of this is conducted later in the thesis using an optical interferometer to measure the stability of the voice coils (Chapter 3, section 5.4.3).

7. アクチュエーター性能／ACTUATOR PERFORMANCE

7.1 フォーカシングアクチュエーター／Focusing Actuator
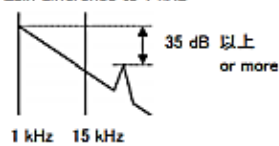
項目 Item		規格 Specifications	信頼性試験規格 Reliability specs	特記事項 Remarks
最大定格 Maximum ratings				
	コイル許容電流 Allowable current of coil	220 mA rms	———	連続 Continuous
対物レンズ可動範囲 Working area of objective lens		+1.1 mm 以上 or more −0.7 mm 以上 or more	———	水平状態を基準とする。 With reference to the level posture.
電気特性 Electrical characteristics				
	コイル直流抵抗 DC resistance of coil	5.0Ω ±1Ω	———	コネクタ部で測定 Measured at the connector part
	インダクタンス Inductance of coil	70μH ±6μH	———	At 1 kHz, 0.1 V
伝達特性 Transmission characteristics				
	感度 Sensitivity	0.80 mm／V ±3 dB	初期値 ±2 dB Within of initial value	At 5 Hz, FPC を含む With FPC
		2.20 μm／V ±2.5 dB	初期値 ±2 dB Within of initial value	At 1 kHz, FPC を含む With FPC
	共振周波数 (fo) Resonance frequency	60 Hz ±6 Hz	初期値 ±8 Hz Within of initial value	
	共振ピーク量 (fo peak) Resonance peak	16 dB 以下 or less	初期値 ±8 dB Within of initial value	
	位相遅れ Phase delay	200 ° 以下 or less	———	At 1 kHz,ピーク 点を除く Excluding peak point
	二次共振 Secondary frequency resonance peak	20 kHz 以上 or more 40 dB 以上 or more	———	1 kHz とのゲイン差 Gain difference to 1 kHz 40 dB 以上 or more 1 kHz 20 kHz
極性 Polarity		F+ 端子に +電位を印加した時、ディスクに近づく方向へ移動。(+Z 方向) When a plus voltage is applied to F + terminal pin, the objective lens approaches the disc (in +Z direction).		

※三洋電機(株)標準測定器による
With SANYO 's standard measuring equipment.

Figure 20: Table of summary specifications for the focus axis voice coil motor found in the Sanyo SF-HD65/HD850 (taken from the SF-HD65 specification sheet by Sanyo, Japan).

7.2 トラッキングアクチュエーター／Tracking Actuator

項目 Item		規格 Specifications	信頼性試験規格 Reliability specs	特記事項 Remarks
最大定格 Maximum ratings				
	コイル許容電流 Allowable current of coil	220 mA rms	——	連続 Continuous
対物レンズ可動範囲 Working area of objective lens		±0.4 mm 以上 or more	——	
電気特性 Electrical characteristics				
	コイル直流抵抗 DC resistance of coil	3.7Ω ±1Ω	——	コネクタ部で測定 Measured at the connector part
	インダクタンス Inductance of coil	9μH ±6μH	——	At 1 kHz, 0.1 V
伝達特性 Transmission characteristics				
	感度 Sensitivity	0.60 mm／V ±3 dB	初期値 ±2 dB Within of initial value	At 5 Hz, FPC を含む With FPC
		1.62μm／V ±2.5 dB	初期値 ±2 dB Within of initial value	At 1 kHz, FPC を含む With FPC
	共振周波数 (fo) Resonance frequency	61 Hz ±6 Hz	初期値 ±8 Hz Within of initial value	
	共振ピーク量 (fo peak) Resonance peak	16 dB 以下 or less	初期値 ±8 dB Within of initial value	
	位相遅れ Phase delay	200° 以下 or less	——	At 1 kHz,ピーク点を除く Excluding peak point
	二次共振 Secondary frequency resonance peak	15 kHz 以上 or more	——	1 kHz とのゲイン差 Gain difference to 1 kHz
		35 dB 以上 or more	——	35 dB 以上 or more 1 kHz 15 kHz
極性 Polarity		T+ 端子に +電位を印加した時、ディスク外周方向へ移動。(+X 方向) When a plus voltage is applied to T + terminal pin, the objective lens moves toward the periphery of the disc (in +X direction).		

※三洋電機(株)標準測定器による
With SANYO 's standard measuring equipment.

Figure 21: Table of summary specifications for the tracking axis voice coil motor found in the Sanyo SF-HD65/HD850 (taken from the SF-HD65 specification sheet by Sanyo, Japan).

2.2.4 SF-HD65/850: sensing – two multi-segment photodiodes

As discussed in Sections 2.1.1-2.1.4, optical pickups have inbuilt multi-segment photodiodes to make a number of measurements, including the tracking and focus errors. Presented in Figure 22 is an optical microscopy image taken of the integrated photodiode present in the Sanyo SF-HD65/850 that is used to sense the reflected signals from either the DVD or CD laser diode. Here, and later in Figure 22, we see that there are two sets of ABCD quadrant photodiodes for each laser and a single pair of E and F photodiode segments for the CD laser. This is because the SF-HD 65/850 uses the push-pull method for calculating the tracking error for the CD laser and differential phase detection for the DVD laser. Furthermore, it can be found what the typical bandwidth of these sensors are: 30 MHz for the CD photodiode segments and 45 MHz for the DVD photodiode segments (Figure 22(b)).

Figure 22: (a) Multi-segment photodiode found on the Sanyo SF-HD65/850 and its specification (b) (taken from the SF-HD65 specification sheet by Sanyo, Japan).

In addition to the specification of the electrical properties of the integrated photodiodes, a schematic presented in Figure 23 shows how the photodiode current outputs are mapped internal to transimpedance amplifiers, with the reference voltage (Vref) incident on the positive input. This diagram shows the function of the switching pin (SW) (i.e. from CD to DVD) and how the sum (RF) pin is calculated from the quadrant photodiode. Additional information about how the high-frequency modulation component interfaces to the external FPC pinout is also displayed.
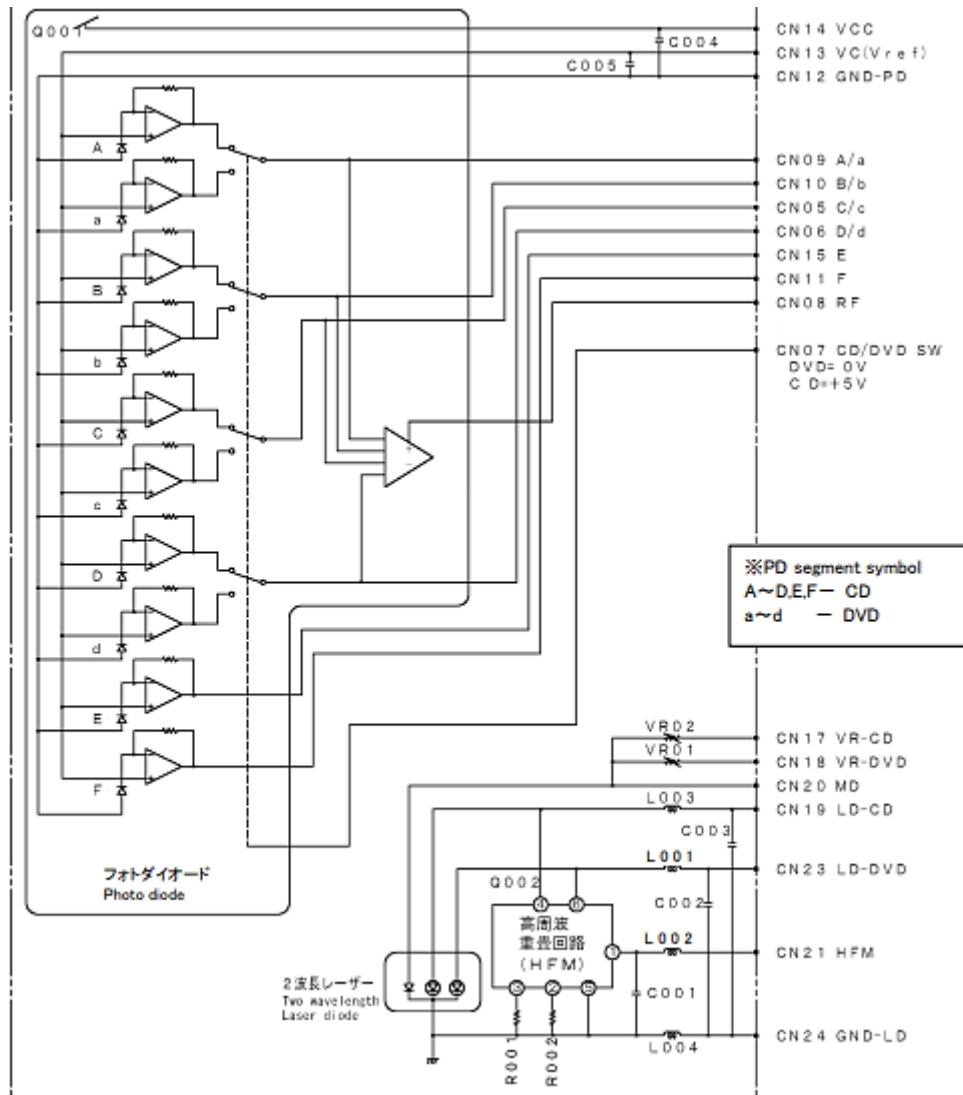
Figure 23: Circuit schematic of the wiring of the multi-segment photodiode and high-frequency module onboard the Sanyo SF-HD65/850 optical pickup (taken from the SF-HD65 specification sheet by Sanyo, Japan).

2.3 Sanyo SF-HD65/850 control electronics

In this section, details surrounding the development of the custom-built control electronics used to interface with the Sanyo SF-HD65/850 optical pickup unit are described. An explanation of the electronics is divided into the same principal functions of the optical pickup as previously commented upon (i.e. emission, actuation and sensing). The electronics consist of three printed circuit boards (PCB) each responsible for different aspects of integration with the OPU. The three boards are shown in Figure 24, where: (a) shows a signal distribution board using screw terminal blocks; (b) shows the PCB responsible for automatic laser power control, focus error calculation and physical connection to the OPU; and (c) shows an Arduino-based 16-bit dual-axis voice coil control board.
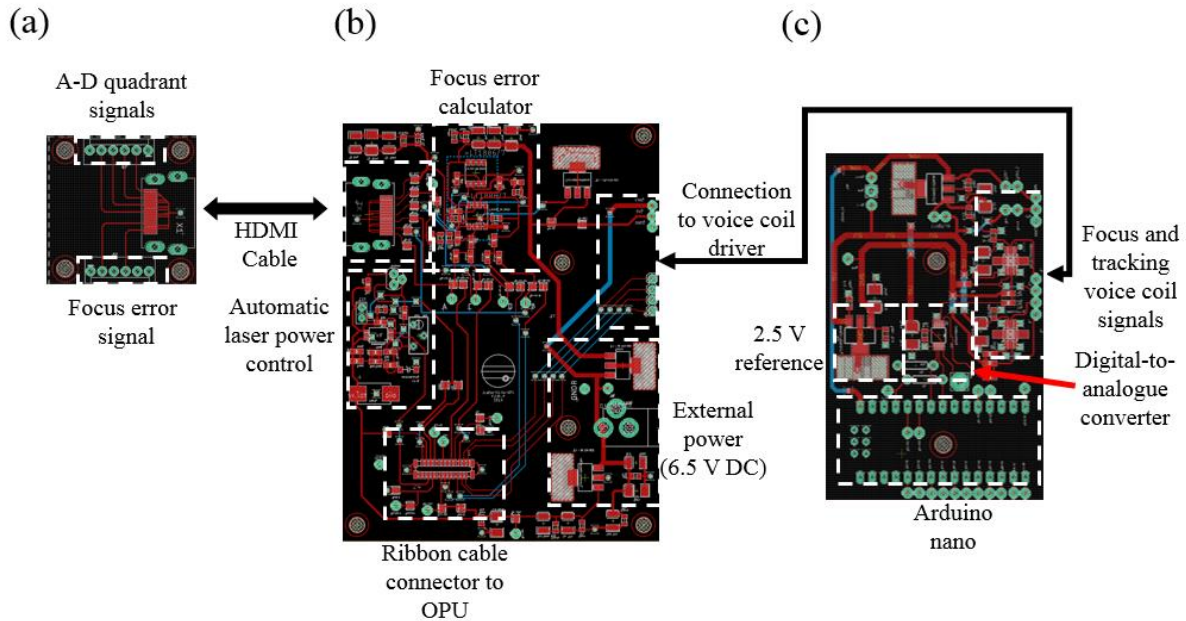
Figure 24: The three PCB designs used to power, control and receive signals from the Sanyo SF-HD65/850 optical pickup where: (a) is a signal breakout board, (b) is a laser power and FE calculator board and (c) is a control board for the dual-axis VCM motors.

Arrows between the boards show how they connect to each other. Figure 24 (c) is placed on top of Figure 24(b) and located via seven header pins and two mechanical bolt fixings. The boards in Figure 24(b) and Figure 24(c) are then connected to the OPU via a FPC ribbon cable and connected to the signal distribution board via a shielded HDMI cable. The signals from the distribution board can then be passed to a signal capture instrument, such as an oscilloscope or a data acquisition (DAQ) card like the NI 6366 USB DAQ. Further information about each of the main functions of the control electronics can be found in Sections 2.3.1, 2.3.2 and 2.3.3.

2.3.1 Emission control electronics

As outlined in Section 2.2.2, the emission functions on the SF-HD65 are to enable the CD or DVD laser, using the CD/DVD SW, VR-DVD and VR-CD pins, to automatically power the laser diode using feedback from the inbuilt monitoring diode, and to enable or disable the HFM chip, as required.

In order to appropriately turn on and automatically control the power output of the laser onboard the optical pickup, the automatic power control circuit suggested in the Sanyo SF-HD65 spec sheet (Figure 25 (a)) was used. Here, the monitor diode on board the TOLD2000MDA/SDA (Toshiba, Japan) is used as the '+' input into a NJM2904 (New Japan Radio, Japan) single-supply dual-operational amplifier, allowing it to be used as feedback from the laser in the automatic power circuit. A variable resistor (VR) (i.e. noted by the VR symbol with a value of 2k2 ohm in (Figure 25 (a)) allows a tuneable resistance to exist between the '-' input of the operational amplifier and ground. Initially, this should be adjusted such that the APC reference voltage in the circuit is equal to 180 mV, resulting in an emission

power through the objective lens of approximately 0.3 mW. The result of subsequently varying the resistance of this VR allows the laser intensity to be adjusted.

To develop the circuit schematics and PCB designs, Autodesk Eagle CAD was used with assistance from M. Loutit (Science Electronics Workshop, School of Physics, University of Bristol.) The specified APC circuit suggested for the Sanyo SF-HD65 is displayed in Figure 25 (a), the circuit schematic developed on Autodesk Eagle CAD in Figure 25 (b) and the PCB layout in Figure 25 (c).
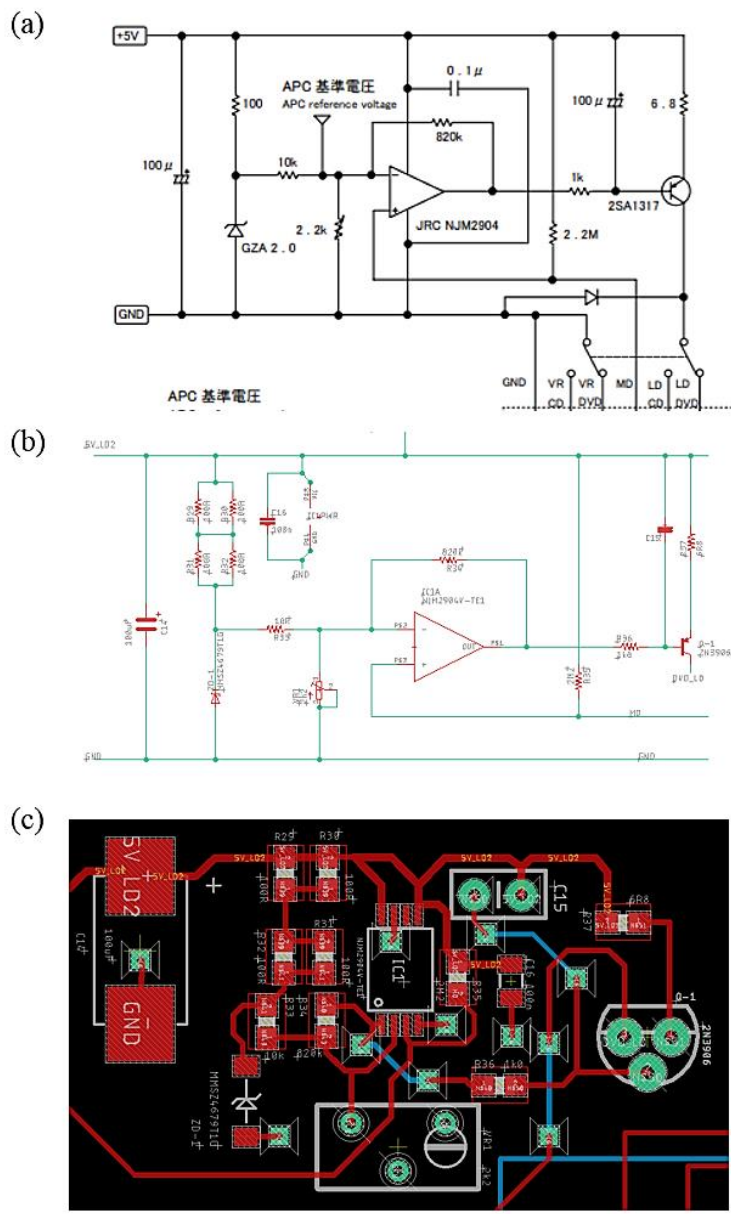
Figure 25: The suggested automatic laser power circuit (APC) schematic for the Sanyo SF-HD65 taken from the specification sheet in (a), an Autodesk Eagle CAD schematic developed in this work (b) and the PCB layout for (b) is presented in (c) (Higher resolution versions of a-c are available in the digital appendix).

2.3.1.1 Power output testing of the Sanyo SF-HD65/850 emission electronics

Having constructed the APC circuit, recommended by Sanyo in the specification sheet for the OPU (Figure 25 (c)), an evaluation of the laser power emission with these control electronics was carried out using a calibrated PM100D (Thorlabs, US) power meter with an S130C (Thorlabs, US) photodiode sensor. For this measurement, the power meter was held at a distance of 5±1 mm and set to 5mW sensitivity range. The APC circuit was then set in the range 50-250 mW, incrementally increasing by 50 mW and measured for 300 seconds at a rate of 1 kS/s. The result from this are shown in Figure 26.
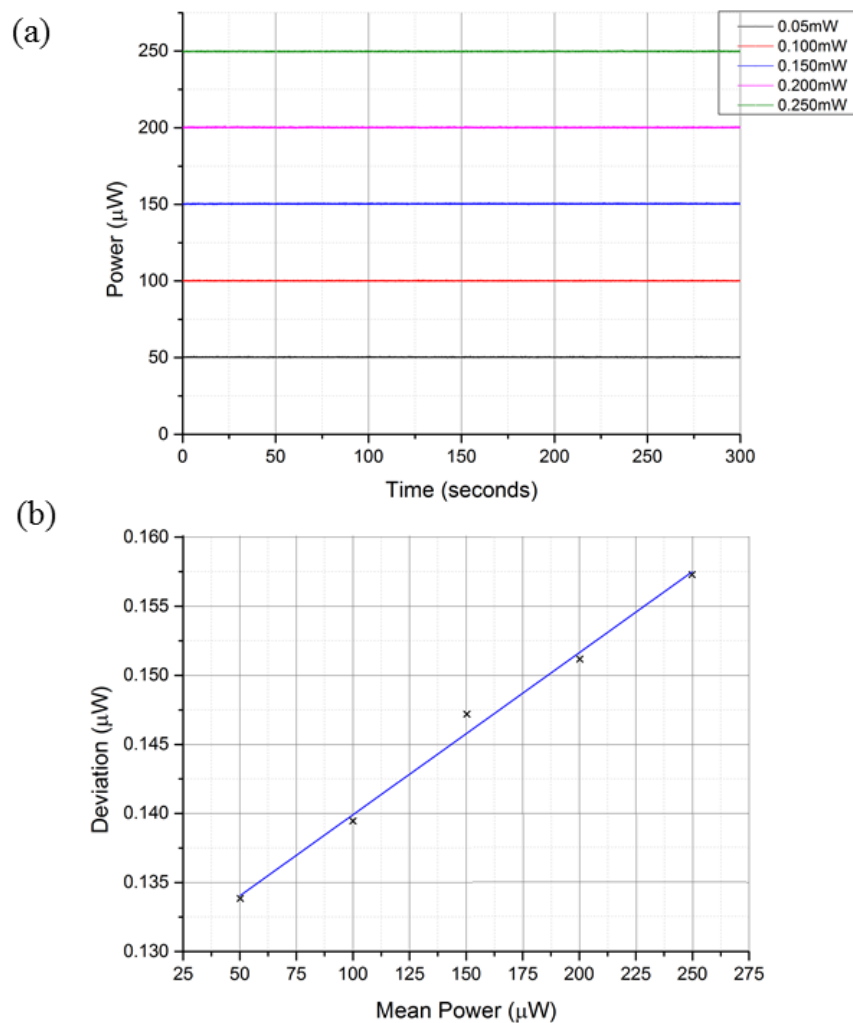
Figure 26: Evaluation of the power output from the DVD laser on the Sanyo SF-HD65 optical pickup where (a) shows the power intensity of the laser captured over 300 s at five different laser powers and (b) the associated deviation from the mean power over that time period.

Here we see that the laser power appears stable over 300 seconds with a standard deviation of less than ± 0.15% of the mean power in all cases. Whilst the deviation rises linearly (Figure 26 (b)), it is noted that this represents a fall in percentage error with a standard deviation about the mean measured to be 0.158 μW at a power of 250 μW corresponding to 0.06%.

2.3.2 Actuation control electronics

As described in Section 2.2.3, the Sanyo SF-HD65 has a dual-axis voice coil motor surrounding the objective lens that is typically used for adjusting the position of the laser to minimise the focus and tracking errors measured by the pickup.

From the specification sheet we see that the sensitivity of the focus actuator is 0.8 mm/V and 0.6 mm/V for the tracking axis when moved slowly at a frequency of 5 Hz. Looking at the physical range of the axes (i.e. focus: 1.8 mm and tracking: 0.8 mm) we see that this translates to a voltage range of 2.25 V and 1.33 V. Selecting a digital-to-analogue converter with an output range of 0-5 V would result in the following approximate resolutions: 10-bit: 4 μm (F) & 3 μm (T); 12-bit: 1 μm (F) and 0.7 μm (T); 14-bit: 0.2 μm (F) and 0.2 μm (T); 16-bit: 60 nm (F) and 45 nm (T); 18-bit: 15 nm (F) and 11 nm (T).   As such, the lowest bit depth to achieve nanoscale (i.e <100 nm) resolution was chosen as a compromise between digital processing times and resolution. An analogue devices AD5667 (Analogue Devices, US) dual-channel 16-bit nanoDAC with I2C interface was chosen to provide the analogue voltage and a compact Arduino Nano microcontroller was used to digitally interface to a computer via serial communication.

The AD5667 nanoDAC has a maximum current output of 30 mA per channel, much less than the maximum current required to drive each of the voice coil axes. Therefore, the circuit requires the implementation of high output drive (i.e. >300 mA) operational amplifiers, such as the TLV4111 (Texas Instruments, US) chosen for this application, see Figure 27 (a) for the circuit configuration. With the use of a 2.5 V reference, the 0-5V can be used to supply both forward and backward motion about the equilibrium position of the lens in each axis. This is done by using a potential divider at the output of the DAC and a voltage follower circuit with the TLV4111 to supply the high current required to move the voice coils. The circuit configuration showing how the Arduino Nano connects to the nanoDAC which connects to the two TLV4111 op-amps is shown in Figure 27 (b) and the layout of this on the PCB in shown in Figure 27 (c) (higher resolution versions of the images in Figure 27 can be found in the appended media storage).
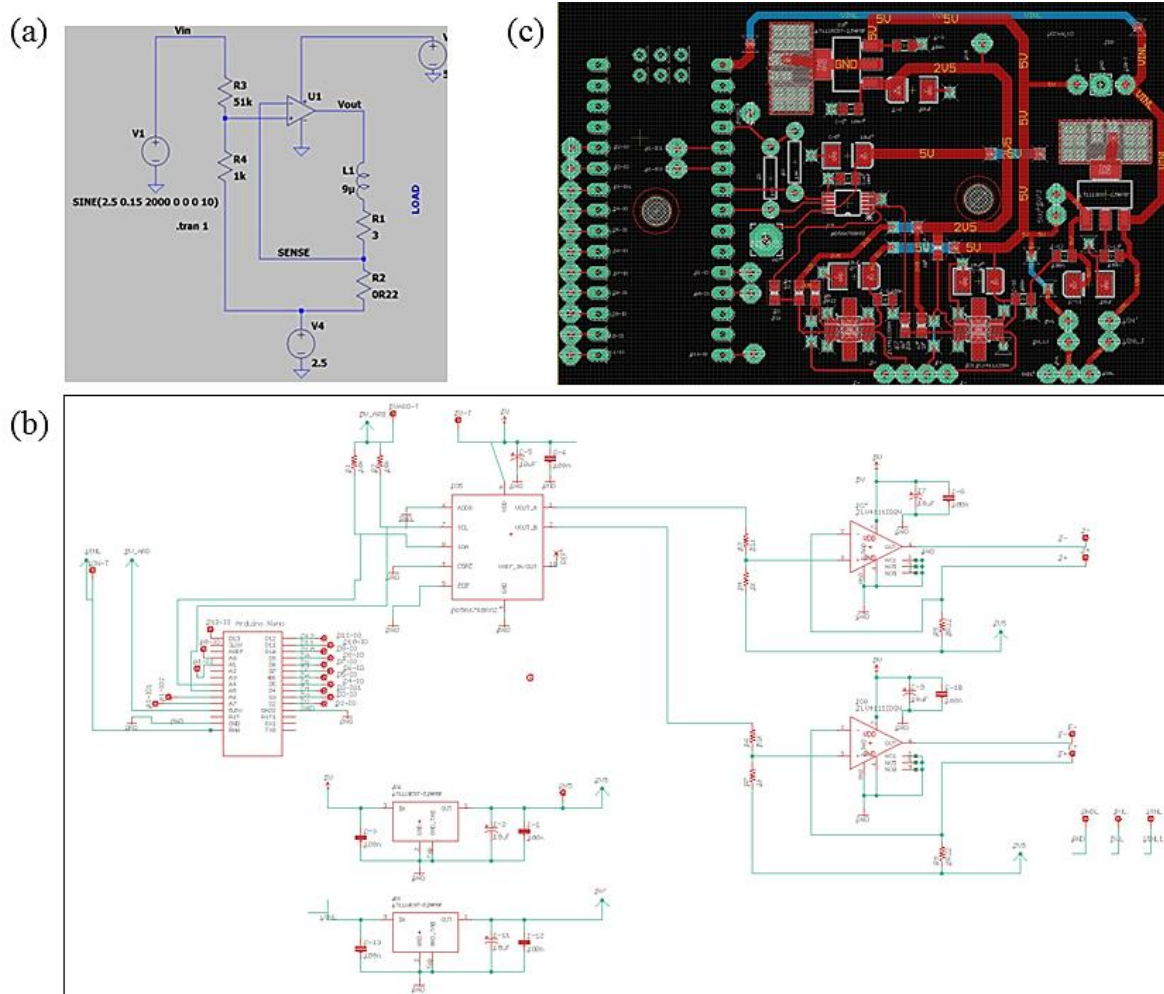
Figure 27: An LTspice circuit schematic designed for driving a single-axis voice coil motors is shown in (a). An Autodesk Eagle CAD board schematic is shown in (b) showing an Arduino Nano (left) communicating to a 16-bit digital-to-analogue converter (middle) which sends analogue voltage signals to two single voice-coil drivers (right) based on the LTspice simulation shown in (a). In (c) a PCB layout for (b) is presented.

2.3.1.1 LTspice simulation of the Sanyo SF-HD65/850 actuation electronics

The circuit required to drive the voice coil motors on the optical pickup unit was designed and simulated in LTspice, with the assistance of M. Loutit. Here, the circuit is tested by simulating the nanoDAC as a voltage source, which in this simulation has an output of a 2 kHz sinusoidal oscillation with peak-to-peak amplitude of 5V. The probes, labelled in Figure 28 (a), are placed at the voltage output of the voltage source (V1), either side of the simulated voice coil (V2 and V3) and a current monitor was placed around the simulated voice coil to see what the maximum current provided could be. The measured properties of the circuit can be found in Figure 28 (b).
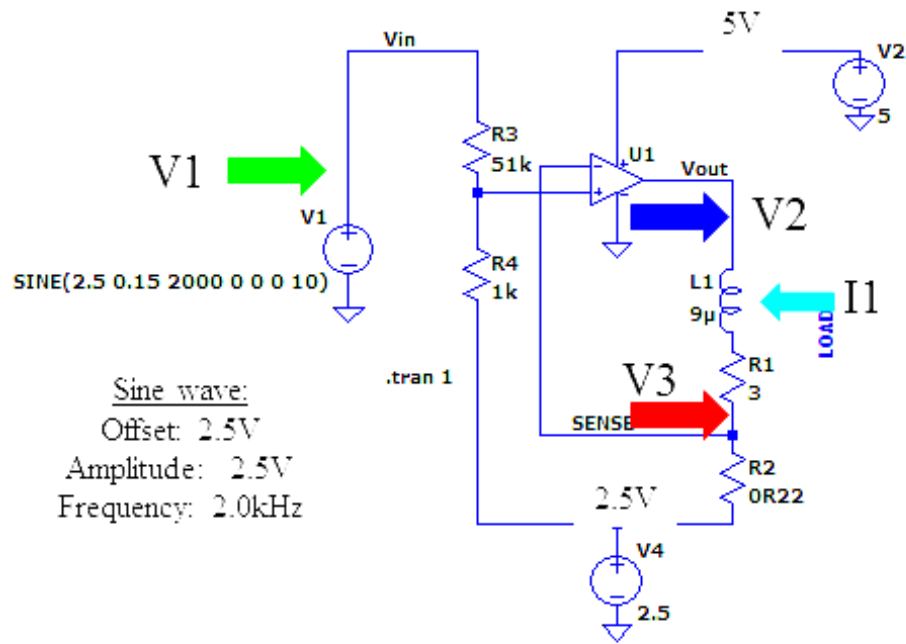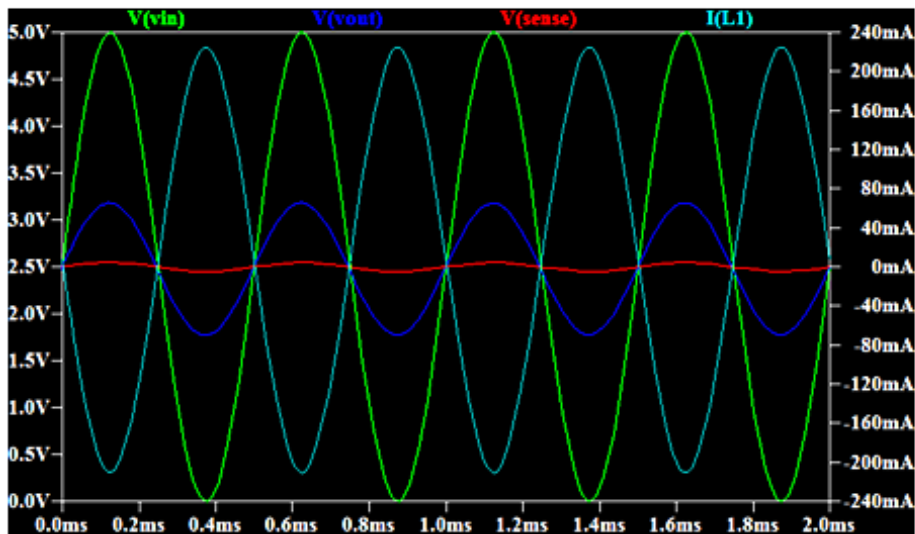
Figure 28: LTspice simulation of the circuit used to move the voice coil motors on the Sanyo SF-HD65/850 optical pickup. (a) Circuit developed in LTspice for simulation, with the location of the simulation probes shown with arrows (i.e. V1, V2, V3 and I1) corresponding to the coloured lines plotted for each probe in the graphs below (b). 'V' probes represent voltage and 'I' current.

From the LTspice simulation we see that over the full range of the simulated nanoDAC (i.e. 0-5V) and the current through the voice coils provided by the TLV4111 is ±210 mA, just less than the maximum allowable current through the coil of (i.e. 220 mA from Figure 20 and Figure 21). As such, this should permit use of >95% of the voice coil range per axis. Experimental evaluation the voice coil motion is carried out in Chapter 5, Section 5.4.3.

38

2.3.3 Sensing control electronics

As discussed in Section 2.2.4, the Sanyo SF-HD65/850 has a built-in 10 segment photodiode sensor used to make a measurement of the focus or tracking error of either the CD laser or the DVD laser. As the experimental work carried out with OPUs in this thesis is only focused on the response from the astigmatic detection system signals, this section looks at how the A-D photodiode quadrant signals can be processed in two ways: direct; and via the operational amplifier-based focus error calculator. Figure 29 highlights the two pathway options available for the sensor signals from the OPU on the control PCBs.
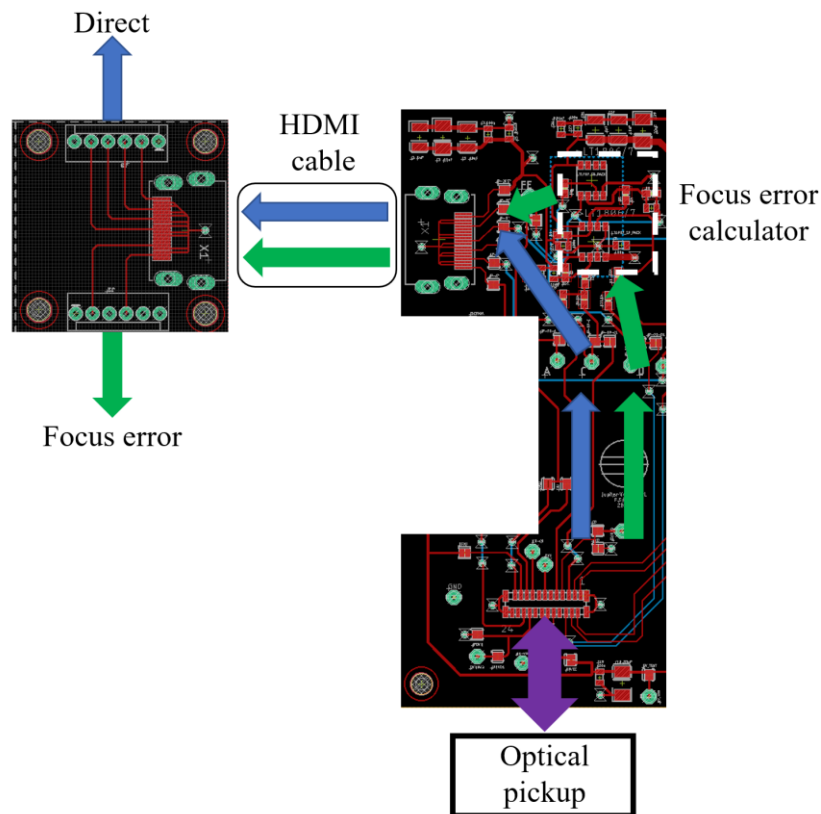
Figure 29: Two parts of the PCBs used to receive and process photodiode signals from to the Sanyo SF-HD65/850 optical pickup. Blue arrows show the approximate path of the photodiode signals directly from the optical pickup. The green arrow shows how the signals are passed to the focus error calculator on the board before being transmitted down the HDMI cable.

The two pathways for the photodiode sensor signals offer different options for signal processing. The benefit of allowing all quadrants to be accessible for simultaneous digitising on the HDMI breakout board is that different calculations can be processed in software such as: FE (equation 2, p.20), NFE (equation 3, p.20); sum signal (SUM: A+B+C+D); horizontal angle ($S_x = $A+B – C+D); and vertical angle ($S_y=$ A+D – C+B); and others. By recording the four channels directly it allows for reprocessing of these values in post-processing.

Calculating the focus error in hardware reduces the number of channels that need digitising from four to one. This can be useful when a limited number of channels are available (i.e <4 channels) on the analogue-to-digital converter. A second key advantage is that by passing the signals simultaneously through a set of operational amplifiers, the op-amps can act to minimise the noise mutually present on the signals via common-mode rejection. Furthermore, op-amps can be used to removed voltage offset from signals and scale the output to match the preferred range of the analogue-to-digital converter being used to capture data. The following section (2.3.3.1) describes the focus error calculator in more detail.

2.3.3.1 Onboard FE calculator of photodiode signals

As discussed in Section 2.1.2, the focus error signal is calculated via Equation 2. Simultaneously digitising all quadrants (A-D) and processing them in software is one way the FE can be calculated. This section looks to show how this can be achieved using two summing amplifiers and a difference amplifier, thus reducing the number of output sensor channels that need to be captured. The LTspice circuit used to develop this is displayed in Figure 30 (a), the resultant Eagle CAD circuit in Figure 30 (b) and the PCB layout in Figure 30 (c). The circuit was designed so that the focus error calculator could be activated or deactivated with jumpers to avoid it supplying additional electrical noise to the ground plane.

A dual op-amp integrated chip (LT1807, Linear Technologies, UK) is used to provide the first pair of summing operations, i.e. (A+C) and (B+D), then invert them w.r.t 'V$_{ref}$' (2.5 V) and multiply by a gain (i.e. 'G$_1$' for A+C and 'G$_2$' for B+D) giving the output to each summing amplifier, named 'AC'=G$_1$ (A+C)$_{-2.5V}$ and 'BD'=G$_2$ (B+D)$_{-2.5V}$ where the subscript refers to where the signal has be inverted w.r.t. V$_{ref}$. The two signals are then passed to a difference amplifier, with gain (G$_3$), where the 'BC' signal is incident on the positive terminal of the op-amp and the 'AC' is incident on the negative terminal, giving:

$$V_{Out} = G_3 \; (BD - AC) \tag{8}$$

$$V_{Out} = G_3 \; (-G_2(B + D))_{-2.5V} - (-G_1(A + C))_{-2.5V} \tag{9}$$

$$V_{Out} = G_4 \; ((A + C)_{-2.5V} - (B + D)_{-2.5V}) \tag{10}$$

$$(\text{where}, \; G_4 = G_3 \times G_1 \,, as, G_1 = G_2)$$
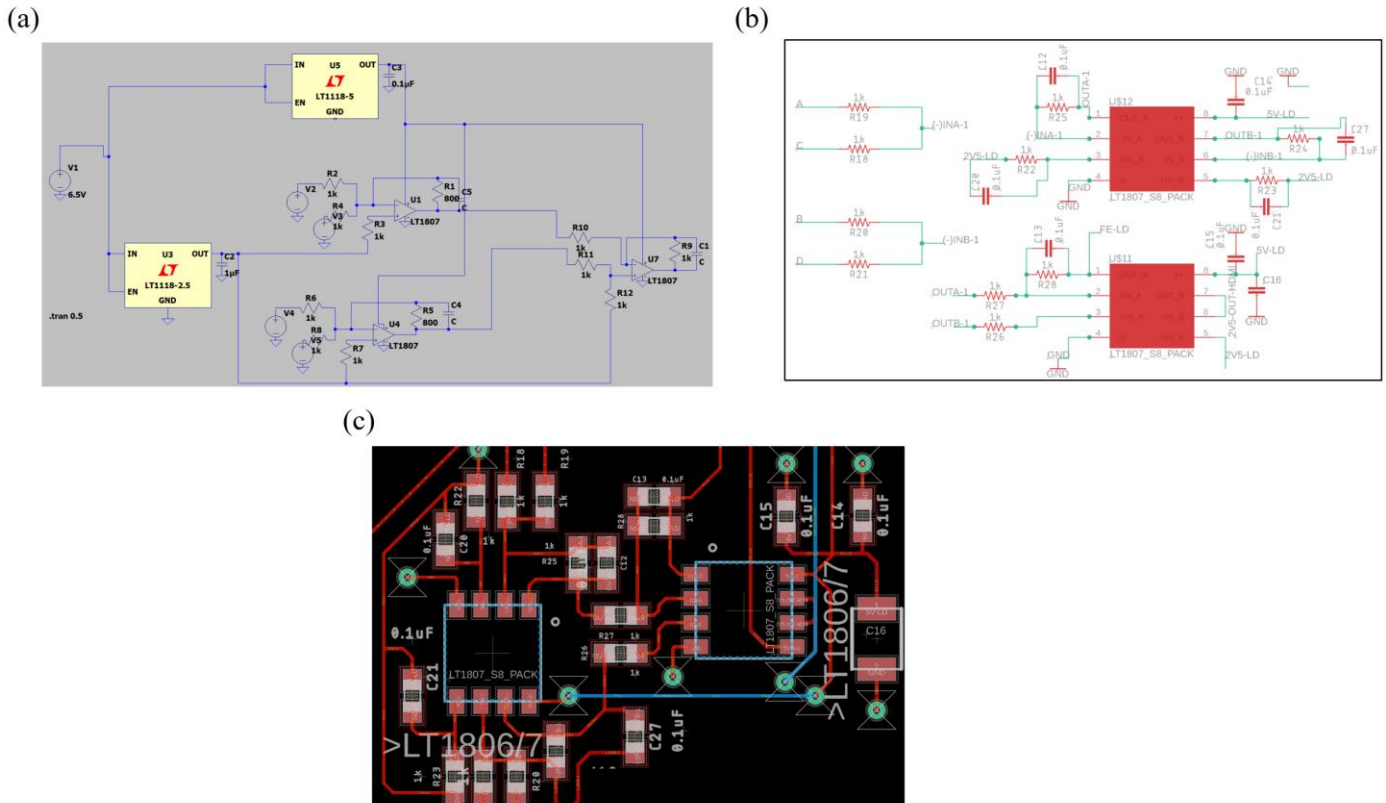
Figure 30: Focus error calculator circuit where: (a) is a LTspice simulation of a focus error calculator (b) is an Autodesk Eagle CAD schematic for focus error calculator circuit; and (c) is an Autodesk Eagle CAD board layout of this circuit.

2.3.3.2 LTspice simulation of the Sanyo SF-HD65/850 sensing electronics

The focus error calculator circuit was designed for use with the 16-bit analogue-to-digital converters on the NI USB-6636 (National Instruments, US), which had differential inputs that could be set with a configurable input range of ±2 V. The circuit was designed such that the op-amps could be powered between +5 V and ground to avoid the need to provide a negative voltage (e.g. -5V) on the PCB.

For the LTspice simulation, real signals taken directly from the quadrant photodiode on the Sanyo SF-HD65 optical pickup were used. These sensor signals had been captured while oscillating a reflective silicon substrate through a distance greater that the linear range of the focus error response using a piezo driven nanoscanner (discussed further in Chapter 5) whilst the OPU was operated in DVD mode. Figure 31(a) demonstrates how these signals were passed through the circuit to find the focus error signal (green arrow). A graphical representation of probe results from the LTspice simulation can be found for each location in Figure 31 (b). As the motion range is greater than the linear detection range we see that response travelling passed and back through the turning points of the s-curve, causing apparent flattening at the 3.1 V peaks and the 2.0 V troughs.
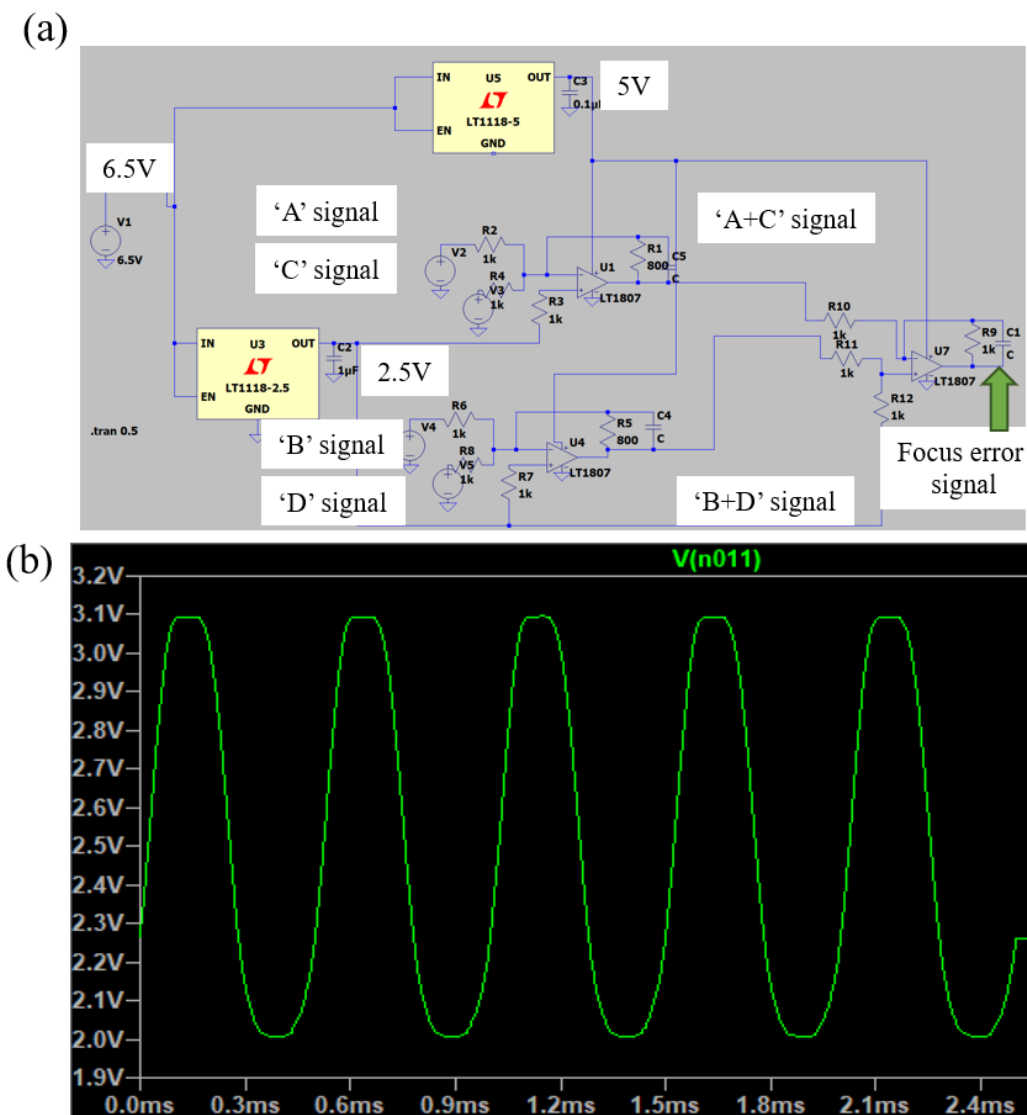
Figure 31: LTspice simulation results from the focus error calculator circuit where (a) shows the circuit schematic with probe location; and (b) shows the graphical output of the FE probe (green arrow).

Using the waveforms taken from the optical pickup, whilst the emission laser had been set to 0.3mW, the focus error calculator found the linear response range to be equal to 1.15 V. Assuming a linear range of 6 µm this corresponds to a maximum resolution of ±0.15 nm using the 16-bit ADCs in the NI USB-6366 DAQ with a laser power of 0.3 mW (as emitted from the objective lens).

2.4 Linear response of the Sanyo HD-65/850 astigmatic detection system

In the final investigation with the Sanyo SF-HD65 reported in this chapter, an evaluation of the DVD astigmatic detection system for linear displacement measurement is carried out whilst being used the control electronics described in the previous Sections (2.3.1-2.3.3). This evaluation is aimed to determine three key properties: the measured length of the linear region of the response curve for the DVD laser; the

measurement resolution of the detection system; and the power density spectrum to assess if there were any erroneous frequency components due to electrical noise sources in the custom-built electronics.

"The response of the astigmatic system was determined by placing a reflective silicon (Si) wafer on a calibrated nano-positioning stage (NPXY60Z20-257, nPoint US). The position of the Si wafer was measured by digitising the inbuilt capacitance sensors in the stage using a National Instruments (USB-6363) data acquisition (DAQ) box. This DAQ simultaneously measured the QPD output which was used to calculate the FE signal." A half-cycle of a 10 µm triangular waveform was then passed to the nano-positioning stage and the astigmatic response captured. In Figure 32 (a) we see the astigmatic response curve plotted against displacement of the NPXY60Z20. The characteristic 's-curve' shape is noted and the inter-focal distance was calculated to be 5.225 µm. A zoomed section of this response curve is then displayed in Figure 32 (b) showing the bit limit of the signal in the y-axis and the spread of the NPXY60Z20 displacement in the x-axis, demonstrating that that the spread of the data (i.e. maximum minus the minimum) is approximately ± 2.5 nm. By looking at the power spectral density plots we see no significant electrical spikes present other than one common to both spectra measured at 153.9 kHz.
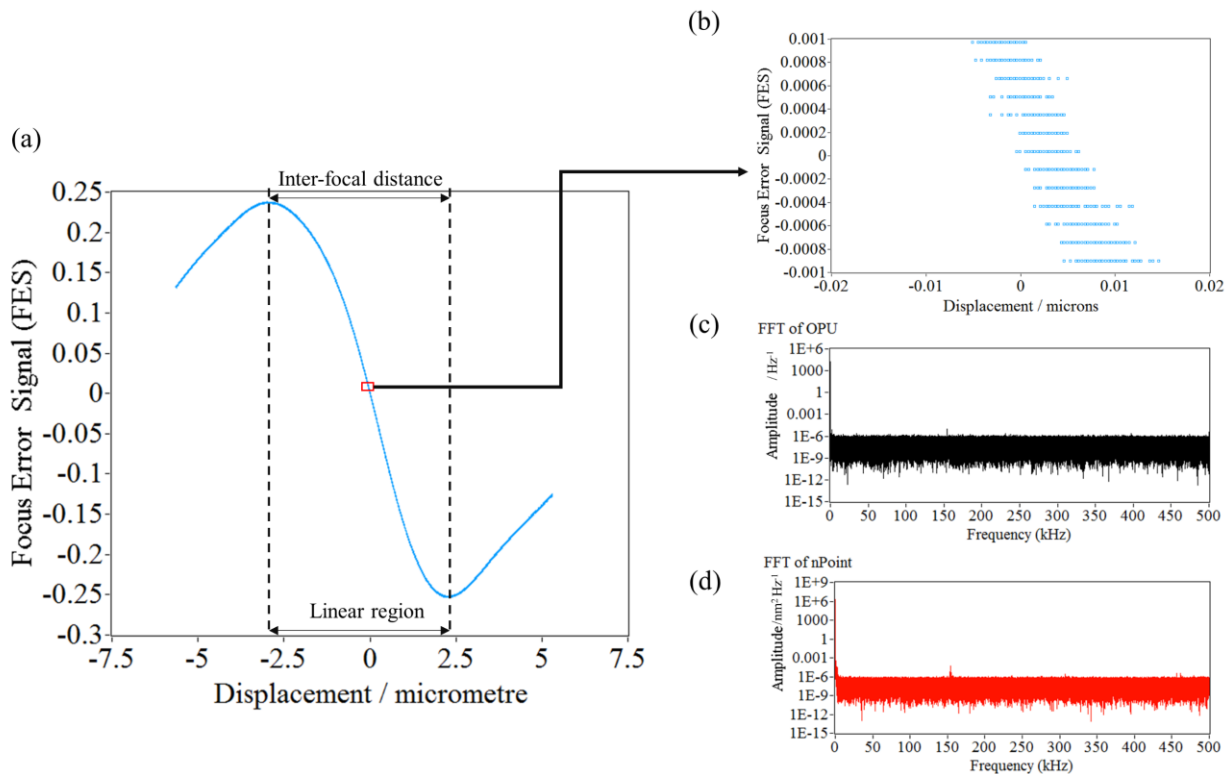
Figure 32: Response curve from the astigmatic detection system on the Sanyo SF-HD65 plotted against the linear displacement of a Silicon wafer mounted onto a NPXY60Z20 (nPoint, US) nanopositiong stage (a). A zoom-in of the region of the red square is presented in (b). The power spectral density graphs for the OPU FE signal (c) and the NPXY60Z20 (d) are presented where sampled at 1 MHz.

2.5 Conclusions

In this chapter, the background of optical pickups has been explored with the key theories and mechanisms underpinning their functionality described. Here, the differences between the three common types of OPUs (i.e. CD, DVD and Blu-ray) have been described and their differences in physical properties reviewed. The principal measurement systems typically found in optical pickups (i.e. focus error detection and tracking error detection) have been detailed, followed by the multi-axis actuator system that is used to correct for the measured error.

A detailed explanation of the SF-HD65/850 (Sanyo, Japan) optical pickup used throughout this thesis has been presented. The primary functions of emission, sensing and actuation have been outlined to give motive to the requirements of the electronics required to interface with the OPU. Here we see this OPU has both CD (790 nm) and DVD (650 nm) emission lasers with an inbuilt monitoring diode and the capability for a high-frequency module to be enabled. Subsequently, the location and properties of the dual-axis (i.e. focus and tracking) voice coil motors are presented, highlighting that both voice coil motors have ranges $\geq$ 0.8 mm and required up to 220 mA of current to utilise the full range of motion. The final aspect of the SF-HD65/850 OPU that was described in depth was the sensing capability of the system. To sense, the SF-HD65/850 OPU makes use of a multisegmented photodiode built into the optical pickup, which allows the focus and tracking errors to be calculated. Further investigation reveals that the voltage outputs from these photodiode segments can either be accessed for the DVD or the CD and that they have different associated sensing bandwidths (i.e. CD: 30 MHz and DVD: 45 MHz).

In order to make use of the range of measurement and actuation systems within the optical pickup, custom electronics were developed and built at the University of Bristol. Consisting of an automatic laser power circuit, a dual-axis voice coil driver and a focus error calculator these control electronics are used throughout the experimental work described in Chapters 3, 4 and 5. An overview of the functionality and design of these electronics has been presented. In cases where aspects of the circuit have been evaluated using a calibrated sensor or an LTspice simulation, the results have been presented in the relevant section. Whilst these control electronics have been developed for use with the SF-HD65/850, the principal components, such as the automatic power circuit, dual-axis voice coil driver and focus error calculator, could be used with other optical pickups with little modification.

Finally, the astigmatic detection system response for the DVD mode of the Sanyo SF-HD65 was used out to validate integration of the emission and sensing electronics for measuring linear displacement outside of its typical mode of operation. Using a reflective silicon wafer that was actuated by an NPXY60Z20 (nPoint, US) nano-positioner, the linear displacement response curve from the astigmatic system in the OPU was found to have an inter-focal distance of 5.225 µm and effective

resolution of approximately ±2.5 nm. It was also found that the control electronics does not contribute any significant sources of oscillatory noise.

Chapter 3: 'Hi-Fi AFM': high-speed contact mode atomic force microscopy with optical pickups

---

Disclaimer: *This chapter contains text originally written by F. Russell-Pavier as part of a submission to The journal of Measurement Science and Technology (Institute of Physics, IoP) with the same title as this chapter. Where this text has been used either partial or fully within a section, quotation marks have been placement around the relevant body of text in accordance with the recommendations of the Graduate School, School of Physics, University of Bristol.*

Furthermore, a study that was published in Nature Communications entitled 'DNA nanomapping using CRISPR-Cas9 as a programmable nanoparticle' is used as a case study of the instrumentation developed here. Data from this article, captured by the instrument developed in this work and collected by L. Picco, O. Payton and F. Russell-Pavier, has been reproduced with the permission of the lead author and the principle investigators. The text in this chapter, reporting this study, has been written by F.Russell-Pavier.

3.1 Chapter overview

"Here, we demonstrate the use of an optical pickup unit (OPU) typically found in PCs, hi-fis and games consoles worldwide, as a vertical detection system within in a HS-AFM operated in contact mode. High-speed atomic force microscopy (HS-AFM) is a powerful emerging technique used to gain insight into real-time nanoscale dynamics and phenomena across the sciences. By performing measurements of material properties, abundancy counting and dimensional analysis, it enables a new generation of discoveries at the atomic scale. A demonstration of the OPU displacement performance is compared to that of a commercially-available laser Doppler vibrometer with ±15 pm resolution. Sub-nanometre sensitivity is achieved with an OPU, presented via the identification of two resonant modes of a cantilever stimulated by ambient thermal excitation. To demonstrate the large dynamic range of the sensor at fast scan-speeds, surface profiles with step heights in excess of 100 nm and surface textures less than 10 nm were collected using a custom OPU-based HS-AFM and compared with an equivalent LDV system. The high-fidelity measurements are extended to visible length scales in short timescales by imaging areas of up to 200 μm^2 at a pixel rate of 2 megapixels/s, tip velocity of 10 mm/s and area rate of 25 $\mu m^2 s^{-1}$." (2)

In this chapter, the imaging ability of an OPU based HS-AFM is evaluated using two case study applications in relation to the fields of genomics and material science. Firstly, the instrument was used in tandem with new-generation short-range mapping of labelled genetic material (e.g. <150 base pairs) via a technique developed with Mikheikin *et al*. to image DNA with markers (1) at Virginia

Commonwealth University. The sample used for this evaluation consisted of DNA strands (~300 pm tall) labelled with CRISPR-Cas9 markers (3 nm tall) deposited from solution onto a flat and freshly cleaved mica surface. The data taken from the OPU HS-AFM demonstrates the use of DVD optics being used in an HS-AFM to image CRISPR-Cas9 labelled genetic material. Here, the spacing of the bound CRISPR-Cas9 markers on the DNA molecule can be used to identify the genetic material present. The genetic material chosen for this study were the HER2 and TERT gene sequences where the CRISPR-Cas9 was bound at 145 base pairs (bp) (TERT) and 357 bp (HER2) apart, corresponding to a physical distance along the DNA molecule of 46.9 nm and 114.1 nm, respectively. The detailed application case study, described later, shows how the OPU-based HS-AFM can identify these markers and measure the distances between them, allowing the genes to be identified. Such measurements can be used to look at the relative abundance of the two genes, which can give medical diagnostics information as to the relative expression of the genes, which, in turn, can be related to the health of tissues. In this case, where an over expression of HER2 may be present, this can be indicative of cancerous tissues.

The second application case study that was used to evaluate the OPU-based HS-AFM was a thermally-sensitised Type 304 stainless steel, prepared by Ms S. Moore at the University of Bristol. This material is widely used in construction and commonly undergoes in situ thermal elevation due to processes such as welding. The thermal elevation can lead to the metal becoming thermally-sensitised, where thermally-sensitised is defined if the chromium concentration diminishes to 12-14 wt%. Such an effect can make the grain boundaries in the material susceptible to corrosion. This corrosion can result in bulk material failure and critical infrastructure failure. Such occurrences can develop into highly serious safety concerns and outage of industry, leading to damage to commercial interests. Imaging the state of the thermally-sensitised AISI Type 304 stainless steel at the nanoscale can reveal crucial information about the grain boundaries and the presence of precipitates. This information can then be fed into modelling of corrosion (e.g. stress corrosion cracking) (58) and help in developing mitigation against processes in this widely used material. In this chapter it is shown how the OPU HS-AFM can be used to inspect and identify key surface features, including multiple precipitates and multiple triple-point grain boundaries.

3.2 Background

"OPUs, developed for reading or writing to optical discs such as CD, DVD and Blu-Ray, have already shown potential as low-cost nanoscale sensors within a number of applications. These include AFMs, straightness measurement devices and touch trigger probes, amongst others (6,7,33,40,59–61). Building upon the mass-production of these devices proves an effective way to develop new measurement capabilities.

OPUs are designed with several optical and mechanical properties that are advantageous for use as high-bandwidth nanoscale displacement sensors and nanoscale actuators. Firstly, the outgoing laser beam is focussed through an objective lens to a sub-micrometre-sized spot. Additionally, the OPU contains an inbuilt quadrant photodiode with an operational bandwidth of tens to hundreds of MHz, and the ability to translate internal optical components with nanometre resolution (27). This makes OPUs ideally suited for the monitoring of micro-mechanical cantilevers used in AFM for surface profile measurements. The change of application space for OPUs in this way was first demonstrated by Quercioli *et al.* with a CD OPU in 1999 (6). Since then, studies have demonstrated the use of OPUs within traditional forms of AFM. These methods are constrained by physical and electrical properties, as described later, which do not permit the full utilisation of the higher sensing bandwidths that the OPUs are capable of. Importantly, OPUs also promise a large increase in measurement opportunities and throughput, by facilitating simultaneous 2D angular and displacement measurements via the onboard quadrant photodiode (25)."

3.2.1. High-speed atomic force microscopy

"Historically, AFM has been known to produce topographical maps at a rate of line scans per second, or frames per hour. Consequently, it has been considered by many as too slow to be a viable method to practically characterise large sample areas (square millimetres). Since the inception of AFM (62), surface probe techniques have been developed in a variety of imaging modes (63–65), and varied according to the sample and measurement requirements. One variant which improves upon rates of previously demonstrated techniques is contact mode HS-AFM (19,66,67)."

"Significant breakthroughs by Payton *et al.* showed that by measuring the displacement of the known node above the tip on the cantilever, rather than taking an angular measurement via beam deflection (68), the resultant height map would be less susceptible to unwanted flexural and torsional vibrational modes excited along the cantilever (21). This is an important consideration when imaging at higher speeds, as higher tip velocities over the surface allow for greater excitation of the cantilever's resonant modes. Furthermore, by using a cantilever with a low spring constant and high mechanical compliance to the surface topography, the system can be operated without an active constant height mode control loop. This reduces the digital processing time required for each height measurement compared with other implementations (69–72) and enables scanning at high rates."

"Statistical confidence in measured sample properties is enhanced by HS-AFM, since it can be used to collect many frames in short time periods (minutes) with high pixel density. Generating the equivalent number of frames with the same resolution, at the more typical lower rates common to traditional AFMs (hours-days), is impractical and can lead to less populous datasets being collected over smaller imaging areas. This, in turn, can result in assumptions of homogeneity across the sample being inferred from a relatively small measured sample size. Crucially, this may translate to selective bias in the measurement of material properties. A key benefit of HS-AFM is that it takes much less time to analyse the material

properties of the sample surface, which allows measurements to be taken over longer distance and larger areas, enabling nanoscale measurements to be linked to microscopic length-scales. In other applications, the temporal resolution allows dynamic behaviour at the nanoscale to be observed (73–76)."

"The existing commercial HS-AFM used in this work, incorporating a laser Doppler-shift vibrometer (LDV) to detect the cantilever's motion, has been developed by Bristol Nanodynamics Ltd. and the University of Bristol. The LDV detection system (OFV-534) and decoder card (DD-900) made by Polytec GmbH can collect 2.5 million measurements of the cantilever displacement per second, with a resolution of ±15 pm. This enables the HS-AFM to resolve atomic steps with multiple frames per second. This HS-AFM has been shown to be an extremely useful tool when conducting analyses of 2D materials (22,23) and genomic mapping (1). In both cases, the increased speed has permitted the measurement of nanometre and sub-nanometre features at tens to hundreds of times per minute. This allows for large sample sizes to be measured in practical timeframes."

"Previous instrumentation research with OPUs has been seen in a large number of exciting configurations for bio-sensing and material analysis (32,61,77,78). Studies of OPUs as a detection system in AFMs have primarily focussed on tapping mode and at lower rates than reported here (6,25,27,60,79). A study of HS-AFM, demonstrated in tapping mode with a specially manufactured small cantilever with resonant frequency >1 MHz, has been reported (60). This was used to image at rates up to 1.4 mm/s. Higher speeds were made possible by reducing the cantilever to dimensions much below those found in typical cantilevers. However, this increase in speed is limited by the achievable, practical reduction in dimensions. Whilst a contact mode configuration has previously been reported (60,80), the method differs from that explored here. The methodology from the work presented here promises full utilisation of the OPU bandwidth (tens to hundreds of MHz). Which gives tremendous potential for HS-AFM to spatially map materials, across nine orders of magnitude, within hours."

3.3 Method

3.3.1 Physical layout of the OPU and other key components in the HS-AFM

"For contact mode HS-AFM the OPU used as a detection system, as illustrated in Figure 33. A flexible contact mode cantilever (MSNL-C, Bruker) with a spring constant of 0.01 N/m is used. Figure 33 also shows how the cantilever, sample and high-speed parallel flexure stage are positioned in relation to one another. Here, a purpose-built dual axis parallel flexure stage, spark-eroded from aluminium block, is used as the HS-AFM scan stage. Ceramic piezoelectric actuators (SA050510, PiezoDrive) on each axis are used to generate a high aspect ratio (1:1000 Hz) Lissajous path. These actuators enable the sample to be scanned underneath the cantilever at rates of up to 64 µm²/second. The system allows each fundamental cantilever measurement to be used inter-changeably, for imaging either large areas (e.g. >1 µm²) at 1 Hz, or smaller areas (e.g. <1 µm²) at tens of Hz."
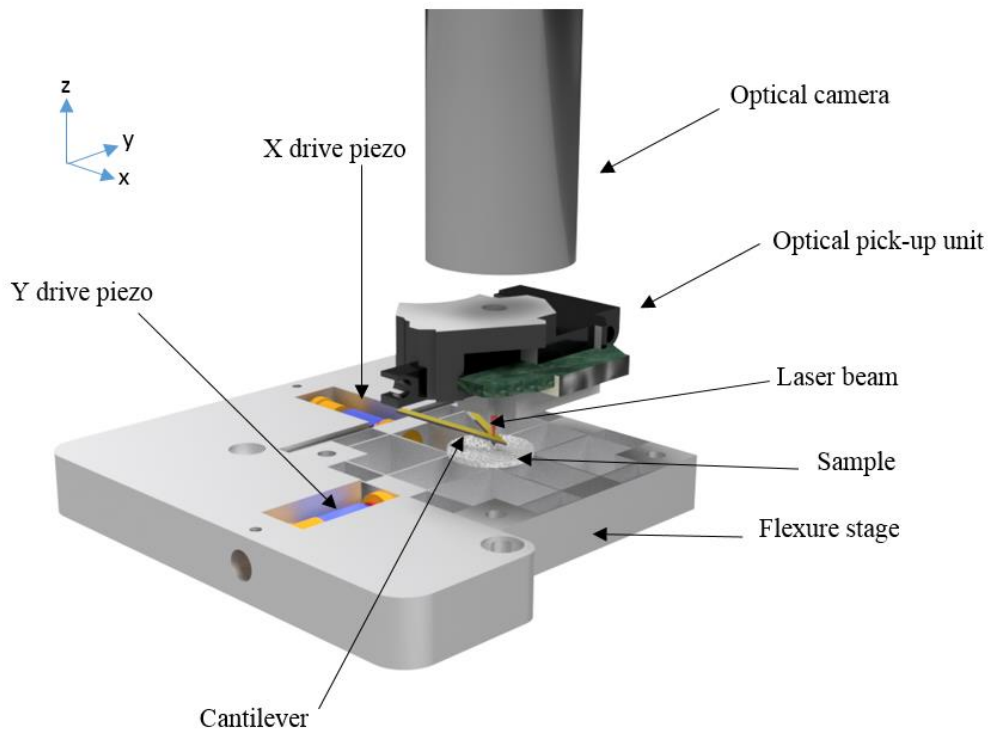
Figure 33: "3D schematic of an OPU-based HS-AFM, with key components labelled (not to scale). The connective superstructures have been omitted for simplicity."

"As OPUs aren't typically used in the configuration described in Figure 33, custom electronics developed at the University of Bristol were produced to provide automatic power control to the laser, and to allow for position control of the objective lens in two axes. The principal aim of the system is to position the laser spot accurately and stably on the cantilever, to translate the sample underneath the cantilever and to acquire the focus error signal (FES) (as described in Chapter 2, Section 2.1.2) from the quadrant photodiode (QPD)." Here the sample is typically mounted with adhesion silver DAG 1415M (Agar Scientific, UK) onto an aluminium pin stub, commonly used in other techniques such as scanning electron microscopy, which is secured to the flexure stage via a locking grub screw in the central platform. In addition, the high-speed scanner was placed upon a dual-axis stack of x2 ECS3030 (Attocube, Germany) linear translation stages for enabling long-range motion with their range extending up to 30 mm by 30 mm in each axis.

3.3.2 System schematic of the OPU HS-AFM

To communicate an overview of the instrument, a systems diagram is displayed in Figure 34. It shows how the process of using the astigmatic system (Chapter 2, Section 2.1.2) is integrated with the data acquisition (DAQ) (NI 6363 USB multifunction I/O device, National Instruments, USA) device. Four 16-bit analogue inputs (AI) were used on the DAQ at a sampling rate of 2 MS/s per channel to simultaneously digitise each of the quadrants from the QPD. The DAQ was also responsible for

outputting the sinusoidal drive signals at 16-bit 2 MS/s per channel to the amplifier, which, in turn, drove the two piezoelectric actuators (Figure 33) that made up the fast- and slow-scan motion in the Lissajous scan path where typical frequencies of oscillation where set to be 1 kHz and 1 Hz, respectively. Further information surrounding the scan paths and why they are used in this system are summarised in the high-speed nanopositioning chapter (Chapter 5).
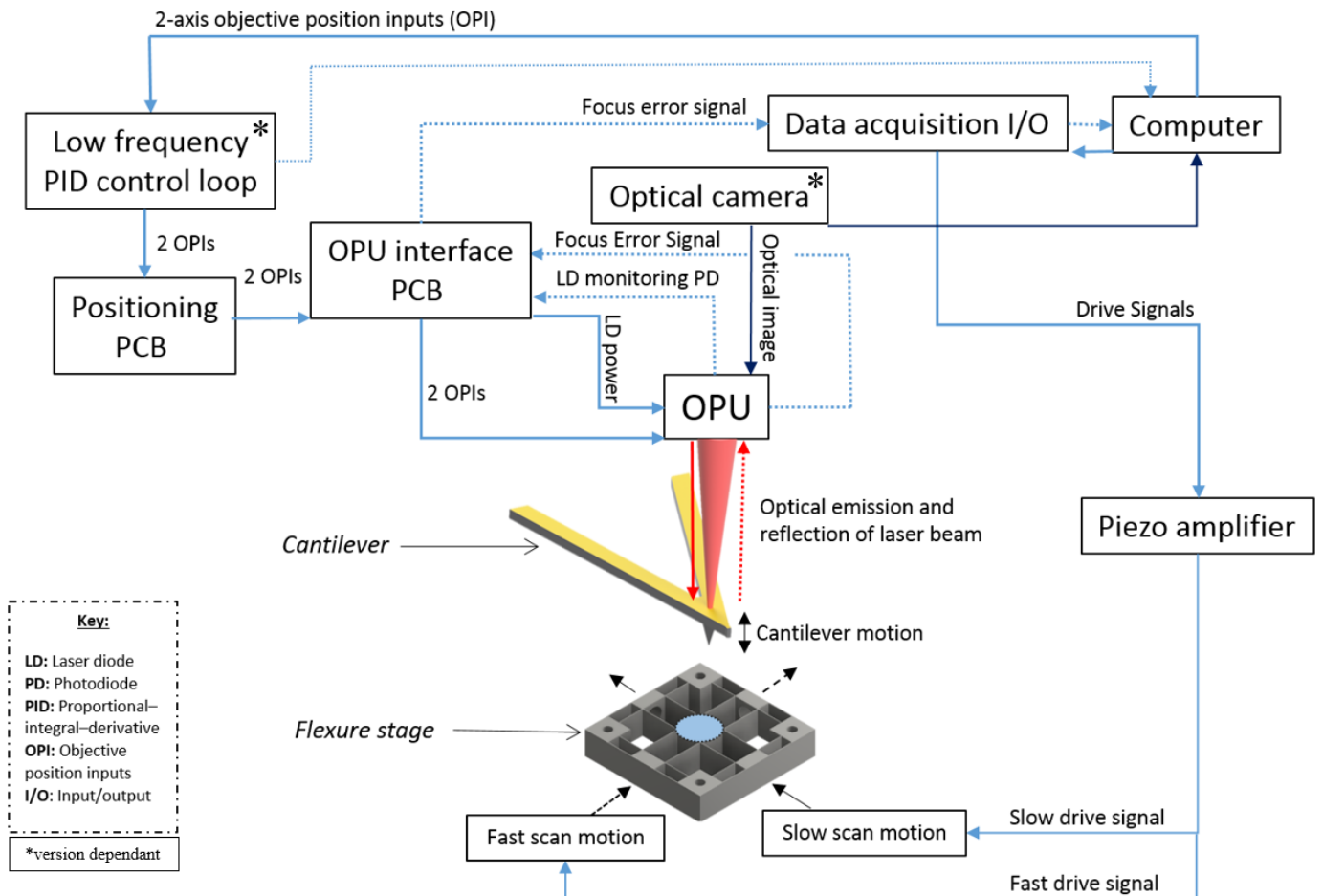
Figure 34: "System schematic of an OPU-based HS-AFM to computer interface, with key components labelled."

Here, two bespoke printed circuit boards (PCBs), outlined in Chapter 2 Section 2.3, were designed and developed with support from Magnus Loutit in the School of Physics Electronic Workshop, University of Bristol to conduct different operation functions. The positioning PCB was responsible for controlling the dual-axis (i.e. tracking and focus) VCM found in the Sanyo HD-850/65 optical pickup. This was communicated to an embedded Arduino Nano on the PCB over serial (I2C), which, in turn, instructed a dual-channel digital-to-analogue convertor (DAC) via I2C to output the relevant voltages to two current-driving op-amps. Further information on the electronics, evaluation and method of operation are found in the high-speed nanopositioning chapter (Chapter 5). The second 'OPU interface' PCB contained the automatic power control circuit for the laser and a few digital logic (e.g. high or low) solder jumpers that could be used to enable or disable the CD or DVD laser in the

Sanyo HD-850/65. In some versions of this board, an onboard FES calculation was also performed in hardware using a two-stage op-amp circuit, as described in Chapter 2 Section 2.3.3.1. To minimise any interference to the electric signals, the electronic path length between the two PCBs and the OPU was minimised by having the PCB as close to the OPU as was practically possible. To pass the focus error signals and quadrant signals back to the computer, commercially-available shielded cables, such as HDMI cables, were used, allowing for ease of interfacing between the modular PCBs in the system.

The vertical arrangement of the superstructure components and actuators in the OPU HS-AFM are then ordered in the way outlined in Figure 35.
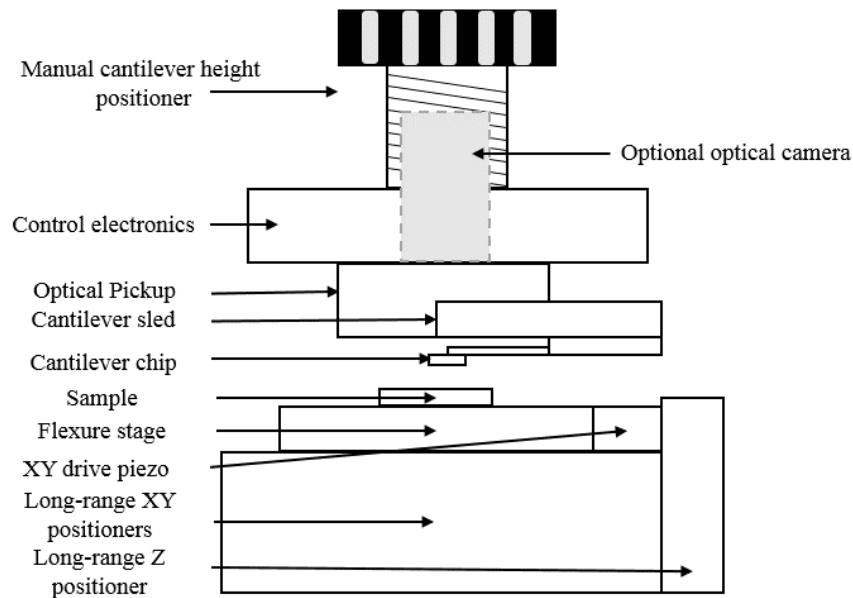
Figure 35: Physical system schematic of the location of the principal components in the OPU-based HS-AFM (not to scale).

This physical arrangement of components was then configured in several different versions of the instrument as the research evolved. In the next section we see an overview of how this physical arrangement of components took several forms as additional degrees of freedom of automation became integrated.

3.3.3 Matrix of the HS-AFM versions developed in this work

Throughout this project, three distinct versions of the OPU HS-AFM were developed due to improvements in design, different operational requirements, automation and improvements in imaging method. A matrix detailing these HS-AFM versions and the corresponding cantilever positioners (i.e. sleds) that were also developed for each version are itemised in Figure 36 (d-g). Key components are labelled, and a short name itemised in a table Figure 36 (h).

In the initial prototype (Vers. 1, shown in Figure 36 (a)) the OPU head superstructure was made from a simple construction of two DVD drives fastened together at 90° to one another

(labelled 2, in Figure 36 (a)), fixed to a mounting plate and in turn attached to a manual vertical stage (VAP10/M, Thorlabs, USA) (labelled 1, Figure 36 (a)), which could be used to coarsely adjust the height of the OPU head (labelled 2, Figure 36 (a)) over a long travel range by hand. Fixed on the underside of this head was an OPU (labelled 7, Figure 36 (a)) with a manual cantilever sled (Figure 36 (d)) attached to the front of it which was developed with the Mechanical Workshop (School of Physics, University of Bristol). The sled enabled the lateral adjustment of the cantilever in the perpendicular axis to the voice coil tracking actuator, with a fine pitched screw thread (labelled 12, Figure 36 (d)) which could be rotated by hand, allowing for the laser to be located on the measurement site above the tip on the cantilever which was secured to the cantilever paddle (labelled 11, Figure 36 (d)). Underneath this is where the high-speed flexure stage was placed (labelled 4, Figure 36 (a)) on top of a manual XYZ stage (M-562-XYZ, Newport, USA) (labelled 5, Figure 36 (c)) actuated by fine-pitch manual micrometre actuators.

Version 2 (shown Figure 36 (b)) differed due to the OPU head superstructure (labelled 2, Figure 36 (b)) being constructed from a 3D-printed triangular casing which allowed for much better clearance, housing of the PCBs (labelled 6, Figure 36 (b)) and external optical access when bringing the head into contact with the sample surface. In this version, the cantilever sleds (sled 2 and sled 3) had automated positioning of the cantilever paddle (labelled 11, Figure 36 (e-f)) using a stepper motor in sled 2 (labelled 13, Figure 36 (e)) or a geared motor with dual optical encoders (with further evaluation of this found in Chapters 4 and 5) in sled 3 (labelled 10, Figure 36 (f)). Here, the cantilever was also secured magnetically to the frame (labelled 14, Figure 36 (e-f)) allowing for easy replacement of the cantilever chip. In Version 2, the long-ranging XYZ positioner (labelled 5, Figure 36) consisted of two Attocube ECS3030s stacked 90° rotated from one another for the XY axes, with a Picomotor linear actuator (8302, Newport, USA) for the Z-axis.

In Version 3 (Figure 36 (c1-c2)), a different arrangement of the OPU head superstructure is presented and the optical camera has been omitted. Here, the superstructure is a hinged system allowing the OPU and sled (labelled 7/8, Figure 36 (c1)) to point in either the horizontal, so the shadow of the cantilever can be projected onto the wall for locating where it is, or vertical, to engage with the sample surface below. Much of the rest of the system remains unchanged other than a redesign of the cantilever paddle to allow for more secure attachment to the sled frame (labelled 14, Figure 36).
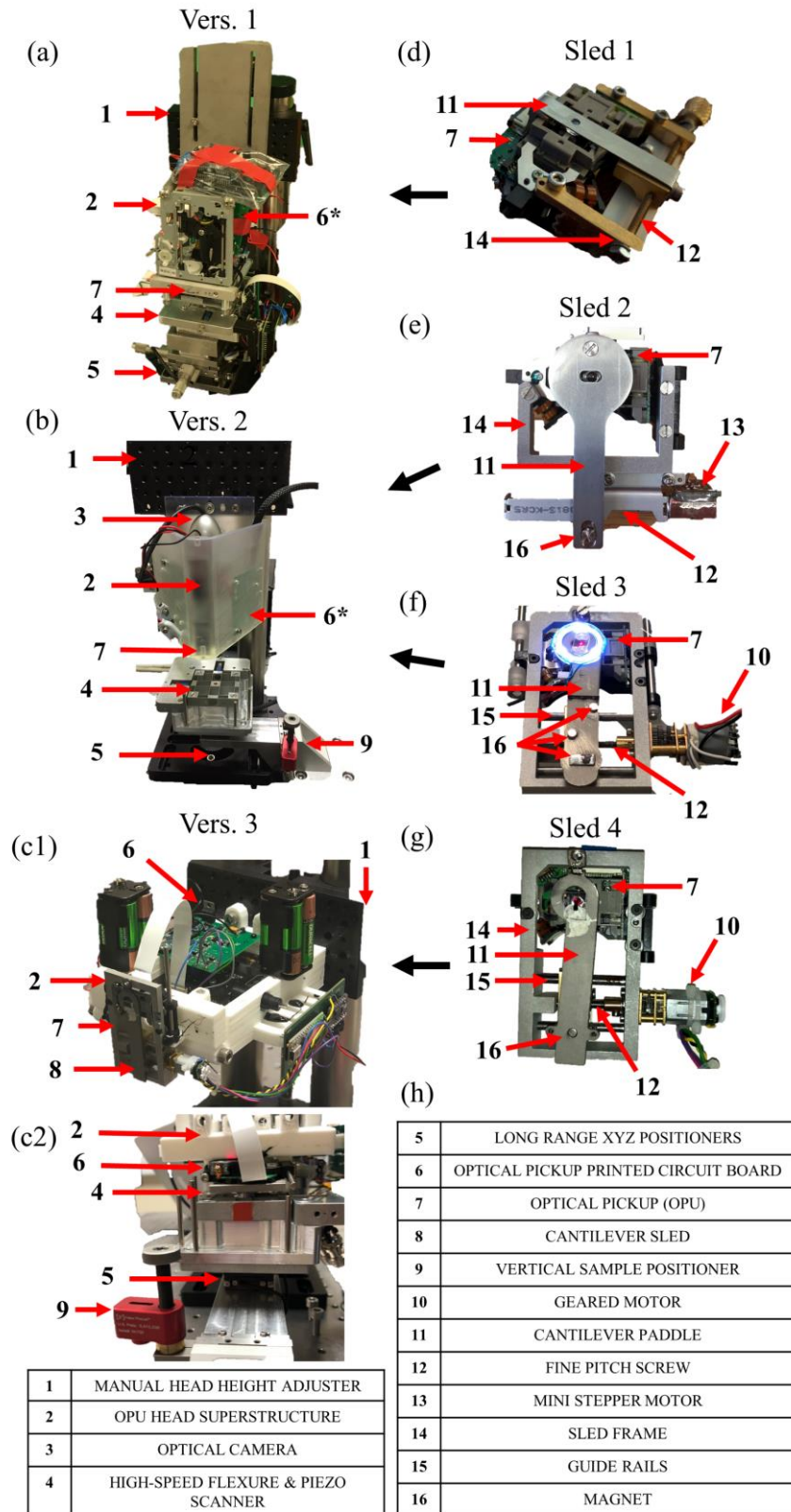
Figure 36: Version matrix of the OPU HS-AFM (a-c2) with each version's corresponding cantilever translation sled (d-g). The principal components are labelled and named in the table (h).

3.3.4 Control software used for the OPU HS-AFM

The hardware took many physical forms but the user facing control software written in LabVIEW stayed mostly consistent throughout. To summarise the principle functionality of the software, the three main user interaction panels are displayed in Figure 37 (a-c), where Figure 37 (a) shows the primary controls to instruct functions such as voice coil position (tracking and focus), geared/stepper motor position, DAQ I/O sample rate, high-speed scanner waveforms, incoming QPD or FES signals, real-time optical view (24 fps), real-time HS-AFM view (1 fps) and Fast Fourier Transformation (FFT) of the FES (more detailed data presented in the Results section).

In addition to the primary user panel, a second user panel can be enabled to manage the long-range sample exploration via control of the dual-axis ECS3030 stack. As shown in Figure 37 (b), this can be operated as a roaming interface to navigate using the up/down and left/right lateral directions across the sample, as well as requesting a 'Go to location' command. In this panel, settings such as the frequency and voltage for the ECS3030 actuators can be set too. These settings define how the internal PZT ceramic acts to move the stage using a stick-slip mechanism. For automated long-range (10s of micrometres) exploration of the sample, a serpentine raster path could be generated by setting the dimensions of the serpentine (i.e. origin, step length in x and y, and number of steps in x and y). For each new location in the serpentine, a dwell time can be set as the user defines.
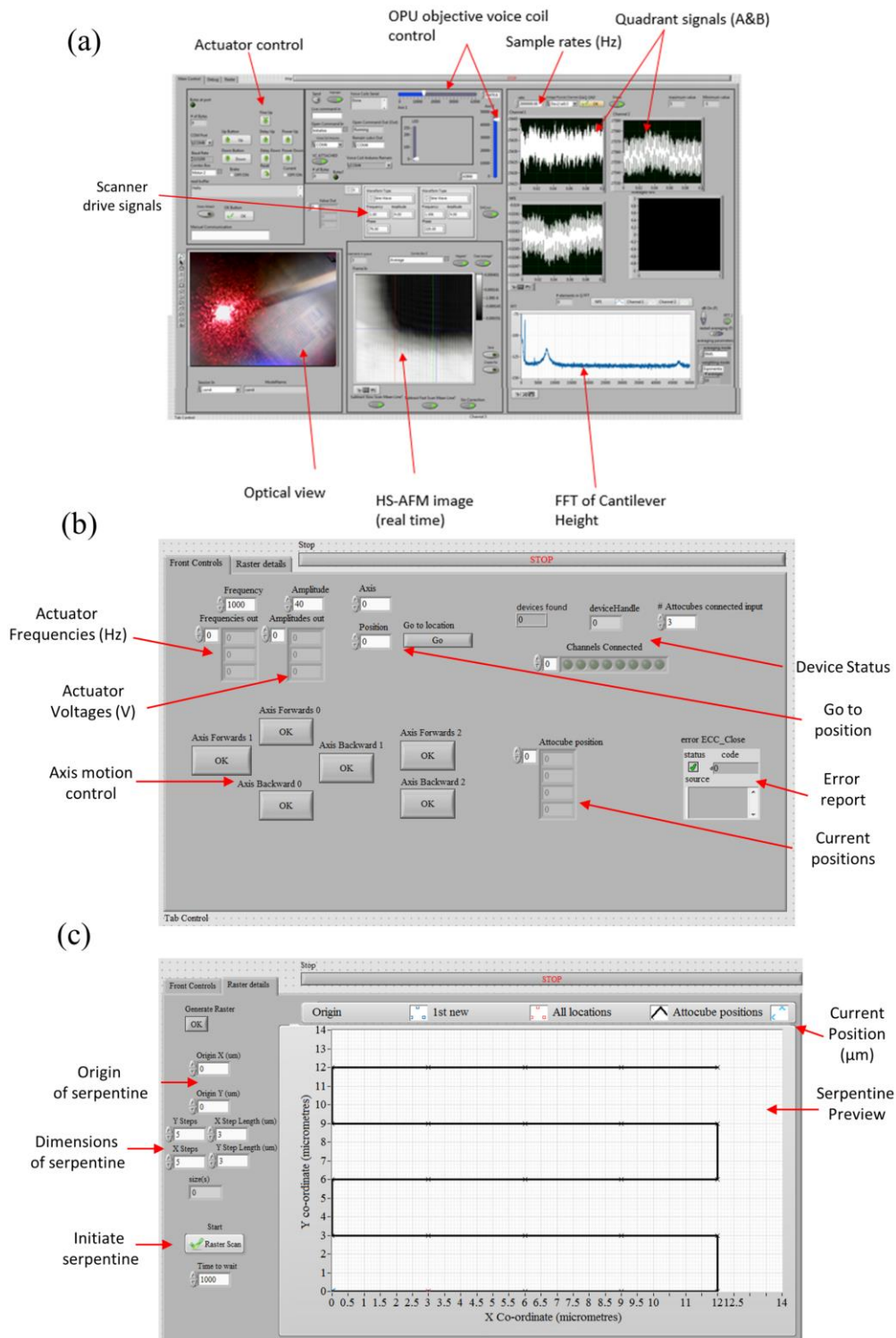
Figure 37: Main user interface for controlling the OPU HS-AFM, with key controls and indicators labelled. (a) Main control interface reporting information from the optical camera and data acquisition card, and sending commands to voice coil motors on the OPU and motors commands. (b) Panel for communicating with Attocube ECS3030 actuators in up to three axes. (c) How a serpentine raster path can be generated and monitored to enable long-range sample exploration.

3.4. Results

3.4.1. Displacement sensing of the cantilever

"The optical image, shown in Figure 38, demonstrates that the OPU can be used as an optical microscope by utilising the optical path through the objective lens. The objective lens is translated and focussed by the inbuilt voice coil motors. The microscope can be used for identifying the position of the laser spot and the cantilever. It is also essential for ensuring that the laser spot is correctly placed directly above the tip of the cantilever. The optical image can also focus on the sample, allowing regions of interest to be found prior to engaging the cantilever into contact with the surface."
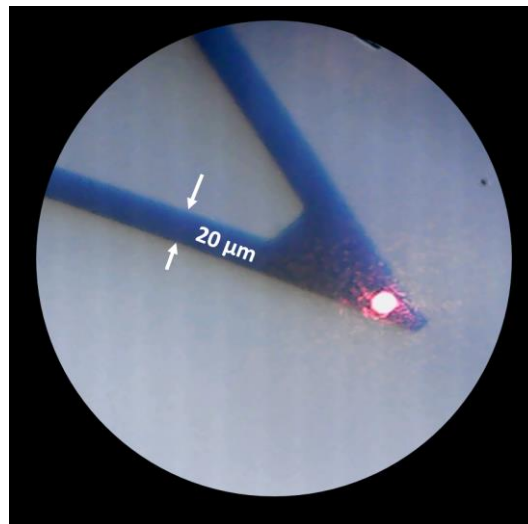
Figure 38: "Optical view through Sanyo HD65 OPU of laser spot incident on an MSNL–C cantilever."

"To test the fidelity and alignment of the detection system, the FES displacement measurement can be used to identify the resonant modes of the free cantilever due to thermal excitations in air and calculate the sensitivity of the astigmatic detection system (ADS). With the assistance of Dr N. Shatil, a model outlined by Stark *et al.* (81) was used to predict the resonant frequency amplitudes of these expected thermomechanical contributions to the signal, as shown in Figure 39 alongside the data measured by the OPU and LDV. The MATLAB (Boston, USA) code used to implement this can be found in the appended media storage to this thesis, alongside further description of the model and the physical parameters used."

"Using this model for the thermal excitation of the MSNL-C cantilever, the amplitudes of the first two modes are expected to be 0.838±0.24 nm and 0.125±0.04 nm. Here, we assume the parallel beam approximation (PBA) to compensate for the v-shaped geometry of the cantilever. In addition, we assume that thermal energy is only imparted from the surrounding thermal bath and that there is no significant thermal excitation from the laser (typically 0.3 mW at emission from the objective lens of the OPU). It is then possible to identify these experimentally by looking at the power spectral density of the focus error signal whilst the laser is incident on the MSNL-C cantilever: The FFT of the FES is determined by

calculating the power spectral density of the focus error signal whilst the laser incident on the MSNL-C cantilever,

$$S_p(f) = \frac{\Delta t}{T} \left| \sum_{n=1}^{N} v_n e^{-ifn} \right|^2 . \tag{11}$$

where the power spectral density, (S_p), is a function of the frequency components, (f), in the signal made up of discrete voltages, (v_n), sampled in Δt over a time period, (T). By taking a power spectrum, sampled at 2 MHz, for both the OPU and LDV signal responses it is possible to identify the first two resonant modes and measure their contributions to the signal."
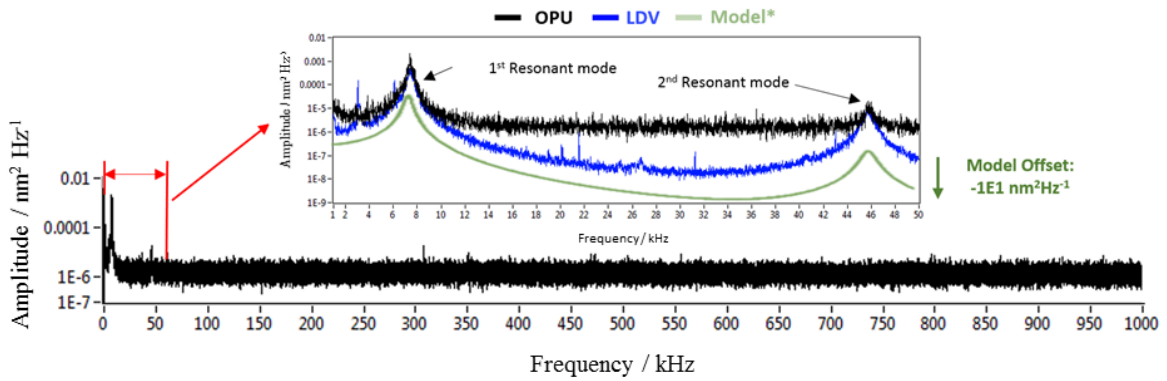
Figure 39: "Power spectral density (PSD) of the OPU's focus error signal (black) for a cantilever in free air. The 1st and 2nd modes can be seen at the expected locations in the sub-section of a spectrum and plotted with the LDV PSD (blue). The model (green) is offset in the y-axis for comparison against data."

"By looking in the frequency domain, resonances excited by the thermal energy in the room at (293.2 K) were identified. The first peak was found at 7.44±0.24 kHz. This corresponds to the first flexural resonant frequency expected for the MSNL-C cantilever specified as 7±3 kHz by the manufacturers (82). The amplitude for this mode was found to be 0.631±0.11 nm. The second peak was found at 45.8±0.35 kHz with an amplitude 0.117±0.05 nm corresponding to the 2nd predicted resonant mode. In both case, there is a slight overestimation of the amplitudes but within calculated uncertainty so otherwise there is good agreement to the model. The noise floor across the entire spectrum of the PSD is flat and approximately equal to 5 pm^2.kHz^{-1} compared to 0.05 pm^2.kHz^{-1} for the LDV system."

3.4.2 HS-AFM imaging comparison

"To further compare the imaging capabilities of the OPU and the LDV HS-AFM a grid of square pits arranged in a 'waffle' pattern, formed from titanium evaporated onto a flat silicon substrate, was measured (Figure 40). In each case, the sample was mounted on the same scanner and imaged with a scan amplitude 5 µm × 5 µm. Each HS-AFM image has 0.5 megapixels and took 0.5 seconds to collect, with no flattening or other correction of the image used."
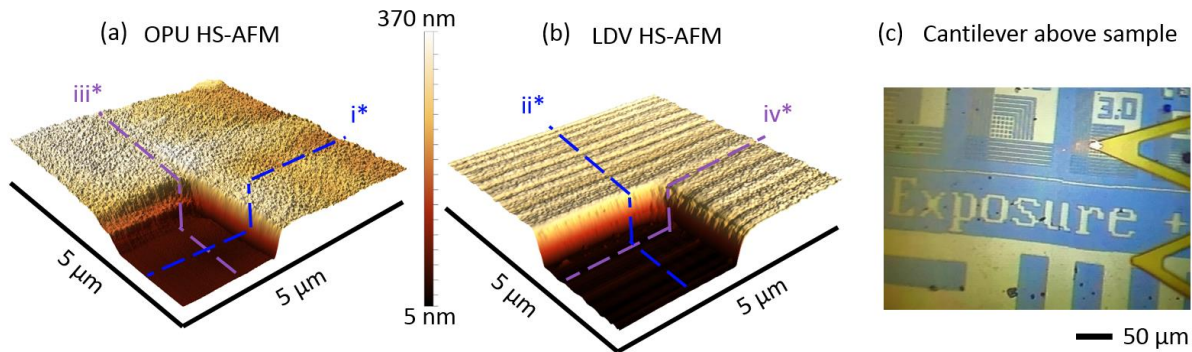
Figure 40: "Unfiltered data from the sample. (a) A 5 μm by 5 μm map of the silicon-titanium grid made using the OPU-based HS-AFM (line profiles labelled i* slow-scan and iii* fast-scan). (b) A 5 μm by 5 μm map of a silicon-titanium grid made using the LDV-based HS-AFM (line profiles labelled ii* slow-scan and iv* fast-scan). (c) Optical image of the cantilever, laser spot and Si Ti surface as imaged through the LDV-based AFM."

"By looking at the line profiles from Figure 40, in more detail in Figure 41, across the two surfaces it is possible to see the contrast in the heights of the two materials. Furthermore, for the OPU line scan, the contrast in the height deviation or roughness from the higher regions is much more than that in the lower regions, as expected due to the contrast in surface texture between silicon wafer and evaporated titanium."
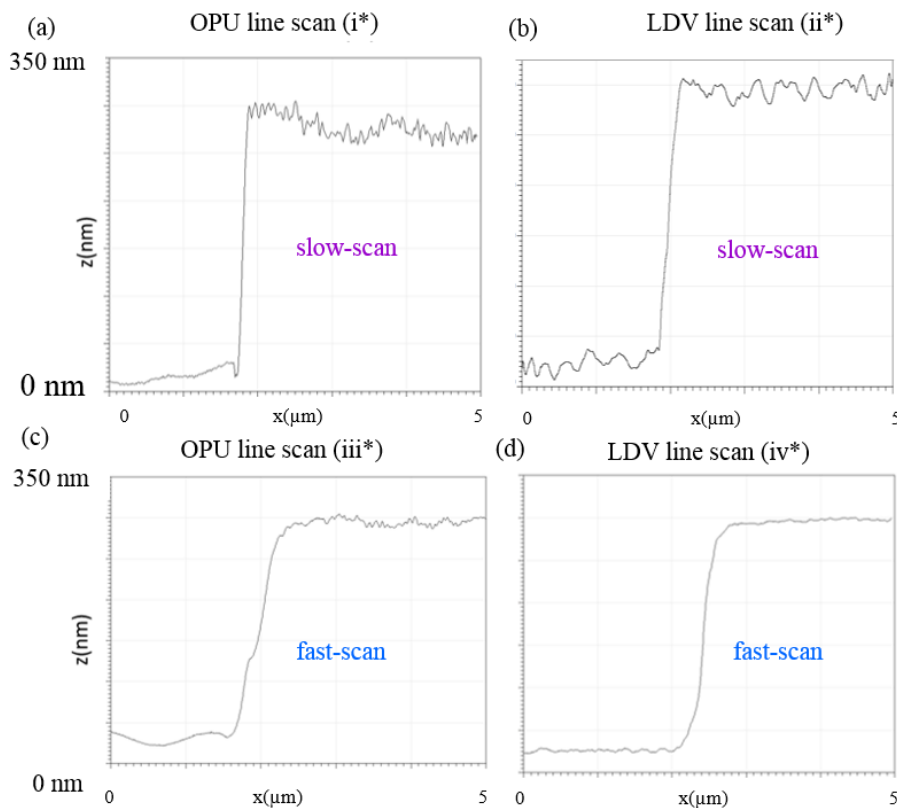
Figure 41: "(a)-(d) Line scans showing the cross-section through the OPU- and LDV-based HS-AFM datasets labelled by the lines (i*-iv*) in the prior figure".

"Figure 42 demonstrates the technique's ability to successfully image step heights greater than 250 nm, while still tracking the surface roughness of the material with enough resolution to distinguish between the two materials. This surface roughness contrast is less apparent in the LDV data due to a low frequency measurement drift in the LDV measured surface profile, which appears as lines running parallel to the fast-scan direction (bottom left to top right) over the surface in Figure 40 (b). This drift is more obvious in cross-sections in the slow-scan direction than the fast-scan Figure 41 (b), and can be corrected for using a number of post-processing methods such as median line flattening (see Chapter 6, Section 6.2) (45). Figure 42 shows the surface after implementing this compensation by sampling right to left, and compares it to the OPU-measured profile."
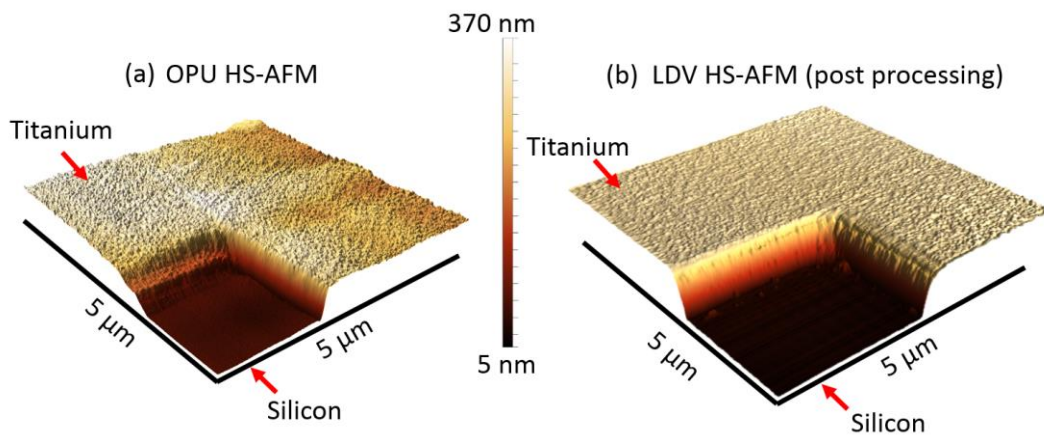
Figure 42: "HS-AFM topography maps of titanium evaporated on silicon wafer as measured by two HS-AFMs with different detection systems. OPU-based system (a) and LDV-based system (b) having used median line removal."

"We demonstrate the rapid scalability and stability of the OPU-based instrument by extending our field-of-view beyond that of a single frame. By translating our high-speed window to 30 different, but overlapping (50 % overlap), locations, within 90 seconds, it is possible to generate a composite image. Figure 43, shows this composite image made of 3.65×10^6 uncompressed pixels. It is presented side-by-side with an equivalent LDV-based HS-AFM composite image."
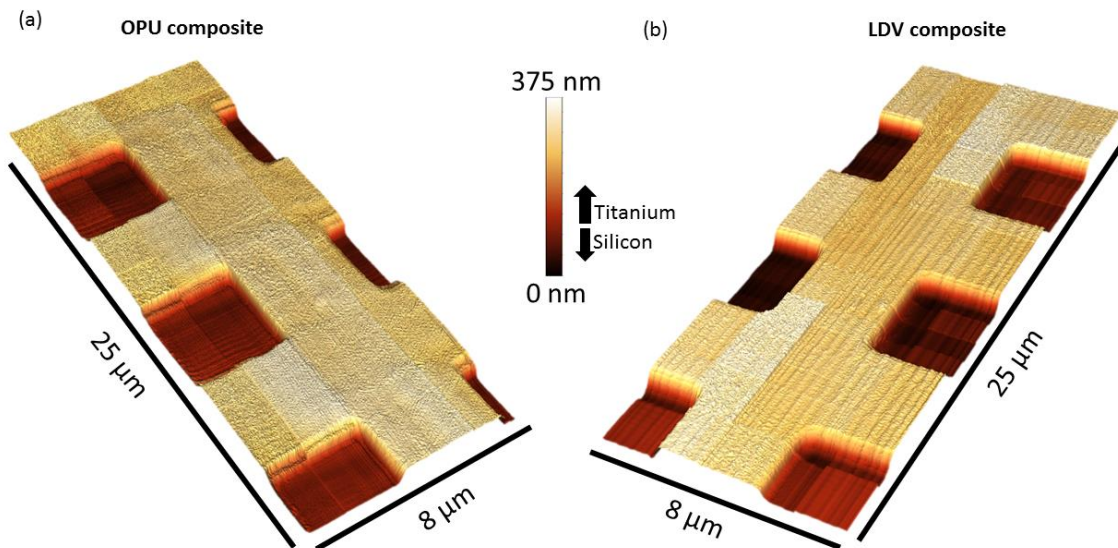
Figure 43: "Composite images, from 30 sub frames, made by both the OPU- (a) and LDV-based (b) HS-AFMs. The composites are 3.65 megapixels in size and taken in less than 90 seconds with a mean tip velocity of 10 mms^{-1}."

3.5 OPU-based HS-AFM: Application case studies

In Section 3.4, the OPU-based HS-AFM measurement capability was validated against a commercially-available LDV-based HS-AFM in two ways: firstly via the detection of two resonant modes (0.621±0.11 nm and 0.117±0.05 nm) of the MSNL cantilever; and, secondly, via the imaging of a silicon titanium grid with features on the order of tens-to-hundreds of nanometres. Whilst this can be used to validate some of the instrument's performance, neither of these studies directly show the instrument to have a tangible impact across scientific or 'real-world' application. Therefore, motivated by the impetus to show how the imaging capabilities could be used for real world application two studies were undertaken to assess if the OPU HS-AFM was able to image the critical nanoscale/sub-nanoscale surface features that are typically only resolved via AFM.

The two case studies involving the imaging of CRISP-Cas9-labelled DNA and thermally-sensitised AISI Type 304 stainless steel were chosen due to the maturity of sample preparation for HS-AFM because of prior related studies with the commercially-available LDV-based HS-AFM (58,83) and their links to current and ongoing research of interest to collaborators interested the capabilities of HS-AFM. Furthermore, the two case studies have been taken from two very different fields: genetics; and metallurgy. which go some way to highlight the diversity of impact that the technique of OPU-based HS-AFM offers. The two samples also differ from one another in terms of size, mass and transparency, which, in turn, demand different requirements from the instrument.

3.5.1 CRISPR-CAS9 as a programmable nanoparticle

3.5.1.1 Background

In this study, the OPU-based HS-AFM (Vers. 1, Figure 36) was used alongside the LDV-based HS-AFM (Bristol Nanodynamics, UK). To image labelled genetic material (i.e. DNA molecules) with CRISPR-Cas9 bound to specific target locations. The overall collaborative study was published entitled 'DNA nanomapping using CRISPR-Cas9 as a programmable nanoparticle', Nature Comms. (1) and was later showcased in The Kavli Prize collection 2018 by Nature due to its relation to the work for the Nanoscience-themed Kavli prize, which was awarded to Emmanuelle Charpentier, Jennifer A. Doudna and Virginijus Šikšnys, for their pinnacle research into CRISPR-Cas9.

The method for labelling the DNA and preparing the sample was carried out by J. Reed et al. from the Virginia Commonwealth University. The LDV-based HS-AFM was a 1st generation system from Bristol Nanodynamics and the OPU-based HS-AFM (Vers. 1, Figure 36) had been developed and built by F. Russell-Pavier with significant contributions from Dr O. Payton and Dr L. Picco at the University of Bristol and transported to VCU for this study. Previous studies by Mikheikin et. al. (84) had shown the LDV-based HS-AFM (Bristol Nanodynamics, UK) to have appropriate resolution and imaging capability to resolve the 'backbone' of DNA, enabling contour measurements to be conducted and specific genes to be identified by length. By permitting this stable and high-resolution imaging of genetic molecules (i.e. DNA) at this fundamental level using HS-AFM, novel observations had been previously made in identifying spurious genetic material in DNA purification systems (83). As such, the LDV HS-AFM was once again well suited to 'bench-mark' the surface being imaged, as in the previous section with the silicon titanium grid, so that the image outputs from the OPU HS-AFM (Vers. 1, Figure 36) could be validated.

Both the OPU- and LDV-based HS-AFMs were used in a similar configuration as in the previous study in Section 3.4.2 with the MSNL-C cantilever. However, in this work the long-range positioners on the two HS-AFMs were Smaract (X: SLC-1760, Y: SLC-1750, Z: SHL-20). The software presented in Figure 37 was used to carry out the experiments. Due to the transparency of the mica sample, illumination could be supplied from below the sample via a beam splitter on which the sample was placed. This permitted a well-resolved optical image and enabled the identification of markers on the mica surface which divided up the mica disc into four quadrants of different gene types.

3.5.1.2 CRISPR-CAS9 study: Method

Due to the focus of this chapter, the details outlined in this case study will be primarily focussed on the experimental work and data collection aspect of the study. Fewer details on the genomic underpinning are reported here. A full description of the method by which the samples were prepared and further information on the methodology can be found in the methods section of the principal paper

related to this work (1), where previously developed experimental protocols were used (85) to prepare the samples for HS-AFM.

The samples were first prepared by targeting sites on the DNA amplicons with the Cas9-sgRNA via incubation and subsequently fixing them in place with formaldehyde. A secondary step was then to remove unbound Cas9-sgRNA with a magnetic-bead-based system (1). The amplicons were then held in solution in a deposition buffer (10 mM TRIS, 10 mM MgCl$_2$, pH=7.6) and subsequently 1 mL of the 100 ng/μl solution was deposited onto a freshly-cleaved 10 mm diameter mica disc. The sample was then incubated for 90 seconds, washed with Milli-Q^{TM} H$_2$O (200 μl, repeated three times) and baked at 120°C for 20 minutes.

3.5.1.3 CRISPR-CAS9 study: Results

A significant study that was captured by the LDV-based HS-AFM was to evaluate the accuracy of the binding of the CRISPR-Cas9 to the DNA molecule of the TERT and HER2 genes. In Figure 44, we see how the number of base pairs (bp) between the two markers corresponds to the physical distance along the DNA strand. For TERT this is 145 bp and for HER2 it is 357 bp. These measurements, conducted by Dr. A. Olsen (Virginia Commonwealth University) and analysed by Dr. O. Payton showed that for 502 repeat measurements of the TERT gene there was a labelling efficiency was of 88%, with 5% of labels lying outside the 95th percentile confidence index. The same study was carried out on the HER2 gene for 504 repeat molecules with a 90% labelling efficiency and 5% of labels lying outside the 95th percentile.
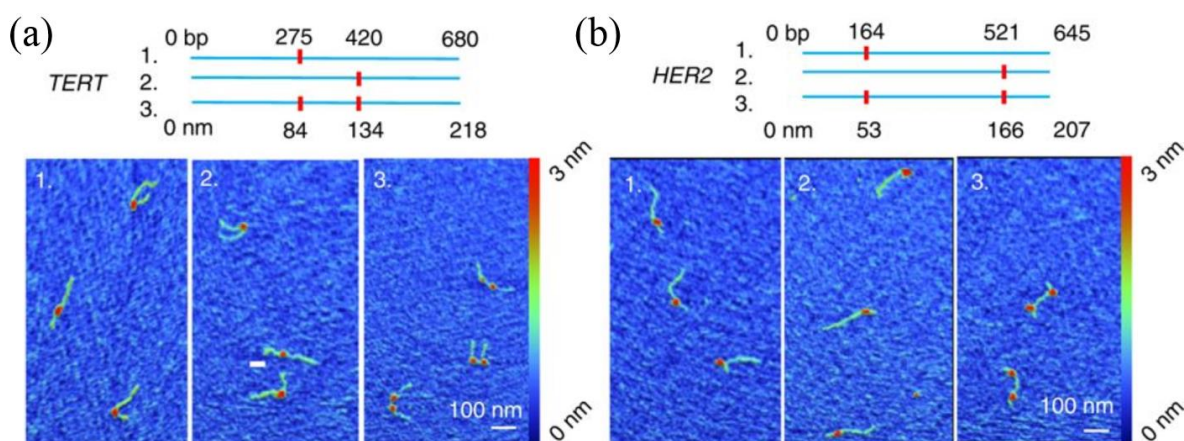
Figure 44: Six HS-AFM images taken with an LDV-based HS-AFM demonstrating labelling of the CRISP-Cas9 molecule to the genes of TERT (a) and HER2 (b), with location in base pairs plotted above.

From the images seen in Figure 44, it is possible to see both the CRISPR-Cas9 markers (red) and the DNA backbone (teal) on a freshly-cleaved mica surface (blue), which typically have heights of 3 nm and 300 pm, respectively. With the DNA backbone being <1 nm tall, it provided a surface feature

that would challenge the minimum detectable height in the OPU HS-AFM, which when monitoring a cantilever was found to be no less than 0.117±0.05 nm.

Figure 45 shows an example HS-AFM image captured by the OPU-based HS-AFM of TERT amplicon labelled by two CRISPR-Cas9 labels by F. Russell-Pavier, with instrument operation assistance from Dr L.Picco, Dr O. Payton and Dr. A. Olsen. Images of this surface were then repeated for 230 measurements of the CRISPR-Cas9 spacing for the TERT gene. These measurements were repeated on a different quadrant of the freshly cleaved mica disc where HER2 genes were present and repeated for 270 marker spacings. Histograms of the results from these measurements can be found in Figure 45(b) and Figure 45(c). A line profile of one pair of markers is also displayed in Figure 45(d). The median marker spacing, measured from the centroids of each pair CRISPR-Cas9 markers, was found to be 47.7 nm (s.d. 8.1 nm) for the expected distance of 46.9 on the TERT amplicon. For the HER2, the equivalent measurement was found to be 108.2 nm (s.d. 17.1 nm), where 114.1 nm was expected.
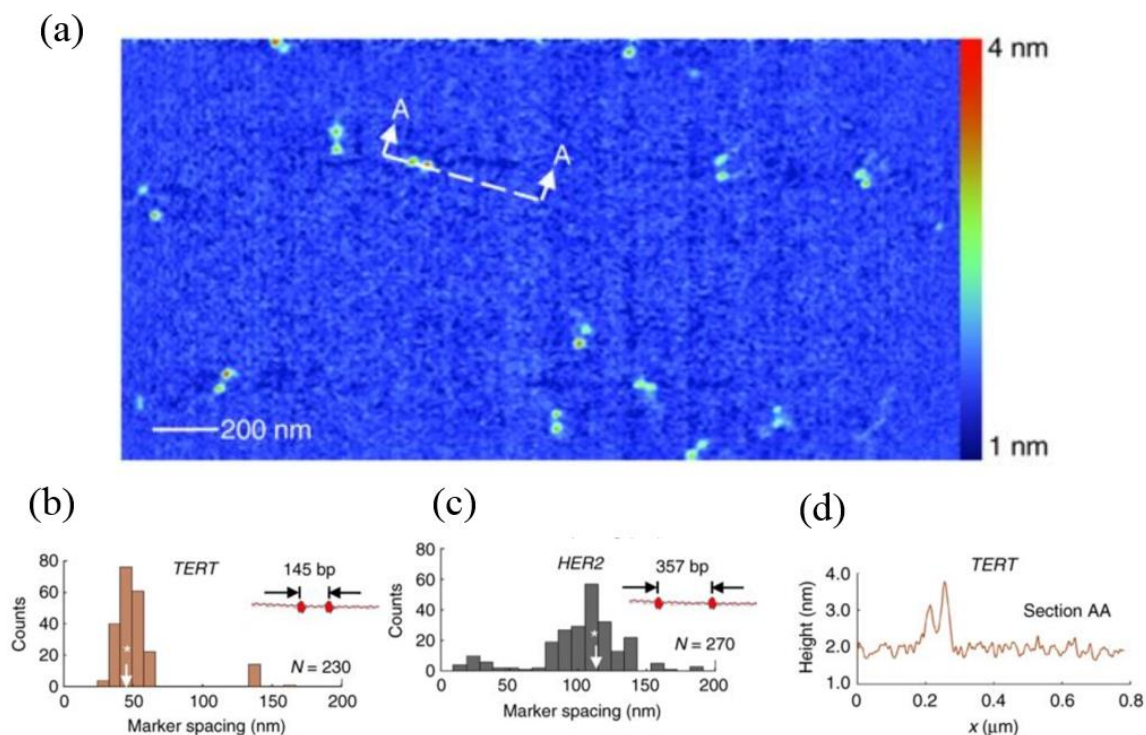
Figure 45: OPU-based HS-AFM (V1) image (area 1.25 µm by 2.5 µm) (a) of several CRISPR-Cas9-labelled TERT genes. Marker spacing distributions of TERT genes (b) and HER2 genes (c) imaged by the system. (d) a line profile through the dashed line presented in the image (a).

Also barely visible against the background in Figure 45 is the backbone of the TERT amplicon, in several instances of both cases-where the amplicon has been labelled and where it is unlabelled. The shape of the labelled TERT amplicon, where visible, also exhibits similar spatial properties to those captured by the LDV, where the molecule displays a sharp bend introduced by the sgRNA-Cas9.

A further three-dimensional view of another example image from the same surface can be found in Figure 46. Line profiles of the three types feature: 1: the DNA backbone of the TERT amplicon; 2: the CIRPR-Cas9 molecule; and 3: the cleaved mica surface, are plotted onto the same height graph for visual comparison.
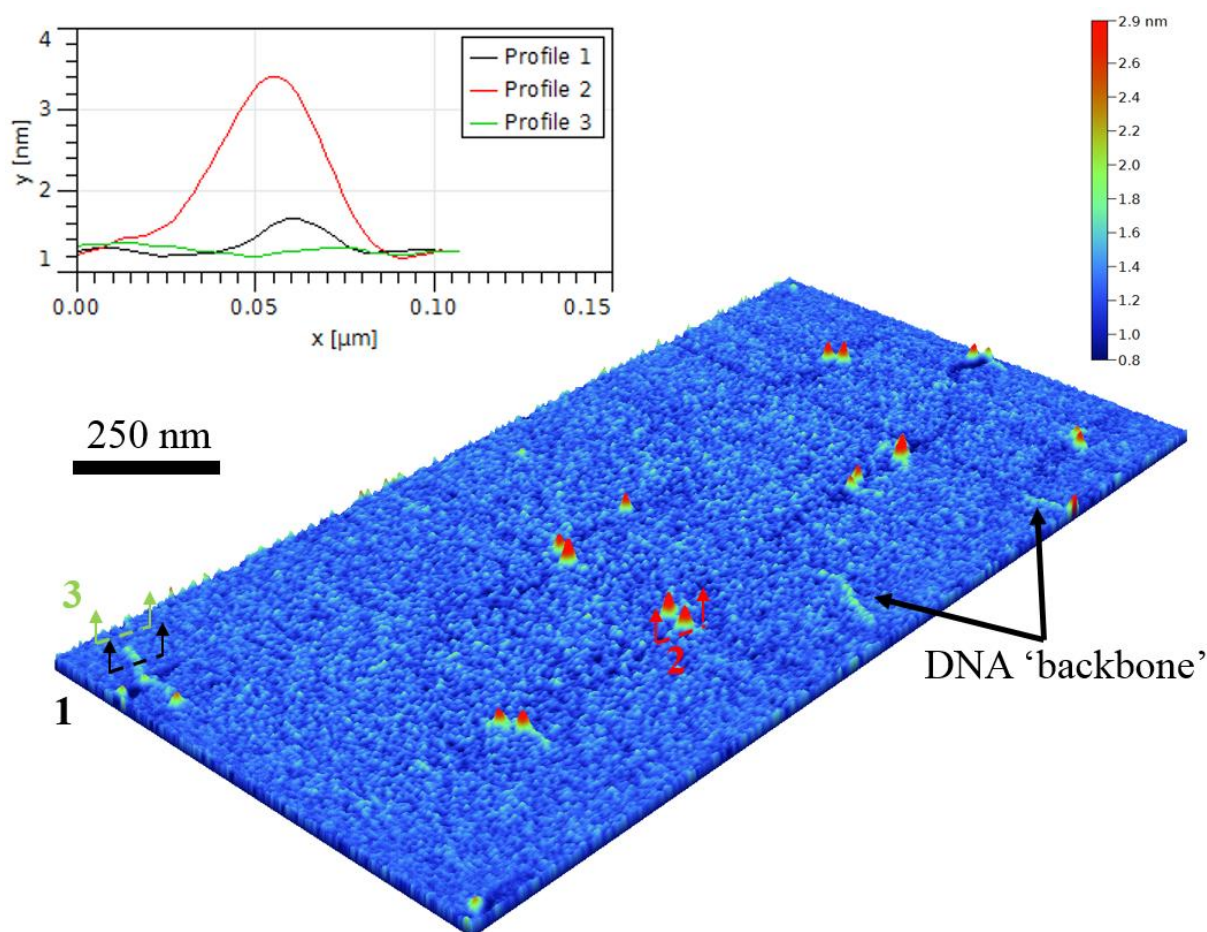
Figure 46: Line profiles (width 10 pixels) of parts of an OPU-based HS-AFM image (area 1.25 µm by 2.5 µm) of the three distinct features: 1- DNA 'backbone' of TERT amplicon; 2- CRISPR-Cas9 molecule; and 3- cleaved mica surface.

3.5.1.4 CRISPR-CAS9 study: Conclusion

By successfully imaging the CRISPR-Cas9 molecules attached to HER2 and TERT amplicons using the OPU-based HS-AFM, this hardware was shown to be able to accurately perform measurements on short-strand amplicons that, in turn, could be used for healthcare diagnostics. Due to the small heights involved (e.g. DNA backbone ~300 pm) this application challenges the detectable limit of the HS-AFM as a multi-axis system, where equivalent studies at that scale (i.e. Figure 39) have only validated sub-nanometre resolution in non-imaging applications. Moreover, this application benefits tremendously from the high-speed capability offered by the OPU to supply further statistical

confidence due to high-rate AFM imaging. Further potential of this method has yet to be fully explored, as the imaging speeds could increase by factors of 10-100 times with the integration of Blu-ray or HD-DVD optical pickups as vertical cantilever detection systems. In addition, the compact, mass-produced and low-cost nature of the optical pickup and the vast abundance of genetic material present in even one of the 10^{14} cells (i.e. ~2 metres of DNA per cell) in the human body make for an exciting combination to tackle a wide host of fundamental measurement challenges in genomics.

The measurements made by the OPU-based HS-AFM showed that if could correctly measure the marker spacing within the error of the instrument for both the TERT and HER2 amplicons after 230 and 270 repeats. However, in this type of parallel flexure stage it has been reported that small lateral errors can exist within the high-speed scan path and image formation (86). Such lateral errors are likely to result in both lateral compression and extension of regions in the image. As such, due to the freedom for the genetic materials to align in any lateral orientation, the errors are unlikely to result in a significant systematic uncertainty. This measurement uncertainty results in a broadening of the distributions of inter-marker spacing, akin to those displayed in Figure 45(b) or Figure 45(c), around the mean. To attempt to minimise this measurement error, further evaluation of the high-speed scanner using a fibre interferometer is performed in Chapter 5.

3.5.2 Thermally-sensitised AISI stainless steel type 304

In this study, an OPU-based HS-AFM (Vers. 2) was used to inspect the nanoscale surface topography of a thermally-sensitised AISI Type 304 stainless steel (SS). As mentioned in the Chapter Overview (Section 3.1), this metal is found ubiquitously amongst industrial and commercial applications, such as power generation plants and construction. This material is often implemented as a critical part of infrastructure due to its resistance to many corrosive environments (e.g. cookware and building exteriors, hence the name 'stainless') and the highly performant physical properties, such as ductility and strength. It is also implemented in commonplace applications such as domestic appliances and fasteners such as screws.

Here, the sample differs from the previous case study involving DNA molecules being deposited onto a freshly-cleaved flat mica surface, as this study is conducted on a subsection of a piece of homogenously-treated material that is removed from the bulk and polished, via the process outlined in Section 3.5.2.1, so that it is sufficiently flat for AFM. As such, two assumptions are made: firstly, that the sample surface that is imaged is representative of the bulk material and has not been taken from a special part of the bulk; and, secondly, that the sample preparation does not modify the surface features to any great extent compared to how they exist in the bulk. Therefore, any properties measured on this two-dimensional sample are representative of the global properties or distributions of the

three-dimensional bulk material. Moreover, the AFM features are much more varied and unpredictable due to the complex composition of the material, thermal treatment and crystalline structure.

3.5.2.1 Steel Type 304 study: Background

The composition of AISI type 304 SS primarily consists of iron (~70%), chromium (~18%) and nickel (~10%), and it is classified as an austenitic SS. As an austenitic steel, it is effectively a non-magnetic material making it a suitable sample to image with the OPU-based HS-AFM that brings many magnetically sensitive components (i.e. the VCMs) into proximity with the sample. However, a small amount of magnetism can be introduced via cold-working. Other types of SS (e.g. ferritic) could prove more problematic to image as they mostly exhibit stronger magnetic properties, which would cause a stronger magnetic coupling between the scanning sample and the OPU detection system due to the embedded VCMs.

However, Type 304 SS is not completely resilient to corrosion and it is susceptible to localised corrosion mechanisms if the sample becomes sensitised, such as via pitting and stress corrosion cracking (87). These localised processes can result in complete component (e.g. pipe) failure. Processes that cause thermal elevation of the sample, such as welding or irradiation in nuclear applications, can lead to changes in the composition of the grain boundaries present in the crystalline structure. Thermal elevation can cause the chromium in the Type 304 SS to diffuse away from the grain boundaries and combine with carbon to form chromium carbides ($M_{23}C_6$), which have different resultant material properties compared to both the chromium depleted grain boundaries and the bulk material (58). The SS is defined as 'thermally-sensitised' when the Cr locally diminishes to 12-14 wt%. Altering the material into three distinct material compositions changes the local physical properties of the sample (e.g. becoming more brittle) and creates initiation sites for processes such as intergranular fracture. Previous studies have shown that EBSD (88), TEM (89) and AFM (67) could be used to map out the abundance of the carbides found along the grain boundaries, typically 1-10s nanometre(s) in diameter. By resolving and identifying carbides, information about their sample-wide abundance and dimensions can be used to inform which regions have undergone more severe grain boundary elemental segregation due to thermal sensitisation and are therefore more susceptible to intergranular corrosion. In addition, this information can also be used to inform models of $M_{23}C_6$ carbide formation (90).

3.5.2.2 Steel Type 304 study: Method

A 1 mm thick sheet of AISI Type 304 SS supplied by Goodfellow Cambridge Ltd was thermally sensitised by Dr. R. Burrows (University of Bristol & National Nuclear Laboratory) by heating it to 600°C for 70 hours, as reported in literature (58). In this study, a 20 by 5 mm sample was cut out and subsequently polished, via a method previously reported in detail in literature (91), by Ms S. Moore. To achieve the correct surface finish suitable for SPM, it was polished with silicon carbide grit paper (P600 to P4000), incrementally. Two subsequent steps included using diamond paste (KD

diamond pastes, Kemet International Ltd.) and a vibropolisher (Vibro^{TM}, Buehler) with colloidal silica for 12 hours to complete the fine material attrition. A subsequent cleaning process involved using diluted detergent to remove any residue colloidal paste, followed by sonication with ethanol and then isopropanol. Finally, the sample was rinsed using Milli-Q^{TM} water to remove stray dust or salt that may be present on the surface before imaging.

The sample was then mounted on to a 12.5 mm diameter aluminium pin stub using Adhesion Silver DAG 1415M (Agar Scientific, UK), which was subsequently fastened to the high-speed scanner. Due to the opaque nature of this sample and its high reflectivity (i.e. essentially a mirror), locating both the cantilever and any prominent surface features was very difficult using the optical image. As such, the cantilever was aligned with the astigmatic system in the OPU using the silhouette method whilst the sample was far from the detection head. To do so, the OPU focussing voice coil actuator can be withdrawn into the housing so the cantilever's silhouette is projected onto a screen surrounded by a circle of stray laser light. A combined motion of the tracking voice coil actuator and the cantilever sled can allow for the silhouette of the cantilever to be placed centrally within the circular projection of light. Furthermore, the location of imaging on the sample could only be approximated to ±0.5 mm due to poor optical resolution of any distinguishable surface features. Due to the expected prevalence of grain boundaries across the metal, it was not necessary in this study to land anywhere other than on an arbitrary location on the sample.

3.5.2.3 Steel Type 304 study: Results

Once the system was imaging, the long-range positioners (i.e. ECS3030, Attocube) were used to navigate around the sample to find regions of interest, such as carbides or grain boundaries. As grain boundaries had not yet been imaged by this system, a single line or trench was not sufficient to guarantee that what was being imaged was a grain boundary. Therefore, features that showed co-incidences of several grain boundaries, such as a triple-point, or a significant fraction of a small grain boundary were required to give confidence to the inspection. Grains size ranged from 1-10s of micrometres, whereas the imaging window of the OPU-based HS-AFM was a 4 μm by 4 μm area per second and, therefore, grain boundaries, whilst abundant, represent a minority of the surface.

After making contact with the surface, a small grain was soon identified that could be entirely imaged within a single frame. An example frame displaying this is shown in Figure 47 (a). In imaging the extent of a grain boundary, confidence was given to the assayer that these features were indeed the boundaries between grains of the SS. In Figure 47 (b), another HS-AFM frame is presented showing a triple-point where the boundaries of three grains meet. Within the grain boundaries several carbides can be seen. Three pairs of line profiles, in Figure 47 (c) to (e) sample across boundaries and show the 'trench' of the grain boundary (black) and 'bump' of the carbide, in each case. Also present on the

surface in Figure 47 (b) is a cluster of high features which most probably represents salt or residual polishing substance, such as colloidal silica.
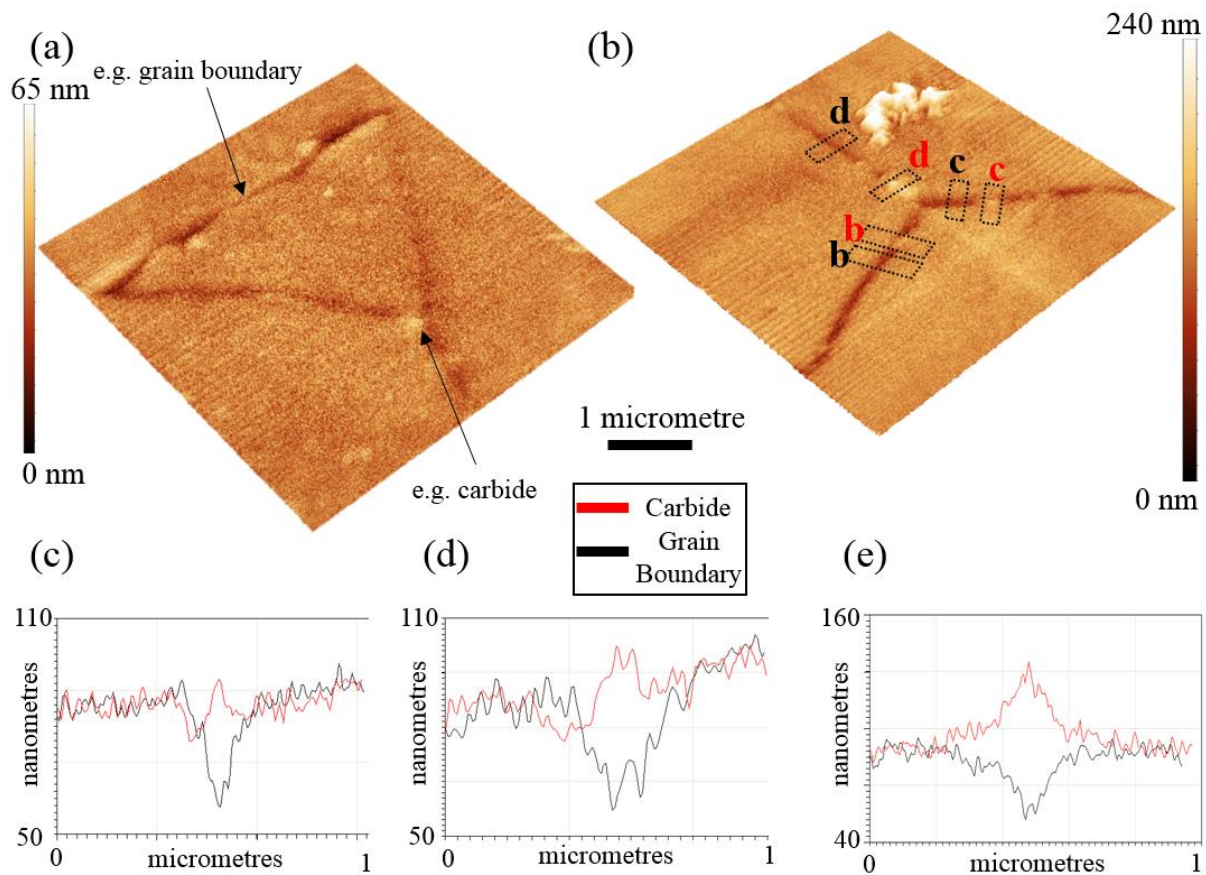
Figure 47: Two side-by-side OPU-based HS-AFM images (area 4 μm by 4 μm) of the same sample of thermally-sensitised AISI type 304 stainless steel. (a) Small grain bounded by three prominent grain boundaries, (b) Intersection of three grain boundaries where six line profiles of the surface have been extracted to reveal $M_{23}C_6$ carbides in grain boundary. The three pairs of line profiles (b-d) have been plotted in (c)-(e).

3.5.2.4 Steel Type 304 study: Conclusions

In this application case study of HS-AFM, using an OPU detection head has shown nanoscale surface features (e.g. grain boundaries and $M_{23}C_6$ carbides), critical to the understanding of corrosion mechanisms in AISI type 304 SS, with a high temporal resolution, within the field of AFM, of 1 frame per second. Such results demonstrate how an OPU-based HS-AFM is well suited for long-range mapping of material topology, where the features of interest may extend well beyond a single frame. Identifying the prevalence of such surface information across a sample can prove highly valuable for material forensics on either post-operation plant components from industry or on independent proxy samples that have undergone conditioning akin to those found in industrial applications. In addition, dimension characterisation and abundance of grain boundary carbides can be used as input data to

models predicting localised corrosion mechanisms rather than having to input values based upon assumptions.

The results shown here are very complementary to those result shown in Chapter 5, where we see how optical profilometry with optical pickups can be used to identify grain areas over hundreds of micrometres with a coarser resolution. As well as providing the ability for long-range mapping, the system has the temporal resolution to watch dynamic surface events. With further development work, the instrument has the potential to use a combination of long-range surface study (i.e. via high-speed optical profilometry) and OPU-based HS-AFM to observe micro- and nano-scale surface corrosion in real-time, as was done by Ms S. Moore (58) using a commercial LDV-based system (Bristol Nanodynamics, UK). Such observations would shed new lights on the temporal nature of driving mechanisms behind corrosion found in this material (i.e. AISI type 304 SS), as well as providing a method that could be used widely with other metal studies and indeed surface corrosion processes.

For identifying grain boundaries and spatial features, AFM results can be combined with other techniques (e.g. electron backscatter diffraction (EBSD) or tunnelling electron microscopy (TEM)) using correlative microscopy (92). Combining AFM with other techniques such as optical microscopy, scanning transmission electron microscopy (STEM) or EBSD permits observations to be made around the correlation between crystallographic orientation and carbide formation (93), whereas imaging the sample with a technique such as TEM, gives further information about the exact chemical composition of the material (93). This chemical composition, combined with the sites of carbides in the grain boundary, can be used to observe how the localised thermal sensitisation has changed the segregation of the material and indicate how the local material properties have been altered.

3.6 Discussion

"The quality of the Si-Ti surface profiles demonstrates that an OPU detection system is a very suitable candidate for contact mode HS-AFM, capable of producing topographical surfaces equivalent to those obtained using a high-quality commercial HS-AFM. The consequence of such results gives promise of both the reduction in the cost of performing HS-AFM and a vast increase in measurement throughput (pixels per second). Mikheykin et al. (1) made use of this technique in which two HS-AFMs, with either LDV or OPU detection system, carried out length assays of DNA molecules. In that work, the OPU-based HS-AFM was demonstrated to be capable of imaging DNA backbones of ~300 pm in height. Sub-nanometre resolution will likely be critical for other potential HS-AFM use cases such as the evaluation of atomic step heights in new classes of 2D materials (22)."

The OPU-based HS-AFM was a key aspect of the collaborative study with Mikheikin et al. (1) to map TERT and HER2 amplicons marked with CRISPR-Cas9 molecules. This study demonstrated a water-layered, mediated, passive feedback method of HS-AFM based on an OPU detection head, to repeatedly achieve sub-nanometre resolution and support a significant scientific breakthrough. Although

OPU-based AFM systems have been used in the past to image DNA structures (33), the imaging rate was much slower than in the case study reported in Section 4.1 (i.e. 0.2 lines per second reported in previous work compared to 1000 lines per second as reported here) and lower pixel density (256 by 256 pixels compared to 500 by 1000 pixels). Other prominent works in this area, performed by the same group (60) showed how high-speed imaging could be achieved using optical pickups in tapping mode via the integration of a specialised small cantilever with a resonant frequency of 5.5 Mhz. This work implements an off-the-shelf and widely available cantilever (MSNL, Bruker). Other method variations include a 700,000 increase in explorable measurement area (17 μm by 17 μm versus 2 cm by 2 cm) (60). These method variations address the need for nanoscale technologies to be scalable. Firstly: scalable in terms of both imaging across several orders of magnitude; and secondly: scalable, in terms of improving the ease to replicate the instruments (based on mass-produced components) to enable a number of equivalent systems to work alongside one another and, therefore, the paralysation of AFM imaging. Both aspects aim to enable more comprehensive AFM-based studies than are typically associated with the technique and attempt to bridge the 'nanoscale-to-microscale' measurement gap.

Further work could look to utilise the higher bandwidth of the ADS (> 45 MHz). The OPU detection head may be used to monitor higher modes (> 2nd) of the cantilever and high AFM imaging rates. Such higher bandwidth could be captured by replacing the multi-channel USB DAQ from National Instruments with a DN2.445-04 based digitizerNETBOX (Sprectrum GmbH, Germany). Using the displacement measurements alongside the angular measurements offered by the ADS, in frequency domain further channels of information such as contact resonance or friction mapping can be explored (94). The integration of different types of optical pickups such as Blu-ray or HD-DVD which typical utilised 405 nm would look to increase the sensing bandwidth of the system, reduce the spot size of the laser (e.g. ~500 nm) and increase the sensitivity of the astigmatic focus error response." Whilst, initial studies into powering and controlling the PHR-803T optical pickup (typically used in XBOX 360) were undertaken, a fully integrated HS-AFM wasn't evaluated in the scope of this thesis.

3.7 Conclusions

"An OPU-based HS-AFM has been developed and evaluated with its performance compared against a commercially available LDV based HS-AFM. Results show that the resolution of the OPU-based system can measure sub-nanometre, thermally excited, resonant modes of a commercially-available AFM cantilever agreeing with both a theoretical model and independent LDV measurements. Subsequently, the two instruments were used to perform HS-AFM over an area of 200 μm^2 generating 3.65 megapixel images in 90 seconds. In the presented HS-AFM images the OPU was shown to offer better unfiltered stability than the LDV, although it was shown to have a higher noise floor in the power spectrum."

In addition to validating the instrument using a free cantilever in air and a silicon-titanium calibration grid, two 'real-world' use cases of the technique have been reported from two different

disciplines: genomics; and metallurgy. In the genomics case study into DNA amplicons labelled with CRISPR-Cas9 molecules, the OPU-based HS-AFM was able to resolve key nanoscale and sub-nanoscale surface features that could be using for healthcare diagnostics. These results give significant purpose to the instrumentation development reported here and in future developments as these genetic samples require a unique set of imaging capabilities that are well-matched to AFM. The key output values, such as inter-marker spacing between DNA markers, also benefit from repeat measurements resulting in improved statistical confidence, provided via the high measurement bandwidth found in the optical pickups.

A second real-world use case of the OPU-based HS-AFM technique reported in this chapter involved the study of the surface features of a thermally-sensitised AISI type 304 stainless steel. Here, the high temporal resolution was used to navigate around the sample and resolve important surface information, such as grain boundaries, within a single frame which took <1 second to create. It was proposed that the high speed (in the context of AFM) can be used to provide a comprehensive sample-wide study of nanoscale surface features, as has been reported for metals before (67), or to observe the temporal properties of the driving mechanism behind surface corrosion events, such as pitting, as observed by Ms S. Moore (58), which can lead to bulk material failure and loss of critical infrastructure in industry. As such, the technique has been shown to be valuable for both post-operation material forensics and observing surface corrosion dynamics, both of which can help inform how to mitigate against key causes of corrosion, thus prolonging operation life of components and improving the mechanical integrity of components.

"It is further postulated that, since the mechanical upper limit of this form of HS-AFM imaging has not yet been found, the imaging frame rate of the method can be increased to meet the maximum bandwidth of the detection OPU (which can exceed 100 MHz). With other forms of digital storage becoming popular and more compact, compared with optical media discs, several decades of research have been left with a dwindling purpose. With the increasing demand for the characterisation of the building blocks within nanotechnology, we propose a route to utilising optical pickups to support this. The presented research has demonstrated OPUs as a scalable and sustainable toolset for exploring the nanoscale and extending these measurements to macroscopic lengths."

Chapter 4: Astigmatic optical profiler for large-area surface mapping and real-time imaging

4.1 Background

The working principles of an optical profilometer involve making a measurement of the topography of a surface using the interaction of light; this can be done at a single location, via a line scan across the surface or by scanning the sample in two dimensions. As such, an optical profiler typically consists of an optical detection system and a single/multi-axis scanner to move the sample. Optical profilers are used in many material characterisation studies across various length scales (95) being used to image anything from human-sized infrastructure, such as settlements (96), roads (97) and contact lenses (13), or microscale biological samples, such as live cell imaging (98) and some instance even offering nanoscale lateral resolution to give scope for imaging such samples as viruses (99). The method of detection in optical profilometers detection varies widely with some being based on optical dispersion (11), interferometry (100), astigmatic (12,95) or structured light (101). In this chapter, experimental work builds upon both this previously-reported literature and studies carried out in this thesis on using the astigmatic system and voice coil motors in OPUs for development of application-specific optical profilers.

As seen in Chapter 2 Section 2.2, the Sanyo HD850/65 contains an astigmatic detection system, used in typical operation to regulate the focus of the optical pickup when reading from an optical media disc. It has been reported in literature (1,2) and Chapter 3 that this optical pickup has sensitivity to sub-nanometre displacements capable of resolving amplitudes of the primary mode (0.0631 ± 0.11 nm) and secondary mode (0.117±0.05 nm) of an MSNL-C (Bruker, USA) cantilever with a reflective gold-coated topside, excited by room temperature air molecules. Nanoscale resolution was also achieved later in Chapter 5 when imaging a silicon substrate placed on the side of a kinematic parallel flexure stage and its scanning motion monitored. In this case, the astigmatic detection system is used on a homogeneous surface, in terms of both the material and the geometry. Therefore, the focus error signal (FES) response (i.e. s-curve) will be repeatable and the response could be calibrated in this application using an interferometer. These two previous applications vary from the one reported in this chapter, which looks to use the astigmatic detection system directly on a sample to inspect local topography and surface feature contrast related to similar work reported in literature

The foundation of the optical profilometers developed in this chapter and in previous works (9,12,13,33,102,103) is to translate a sample with respect to the astigmatic system and utilise the small laser spot size (~1 μm), high bandwidth (45 MHz) and high displacement sensitivity (~1 nm) present

in the optical pickup hardware. However, for the instrumentation development in this chapter it must be appreciated that the response from the astigmatic system is known to vary with physical parameter, such as depth of surface liquid (33), roughness changes (104) and sample material (13). As such, when scanning laterally across a multi-material sample or one with changing surface geometry it cannot be assumed that any focus error response holds true unless it is inspected on a pixel-by-pixel basis (104). Many of the data presented in this chapter therefore display the response from the astigmatic system in terms of normalised contrast. For evaluation, the variation in FE response curve is also demonstrated within an optical profilometer image of a UO_2 thin film, by modulating the height of the sample with a closed-loop nanopositioner similar to previous studies in literature (104).

There are many advantages in using the astigmatic detection system in optical pickups for surface scanning microscopy. Firstly, a major advantage over contact surface microscopy techniques (e.g. atomic force microscopy) is that it is non-contact and, therefore, not limited by the sample requirements as in SPM (105). For example, the imaging performance is not dependant on such surface properties as the adhesion of particles on the surface (91), the frictional properties (106) or sample stiffness changes (94). In addition, the astigmatic system in OPUs is compact, low-cost and can be operated in a wide range of conditions, such as those typical of the consumer product. Sample preparation is also not as extensive as is common in other non-contact surface microscopy techniques, such as scanning electron microscopy (SEM) (107), where applying a conductive coating or imaging under vacuum are common practices. As such, the astigmatic system has tremendous potential in biological applications where imaging can be conducted on a sample, such as a cell or bacteria, in vivo in open air or in liquid environments (33). As with other optical techniques, the spatial resolution is constrained by the Abbe diffraction limit (e.g. 540 nm for the Sanyo HD85 with an NA of 0.6) due to the following equation:

$$d = \frac{\lambda}{2NA} \tag{12}$$

where d is the resolvable length, λ is the wavelength of the light used and NA is the numerical aperture of the optical system. It can also be complementary to techniques such as AFM or optical microscopy, acting to bridge the gaps between the micro- and nanoscale (108).

As the optical pickups also have multi-axis voice coil motors (VCM), aligning the astigmatic system with the sample becomes trivial and has the potential to be automatically regulated to ensure in-focus operation, as in optical disc players. In the work presented here, the potential for the VCMs in the OPUs has been explored to be used as the principal scan axes in the optical profiler for high-speed scanning. As seen in more detail later in Chapter 5, Section 5.4.3, the tracking VCM can be translated over 10s of micrmetres and frequencies of 100s-1000s of Hertz. It has also been shown in literature (27) how these same VCM motors can be modified with additional components, including adding a flexure frame to make the system stiffer, thus adjusting the resonant frequency and altering the distance

travelled per volt for the voice coil. In this example, the modified OPU voice coil could then be calibrated and used to provide vertical actuation of a cantilever in a custom-built AFM.

In this chapter, an astigmatic optical profilometer is created using scanning components common to the 'Hi-Fi AFM' (2), such as the ECS3030 (Attocube Systems AG, Germany), the automatic power control (APC) PCB and a modified version of the VCM PCB. The profilometer is further developed to work in real-time producing 1 frame per second over 100s of square micrometres by enabling scanning motion via the inbuilt VCMs in the OPU. Subsequently, the optical profilometer is developed such that a pair of OPUs become responsible for dual-axis scanning, sample height modulation and the focus error response in an optical profilometer, enabling a high-rate low-cost configuration to observe dynamic microscale events and explored significant fractions of a millimetre within minutes. The final study into optical profilometry in the chapter adapts a combination of these methods into creating a specific tool for scanning and locating AFM cantilevers on an MSNL (Bruker, USA) cantilever chip used in HS-AFM.

In the following section in this chapter, the methods used to develop different forms of an OPU-based optical profilometer are outlined. The initial configuration looks at validating the OPU as a detection head for optical profilometry using a calibrated three-axis XYZ nPoint nanopositioning stage (XY60Z20-257, nPoint, USA) to slowly scan the sample, in two dimensions with a raster pattern, whilst making use of the focus error detection system to extract relative contrast on the sample surface. The method is then developed to increase the imaging rate from 75 seconds per image, as with the initial method, to 1 frame per second. This is attempted by changing the origin of the fast-scan axis from the nPoint to the OPU's tracking axis voice coil. This increases the line scan rate but removes the ability to sense the position of the scan in this axis. Instead, images formed by this technique can be calibrated after collection either by correlating two images from overlapping locations and then using the closed-loop slow-scan positioner locations to establish a pixel-to-micrometre value or by using a calibration curve for the voice coil using external measurements from interferometers, such as the results presented later in Chapter 5. The next iteration of the method looks to modify the system by using the tracking axis voice coil in a second optical pickup on which the sample is now mounted, to scan the sample in the slow-scan axis thus negating the need for the XYZ nPoint nanopositioner and permitting what is named the 'All-OPU' profilometer. The final form of this method that was developed in this work was tuned for use within an atomic force microscopy (AFM) to image the location of a AFM cantilever with respect to the astigmatic detection system. As such, the slow-scan axis is now provided by a custom-built actuator mounted to the front of a single OPU. This device was previously introduced as a cantilever sled in this thesis in Chapters 2 and 3.

4.2 Standard mode optical profilometry with an OPU

4.2.1 Arrangement of actuators and sensors for the standard mode optical profilometer

In this configuration the optical pickup is placed above a XY60Z20-257 (nPoint, USA) nanopositiong piezo stage (Figure 48), which has a lateral range in the 'X_F' and 'Y_S' axes of 60 µm and a vertical (i.e. towards OPU) range of 20 µm. The XY60Z20 is controlled with the C.400 (nPoint, USA), which is responsible for providing the scan path that makes up an image (described later), whilst the astigmatic system remains stationary. Underneath the XY60Z20 stage are two ECS3030 (Attocube Systems AG, Germany) responsible for translating the scan window over distances up to 30 by 30 mm in a raster scan fashion (i.e. axes X_{RA} and Y_{RA} in Figure 48).
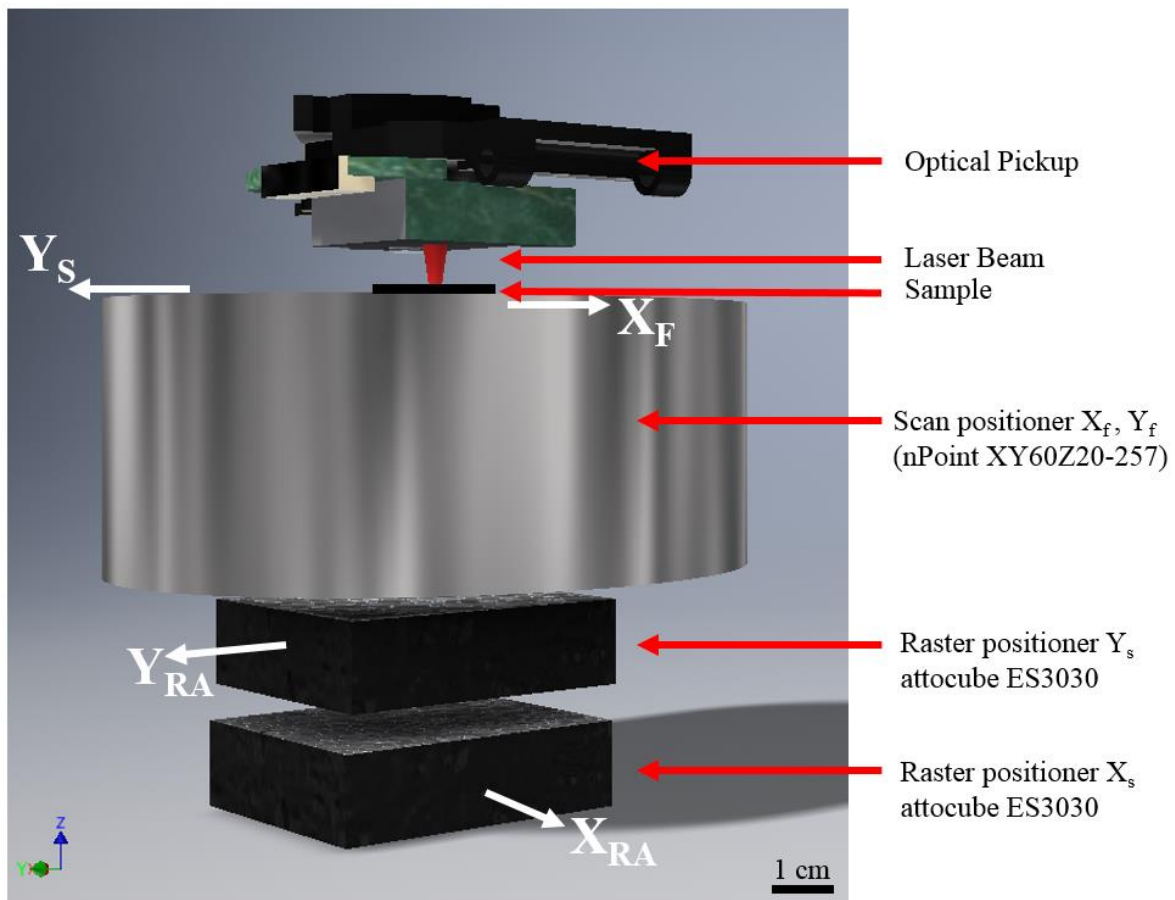
Figure 48: 'Exploded diagram' of a standard mode astigmatic optical profilometer with a Sanyo HD850 OPU, XY60Z20 nPoint closed loop scanner and two ECS3030 Attocube long-range scanners.

To avoid any issues connected to clock drift or phase offset between the driving of the stage and digitising the focus error signal, a multi-functioning NI USB-6366 DAQ with two analogue outputs (AO) (16-bit up to 2 MS/s) and eight analogue inputs (16-bit up to 2 MS/s) were used to drive the fast (X_F) and slow (Y_S) scan axes via the analogue inputs in the C400 controller box to share a common clock. The capacitor sensors on each axis of motion in the XY60Z20 were outputted by the C400 as

analogue voltages. These were simultaneously digitised with the ABCD quadrants from the OPU using the two analogue input (AI) channels on the NI USB-6366.

4.2.2 Scan parameters for the standard mode optical profilometer

In this 'standard' profilometry mode, a raster scan path is sent to the XY60Z20-257 to translate the sample with continuous motion made from 150 steps of 0.129 volts in each axis. A scan routine was established to generate a scan path with parameters: Origin X; Origin Y; X step length; Y step length; number (#) of steps in X; number of steps in Y; and number of steps to send to C400 controller per second (as seen in Figure 49). As a result, a single complete image (i.e. one full cycle of the slow scan: trace and retrace) is taken in 75 seconds and extends to a range of up to 55 μm.
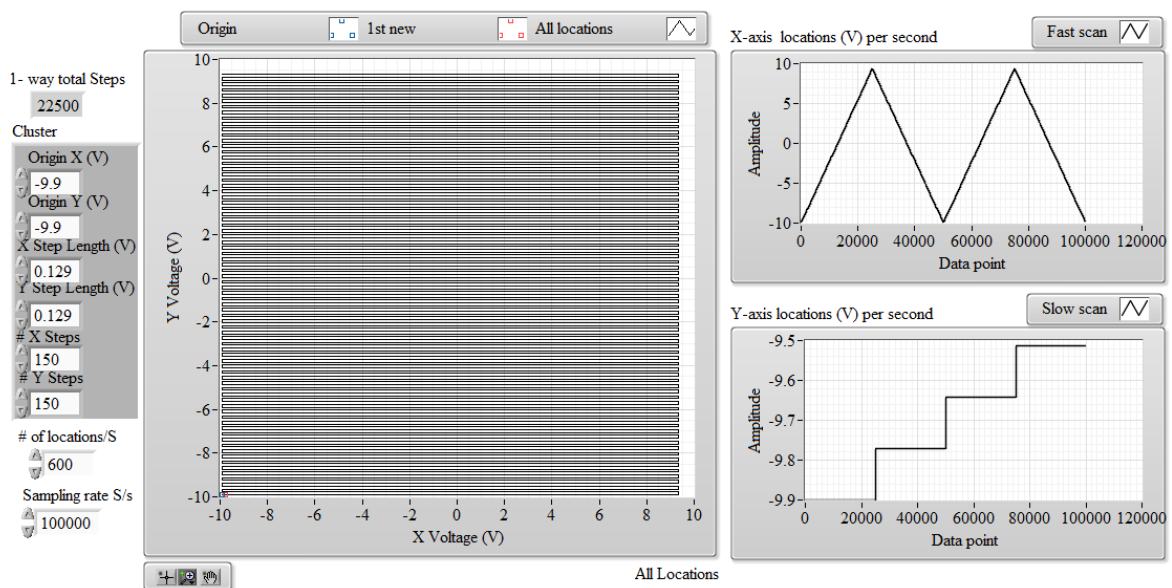
Figure 49: Analogue scan signals sent to the C400 controller (nPoint, USA) to move the XY60Z20-257 nanopositioning piezo stage during optical profilometry image capture.

In addition, a second sub-routine (created in LabVIEW, National Instruments, USA) was implemented to conduct a lower frequency raster scan over a larger area using the ECS3030 dual-axis actuator stack. In this configuration, large-area raster scans of eight by eight sites with a step size of 35 μm were most typically used. The z-axis sample height modulation, provided by the XY60Z20-257, also allowed for the possibility of taking an astigmatic response curve (e.g. the focus error signal) at different points in the image. This capability allows for an imaging method involving modulation of the OPU-sample distance to be implemented, as explained in literature (104), to attempt to remove the effect of reflectivity changes or to modify the height of the sample to account for sample slope.

4.2.3 XYZ image building routine

The capacitance sensors inside the nPoint XY60Z20-257 output an analogue voltage to represent the stage's position between ±10 V which corresponded to their full translation range (i.e X & Y: 60

μm and Z: 20 μm). By comparison the output of the OPU quadrants (i.e A-D) were typically in the range of 1.6-4.5 V, meaning that the USB-6366 was set to the ±10 V AI range and 100 kS/s/ch AI bandwidth. To capture optical profilometer data, custom software, written in LabVIEW, pre-allocated a 16-bit array of 1000 by 1000 elements was pre-allocated in memory. In turn, the elements of the array were populated using the scan path data, as measured from the capacitance sensors. The sensor data mapped to the 2D array such that +10 V corresponded to the 1000th element and –10 V corresponded to the 1st element. For each measured coordinate of the scan path the data from the ABCD quadrants on the photodiode could be attributed to have a fill dimension (i.e. f_x pixels by f_y pixels). In the cases where multiple values were taken in the same location, the mean of the typically-used z-channel signal, the normalised focus error (NFE) signal, taken in that location was displayed in the final image, where NFE is calculated as reported in Chapter 1, Section 2.1 i.e.:

$$NFE = \frac{(A+C)-(B+D)}{A+B+C+D} \tag{13}$$

The output from the astigmatic system was then cumulatively added into the 2D array for each location (i.e. the sum array), and the number of NFE entries at each pixel were stored in a separated array (i.e. the pixel stack array), until it was reset or the dual-axis positioners (ECS3030) moved to a new location. Therefore, for each image an average array, or more precisely a mean array, could be determined by dividing the sum array by the pixel stack array.

4.3 High-speed mode optical profilometry with an OPU

4.3.1 Arrangement of actuators and sensors for the high-speed optical profilometer

The high-speed mode was very similar to the standard mode described in the previous section. For instance, in this mode the ECS3030 dual-axis actuator stack still performed the same function to raster scan over large areas (up to 10s of millimetres). However, the XY60Z20-257 now just provided a slow-scan signal (Y_s). The fast-scan is instead created by the oscillation of the tracking voice coil motor (VCM) in the OPU, which can scan with greater amplitudes and at higher frequencies than the XY60Z20-257 but without the benefit of closed-loop sensing. To do this, the VC PCB described in Chapter 2, Section 2.3.2 was used, which implements a 16-DAC commanded over I2C by an Arduino Nano. Custom code written on both LabVIEW and Arduino IDE integrated commands into the VCMs, with the rest of the instrumentation governed by the NI USB-6366 DAQ.

4.3.2 Scan parameters for the high-speed optical profilometer

In this instrument, it was found that to avoid significant clock offsets due to the relatively slow computation processing, notorious (109) low-quality crystal oscillator and the low-rate serial communication, all found on the Arduino Nano, an interrupt command (i.e. attachInterrupt()) could be used to trigger the timing of Arduino Nano functionality, thus timing the fast-scan motion of the OPU

VCM (X_f). To do this, a digital 'pulse' signal was outputted from the NI USB-6366 DAQ, to trigger the interrupt, simultaneously with the scan path output to the nPoint C400 controller for the Y_s-axis motion. On the Arduino, the interrupt command triggered the Arduino to immediately index the next value in a pre-allocated 'scan array'. The scan array consisted of a single cycle of a sine wave (created by a simple function which was called scangen() see code in thesis digital media storage). Indexing the pre-allocated array was found to save computation time rather than using the 'sin()' command native to the Arduino libraries within the interrupt loop.

To enable real-time imaging (i.e. 1 frame per second) using the astigmatic system without tremendous loss (e.g. >50%) of scan amplitude in the imaging window, a VCM scan frequency of 200 Hertz with an amplitude of 0.6 V_{Pk-Pk} was chosen (Chapter 5, Section 5.4.3), which resulted in a 35 µm scan amplitude. The image was then constructed in a similar way to in Section 4.2.2, where the locations for the voice coil were synthesised using a scan path generator which would estimate the location of the voice coils based upon the timing of the pulse produced by the NI USB-6366 DAQ. A phase offset parameter was also implemented so any of the x, y or z waveforms could be offset w.r.t. one another should there be a noticeable phase delay between any motion or sensor data in any of the axes.

4.3.3 Discussion of high-speed profilometer

Some significant advantages come with the increased frame rate compared with the standard mode described in the previous section. These include using an inbuilt feature of the OPU rather than requiring an additional axis of closed-loop low-rate nano-positioning to provide the open-loop high-speed scanning, giving scope for reducing the cost of the method and increased temporal resolution. In addition, this modification also frees up one of the two analogue outputs from the NI USB-6366 DAQ, which can instead be used solely for the modulation of the sample height, a modification to the technique that can be used to mitigate against reflectivity changes on the sample, as discussed later in Section 4.6.1.

The development of real-time imaging represents a x75 increase in frame rate compared with the standard mode imaging. This allows for much better temporal resolution that can be used to observe dynamic events or to image much larger areas of a sample in a given time frame. This enables more comprehensive studies of samples and makes the system less susceptible to low frequency (e.g. <1 Hz) drift terms arising from fluctuations in environmental conditions (e.g. originating from thermal arguments and external force, as described in more detail in Chapter 5, Section 6.5.3). Furthermore, by still using the XY60Z20-257 it allows for large sample mass and integration of environment enclosures (e.g. a liquid bath) whilst simultaneously making use of the high frame rate achieved using the VCM. The disadvantages of the high-speed mode compared with the standard mode include using an open-loop fast-scan motion rather than closed-loop, which leads to greater uncertainty in the pixel dimension and a reduction (by ~ 37%) in scan amplitude by using the VCM.

4.4 'All-OPU' mode optical profilometry

4.4.1 Arrangement of actuators and sensors for the 'All-OPU' optical profilometer

In this final iteration of an optical profilometer for general surface imaging, smaller samples are required of area <6 mm x 6 mm and mass <1 g samples. In the instrumentation configuration here, the nPoint XY60Z20-257 was removed from the system and the slow-scan actuator was replaced with another OPU. The sample was mounted to this second OPU and the OPU was rotated 90° w.r.t. the primary detecting OPU, as seen in Figure 50. The main functionality of the ECS3030 dual-axis stack was also shown to be obsolete (later shown in section 4.6.2) but these were kept in the experimental set-up for evaluation purposes. The VCMs in each OPU could be used together to both provide both dual-axis scanning and the raster motion to increase the field-of-view compared to a single frame. As the tracking voice coils have a large travel range (±0.4 mm), the scanning motion can be comprised of AC and DC motion components, where the DC component dictates the location that the frame is captured and the AC component is used to generate the frame scan path. The locations of the raster pattern, or DC components sent to the VCMs, are generated in LabVIEW using a custom-built raster scan sub-vi rather than mobilising the ECS3030 dual-axis stack.
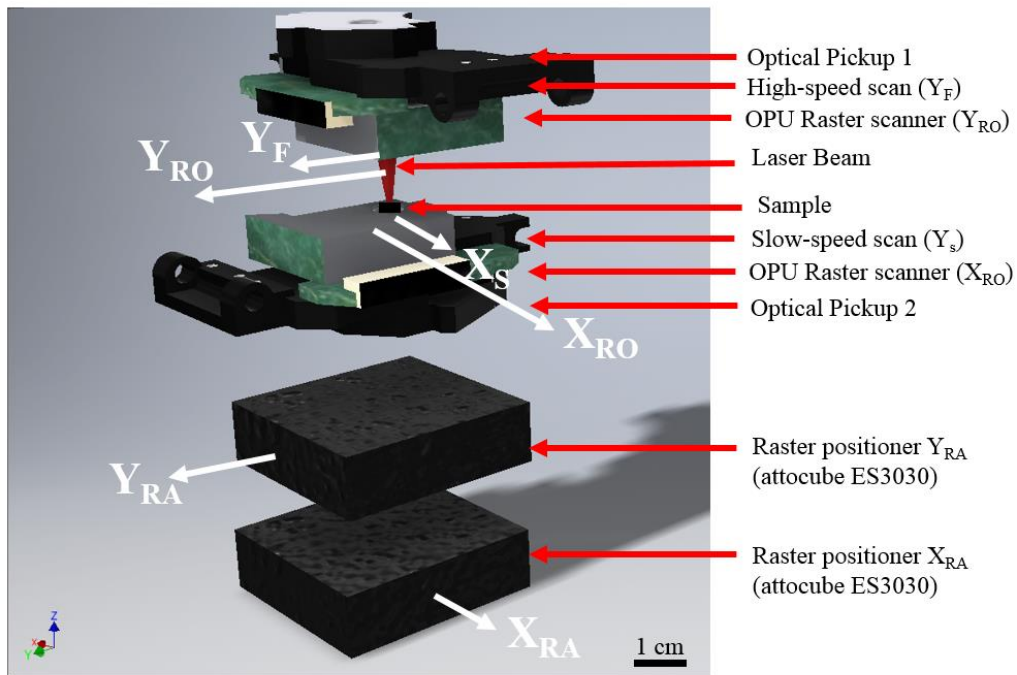
Figure 50: 'Exploded diagram' of the 'All OPU' optical profiler with two Sanyo HD850 OPUs mounted as a standalone optical profiler on top of two ECSx3030 Attocube close loop positioners.

4.4.2 Scan parameters for the 'All-OPU' optical profilometer

The method by which the scan is generated here is the same as reported for the fast-scan axis in the previous section, i.e. by using a pulse signal from the NI 6366 DAQ. However, this is now done for both tracking VCMs, where the second (i.e. lower) OPU is now responsible for the slow-scan motion. The Arduino code responsible for the slow-scan motion is set up to index a new location in a second pre-allocated array (generated via 'scangen()') but where the 'modulo()' command (native to Arduino) is used to calculate the remainder of 'the number of measured pulses' divided by 'the number of pulses needed for one fast scan cycle'. A new value was only indexed in the slow scan if the 'modulo()' command return zero. The slow-scan path was created so it would scan at 1 Hz at 0.2 V_{Pk-Pk}. The combination of the previously-reported fast-scan parameters and these slow-scan parameters result in a typical 37.5 μm by 55 μm scan area being imaged per second. The DC components of the scan, as described in the previous sub-section, can be sent to each Arduino via serial through NI's 'Visa Write.vi' to each respective COM port, for both of the slow- and the fast-scan axes. The focus VCM on either OPU can be used for bringing the astigmatic system into focus on the sample.

4.5 Optical profilometer for cantilever alignment

4.5.1 Arrangement of actuators and sensors for the cantilever optical profilometer

This 'purpose-built' form of the astigmatic optical profilometer was intended to be used solely for the application of the computer-controlled alignment of one of the MSNL (Bruker, USA) cantilevers for inspection or as a pre-cursor to imaging within an integrated HS-AFM. In previous commentary (see Chapter 3, section 3.5.2), a hand driven or motorised cantilever sled and dual-axis OPU VCM was used when away from the surface with the 'silhouette method' to roughly find a grouping of the cantilevers on the chip and place the laser spot in the correct location. However, as an alternative in instances where the silhouette method isn't available (e.g. due to very close proximity to the surface, in a remote place or in an environmental chamber) or for automated alignment of the cantilever, the motorised sled and VCM can be used together to scan over an area suitable to resolve the outline of the cantilever.

For this system, a 50:1 ratio micro-metal-geared motor (Pololu, USA), with a pair of optical encoders as dual encoders, allow to determine direction as well as angular velocity, was attached on the back of a translation frame that in turn bolted to the OPU. A fine pitched thread (pitch: 250 μm/rev), F3SS25 (Thorlabs, US), was then attached to the shaft of the motor and used to drive a linear sled (brass). The motion of the sled was then de-amplified (as described in Section 5.3.4) down the paddle towards the pivot point. The MSNL cantilever chip is then placed so the cantilevers protrude in front of an aperture in the paddle, a schematic of this configuration is shown in Figure 51. The fast scan motion (X_f), as labelled in Figure 51, was provided in the same way as previously described, using the tracking VCM on the optical pickup externally timed from a pulse signal from the NI 6366 DAQ. A geared motor provided the slow scan motion (Y_f) via a custom built 'Geared Motor Controller (GMC)' PCB and executable. The GMC board has a TB612 dual-channel DC or single-channel stepper motor driver and an Arduino Nano, which contains multiple analogue-to-digital converters (i.e. eight 10-bit ADCs) to sample the dual optical encoder data and determine both the speed and direction for the slow-scan motion. This positioning system is examined in more detail in the positioning chapter (Chapter 5).
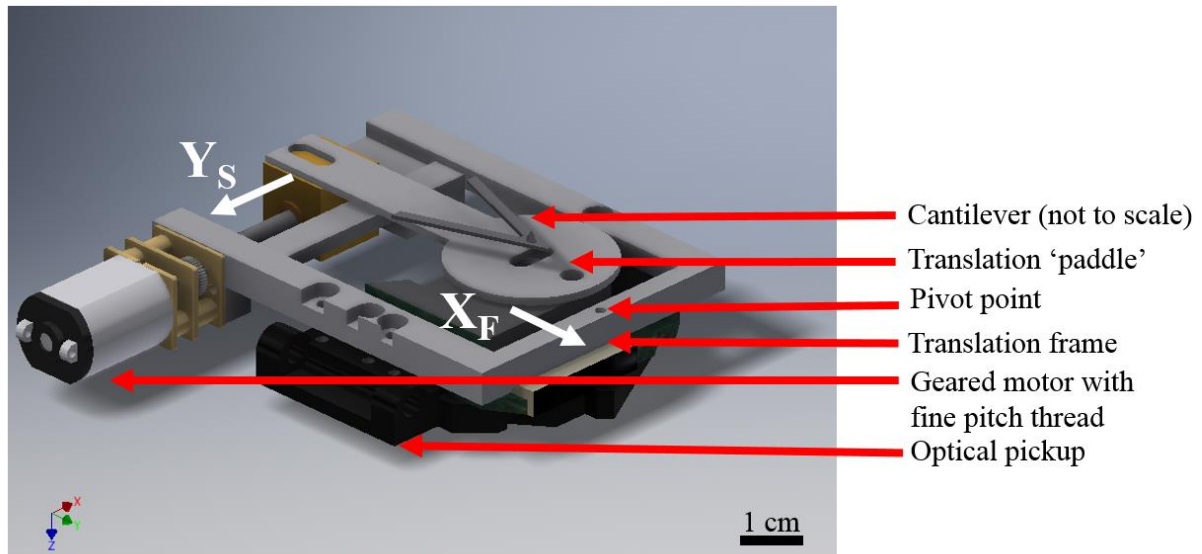
Figure 51: 3D schematic of the cantilever positioner (enlarged for clarity) and optical profiler with a metal micro-geared (50:1) motor and fine pitch (200 μm) drive thread, fast-scan axis labelled as XF and slow-scan axis labelled as YS.

4.5.2 Scan parameters for the cantilever optical profilometer

The Arduino Nano could be instructed over serial via NI's Visa write command to move some number of steps. These steps corresponded to the rotation of one tooth on the geared micromotor, which could be configured with a three or five toothed wheel. By knowing the ratio of the motion of the motor with the output of the gearbox and the pitch of the Thorlabs fine screw (250 μm), the linear actuation rate at the base of the paddle can be calculated, as detailed in the positioning chapter (Chapter 5, Section 5.3.4). While there was no sensing in the fast-scan direction, an estimation for the amplitude of the scan could be made from previous work, where a relationship between V_{Pk-Pk} and scan amplitude was established at 200 Hz. Secondly, the dimension of the subject, the cantilevers, are well-characterised and can be found out from the manufacturer's (Bruker, USA) specification sheet for each of the 10 cantilevers found on the MSNL chip.

4.6. Results

In this section, images are presented to demonstrate the typical use cases for the spatial and temporal resolution of each of the systems outlined in the previous sections. Where necessary, further evaluation of the images or comparisons of the images with other microscopy techniques have been presented. The results are grouped such that they correspond to each of the instruments outlined in the previous section. Whilst a wide range of samples could be used in each case, the samples used have

been chosen as they are interesting to a field of research, or other data are available for comparison, or their topology is well-suited to demonstrate the imaging capabilities of the instrument.

4.6.1 Large-area optical profiler image captured in standard mode

4.6.1.1 UO2 thin film study

To test the performance of the OPU-based optical profilometer a sample that was locally-flat (i.e. having <6 μm of height deviation over 50 μm) and contained a large amount of persistent and ordered structure over several lateral length scales was required. Moreover, it was also intended that the instrument be validated with a study that could benefit future study of that material and the results from this instrument could be compared with other techniques that had been used on the same or equivalent sample; thus, the surface structures could be compared. It was also desired that the sample was reflective and consisted of a mostly-homogenous material.

Therefore, it was chosen that the first study conducted with the astigmatic optical profilometer was on a UO_2 thin film grown by the Thin Film Team (Interface Analysis Centre, University of Bristol) on a 10 mm by 10 mm ceramic substrate mounted to the nPoint using 'Adesion Silver DAG' (1415M, Agar Scientific, UK). Prior to imaging the UO_2 had been placed in a solution of 0.1M H_2O_2 for 60 minutes, to attempt to promote surface corrosion and dissolution of materials on the sample. As such it was expected that the grains present in the thin film should be terraces with low roughness at different heights. Previous equivalent studies had seen oxidation expansion forming within a grain (i.e. given the appearance of several cracks or lines running within a grain). Therefore, the primary objectives for the optical profilometer was to so see if the individual grains could be resolved, image any evidence of intragranular expansion due to oxidation and see if there was any contrast in the heights of the grains present on the thin film. In Figure 52, two sequential 55 μm by 55 μm optical profilometry frames are present (Figure 52 (a) and (b)) alongside a large composited image (300 μm by 300 μm (Figure 52 (c))) of the UO_2 thin film surface. Each of the standard mode frames took 75 seconds to construct before the actuator moved to a new location. One step length between sequential location was set to 35 μm, allowing for an overlap between frames. This step offset was made using the dual-axis ECS3030. In total, 64 locations arrange in an eight by eight site serpentine raster path were used to explore the surface and generate Figure 52 (c).
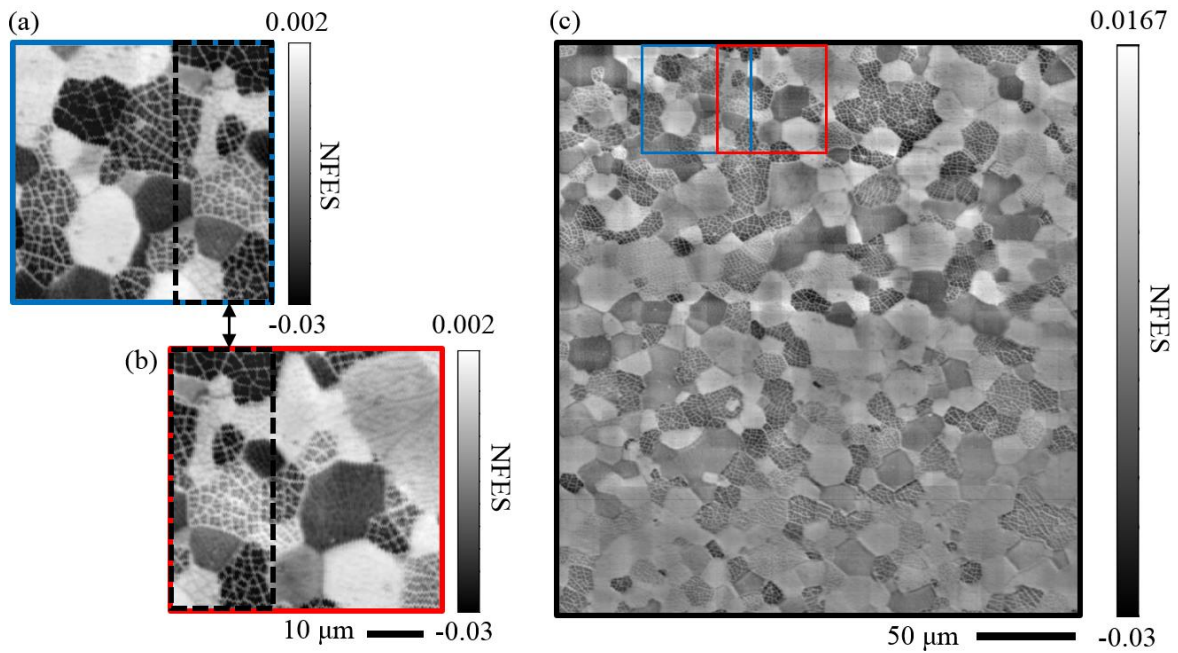
Figure 52: Single sequential optical profilometry images (a) and (b) captured using the normalised focus error signal (NFES with arbitrary units) from the OPU, when scanning over a 300 by 300 μm area of a UO₂ thin film in an 8 by 8 serpentine raster pattern to create a composite image of the surface (c).

The composite image (Figure 52 (c)) was formed from 64 individual standard mode optical profilometry frames using an automated stitching algorithm, outlined later in Chapter 6, Section 6.5.3. From the images, it is clear that there is strong contrast between neighbouring grains, with the boundaries between them clearly visible. In addition, sub-micrometre crack-like structures, formed from expansion due to oxidation on the sample, are repeatedly detected (more clearly seen in Figure 52 (a) and Figure 52 (b)). These features are seen to propagate throughout many of the grains, demonstrating the high effective resolution of the optical profilometer in this case. A separate region of the UO₂ thin film was imaged using SEM and marked out with four fiducial markers (i.e. an easily identifiable mark or shape with a low degree of symmetry). The SEM data for this region are presented in Figure 53 (a). Sub-sections of this area are then presented alongside optical profilometry data for comparison (Figure 53 (b-e)).
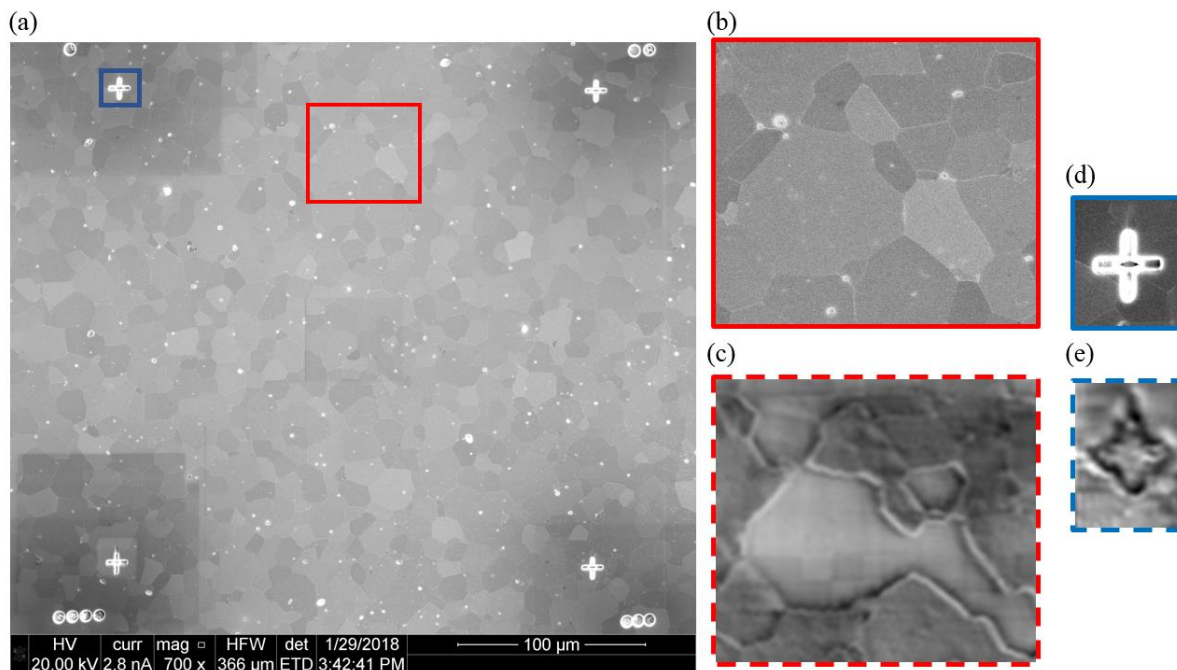
Figure 53: SEM image with fiducial markings (a) of the UO₂ thin film with an arbitary subsection identified for further analysis. SEM of this sub-section (b) is presented alongside optical profilometry of the same region (c) (normalised focus error presented as contrast image). The top-left fiducial marker is imaged using SEM (d) and optial profilometry (e) (normalised focus error presented as contrast image).

The origin of the grain-to-grain contrast differs between the two techniques due to the nature in which the two techniques are interacting with the surface. The SEM images are formed by collecting the secondary electrons liberated from a the top few nanometers (110) of the surface, due to an incident high-intensity electron beam being raster-scanned across the sample. Therefore, the contrast in images originates due to the electron density of the sample and doesn't immediately have a correlation with the height differences of the UO₂ grains. This is unlike in optical profilometry, where the contrast between the grains arises from a convolution of the difference in position within the linear region of the astigmatic response curve and the difference in astigmatic response curve due to the change in reflectivity or other surface conditions such as roughness of each grain. To further understand the nature of this convolution in optical profilometry, extended work was carried out to evaluate how the astigmatic response changed across the region presented in Figure 53 (b-c).

To establish further quantitive evaluation of the sample, it is possible to use the nanopositioning hardware (i.e. XY60Z20-257, nPoint) to modulate the height of the sample w.r.t. the astigmatic detection system and capture a full astigmatic response curve at various points across the image. To demonstrate this, Figure 54 presents a single frame (Figure 54 (a)) taken of the UO₂ and 25 astigmatic system response curves, uniformly spaced by 13.5 μm in a five by five lattice across the sample, as

labelled by the crosses in Figure 54 (a). The height of the sample is modulated with an amplitude of 18 µm at each location.
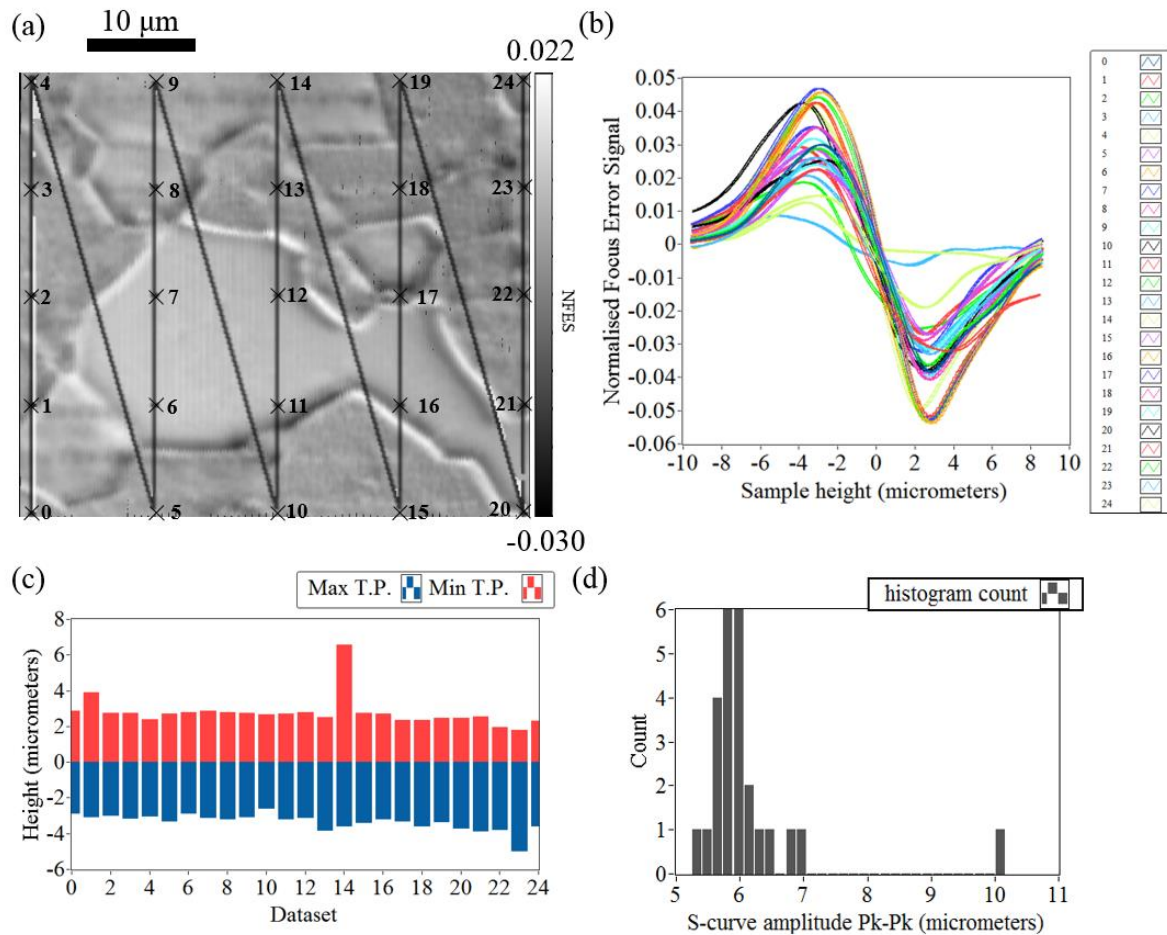
Figure 54: Astigmatic response curve measured with sample height modulation across an optical profilometry image (a) of a UO₂ thin film imaged in standard mode. Characteristic 's-curves' for each of the 25 marked locations in (a) are presented in. (b) Maximum and minimum turning-points of the s-curves are plotted in. (c) Measured distances between the turning points are plotted in (d).

From this inspection it is clear to see, as expected, that the 25 responses (Figure 54 (b)) from the astigmatic system vary at each location across this non-homogenous surface. In Figure 54 (b), both the towards and away response curves have been plotted for each location. By extracting key features of the astigmatic responses, further quantitative information about the sample can be extracted, such as the turning points (T.P.) (i.e. the maximum and minimum NFES) of the response curve and the peak-to-peak distance. We see how these vary in accordance to location in Figure 54 (c) and Figure 54 (d). In one instance, the linear region of the s-curve was found several standard deviations away from the main distribution >10 µm (seen in Figure 54 (d)). Inspection of the focus error curve shows that it does not demonstrate the characteristic s-curve shape, suggesting that the system did not come into

focus. Such an occurrence could arise if a feature or surface material caused light to be significantly scattered, causing diffuse light to be reflected onto the quadrant photodiode integrated chip (QPD-IC).

These responses can be used to extract further information about the topography of the sample. A natural extension to this work for a crystalline material would be to perform a large-area image, such as in Figure 52 (c), to establish the location of each of the grains and then return to the centre of the grain and conduct an NFES response curve. By doing so, more quantitative information about the relative heights of each of the grains could be established rather than just relative contrast. With higher imaging rates, this has the potential to be extended to real-time observation in solution of the corrosion process and lead to a measure of the rate of corrosion.

In addition, the same area can be used to inspect different types of response from the astigmatic system, that is: the sum signal (i.e the total laser light returning from the sample; tilt (i.e. the angular tilt of the laser dot in the x-direction; Sx); and tip (i.e. the angular tip of the laser dot in the y-direction). In Figure 55, three types of response are displayed for the same area of the image, as in Figure 54. Here, the three signals are calculated as follows:

$$Sum = A + B + C + D \tag{14}$$

$$Sx = \frac{(A+B)-(C+D)}{Sum} \tag{15}$$

$$Sy = \frac{(A+D)-(B+C)}{Sum} \tag{16}$$
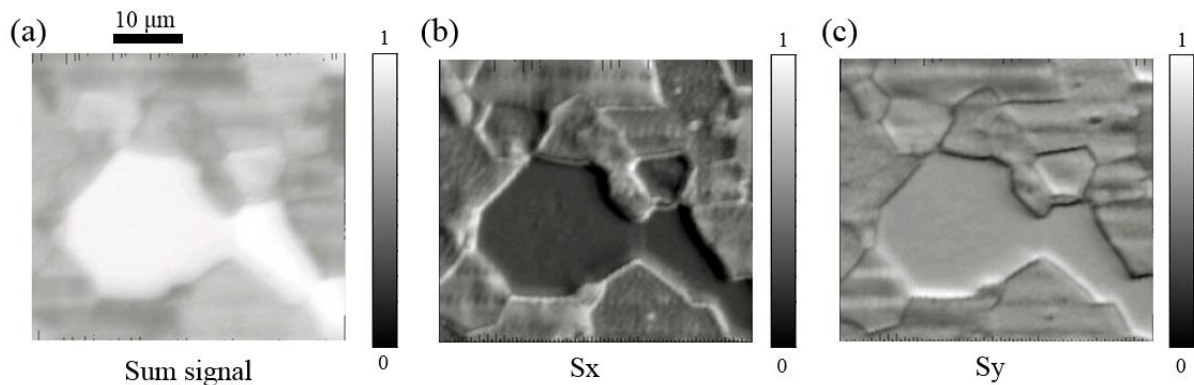
Figure 55: A standard optical profilometry image of a UO₂ thin film take in three astigmatic response modes all displayed in arbitrary units: sum signal (a), Sx signal (b) and Sy signal (c)

Here we see that the grains are even distinguishable using the sum signal, implying that due to their height, crystallographic orientation or surface roughness they have a different level of reflectivity, as measured by the astigmatic system. Given the height changes between the grains (e.g. up to 4 μm), contrast between the grains is seen using the Sx and Sy signals. For each grain, there is no indication of significant gradients, implying that each of the grains are like terraces with some local roughness.

4.6.1.2 Study of leaf surfaces

By comparison to the previous study of a highly-ordered and reflective crystalline structure of a UO_2 thin film for examination of surface corrosion, the following study was undertaken on a leaf impression sample with much more varied surface features. The objective of imaging this surface was to assess if stomata, small pores on a leaf surface used to regulate gas exchange (~10-50 µm lateral width), could be resolved. Future studies could then look to utilise the high-frame rate developed in other versions of this instrument and allow for in vivo observation of the plant's regulation of the stomata opening or closing due to varying ambient condition on a second-by-second basis. As stomata structures are typically in the range of 10s of micrometres across (111), they are known to be notoriously challenging to image with optical techniques. From SEM images reported in literature (111), an indication as to the size (~30 µm) and spacing (10s-100s µm) of the stomata for this species ('Tilia Cordata') was found. These features were seen to be interspersed amongst higher features, such as the veins in the leaves, and therefore, are well-suited to benefit from a non-contact profilometry technique such as optical profilometry. Moreover, the presence of surface features such as hairs and waxes on the leaf make the sample suited to a non-contact technique. The sample was created (by Tilly Hancock, University of Bristol) by taking a surface impression, by pressing the leaf into a film of nail varnish (112).

In Figure 56, a composite image is presented, stitched via the automated algorithm outlined later in Chapter 6, Section 6.5.3, alongside a subsection of the leaf where five stomata structures have been found on the surface in one region of the image. Here, the composite image is once again made from an eight by eight site raster pattern where the step size between sites is 35 µm and focus error signal has been captured using the DVD laser (i.e. with wavelength 650 nm) and the DVD photodiode segments (i.e. a-d).
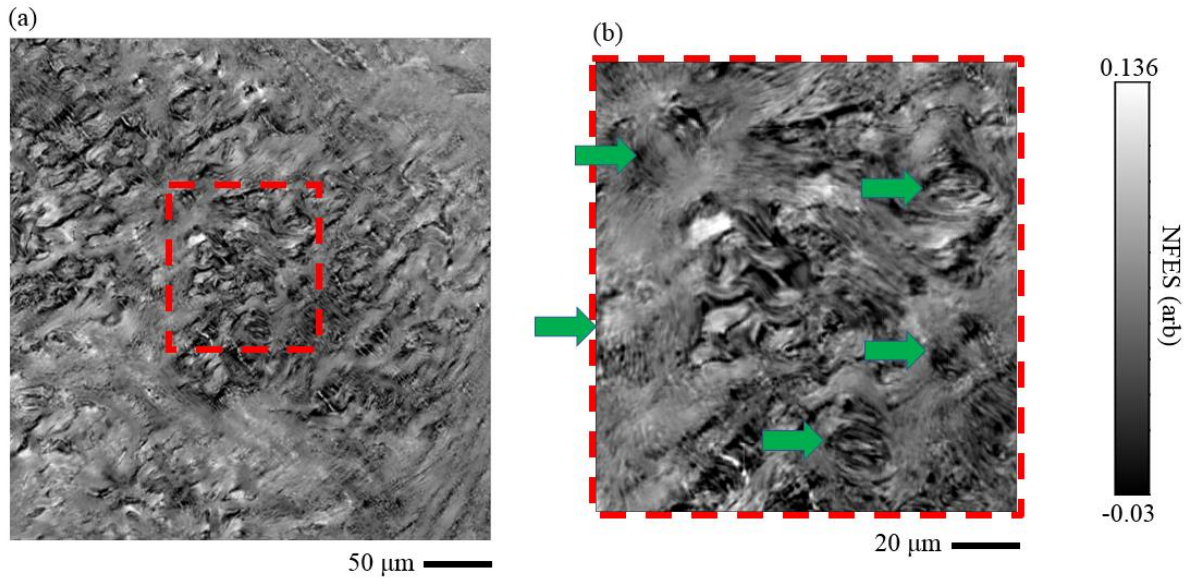
Figure 56: Large area optical profilometry micrographs of a nail varnish impression of a Tilia Cordata (a) with the zoom-in section displayed in (b).

Successful demonstration of imaging and identifying the stomata amongst the surface roughness of the leaf offer the exciting potential for the optical profilometer to be a complementary tool for biological applications, where optical techniques have proved to be challenging in yielding conclusive observations. Furthermore, the optical profilometer can be operated at one of two wavelengths and in environments, such as in a liquid, without required a conductive coating to be applied, as in SEM.

In addition to imaging a nail varnish impression of the leaf surface, work was undertaken to image a living leaf surface in vivo of the species Arabidopsis. For this, the CD laser (i.e with a wavelength of 790 nm) was used to attempt to avoid two absorption peaks of chlorophyll in the range 600-700 nm (113). Figure 57 showcases a previous image taken of this species using an SEM taken by Schnurr et al. (111) (Figure 57 (a)) and optical profilometry (Figure 57 (b)) of the living leaf from the same species.
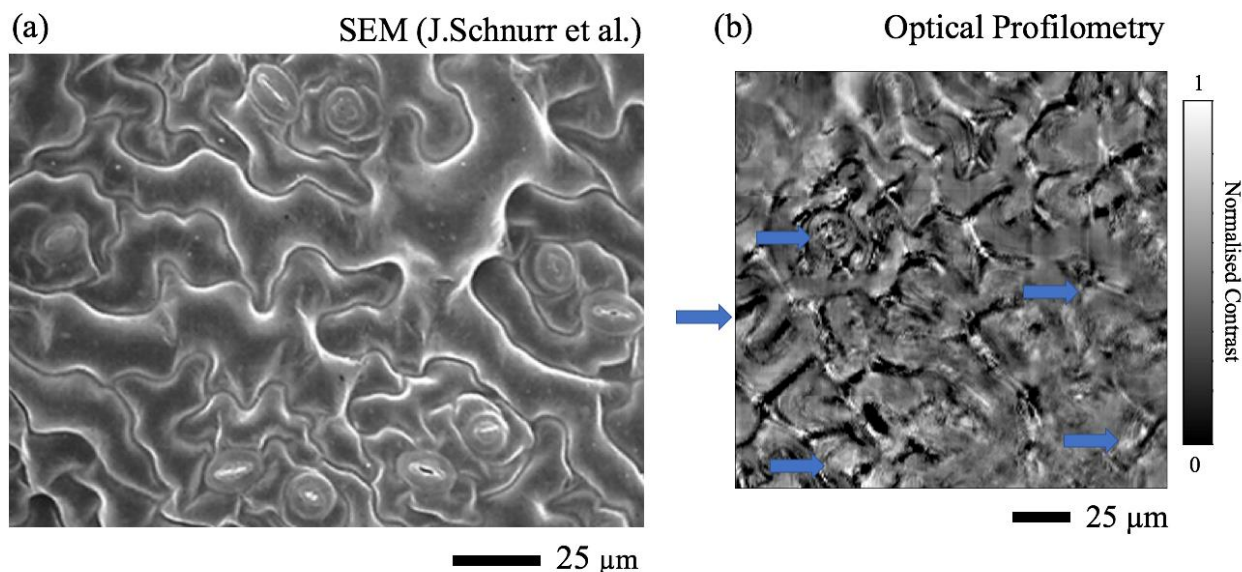
Figure 57: Comparison of an SEM image taken of a dead Arabidopsis (111) **and a living Arabidopsis leaf imaged with a 790 nm wavelength astigmatic optical profilometer, where the normalised focus error signal is presented as normalised contrast (arbitrary units).**

While the surface contrast of the SEM data is much better than that in the optical profilometer, some key outcomes were observed. Using the 790 nm laser, it was possible to get noticeable surface contrast from the topology and range of surface features. Several stomata-like features are also observed on the surface, opening to varying extents, as is seen in Figure 57 (a). Whilst a direct comparison of the same locations on a sample with an additional technique would help to confirm with more confidence that all the features identified are indeed stomata, this is left for future work as it is not a principal aim of the work reported in this chapter.

4.6.1.2 Conclusions from standard-mode OPU based optical profilometry

The results presented from the standard mode optical profilometer imaging a UO_2 thin film firstly showed that the instrument has the resolution to image both fine structure within grains, due to oxidation, and long-range, order allowing for identification of grain boundaries. Properties such as dimension, reflectivity and distribution could then be extracted from these data to feed into a wider study on the formation of the thin film. It was subsequently shown how correlative microscopy could be performed on the sample with the complementary technique of SEM. Here it was shown how surface structures and fiducial markers could be resolved and side-by-side areas of the sample, imaged via each technique, could be compared. On one of these areas selected (i.e. Figure 53 (c)) it was shown how the astigmatic response varied substantially, by taking a sweep through the height range (with amplitude 18 µm (Figure 54 (b)) at multiple locations in the image, when imaging the UO_2. This area of the sample was then used to perform another study which investigated the different ways of processing the a, b, c

and d signals in alternative ways to the normalised focus error signal, showing how alternative information about the sample topography can be extracted.

The synthesised UO_2 film was well-suited to optical profilometry as the sample was flat, highly-reflective and abundant with distinguishable surface features. As an extension to evaluation of the application of this technique, the standard optical profilometer was used in an investigation into understanding the topography of a leaf from a 'Tilia Cordata' plant and to attempt to identify stomata on the surface was undertaken. The initial study into a nail varnish impression of an area of a leaf showed that stomata were resolved by the optical profilometer operated with the 650 nm laser. Such analysis can give information on the properties of the stomata on the surface at the time that the nail varnish impression was made. A subsequent investigation looked to image the leaf directly, but also using the 790 nm (provided by the CD functionality in the optical pickup) laser to avoid the absorption spectrum of Chlorophyll, which is highly abundant in the leaf. It was shown that surface features akin to the equivalent dataset taken by SEM were seen, giving promise to the instrument's capability of imaging a living leaf surface. Future research could look to repeat this study with real-time resolution, tuning the environmental conditions of the plant, and look to capture how the plant regulates the stomata depending on the ambient conditions.

4.6.2 High-speed optical profilometry

4.6.2.1 Droplet evaporation observation in high-speed mode

Whilst the standard mode optical profilometry has shown promising results for large area maps, the temporal resolution of 1 frame per 75 seconds means second-by-second changes to surfaces would go unimaged, images could contain motion blur and become difficult to stitch via image correlation. To improve upon the frame rate of the standard mode imaging schema used in the previous section, the OPU tracking VCM was used for the fast-scan axis (200 lines per second) whilst continuing to use the XY60Z20-257 to provide the slow-scan motion. In this section, results from the high-speed optical profilometer are presented. A sample is required that has temporally-changing nano- and micro-structures to demonstrate the imaging capabilities of this configuration. To achieve this, microdroplets of saline solution (1000 ppm) were deposited onto a polished surface of thermally-sensitised AISI Type 304 stainless steel and the evaporation of the droplets was observed.

Figure 58 shows six frames taken from a 37-second-long video (see the video in the Digital Appendix entitled 'Figure 58.avi') showing the rate at which the saline solution droplets evaporate. As the droplet evaporates the saline solution becomes more concentrated, increasing the likelihood for surface corrosion to occur, as seen in previous studies in literature (114). The observations displayed in Figure 58 act as an example to show how the high-speed instrument can be useful to give insight into any surface changes throughout this event.
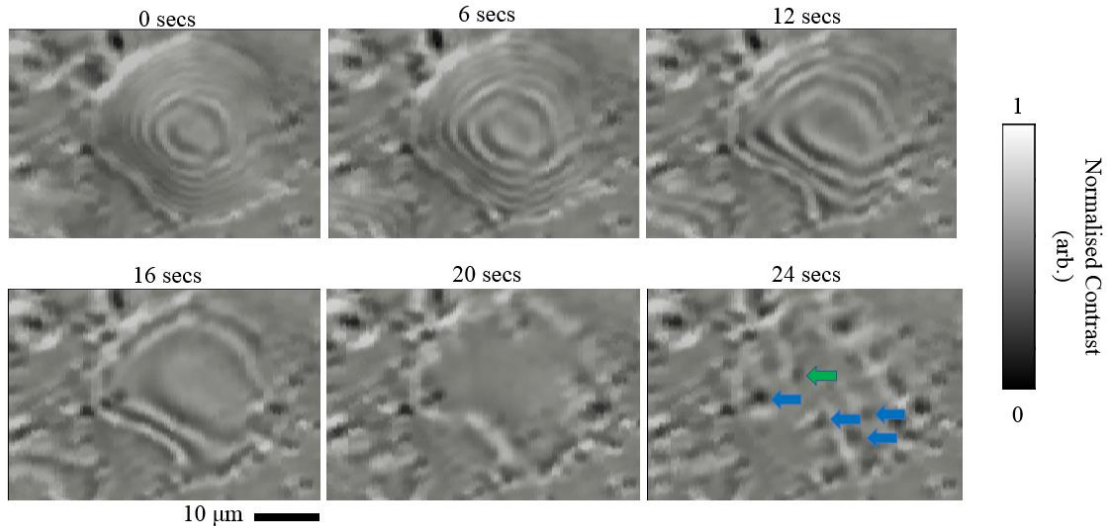
Figure 58: Optical profilometry (in high-speed mode) used to capture the evaporation of a droplet of saline solution with initial concentration of 1000 ppm on a sample of thermally-sensitised AISI Type 304 Stainless Steel using the 650 nm laser in the OPU

Within the area of the droplet, several concentric rings are visible acting almost like contours on the top surface of the droplet. These occur as the laser light constructively and destructively interferes with itself, creating an interference pattern at different heights on the droplet. As some light is reflected off the steel surface underneath it will travel a different pathlength to that reflected off the top surface of the droplet. When combined, the difference in path length changes due to location on the droplet. The laser light causes an interference fringe pattern, where darker areas represent area of destructive interference and lighter areas represent constructive interference, an effect commonly referred to as Newton's rings (114). Primitive estimations, by counting the number of rings or fringe patterns on the droplet where the distance between two light or two dark rings represents a height change of distance equal to the wavelength of the laser light, would suggest that the droplet is 4-5 μm taller in the centre compared to the edges. Further work could be carried out to calibrate such measurements, if the volume of the droplet was needed to be measured accurately to determine the exact volume of the droplet and, therefore, concentration of solution in each frame, given there was no significant change of refractive index with solution concentration.

Observations in Figure 58 show how the improved temporal resolution allows the high-speed mode of the instrument to capture events that would otherwise go unseen when using the standard imaging mode, which would still be halfway through creating a first image by the time the droplet had evaporated. As such, a significant advantage of this technique over performing the equivalent study with AFM is that as it is non-contact the fluid is not disturbed by a mechanical force on the sample. For this type of work optical profilometry and AFM could be highly complementary as AFM could be used

to inspect the state of the surface post-evaporation to indeed determine any changes to surface topography with high resolution.

4.6.2.2 Large area mapping with the 'All-OPU' optical profiler

The next phase of the study looks to evaluate the 'All-OPU' optical profilometry system. In this version of the instrumentation, the nPoint XY60Z20-257 three-axis stage is removed from the system and replaced by a second OPU that is responsible for the slow-scan actuation of the sample. Here the objective is to evaluate whether a pair of OPUs can be used to first create an imaging scan window that is performant enough to repeatably conduct optical profilometry at a frame rate of one frame a second. Subsequently, a second objective of this section is to evaluate if the OPU voice coil scanning system is capable of offsetting the scan window, with an offset or previously-named 'DC component', to extend the field-of-view of the instrument to detect longer-range order and to also replace the need for the ECS3030 long-range positioners.

For this study, the Si Ti NIST sample used elsewhere in this thesis (e.g. Chapter 3, Section 3.4) is used to demonstrate the imaging capabilities of the 'All-OPU' optical profiler. Due to its low sample mass (i.e. < 1g) and small area (i.e. 5 mm by 6 mm), the sample could be mounted onto the secondary OPU responsible for the slow-scan axis (Y_S) scanned at 1 Hz. The primary OPU was then placed above this and was responsible for the fast-scan axis (as outlined in Figure 59).
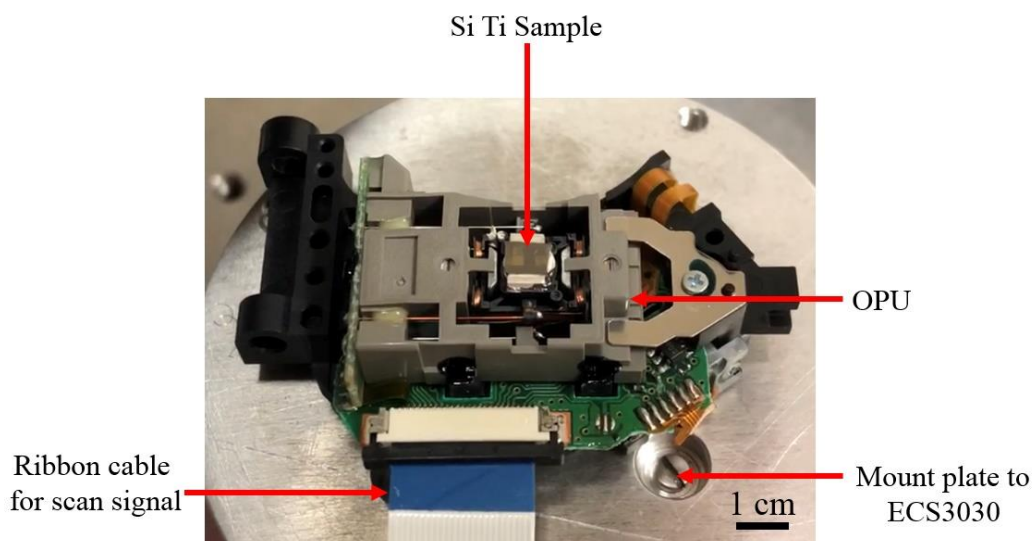
Figure 59: Si Ti NIST sample used for testing the imaging capability of the 'all-OPU' optical profilometer mounted onto the secondary OPU responsible for slow scan motion of the sample.

The two VCM motions (i.e. fast- and slow-scan) were triggered off the same clock, allowing the motion to be synchronised. The fast-scan operated at 200 Hz and required an AC V_{Pk-Pk} of 0.6 V and could then be translated with the DC component in the range from 0 to 1 V. A lower AC drive voltage was required for the slow-scan sinusoid of 0.2 V_{Pk-Pk} and could also be translated from 0 to 1 V. An image of the Si Ti NIST grid is presented below showing parallel and perpendicular lines of Ti on Si

and an equally-spaced grid of Ti squares. These features allow the presence of intra-image distortions due to non-linearity or hysteresis to be inspected. The Attocubes (ECS3030) mounted under the scanning OPU could be used to calibrate the physical dimensions of the scanning frame.

In Figure 60 (a), a single optical profilometer image captured in 1 second by the 'All-OPU' system is presented of the Si Ti NIST sample. A rectangular grid of equally spaced squares is visible on this sample. To assess the internal scanning consistency of the 'All-OPU' open loop scanning, the centre-of-mass (CoM) of each of the squares is determined (Figure 60 (b)) and, using Gwyddion's 'Measure Lattice' tool (Figure 60 (c)), a lattice fit was calculated and the vectors between crossing points or nodes caluated. The vectors between the CoM of the squares are then plotted in a histogram in Figure 60 (d) for the horizontal direction and Figure 60 (e) for the vertical direction. A table in Figure 60 (f) presents these data in summary form, showing that the distance uncertainly corresponds to roughly a third of the typical OPU spot size (55) and, therefore, does not appear to have any significant sources of scanning error.
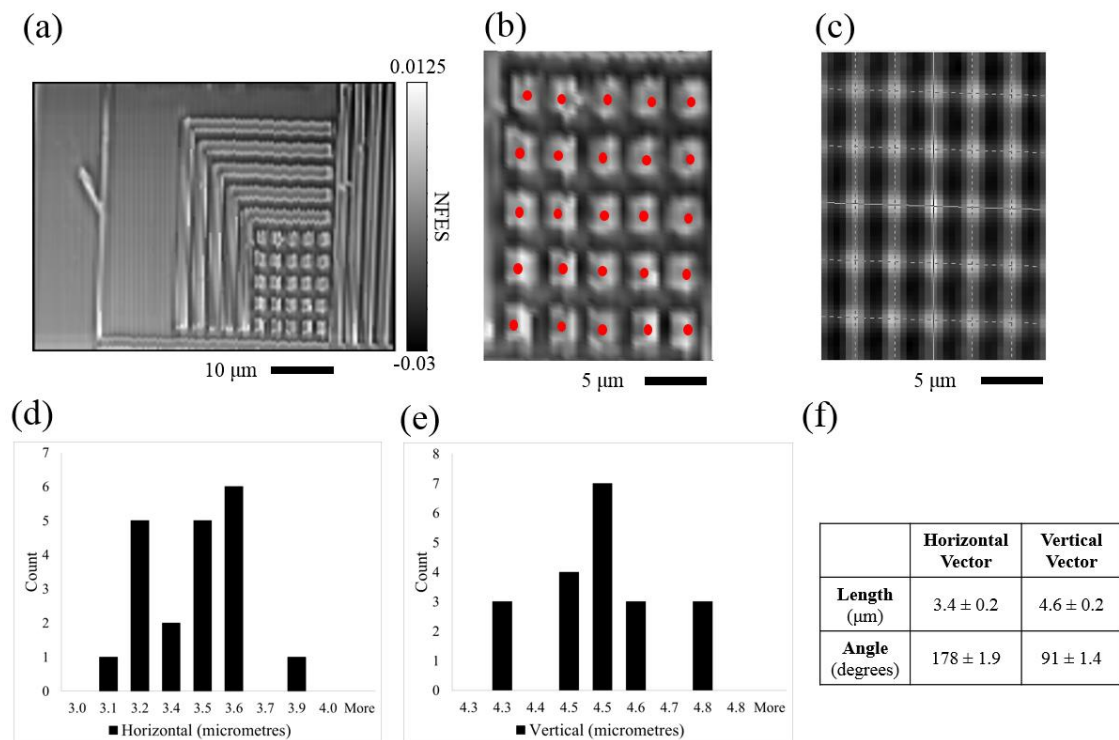
Figure 60: A single image created by the 'all-OPU' optical profilometer of the Si Ti grid is presented in (a), a subsection of the image (b), with the centre of the gridded squares labelled. (c) Estimated lattice projected onto the features calculated by Gwyddion. (d) and (e) Histograms of the horizontal and vertical vectors between features. Lattice parameters from the estimate grid calculated by Gwyddion are tabulated in (f).

To further expand the field-of-view of the instrument a 20-by-20 site raster scan was conducted using the ECS3030, as displayed in Figure 61 (a), extending the field-of-view to several hundred micrometres in each dimension. The composite image was constructed using the actuator positions, owing to the high number of self-similar features on the Si Ti grid causing confusion in the automatic feature correlation (described in Chapter 6, Section 6.5.3). Presented alongside this composite optical profilometry image is an optical image (Figure 61 (b)) of the same grid pattern captured on full magnification by a Leice EZ4 microscope. In addition to assessing VCM's capability for high-speed scanning, their motion is offset by DC values such that a raster scan of the scan window can be carried out, and combining the images from these raster locations results in expanding the field-of-view of the instrument compared to a single frame. Long-range motion (i.e. > 50 µm) was performed with the tracking VCMs in both OPUs around the sample. A four-by-four serpentine raster scan was done by the VCMs and compared against the equivalent raster scan performed by the Attocube ECS3030 on the Si Ti surface.
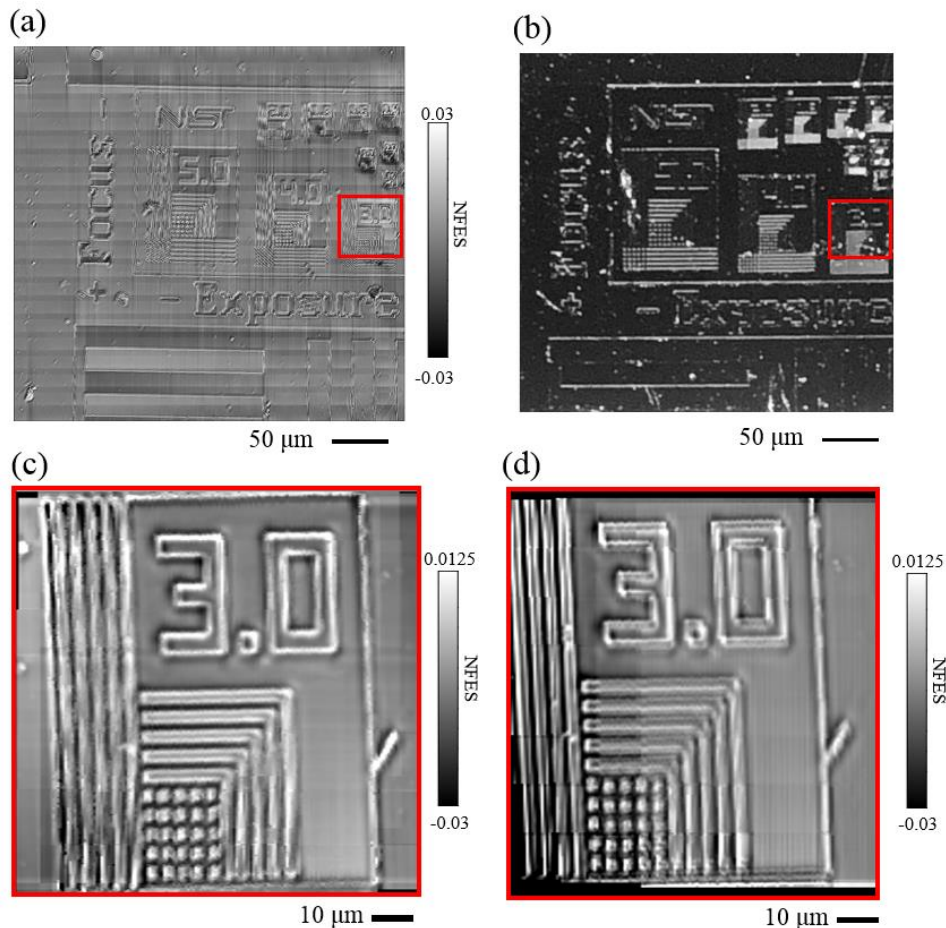
Figure 61: High-speed optical profilometry composite image of the NIST Si Ti grid taken over a large area (a) and equivalent optical microscopy image (b) using the Leica EZ4. (c) Composite image of the Si Ti surface constructed using the Attocube ECS3030 actuators to raster scan the imaging window. (d) Same area of the sample having being raster scanned using offsets sent to the tracking actuators.

4.6.2.3 Drift estimation of high-speed voice coil scanning

The final study carried out on the 'All-OPU' system investigated the open-loop scanning stability of the VCMs over a long time-period. To do this, an area of the Si Ti grid was imaged, left scanning for 180 minutes and imaged again. After this time, an apparent translation of the original surface features across the image was observed. The initial and final images have been averaged, i.e. added together and divided by two, in Figure 62 (a) to represent that extent of this drift component. Four distinct features in the initial and final images have been identified, and vectors between them calculated to make an estimation on the translation drift observed. A table summarising each of the vector components in the horizontal (X) and vertical (Y) directions is displayed in Figure 62 (b).

(a)   (b)

X drift vector (micrometres)	Y drift vector (micrometres)
-3.6	5.31
-3.78	5.62
-3.43	5.62
-3.78	5.78

	X drift vector (micrometres)	Y drift vector (micrometres)
Mean	-3.65	5.58
Std	0.168	0.197
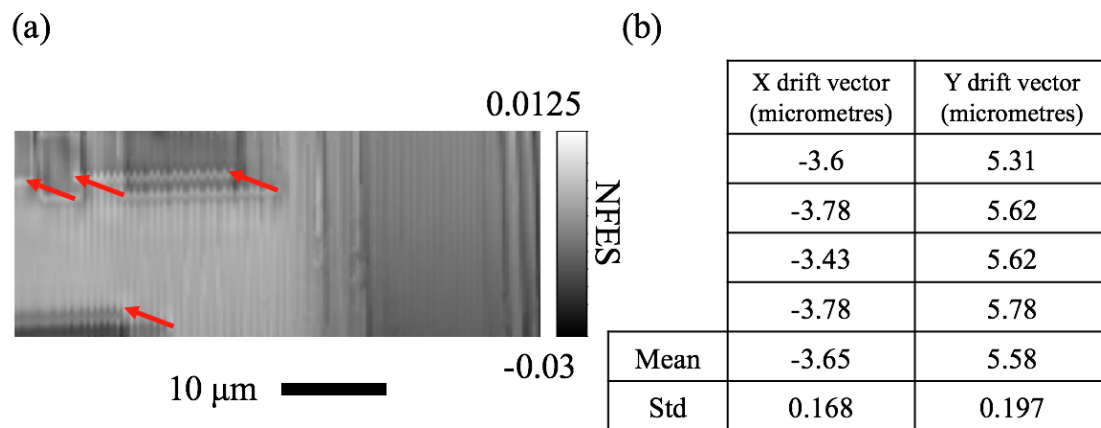
Figure 62: Drift estimation of the VCMs for open-loop scanner motion over 180 minutes calculated by identifying the translation vectors of four key features in an averaged 'All-OPU' high-speed optical profilometry image subsection (a). Horizontal (x) and vertical (y) vector along with their mean and standard deviation (b).

Identifying the translation of the corner features by eye allows four vectors to be calculated. We see that lateral drift is present in both axes, with it occurring to a greater extent in the slow scan axis with moves at a lower frequency and with the added mass of the sample. Given the experiment was done over a time period in which >10,000 frames could have been collected by this system, the magnitude of the drift (i.e. 3.7 µm and 5.7 µm respectively) does not appear to be a significant issue in the 'All-OPU' optical profilometer, as this corresponds to a drift rate of 0.62 nm/s.

4.6.3 Optical profilometry for AFM cantilever alignment

In this section, work is undertaken to evaluate the performance of the geared motor cantilever sled (from Figure 51) for performing optical profilometry on a MSNL cantilever. This is the same cantilever that was used for performing high-speed atomic force microscopy, as detailed in Chapter 3. A detailed evaluation of the geared motor drive mechanism, supplying the slow-scan motion in this configuration, is undertaken later in Chapter 5, Section 5.4.2, measured that a single step of the geared

motor could be determined to be (1 ± 0.5) micrometres. Therefore, when imaging a triangular MSNL cantilever with arm widths of approximately 15 μm, it should be able to determine the presence of the cantilever. The fast-scan motion was supplied by the tracking axis of the optical pickup, as in the previous version of the optical profilometry configuration. The aim of this experiment is to evaluate whether the cantilever sled can be used to create an optical profilometry image comparable to an optical image, i.e. with sufficient resolution to be able to locate the laser spot on above the tip on the cantilever.

For this experimental work, a custom-made aluminium translation frame (Figure 63) was manufactured to allow for a 50:1 geared micromotor to be attached to an aluminium frame whilst also secured to the fine pitched Thorlabs (F3SS25) drive thread. The F3S25 thread went through a brass block which had a F3ESN1P threaded bushing inside it. The brass block was guided via an additional pair of parallel rails. The removable magnetic translation paddle was then secured between the brass block and the pivot point at the top of the frame. An MSNL cantilever chip was mounted on an optically-clear polycarbonate substrate using silver DAG. The polycarbonate substrate acted to reduce the effects due to optical aberrations (e.g. spherical), as reported in literature (33), and act a baffle between the moving objective lens and the cantilever.
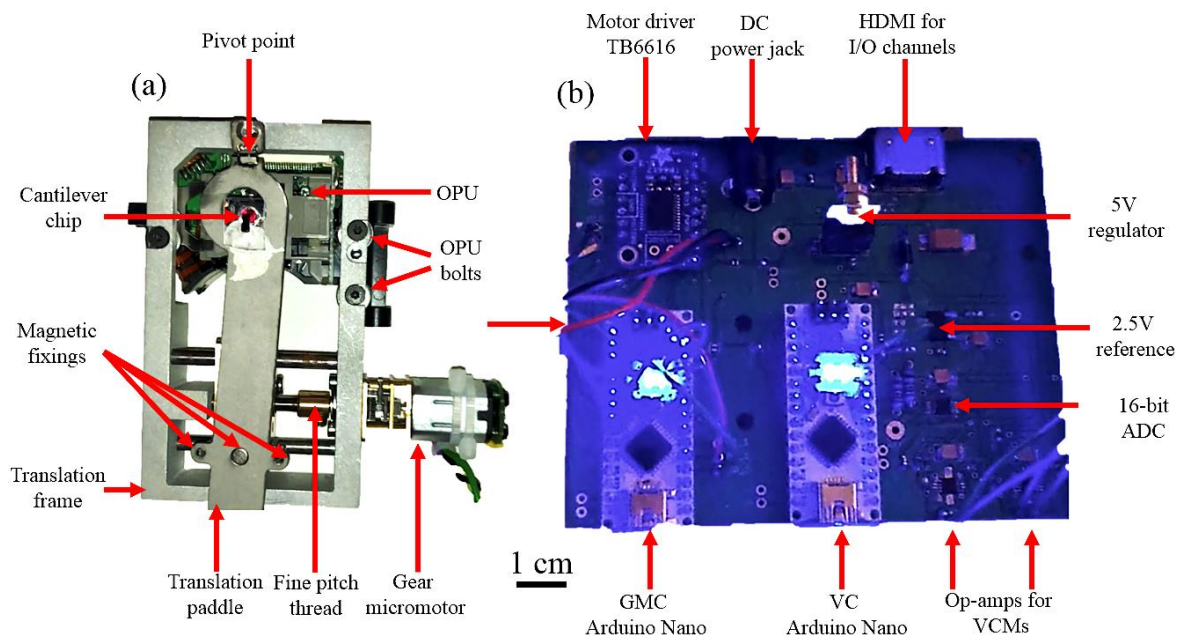
Figure 63: Experimental set-up used for aligning the cantilever with the astigmatic detection system using a geared micromotor and OPU VCM: where, (a) mechanical set-up which can be seen in motion in extended video folder ("figure63.avi"); and (b) dual axis control PCB responsible for the timing and motion of the VCM; and the geared micromotor, with key features labelled.

In Figure 64 an optical image of the MSNL cantilever chip is presented, with five cantilevers visible, which has been taken through the optical microscope present in the LDV, with a x10 objective (Polytec, Germany). Using the cantilever sled optical profiler, it was possible to show that an

MSNL-E (e.g. Figure 64 (b)), measuring 135 μm in length, could be well resolved by the astigmatic system. By incidentally imaging the underside of the cantilever, it is possible to spot the location of the tip. For comparison, the cantilever was also imaged using the standard mode optical profilometer (Figure 64 (c)).
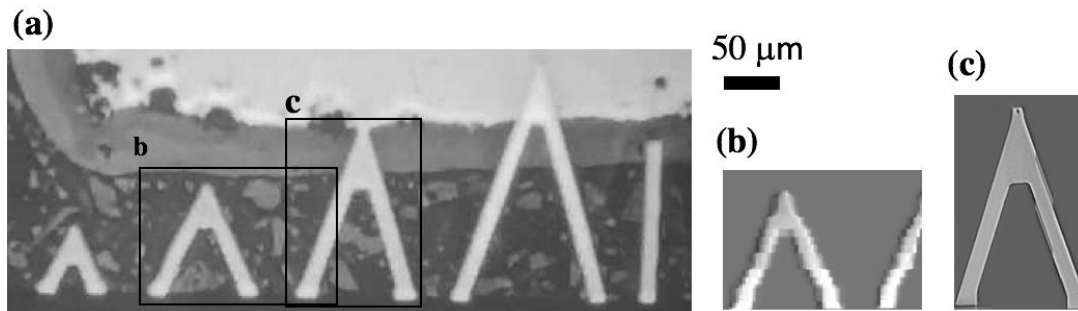
Figure 64: Black and white optical image taken through the illuminated Polytech LDV optical microscope with a x10 objective (a), the MSNL-D cantilever imaged with the cantilever sled system (b) and the MSNL-C cantilever imaged with standard mode optical profilometry using an nPoint XY60Z20-257 nanopositioner (c)

From Figure 64 it is seen that the optical image exhibits the widest field-of-view (i.e up to 0.5 mm) and has reasonably-sharp focus in the 576-pixel wide image with pixel width 0.9 μm, thus, the outline of the cantilever being clearly resolvable. The cantilever sled showed more position uncertainty in Figure 64 (b), with the outline of the cantilever having repeated mismatched rows along its outline. This corresponds to a position uncertainty due to the geared micromotor slow-scan motions of approximately ±5 μm, it is suggested that error is induced by the mechanical connections between the geared motor driven linear sled (with positioning of (1.0±0.5) μm) and the cantilever chip. Operating in the astigmatic system in standard optical profilometry mode with the nPoint XY60Z20-257 and positioning noise ±0.4 nm, a very 'optically sharp' composite image in Figure 64 (c) can be captured with the edge of the cantilever being clearly resolved to (± <1 μm).

In conclusion, whilst the least measurement uncertainty is seen using standard mode optical profilometry, with the highly precise and expensive nPoint XY60Z20-257, the cantilever sled made from a low cost (<£5) geared DC micromotor and Thorlabs fine-pitched thread could be used to locate and image cantilevers from the MSNL chip. As a consequence of these results, further work could be undertaken to improve the stability of the linear motion on the rails. For example, the two steel guide rails taken from a disc drive, visible in Figure 63, showed signs of light corrosion which is a likely cause of inconsistent motion along the bars. Replacing these bars with self-lubricating brass bars would aid the smoothness of the motion in this axis.

4.7 Data storage and processing of optical profilometer data

For storage and readback of the optical profilometry data, which used the same unified file format for all versions of the instrument, a custom-made executable was created using LabVIEW. During imaging, the data were stored in a binary file as a 16-bit 2D array of fixed dimension with the ECS3030 coordinates. The binary files could be loaded into the program, cropped according to the dimensions of the captured data and displayed in either a 2D height map or 3D mesh rendered in real-time. Furthermore, the frames could be analysed in turn, and a mapping of the pixels to ECS3030 coordinates could be established (i.e. akin to that described later in Chapter 6, Section 6.5.2). Where the optical profilometry data were captured using a long-range raster scan, a 'fill canvas' routine could be run to place images in a larger 2D array named the 'canvas' to build up a composite image. In addition, the environment allowed for either the individual frames or the canvas to be exported as a '.gsf' Gwydion file format or as a '.tiff' image file for further processing or presentation, as described throughout Chapter 6. An overview of the graphical user interaction panel is summarised in Figure 65, with key functionality labelled.
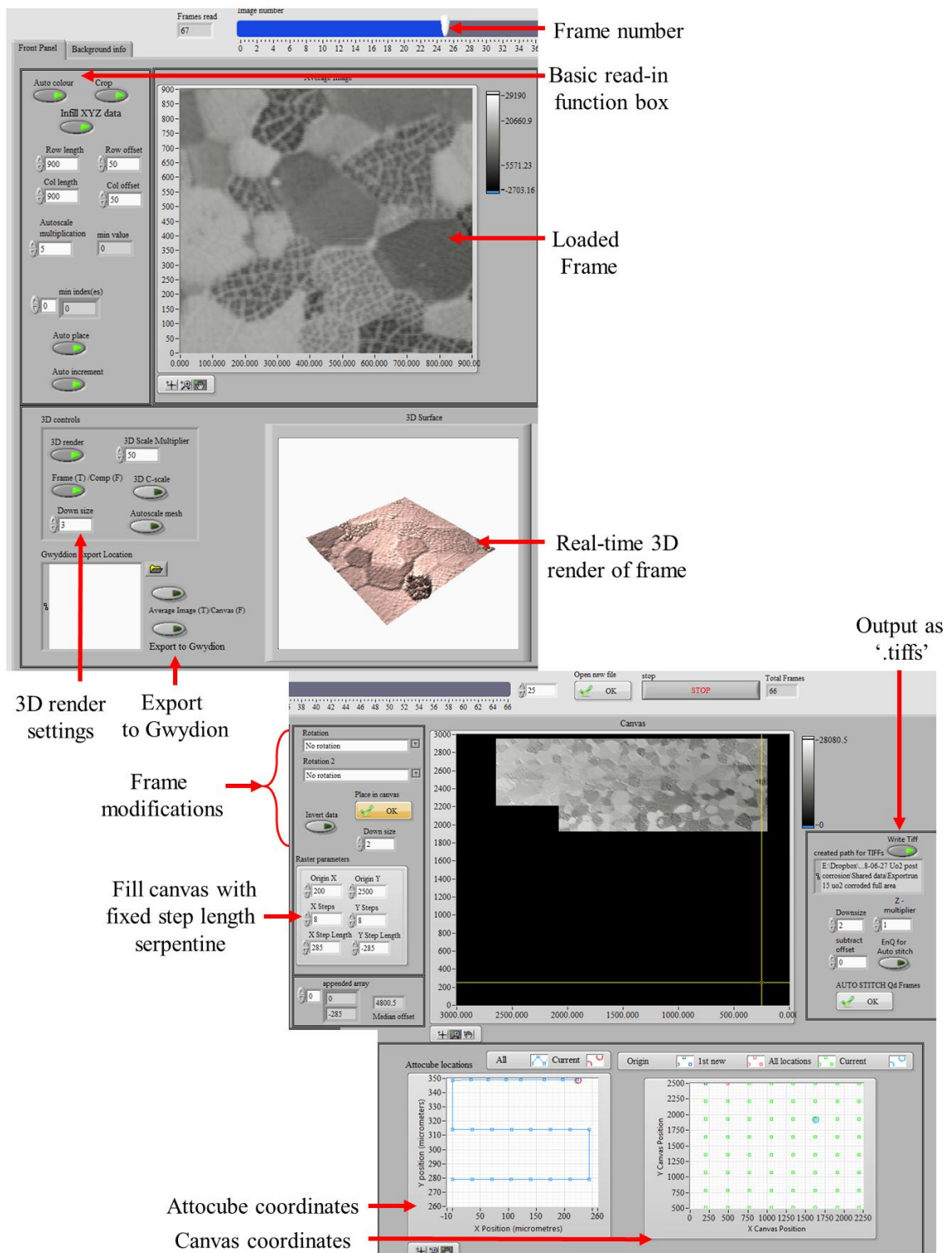
Figure 65: Readback software developed for the unified file format created for the optical profilometry instrument variants developed in this work.

4.8 Conclusions

Overall, in this chapter optical profilometer techniques have been developed building upon previous works in literature (12,13,115), using astigmatic detections systems and voice coil motors found in OPUs to create optical profilometry micrographs of material surfaces. As part of the research reported in this chapter, four OPU-based optical profilometer variants have been created, capable of imaging a wide range of material surfaces. In this work, these have been referred to as 'Standard Mode', 'High-speed Mode', 'All-OPU' and 'Cantilever Sled' optical profilometers. In addition, a bespoke cantilever positioner developed for studies elsewhere in this thesis has also been shown to have the functionality to resolve the outline of an MSNL-E cantilever of length 135 μm.

For each instrument variant, a study has been undertaken using it as an imaging tool and, where possible, evaluated against another technique, such as SEM or optical microscopy. The integration of a three-axis nanopositioner into the standard mode optical profilometer has also be used in tandem with large area contrast maps to provide 25 astigmatic response curve measurements across an image, to better quantify localised height deviations. This was done via sample height modulation of the sample over 18 μm, similar in a method to that reported in literature (104).

The results from the optical profilometers have shown the techniques to readily enable the scientific study of surface details, offering both high resolution and high frame rate imaging tool to help bridge the nanoscale-to-macroscale gap found in material science (108), whilst also demonstrating how this can be done with inexpensive components found in optical pickups. The techniques reported here are very complementary to the HS-AFM studies and instrumentation development covered elsewhere in this thesis (e.g. Chapter 3). Further developments to combine the techniques into a single instrument would prove hugely beneficial for the functionality of OPU-based HS-AFM. Enabling the two techniques in the same detection head would allow for a wide field-of-view and high frame rate of the optical profilometry to observe microscale dynamic events or locate important features (e.g. fiducial markers) before AFM could be used to inspect, with high resolution, the localised topography.

Chapter 5: Nanoscanning and positioning with optical pickups

5.1 Chapter overview

This chapter aims to detail the key methodologies for nanoscale sensing and actuation that underpin the research done in this thesis, and to demonstrate how they were used in experimental application. Throughout the experimental work, several techniques have been implemented in custom-made sensing and actuation configurations. These configurations have often been combined with commercial systems made by companies such as SmarAct (Germany), nPoint (US), Polytec (Germany), Newport (US) and Attocube (Germany) to create instruments with many (i.e. >5) axes of motion and multiple sensors, such as in the HS-AFM detailed in Chapter 3. Building upon experimental work in the previous two chapters, further development has been undertaken to evaluate and reduce position uncertainty in the high-speed scanners used in the optical pickup (OPU) based high-speed atomic force microscopy (HS-AFM) reported in Chapter 3.

This chapter starts with reviewing the limitations of actuators reported in previous literature that operate at the nano-to-micro-length scale by looking at a plot of the two fundamental parameters behind high-speed scanning and positioning for surface microscopy techniques, i.e.: range; and frequency. Following this, a brief definition of key terminology in positioning are described. Several commonly used scan paths that are typically found in SPM instruments and used in this work are then discussed, before moving onto the theory and implementation of the main actuation types: piezoelectric; voice coil motors; transfer and reduction mechanics with DC motors; and ceramic tuning forks. Following this, the principle optical sensors used to evaluate the performance of these actuation types are detailed, including: a fibre interferometer; a laser doppler-shift vibrometer (LDV); and the astigmatic focus error detection system from the Sanyo HD65/850 optical pickup (outlined in Chapter 2, Section 2.2).

5.2 Background

In this section, we address the principles and methods that are relevant to actuation and sensing that enable scanning and positioning at the nanoscale for surface microscopy techniques (e.g. in AFMs or optical profilers). As part of this, we start by comparing the development of nanopositioners conducted in this chapter with a comprehensive review of previous commercial and research positioners reported by B. Kenton (116). Following this, the same dataset is used to give context to the performance of the optical sensors that were used in this work to determine the position of scanners and actuators. Subsequently, the scan paths that are typically used for scanning across 2D areas and enable measurements in surface microscopy are examined in detail. A discussion of the ways in which the true motions of these actuators vary, compared to the desired motion, is presented.

5.2.1 Actuation

Nanopositioner can rarely operate over both long ranges and at high frequency. Therefore, it is not uncommon for an instrument to use actuators in combination in order to achieve the desired combination of range and scanning rate (37). A study carried out by B. Kenton (116) showed the trend in these two parameters (frequency and range) from a number of nanopositioners used in commercial and research activities. Figure 66, graphing the data from this study, shows that the range of nanopositioners investigated decreases with increasing frequency. The fit to this line was found to have a range equal to $30,688\,f^{-0.916}$ (116,117). For comparison, a theoretical limit, based on modelling the first resonance of a 'fixed-free' (i.e. one end fixed, one end free) piezo electric actuator (assuming 1 μm of travel per 1 mm of length) and modelled by B. Kenton et al. (116), is plotted alongside the data in Figure 66, where the gradient of this linear line was found to be $567,460\,f^{-1}$ (116,117) (dashed line Figure 66).
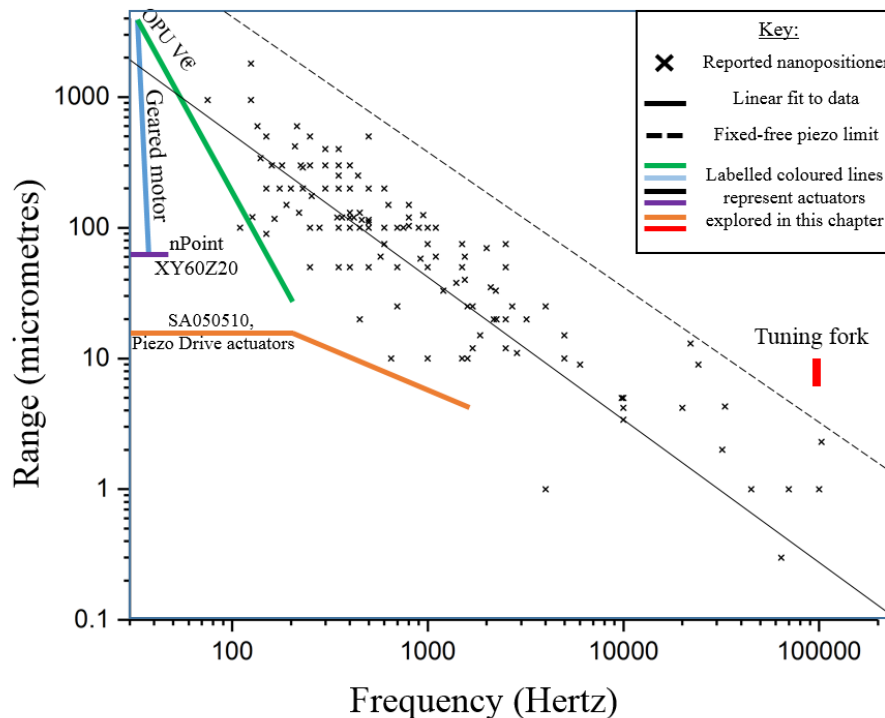
Figure 66: Frequency versus range for a number of research and commercially available nanopositioning stages adapted from data published by Kenton et al. (116)**, where the solid black line is a linear fit to all data (crosses) and the dashed black line represents a "theoretical first mechanical resonance in the actuation mode for a fixed-free piezo actuator (assuming 1 μm of travel per 1 mm of length)" (reproduced from** (117)**), with added approximate performance of actuators relevant to this chapter identified by colour lines.**

5.2.2 Sensing

A wide variety of methods of displacement sensing for nanopositioning are available, many relying on different physical properties of matter, such as strain, capacitance, optical interaction and magnetism (37). With each type of sensor utilising these physical interactions, a discrepancy in operational performances, such as resolution, noise spectra, linear range and bandwidth, are inevitably found. For the experimental work conducted in this chapter, optical sensors have solely been used due to their capacity to work at high bandwidths (e.g. >1 MHz), over a long range (e.g. >100 μm) and ease of monitoring motions externally without mechanical coupling. The three optical sensors used in this work rely on variations in optical interactions to perform the measurement. These are: optical interference; optical Doppler-shift; and optical astigmatism. These are described later in Section 5.4. To relate the performances of the three optical sensors with the actuators described in the previous section, the graph produced in Figure 66 is modified and presented in Figure 67 overlaid with the regions in which the optical sensors described in this chapter are able to measure.
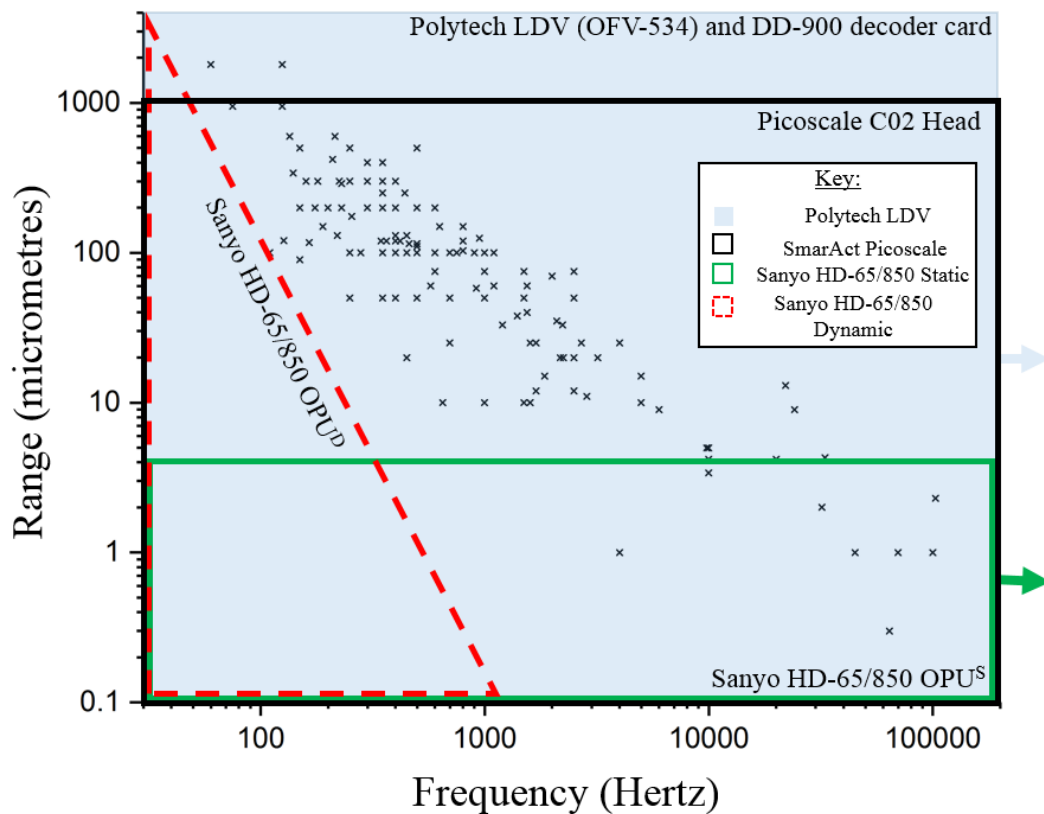
Figure 67: A reproduction of the graph displayed in Figure 66 reproduced with the data published by Kenton et al. (116). Superimposed over the top of the graph are the regions where optical sensors can measure including: a laser doppler vibrometer, a fibre interferometer and an astigmatic detection system in an optical pickup that are reported upon in this chapter.

109

5.2.3 2D scan paths for surface microscopy

Theoretically, there are a vast number of unique paths that could be used to explore a given 2D surface. However, practically speaking, for nanopositioning this set of possibilities is limited by the physical speeds and range (i.e. as discussed in Figure 66) that are required to move to each location. For example, the maximum velocity (v_{max}) of the stage limits the maximum displacement (d_{max}) between two consecutive locations in each time difference (δt) of the drive signal. Equally, d_{max} should be selected such that it makes best use of the spatial resolution of the measurement in the 3rd dimension, where, for example, the spatial resolution in AFM is set by the tip radius and feature height, whereas in a DVD player it would be the diameter of the laser spot. There are a number of typical paths commonly used in SPM measurements (37,118). A summary of the most common types can be found in Figure 68 (62,119–121).
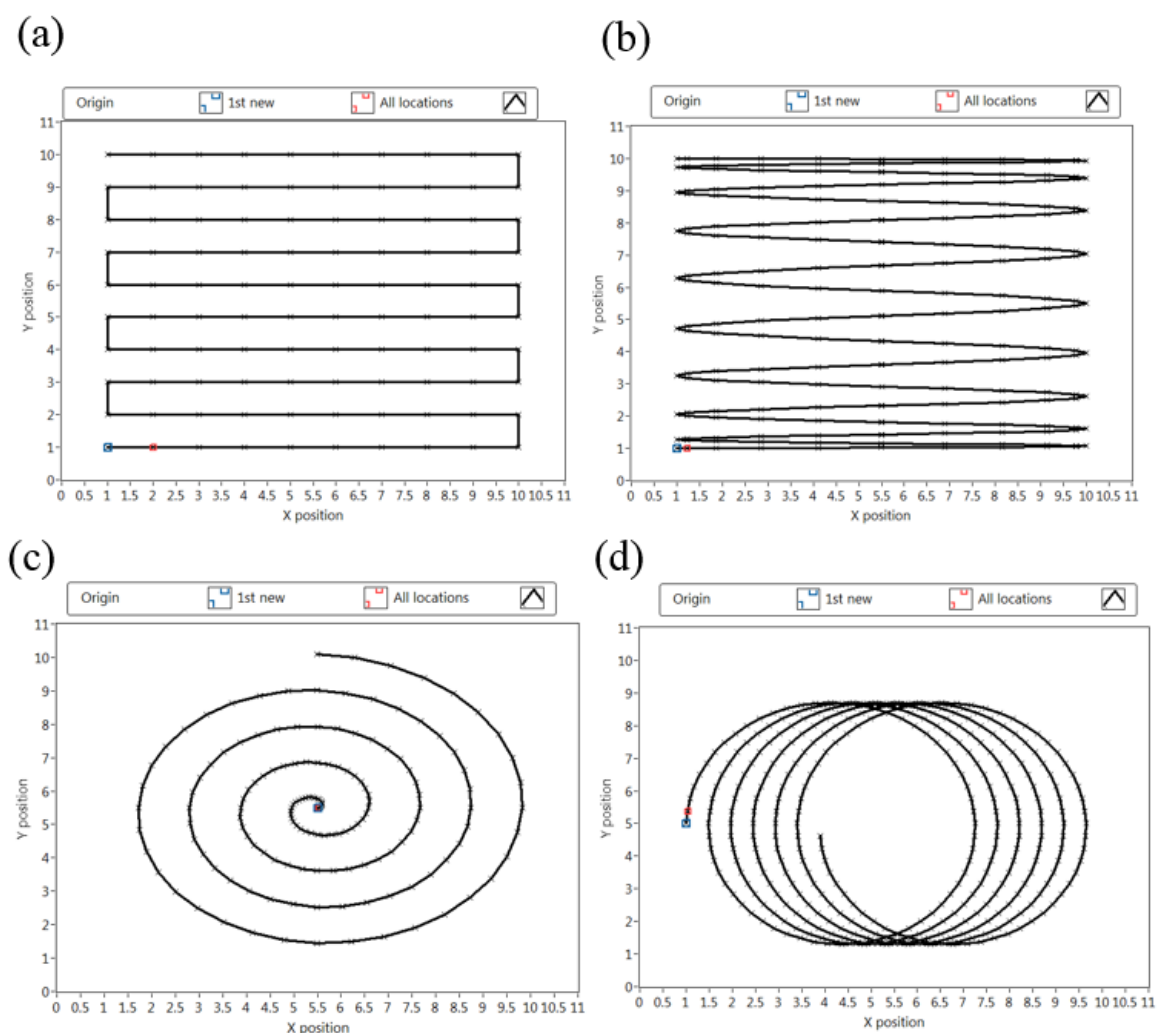
Figure 68: Typical scan paths used for SPM: (a) regular serpentine path; (b) Lissajou curve; (c) spiral scan; and (d) cycloid scan.

Some stage and actuator combinations are better suited to certain types of scanning. This can be further explored by looking at the x and y components (Figure 69) of each path (Figure 68). Continuous (e.g. spiral, Lissajous and cycloid scanning) rather than stepped (e.g. raster scanning) motion tends to be preferential for high-speed scanning as it minimises dwell time and rapid changes in direction.
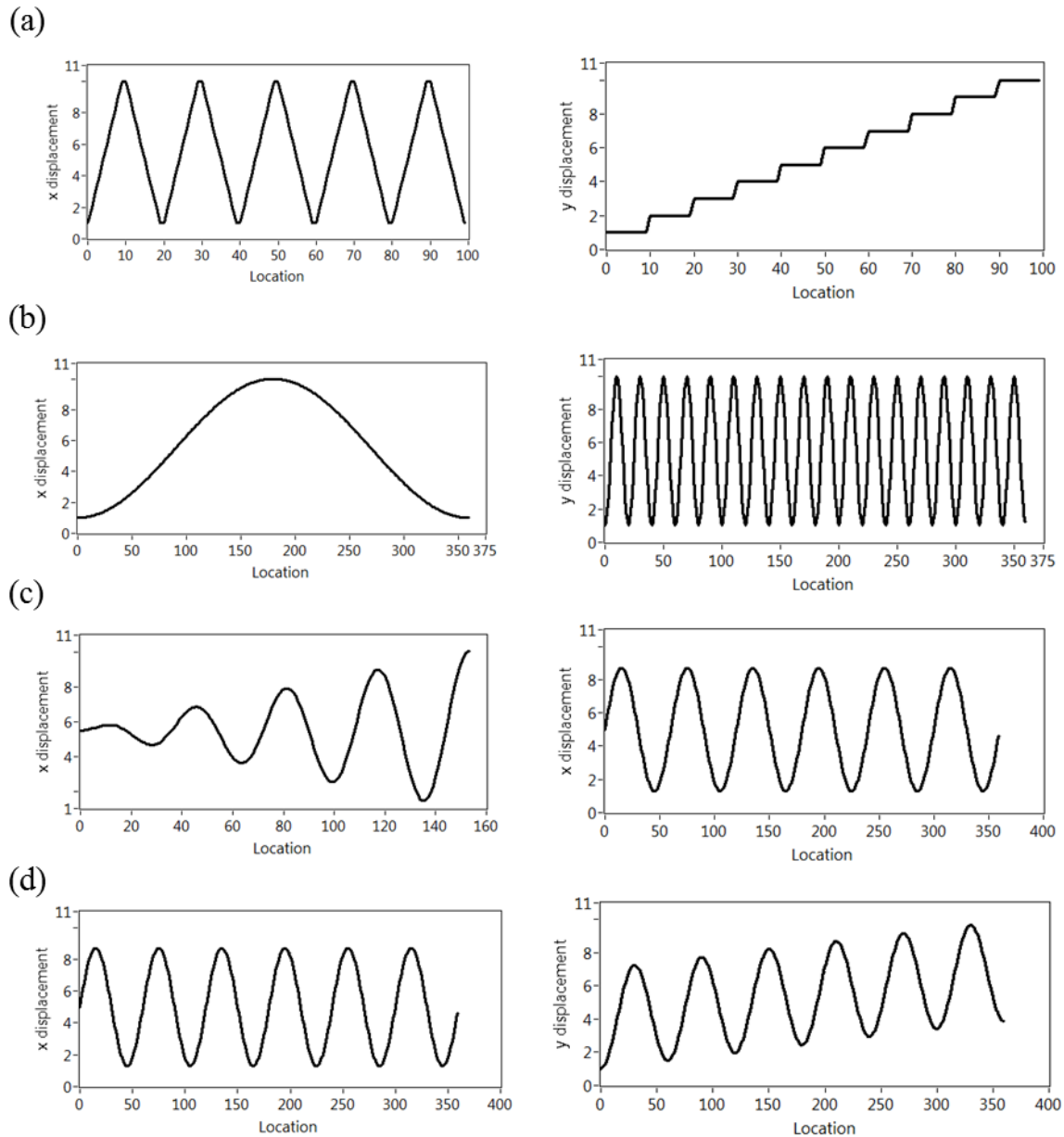
Figure 69: 1D x- and y-axis displacement components for (a) raster, (b) Lissajous, (c) spiral and (d) cycloid.

These paths can be generated using mathematical functions to generate x and y, as outlined in Figure 70.

Name	x-component	y-component
Raster *(function quo$_n$(N) calculates the quotient $\frac{N}{n}$)* *(function mod$_n$(N) calculates the remainder $\frac{N}{n}$)*	For $quo_d(s) + 1 \in 2\mathbf{Z} + \mathbf{1}$: $\{x(t) = v(mod_d(s))\}$ for $quo_d(s) + 1 \in 2\mathbf{Z}$: $\{x(t) = d - v(mod_d(s))\}$	$y(\text{t}) = \dfrac{s}{d}$
Lissajous	$x(t) = A_x \sin(\omega_x t + \delta_x)$	$y(t) = A_y \sin(\omega_y t + \delta_y)$
Spiral	$x(t) = r(t) \sin(\omega_x t)$	$y(t) = r(t) \sin(\omega_y t)$
Cycloid	$x(t) = A_x \cos(\omega_x t)$	$y(t) = A_y \sin(\omega_y t)$

Figure 70: Functions used to generate scan path coordinates typically used in SPM. Where *d* is raster dimension, *s* is step number, Z represents all positive integers, v step velocity (µm.s^{-1}), *t* is time (s), $A_{x,y}$ is the amplitude of sinusoidal waves (µm), $\omega_{x,y}$ is frequency of the sinusoidal waves (Hz) and $\delta_{x,y}$ is the phase (s).

5.2.3.1 Discussion of scan paths

The raster pattern exhibited in Figure 68 (a) works well for systematically covering areas at low speeds. However, when this same method is extended to higher scan speeds or used with large sample masses the quick transition from a high positive to a high negative direction proves difficult for a mechanical system to conform to, due to inertia of the stage. At higher speeds, the δt between consecutive locations may be short. For the HS-AFM system described in the previous chapter this is on the order of a microsecond (e.g. 5 x 10^{-7} s). This is not enough time to invert the motion of the stage without first allowing it to decelerate and accelerate again. In the case where the stage is unable to conform to pseudo-instantaneous change of direction, the true motion will lag the ideal motion. Furthermore, this pseudo-instantaneous change of direction, creates an impulse to the stage and will transfer energy to high-frequency (i.e. kilohertz) resonant modes of the mechanical system causing unwanted motion and excitation which will dissipate through the mechanical system causing positioning error.

By contrast, a Lissajous curve is a widely used path type to scan through areas efficiently (119). Using this sinusoidal motion in both axes, the actuators are moved in a smooth and periodic fashion, giving several benefits. Sinusoidal signals are much more readily available to produce as they are made up of simple standard equations commonly found in function generators. Moreover, the scan trajectory is continuously modulated by small amounts (i.e. relative to the raster pattern), resulting in motions that smoothly accelerate and decelerate the stage. This is much preferable, for a mobile mechanical system, to reduce positioning error and to ensure stability and operational longevity of the components.

For cycloid and spiral scanning (Figure 70 (c-d)), rotation stages offer the advantage of continuous radial motion spinning about a central axis. As with the Lissajou, the modulated sinusoidal motion has preferable compatibility with a real mechanical system due to continuously smooth motion. A typical spiral scanning arrangement has a rotation stage for the sample and radial actuator for the cantilever (122). As such, the centre of the active imaging area is always necessary to be at the centre of the axis of rotation. For homogenous samples this can prove to be sufficient. However, for a sample of an unknown distribution of ROIs that need to be imaged this arrangement can prove insufficient. An additional limitation is the variation of temporal resolution with area as spiral must continually grow for the sample to be explored. For the same velocity of the cantilever and a fixed axis of rotation, this means that the radius grows $\propto$ time to the power of one half (i.e.: $(t)^{\frac{1}{2}}$) .

Rotational scanning can allow for continuous motion over long periods of time without the necessity to change tangential direction of cantilever, which can lead to fewer imaging artefacts and lost imaging time due to time being spent, changing direction for example. Alternatively, cycloid and spiral scan paths can be achieved using two perpendicular linear axes or piezo tube scanners (120). However, in this case, the actuation method means that the cantilever's velocity is continuously changing compared to the central axis. This, increases the likelihood for unwanted excitation of the cantilever.

5.2.4 Deviations from ideal motion and distortion

Whilst ideal motion is expected, the true motion of actuators will be governed by the physical environment that they are in. The assumption that the true motion of the stage is exactly equal to the drive signal waveform is prone to error (86,123). The true motion of the stage is affected in different ways dependent on several electromechanical and ambient factors, such as scan amplitude, frequency, sample dimensions and environmental conditions (124). The EDM aluminium scanner, used in the HS-AFM described in Chapter 3 and by Russell-Pavier *et al.* (2) based on a similar type reported by Schitter *et. al.*(125) for HS-AFM, suffered from two main types of deviation from ideal motion: hysteresis; and cross coupling of the scan amplitudes. In this work, hysteresis refers to the discrepancy in the path taken by the stage (and attached sample) in the expansion (trace) and contraction (retrace) directions of the piezoelectric actuator. Crosstalk or cross-axis coupling of scan motion refers to perturbations seen in the slow scan (SS) axis that arise from motion in the fast-scan (FS) axis,m and vice versa. For further reference a table of terms that describe phenomena common to nanopositioning is displayed in Figure 71.

Term	Description
Abbe Error	Refers to the amplification of positioning or sensing error over distance due to erroneous angular misalignment.
Accuracy	Defined as how close to the intended position or measurement an actuator or sensor is able to be.
Backlash	Refers to errors induced by a change in direction. Often a product of machining tolerances and is found in many conventional translation mechanisms, such as gears and threads.
Bandwidth	**Sensors:** The accurate unfiltered sampling rate of the sensors. **Positioner:** The frequency range over which the stage can perform accurate motion.
Creep	Low frequency erroneous motion or sensing caused by a number of operational factors, such as strain on the positioner or thermal fluctuations.
Crosstalk	The erroneous generation of motion or sensing in an orthogonal axis to the one being actuated, found in multi-axis (i.e. two or more) positioners.
Drift	Continuous erroneous offsetting of sensing or positioning at any frequency up to the maximum bandwidth.
Hysteresis	The discrepancy in motion or sensing between outward and return path in a system.
Linearity	The ability for a sensor or actuator to respond with linear motion given the input is a linear function.
Modular	The function for single- or multi-axis positioners or sensors to be mechanically combined and create a composite system.
Position Noise	The amplitude of the measurement or position fluctuations when the system is commanded to be static.
Resolution	The minimum detectable or moveable positioning step that a sensor or actuator can resolve.
Range	The maximum travel of a position or working distance of a sensor.
Repeatability	The measure of how close a sensor or actuator performs a task two or more times.
Resonant Frequency	The lowest natural frequency of the system where the system will tend to oscillate if it was perturbated with an impulse.
Self-clamping	The ability for a positioner to hold itself at a given position.
Wobble	Found in rotational actuators is the angular misalignment of the measured axis of rotation with the intend of axis of rotation.

Figure 71: Glossary of common terms for positioning and sensing.

5.2.5 Motivation for high-speed atomic force microscopy

High-speed nanopositioners play an essential role in the emergence of high-speed atomic force microscopy (HS-AFM) (18,19,126), to scan the sample back and forth over several micrometres (e.g. <10 µm) at high frequencies (e.g. kilohertz). This allows for nanoscale dynamics to be directly observed over a range of length scales (19,74,75,127,128) and large area material property maps to be created (1,22,129–131). As with many microscopy techniques, the applications of HS-AFM are far reaching throughout science and still offer tremendous potential for new discovery and observation. By enabling high-rate imaging in AFM (several frames per second) the time taken to characterise the sample surface is reduced and material properties can be quantified with extensive statistics owing to the opportunity for more repeat measurements (22). To achieve these benefits, significant consideration of the mechanics of the cantilever and positioners involved in this HS-AFM has given rise to a continually evolving body of research focussed on increasing imaging rates (68,117,125,132–134). High-performing nanoscale actuators and specialist AFM components (e.g. positioners or detection heads) are typically costly (e.g. £100s-1000s) and can represent a high barrier to entry for many researchers seeking to buy or build an enhanced AFM. With constantly improving additive manufacturing techniques (e.g. 3D printing), becoming faster, more precise and cheaper, developments in replacing costly AFM components with low-cost alternatives are being reported in literature (135,136).

Within the field of nanopositioning, a number of different configurations have been successful, as seen earlier in the plot shown in Figure 66. The variation of these positioners differ due to requirements to conform to path type, their physical actuation mechanism and physical dimension constraining the size of the actuators and sensors. For example, the first AFM on Mars (FAMAS) (137,138) had a number of constraints due to weight, power consumption and thermal requirements. This leads to a preference in using low-power voice coil motors instead of more typical piezoelectric actuators for scanning. This same configuration of voice actuators may not be so preferable when imaging with an OPU-based detection head, due to the short focal length of the objective lens requiring the OPU to come into close proximity with the XY scanning plane. As the OPU's objective lens is itself suspended by voice coils, mechanical cross-coupling of the XY actuators and the XZ lens actuators without physical contact is highly likely.

By comparison, parallel kinematic flexure-guided style scanners are a popular design found in HS-AFM(2,19,83,139,140), as they have a low tendency for cross axis motion coupling (or crosstalk) and can be operated at high frequencies. As Yong *et al.* (117) discuss in their review paper, flexure-guided positioning frames are typically manufactured using electrical-discharge-machining (EDM) because high precision machining is required to generate the fine flexures, with consistent thickness and shape, that are incorporated into the stage design. As a result, the materials chosen for use with EDM include aluminium alloy (7075), titanium alloy (Grade 5), Invar alloy (Invar 36) and

Super Invar due to their high stiffness, good electrical conductance and low density (117). The frame is usually actuated using a piezo stack actuator as they can provide a large blocking force, at high frequencies over an appropriate range (e.g. Model: P-887.11, Physik Instrumente, Germany. Force: ≤800 N, Resonant Frequency: <135 kHz and Range: ≤8 μm). A further advantage of piezoelectric actuators for scanning is their high repeatability (86), although they can be susceptible to non-linear responses, creep and hysteresis (141).

5.3. Key actuation types for nanoscale positioning

In order to create physical displacements, there are a number of popular and low-cost methods that can be implemented. Whilst the output of physical motion is common between them, the physical mechanism that enables this varies. For each of the mechanisms, there are a variety of operational characteristics that can be taken advantage of. This section looks to explain the physical mechanism and highlight the key equations behind the methods used where non-commercial or 'DIY' actuators were made to enable critical experiment work carried out in this thesis.

5.3.1 Piezoelectric actuators

Piezoelectricity is a property, exhibited by some materials, where the stress and electric charge within the material are intrinsically linked. Examples of some naturally-occurring piezoelectric materials include bone and tendon (142). Piezoelectric materials can be used, as they are in nature, for actuation and sensing purposes. For high-speed precision nanopositioning, piezo stacks or tubes made from ceramic (e.g. PZT-5A/H) are typically used. The ceramics can be fabricated into a wide range of different compact geometries and require no more than electrode terminals to interface to. Use cases of these actuators extend from linear displacement to bending applications. Low-cost, piezoelectric buzzers can be found in a number of consumer electronics (35).

The accuracy of piezoelectric actuators is a widely investigated field as their performance has a tendency towards a number of motion distortions (143–145). Broadly speaking, these erroneous motions are due to either electrical noise spectra, creep or hysteretic effects. Depending on the actuation bandwidth and the periodic nature of the motion, the dominance of each effect can be reconsidered. Creep is often treated as a lower frequency contribution and will often be the non-intended drift of an equilibrium position of the actuator. Hysteretic effects, however, are typically seen when the actuator performs cyclic motion. The hysteretic effects manifest themselves in a discrepancy between the outward and return paths of an actuator. This discrepancy, from an ideal path, is referred to as a hysteresis loop. To help to measure and correct for these effects, piezo stacks can be fitted with strain gauges, which are used as embedded displacement sensors, or monitored externally by other sensors.

Piezoelectric actuators are characteristically well known for being able to impart a large amount of force from a small package size. For example, the SA070742 150V stack actuator (PiezoDrive) is 42 mm long, has a cross section of 49 mm^2, weighs 15 g and is able to provide a blocking force of 1800

N. The range of motion for this stack is 70 µm. While the range of motion isn't typically large (e.g. millimetres), the phenomenal force (e.g. 100s of newtons) can be used to deform frames which, in turn, will amplify this motion via lever arm amplifiers.

The maximum required current is related to the peak-to-peak amplitude (V_{pp}), frequency (f) and piezoelectric capacitance (C).

$$I_{max} = \pm V_{pp} \pi C f \qquad (17)$$

5.3.1.1 Parallel kinematic flexure stages with piezoelectric actuators

The primary implementation of piezoelectric actuators in this work is to drive each of the two axes of the high-speed scanner, which implements parallel kinematic flexures, to perform AFM as made reference to in Chapter 3. In Figure 72, the arrangement of the piezoelectric actuator with respect to the scanner and sample is shown in more detail.
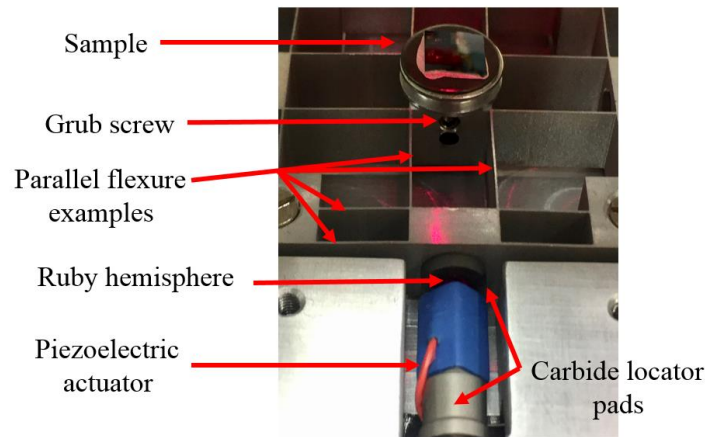
Figure 72: Piezoelectric actuator (P-887.11, Physik Instrumente, Germany) in contact with a carbide pad embedded into a dual-axis high-speed scanner used for AFM (as outlined in Chapter 3) manufactured by EDM.

In the experimental work carried out later in this Chapter (Section 5.4), the performance of this configuration is monitored using a fibre-head optical interferometer (Picoscale, SmarAct).

To drive the piezoelectric actuators, a piezo amplifier box was constructed from a configuration previously developed by O. Payton which used two MX200 amplifiers (PiezoDrive, Australia). Figure 73 shows how this was constructed for amplification of input analogue waveforms.
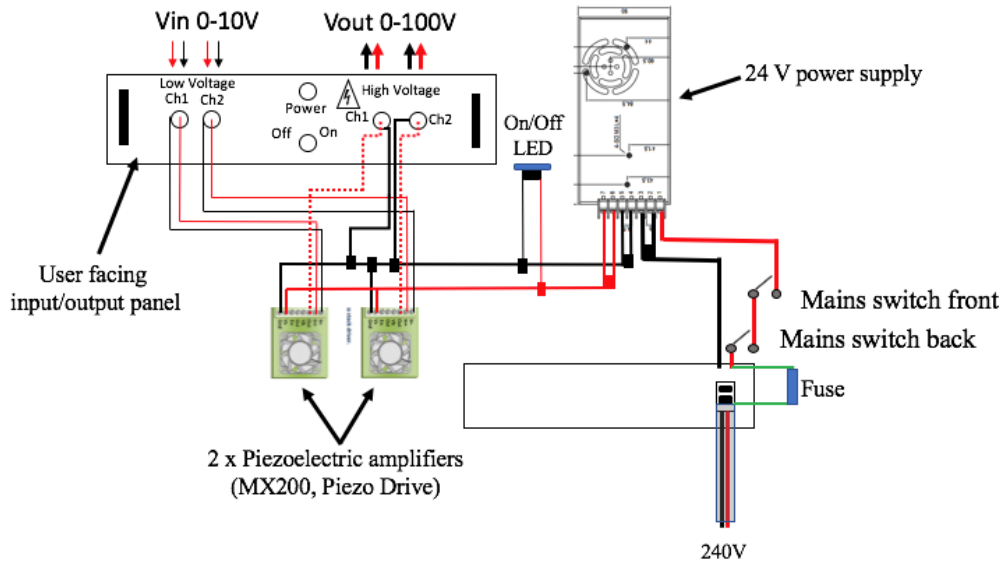
Figure 73: Wiring diagram for the amplifier used to drive the piezoelectric actuators (p-887.11, Physik Instruments, Germany) for high-speed scanning in a custom-made AFM.

5.3.2 Voice coil motors

Most commonly found in consumer electronics as part of microphones, speakers and camera lens actuators, voice-coils are ubiquitously. They are very low cost and comparatively simple to manufacture. The mechanics for creating motion rely on current passing through a wire, creating a temporary magnet, and interacting with a permanent magnet. They have significant advantages compared with other actuation methods due to their large range of motion. However, one shortcoming is that they are not able to provide as much force as piezoelectric. By comparison, the voice linear actuator V-900KPIC (Physik Instrumentation) has a travel range of 1.5 mm with a maximum push force of 0.8 N at a package weight of 40 g.

A voice-coil actuator generates a force by passing current through a wire which is within a magnetic field, typically created by a pair of permanent magnets either side of the wire. The Lorentz force that is generated is related to the current (I) through a length of wire (l) in a magnetic field with strength (B) via the equation:

$$F = Il \times B \tag{18}$$

A simplified schematic of a typical arrangement used to generate this force can be found in Figure 74.
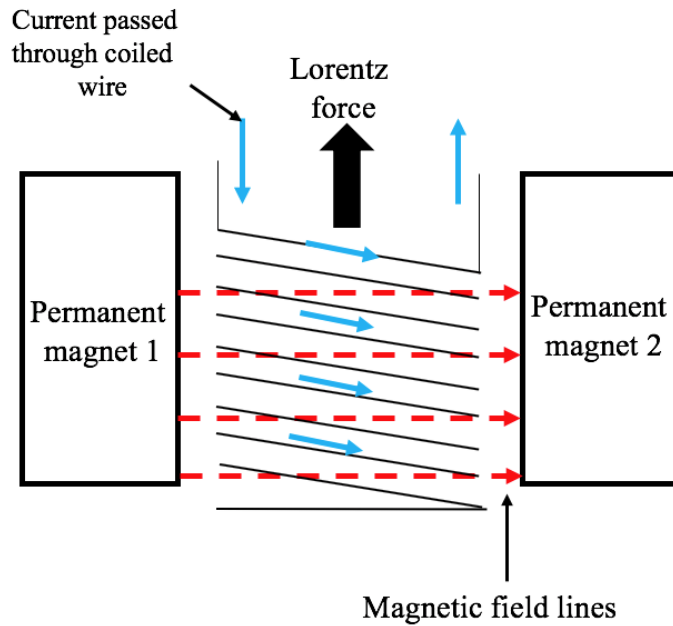
Figure 74: Schematic illustrating how a force is generated in a voice coil actuator by passing a current through a wire in a magnetic field.

Typically, there are many more coils (i.e. up to 100s-1000s) of wire than are illustrated in the schematic in Figure 74.

5.3.2.1 Voice coil motors in an optical pickup

In the commercial application of optical pickups, the function of the device is to read and write to optical media discs. As optical media disc players are embedded in portable products, ranging from cars to laptops, they can be subject to significant mechanical perturbations from external influence. Therefore, within optical pickups there is a multiaxial actuation system that is responsible for regulating the focus and tracking of the objective lens. Depending on the model of the optical pickup, the exact number of the degrees of freedom of actuation can vary and can, in some instances, provide both linear and rotational motion. Most typically there are two linear actuation axes: tracking and focussing. The focussing axis is responsible for maintaining the distance between the disc and the pickup to within the linear region of the astigmatic detection system (as outlined in Chapter 2, Section 2.1.4). The tracking actuator is responsible for maintaining the lateral position of the laser on the path that digital information has been written onto the underside of the disc.

The voice coil motors found in the Sanyo SF-HD65/850 optical pickups have electromechanical specifications that are typical and similar to other OPUs. This OPU has a dual-axis voice coil motor around the objective lens. Further information about the specification of the positioning system in the optical pickup is outlined in Figure 75.

	Current (mA)	Resistance (Ω)	Inductance (µH)	Free travel (mm)	Resonance 1st (2nd) (Hz)
Focus	220	5 ± 1	70 ± 6	> 1	60 (20k)
Tracking	220	3.7 ± 1	9 ± 6	> 1	61 (15k)

Figure 75: Summary specification for the voice coil motors found in the Sanyo SF-HD65/850.

In order to control the actuation of the voice coils on the OPUs, an analogue voltage is inputted into one of two current driving circuits that current passes positively or negatively across the F+, F-, T+ and T- pins on the Sanyo SF-HD-65/850. The actuators are such that they typically sit at an equilibrium position (e_{F0}, e_{T0}), and can be actuated in a positive and negative direction. If zero current flows through terminals F+ & F- (current = I_F) and T+ & T- (current = I_T) then the objective lens remains at equilibrium. By definition, should I_F or I_T be positive then the objective lens will be displaced positively in the respective axis (D_F,D_T). Should I_F or I_T be negative then then opposite is true.
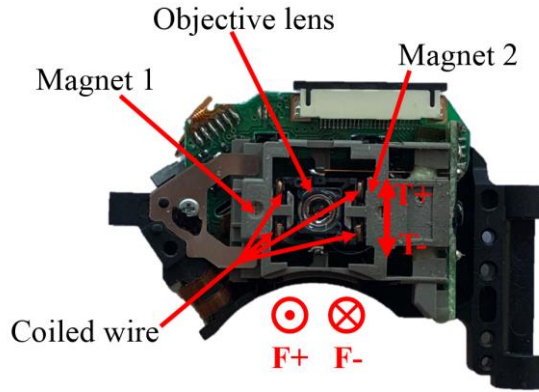
Figure 76: Optical pickup with the focus (F) and tracking (T) axes of the voice coil motors labelled

For commercial use the voice coils are responsible for controlling the positioning to fractions of a micrometres to fulfil their function of maintaining laser focus. For nanopositioning this must be improved to <100 nm. Given the significance of timing, control and computing associated with this field important that these voltages are controlled digitally. Therefore, for the purpose of computer-controlled positioning, the implementation of analogue-to-digital convertors (ADCs) is necessary. The ADCs come in a variety of bit depths, ranging anywhere from 8-14 bit as typical to 16-24 bit is considered to be high-fidelity. The voice coil motors require a moderate amount of current (~220 mA) per axis and, therefore, require amplification of the ADC output. Crucially, the performance of these ADCs and electronic amplifiers thereafter will translate into real electro-mechanic resolution achieved in the actuators at different rates. For example, a 16-bit ADC will, at best, be able to realise a resolution equal to the fraction of the free travel of the voice coil calculated via:

$$\frac{1}{bit\ depth} = \frac{1}{2^{16}} = \frac{1}{65536}$$

(19)

5.3.2.2 Optical pickup voice coil actuation: Method

In this work, a 16-bit ADC (AD5667RBRMZ, Analogue Devices) that communicates via I2C (from Arduino) was used to generate the actuator control voltages. The ADC is combined with two op-amps (TLV4111IDGN, Texas Instruments) to give a suitable level of control. This combination of surface mount chips has a number of advantages for this application. These include high current output per channel (up to 320 mA), high bit-depth (16-bit) and versatile bandwidth (I2C-compatible serial interface supports standard (100 kHz), fast (400 kHz), and high speed (3.4 MHz) modes). The operational voltage range per channel of the circuit output is ±2.5 V. The circuit schematic of these components as they were used can be found in Figure 77.
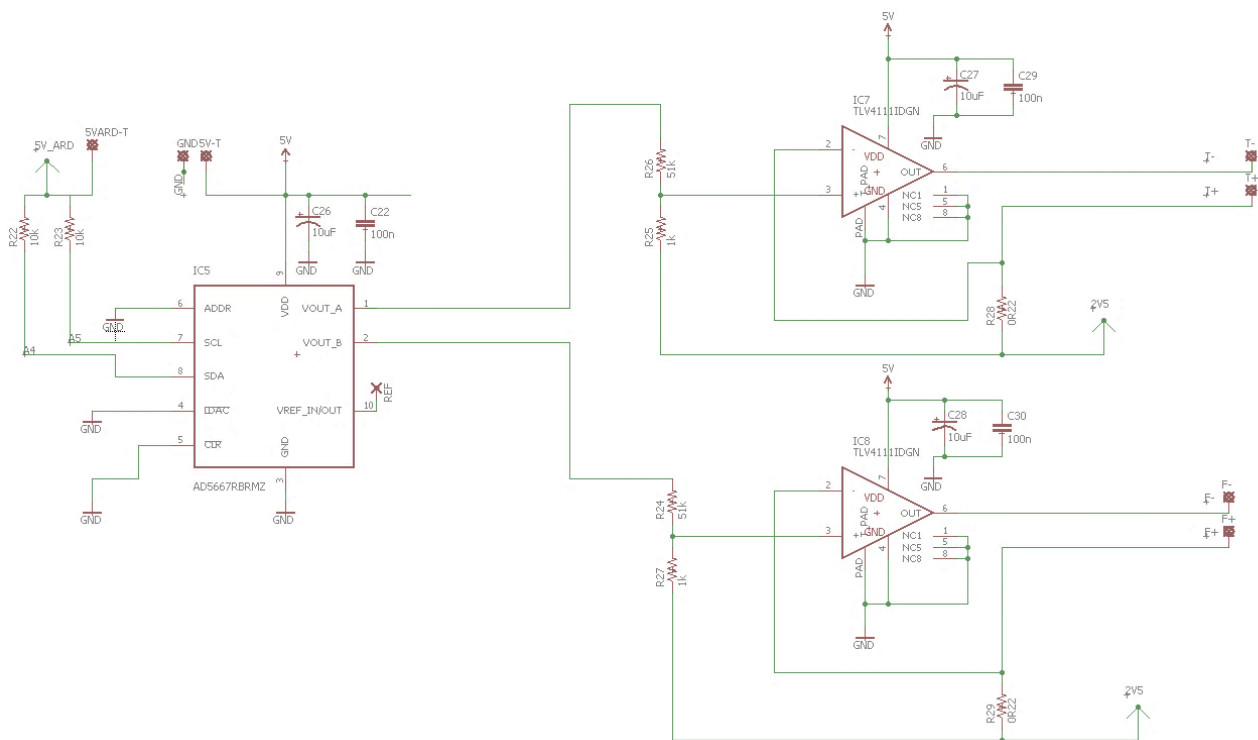
Figure 77: Circuit schematic that can be used to control the voice coil motors of the Sanyo SF-HD65/850 optical pickups. Here, A4 and A5 are analogue pins from an Arduino Nano for I2C communication.

To evaluate the performance of the voice coil actuator, a piece of silicon wafer (0.0262 g) was attached to the object lens and monitored by a 'C01' Picoscale interferometer detection head (SmarAct) and subsequently evaluated at different scan amplitudes with the Polytec laser Doppler shift vibrometer (further details can be found in Section 5.2.1).

5.3.3 Quartz tuning fork actuators for nanopositioning

The tuning fork design is synonymous with music as the frequency which the tuning fork resonates at offers a pitch or note which one or more instruments can be tuned to. Quartz tuning forks (Figure 78), having been first demonstrated around 100 years ago, have continually been miniaturised and been ubiquitously embedded into varied systems acting as a reference for frequency in electronics.

Whilst these tuning forks are much smaller, scaled down by factors of 10s-100s compared to the musical equivalents, the miniature tuning forks operate above audio frequencies and can be found in electronics used as a timing reference in devices such as watches.

The first mode (f_1) of the tuning fork is dependent on the geometry (length l and thickness a) and material (Young's modulus E and density ρ) of the prongs, and can be calculated using the following equation (146):

$$f_1 = \frac{1.76a}{l^2} \sqrt{\frac{E}{\rho}} \tag{20}$$
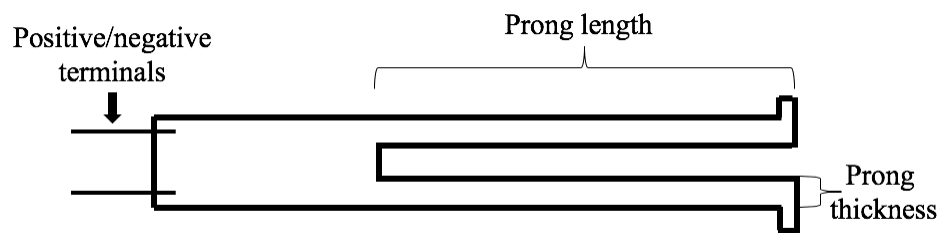
Figure 78: Tuning fork schematic with the key features of its shape identified.

For use in commercial electronics, the frequencies of the tuning forks are typically set to powers of two. This reduces the number of operations being performed by the electronics, to make into useful reference signals such as one cycle per second required for a watch. These mass-produced and commercial grade electronics cost pence and are typical encapsulated in a vacuum cavity to improve thermal stability and increase Q-factor. For the purposes of positioning in this work, the tuning forks were intended to be used in free air. The consequence of this, according to previous studies, reduces the frequency of the first mode (by <1 part in 1000) and Q-factor (by 1000s) (146).

5.3.3.1 Implementation of a quartz tuning fork as an actuator

To make use of the properties of an encapsulated quartz tuning fork, the quartz fork must be carefully removed from a cylindrical casing surrounding it made from aluminium. Two wires (the terminals, Figure 78) leading away from the fork were also fixed in place by a hard-setting resin at the base of the cylinder. The tuning fork was removed by applying several instances of light pressure by hand with a pair of pliers around the casing at the base of the cylinder, causing minor distortions on the aluminium casing and the hard-setting resin to gradually crack and fall out of the cylinder. Repeating this several times, ensuring that the light pressure did not damage the quartz, the tuning fork becomes sufficiently free within the casing, and can then be removed by hand with tweezers. In Figure 79, we see how the tuning fork once removed has been attached to the objective lens of an OPU to provide a prototype 3 - axis high-speed scanner. The terminals could be connected to a low voltage (±10 V) power supply and

oscillated with a sinusoidal waveform of frequency ~100 kHz depending on the specific fork being used and the environment it is being oscillated in (e.g. air, water or vacuum).
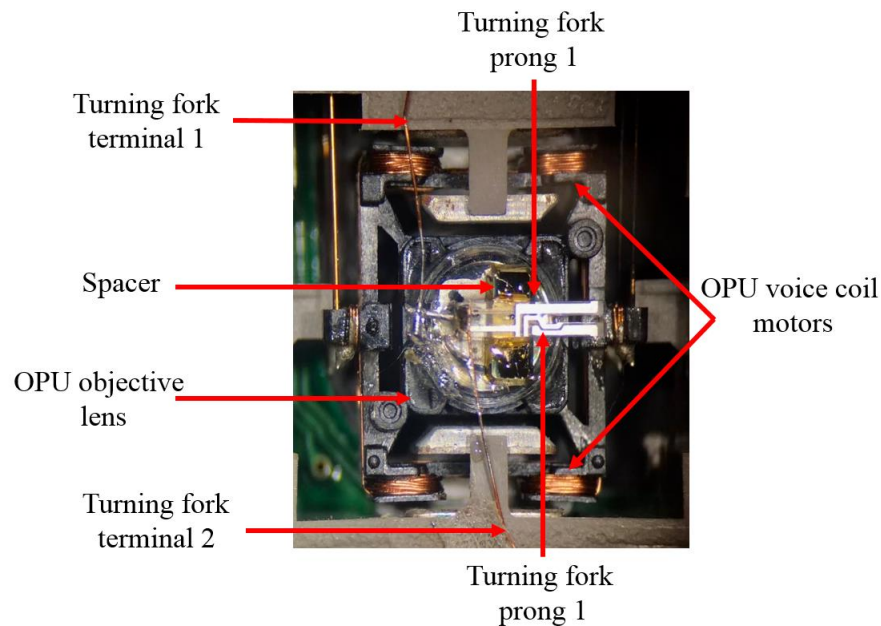
Figure 79: Quartz tuning fork attached to the objective lens of a Sanyo HD65/850 optical pickup, which can be actuated left-to-right and in-and-out of the plane of the image.

5.3.4 Basic reduction and transfer mechanics for nanopositioning

Here reduction mechanics refers to methods by which a small physical displacement can be achieved via a mechanical system that is used to 'de-amplify' a large physical displacement. A well-known example of such a system is a reduction gearbox, also used in this work as a commercial component, in which the gears are used to reduce the output angular velocity from an input angular velocity, and gearing is expressed as a ratio of these two velocities. To achieve nanoscale resolution from an actuator directly often requires expensive and components machined to high tolerances. However, there are many actuator types used in commercial electronics, such as printers, speakers and disc drives that have positioning capabilities in the 1-100s of micrometre range, including optical pickups themselves. These commercial actuators are widely available and have typically undergone stringent testing that will ensure that they have a high level of repeatability over a long operational lifetime. Combining these with reduction mechanics can result in that positioning capability being decreased by several orders of magnitude. Three key methods of reduction mechanics used for nanopositioning in this work are: reduction gearbox; rotary-to-linear threaded drive; and lever-pivot reduction. The reduction capabilities of these can be evaluated using the proceeding equations.

For two meshed gears (a and b), the velocity at the point where the torque is transferred has equal tangential velocity (v_t). However, we know that the angular velocity (ω) is simply related to the radius (r):

$$\omega = \frac{v_t}{r} \tag{21}$$

For a given set of compatible gears (e.g. Figure 80), gear a and gear b, the radii, radius a (r_a) and radius b (r_b), is proportional to the number of teeth ($n_a \ and \ n_b$). Therefore, the reduction ratio is then:

$$\frac{n_a}{n_b} \ or \ \frac{r_a}{r_b} \tag{22}$$
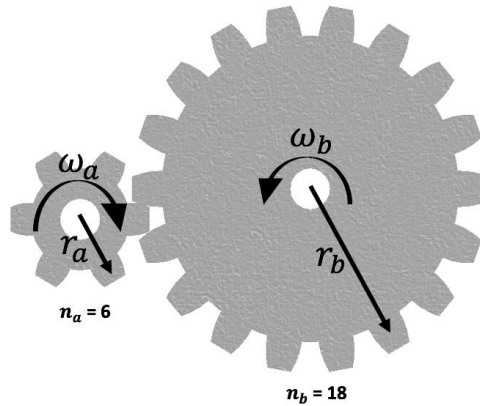
Figure 80: Reduction gearing schematic, with labelling of physical properties.

The rotary-to-linear conversion is transferred from angular velocity (ω), in rad.s^{-1}, to linear velocity (v_l), in m.s^{-1}, with a bar with pitch (p), in mrad^{-1}, via:

$$v_l = \omega p \tag{23}$$
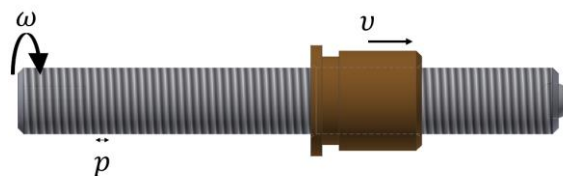
Figure 81: Rotary-to-linear transfer schematic, with labelling of physical properties.

A lever can be used to reduce motion by considering the diagram in Figure 82.
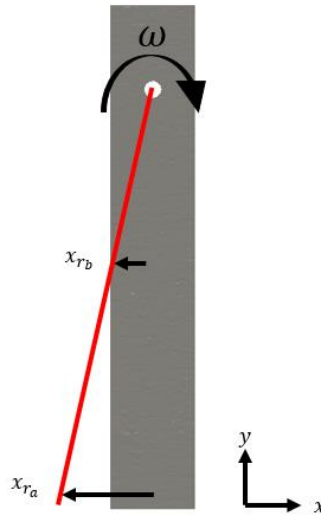
Figure 82: Levered reduction schematic, with physical properties labelled.

The displacement in the x-axis at radii a and b for a given angular velocity (ω) is given by:

$$\frac{x_{r_a}}{x_{r_b}} = \frac{r_a}{r_b} \tag{24}$$

Later in this chapter it will be shown how these mechanical systems can be used in combination to create a compact low-cost positioner for cantilever alignment.

5.3.4.1 Implementation of reduction and transfer mechanics actuators

The methods of reduction mechanics described here, make use of an OPU mounted cantilever positioner (i.e. the cantilever sled from Chapter 3, Section 3.3.3) that permitted for the cantilever to be translated laterally in front of the objective lens, for alignment of the cantilever chip for performing AFM (as outlined in Chapter 3). The requirements of the set-up (Figure 83) involved being able to position the ~ 1 µm wide laser spot onto the topside of the MSNL-C triangular cantilever above the cantilever tip ~ 5-15 µm wide. Furthermore, the system was designed to be used (as described previously in Chapter 4) in a dynamic scanning mode to attempt to perform optical profilometry on the cantilever using this configuration. Further details surrounding this application were discussed in Chapter 4, Section 4.6.3.
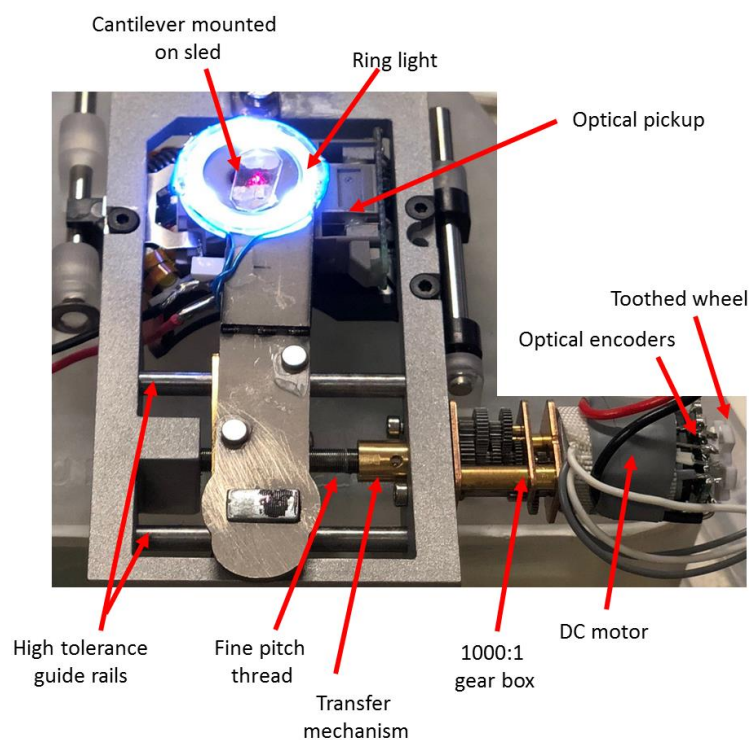
Figure 83: Cantilever sled developed for alignment of the cantilever into the path of the optical pickup to allow HS-AFM to be performed.

5.4 Displacement sensing

As mentioned in Section 5.2.2 of this chapter, several methods of displacement sensing were used throughout the experimental work carried out in this project. In this section, a detailed overview of the principal instruments used to monitor nanoscale displacements in this work are described in turn, where known key performance specifications are tabulated for comparison. The three optical tools used are based upon interferometry, the Doppler shift effect and an astigmatic detection system, respectively and can detect at 2.5 MS/s or greater. Each of these instruments has a different number of channels, optical focusing mechanism, sensing method and associated cost, and is therefore appropriate in different use cases.

5.4.1 Interferometry

Interferometry is a widely-used method for measuring displacement throughout scientific practices at many length scales. A key advantage of using the interference of light as a detection mechanism is that the measurement is a product of the wavelength of the laser light used, which can be narrowly controlled, therefore interferometers are often used as traceable standard in nanometrology (124). To make a displacement measurement via interference, light must destructively and constructively interfere with itself, creating an interference fringe pattern. Therefore, a given measurement using this pattern is inherently calibrated to the wavelength of the laser light used and doesn't rely on a secondary calibration lookup. Furthermore, as light can travel long distances, a

property linked to the coherence length of the laser system, with no carry mechanism other than free space, allowing systems to be designed with a large standoff between measurement point and laser emission. The largest and popular example of this technique exists in the Laser Interferometer Gravitational-Wave Observatory (LIGO). This uses a Michelson interferometer with Fabry Perot cavities (147), making the effective path length of the system 1120 km. This is able to observe displacements 1,000[th] the width of a proton (i.e. $<10^{-18}$m). In this work, this high level of displacement sensitivity isn't required so table-top sized configurations can be used, such as described below.

For determining the position of nanopositioners, interferometry is considered to be highly accurate and the use of collimated light allows the measurement to be made from a distance and does not require direct mechanical coupling to monitor the moving mass. This makes this technique versatile for implementation in a variety of experimental set-ups. The technique is sensitive to ambient condition fluctuations, which may affect the refractive index of air, such as temperature, humidity and pressure. The use of interferometry with positioning stages has been a focus at the National Physical Laboratory, a principal partner in this work, for a number of years (124,136,148–150).

5.4.2.1 Picoscale fibre head interferometer: key sensing details

A commercial instrument used in this work is the Picoscale interferometer (SmarAct GmbH, Germany). A photograph of this is seen in Figure 84. The Picoscale system is used for optical metrology. Its technical specifications are well suited to this line of work. The key properties of the detection system are tabulated in Figure 85.
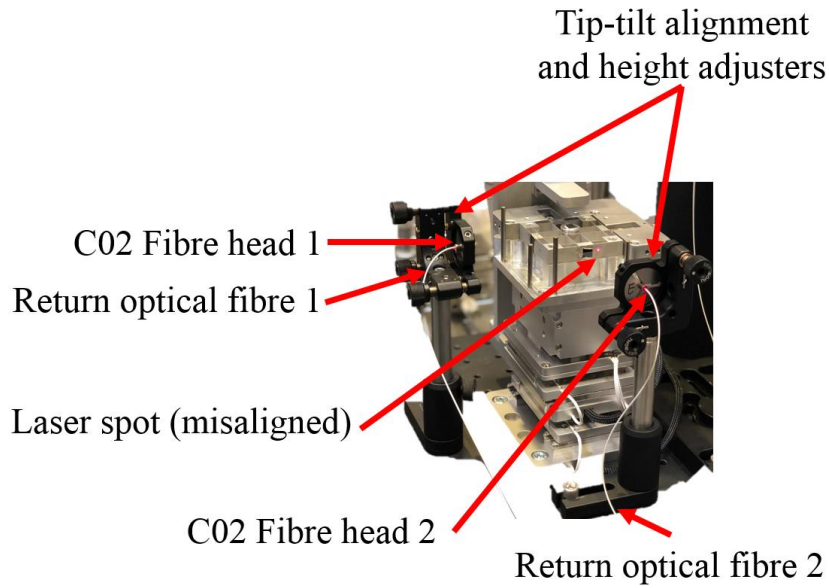
Figure 84: Two C02 Picoscale fibre heads (smarAct GmbH, Germany) incident on the side of a high-speed scanner used for atomic force microscopy.

Key property	Technical Detail	Comments
Displacement resolution	σ: 207 pm @ 1.25 MHz	Sub-nanometre resolution at higher than typical high-speed positioning rates
Standoff & working distance (C01)	13 mm 637 mm	Large working distance allows for tracking over long-range motion
Spot size	400 μm	Allows for low mass reflectors to be added
Channels	Three-channel Michelson Interferometer	Any cross-axis motion between x,y,z can be monitored simultaneously.
Capture rate and timing	Up to 10 MS/s (total) with external clock input	Allows for clock sync with other hardware
Environmental Compensation	Temperature: ±200 mK Pressure: ±2 mbar Humidity: ±2 % Position uncertainty: <1 ppm	Allows for correction in room fluctuations throughout long experiments

Figure 85: Key properties of the Picoscale interferometer with the C01 head attached

5.4.2 Laser Doppler-shift vibrometer

The Doppler-shift effect is well known and widely used amongst a variety of fields for measuring displacement. Equivalent to the pitch change heard due to a passing siren, the same principle of measurement can be used in optics to measure distances smaller that an atomic spacing (10^{-15} m) with a microscope through to distances within the farthest galaxies ($>10^{26}$ m) with a telescope. A shift, in the wavelength of light, is seen by an observer due to the relative difference in velocity between the emitted and light reflected back to the observer (given the emitted and observer are travelling at the same speed). Any differences present to reduce the path length of light cause shortening of the wavelength (blue shift) as seen by the observer, whereas, any motion present that extends the path length causes expansion of the wavelength (red shift) as seen by the observer.

5.4.2.1 OFV-534 laser Doppler vibrometer (Polytec, Germany): key sensing details

An instrument based on detecting the Doppler shift of light and used throughout this thesis is the laser Doppler shift vibrometer detection head (OFV-534, Polytec, Germany) (Figure 86) with the decoder card (DD-900, Polytec, Germany). This displacement detection configuration has a different set of advantages over the Picoscale interferometer. One notable advantage of this instrument is its compatibility with a wide range of optical microscope lenses. A summary of key working properties for the Polytec LDV is found in Figure 87.
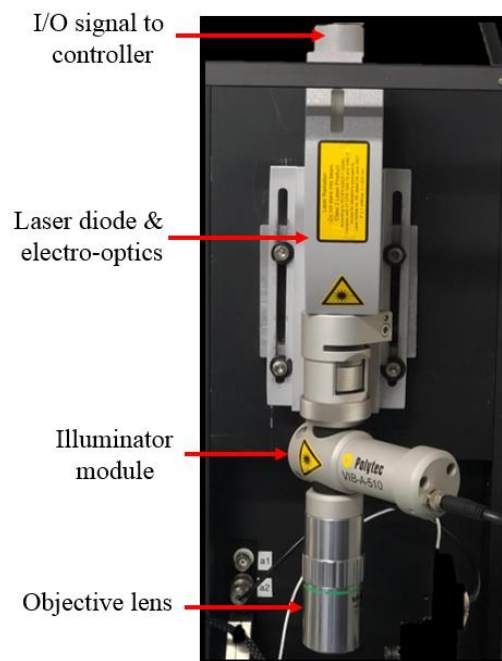
Figure 86: Polytec laser-Doppler shift vibrometer (OFV-534, Polytec, Germany).

Key property	Technical Detail	Comments
Displacement resolution (highest*)	±15 pm*	Sub-nanometre resolution at higher than typical high-speed sensing rates.
Standoff & working distance (WD) (20x)	21.7 mm 1-100,000 µm	Resolution and working distance are interchangeable.
Spot size	1.5 µm	Allows for low mass reflectors to be added. Can be used with cantilevers.
Channels	High resolution optical image and displacement/velocity	Allows for precise positioning of laser spot.
Capture rate and timing	Up to 2.5 MS/s analogue out	Allows for simultaneous ADC with other hardware.
Tuneable range & resolution* (Range : Resolution)	Examples: 1 µm : 0.015 nm 10 µm : 0.15 nm 100 µm : 1.5 nm	Makes equipment adaptable for difference length scales. Examples extend to 16 measurement ranges.

Figure 87: Key properties of the LDV detection head (OFV-534, Polytech) with decoder card (DD-900).

5.4.3 Optical pickups

A detail description of the astigmatic detection mechanism present in the optical pickup to regulate the laser focus in typical operation is found in Chapter 2, Section 2.2. Figure 88 revisits the key externally-identifiable features of the Sanyo SF-HD65/850 optical pickup.
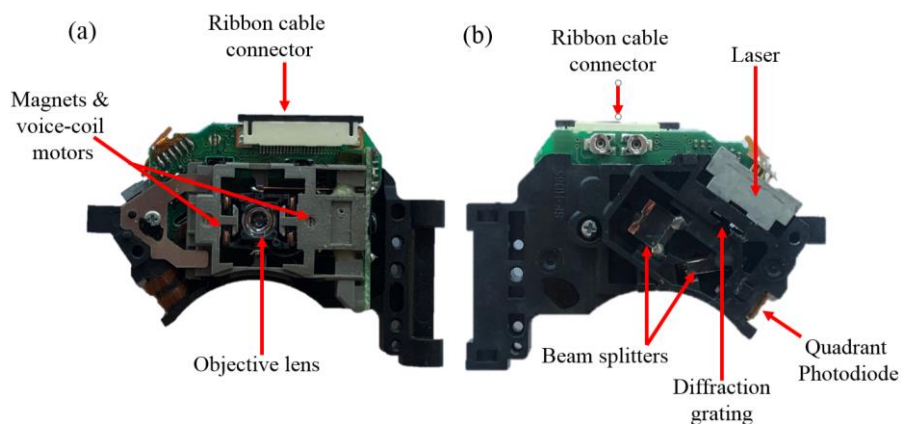
Figure 88: Sanyo SF-HD65/850 optical pickup with key externally visible features labelled.

5.4.3.1 Sanyo SF-HD65/850 optical pickup (OPU) (Sanyo, Japan): key sensing details

For evaluation of the OPU for high-speed nanopositioning a Sanyo HD65/850 optical pickup was used. The OPU was used in a combination with several versions of bespoke PCBs so operational conditions may vary and typical values are expressed unless otherwise stated. A summary of the measurement properties of this device are displayed below in Figure 89.

Key property	Technical Detail	Comments
Displacement resolution	<1 nm	Sub-nanometre resolution at higher than typical high to ultra-high speed sensing rates.
Standoff & working distance	3.05 mm >1 mm	Allows for high resolution tracking over long-range motion.
Spot size	~1.0 µm	Allows for low mass reflectors to be added. Can be used with cantilevers.
Channels	Quadrant photodiode can be used for displacement and 2D angular measurements	Gives three simultaneous measurements if all channels are collected.
Capture rate and timing	Typical bandwidth of 45 MHz analogue output	Allows for simultaneous ADC with other hardware.
System package	<51 x 36 17 mm <£10 Dual wavelength laser Dual axis actuator	Compact solution for nanoscale positioning. Low cost means viable to implement in many axes. Inbuilt hardware capabilities make it versatile.

Figure 89: Key properties of the Sanyo HD-65/850 optical pickups.

5.4 Experimental work

5.4.1 Parallel guided flexure stages with piezoelectric actuators

One key aim, reported in this chapter, was to develop an evaluation set-up for measuring the performance of the parallel guided flexure stages with calibrated CD/DVD OPUs, permitting the detection of deviations from ideal motion. The astigmatic detection system in the OPUs facilitates high-bandwidth sensing (e.g. at megahertz) with nanoscale resolution, over its typical linear range of 6 µm. It is therefore ideally suited in this instance for a typical HS-AFM scanner which scans at an amplitude of 2-5 µm. The OPU detection bandwidth is much higher than other typical positioning sensor types, such as capacitance or strain gauge sensing (37), whilst being greater than or equal to the vertical detection systems used in this form of HS-AFM, such as OPU (2) or LDV (21). Therefore, the OPUs

give scope for monitoring lateral scanner position on a pixel-by-pixel basis whilst HS-AFM is carried out.

5.4.1.1 Stage design

The proposed scan stages were developed and designed using Autodesk Inventor. A design criterion was to have at least one axis with a primary frequency above 2 kHz making them suitable for a fast scan axis in the HS-AFM, which is typically driven at 1 kHz. A second criterion, was for the external dimensions of the parallel flexure frame to be 50 mm by 50 mm. This was imposed in order to fit in the pre-existing stage mount in a commercial HS-AFM (Bristol Nano Dynamics) and to allow for enough space for external optical sensors to be added. Three design variants of a stage used in previous studies (1,2) were chosen for finite element modelling (FEM) and then compared via experimental measurement. Figure 90 shows the two-dimensional top-down view of the three proposed stage designs.
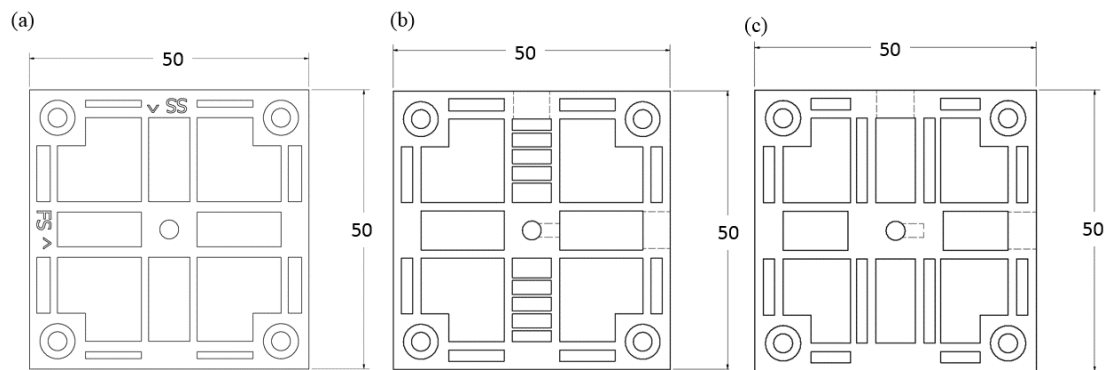
Figure 90: Three scale drawings of dual-axis flexure stages: (a) 'asymmetric' flexure thickness (thicker horizontal flexures as compared to vertical flexures); (b) additional 'cross flexures' in one axis; and (c) 'rectangular' with additional flexures. The dimensions shown are in millimetres. The location of the piezoelectric actuators, sample and sensors are further explained later in the next section.

There are very many variants of the original stage design that are possible. Therefore, this work does not explicitly attempt to explore the large parameter space of all possible design variations. Instead, the work focusses on three distinct variations to the original design and uses these as case studies to be evaluated using the OPU-based positioning set-up. Figure 90 (a) ('asymmetric) shows a stage with all horizontal flexures of increased thickness as compared with the vertical flexures. Figure 90 (b) ('cross flexures') shows a stage with additional cross flexures to make the vertical parallel flexures stiffer. Figure 90 (c) ('rectangular') shows an additional pair of flexures running vertically to provide additional stability to the centre of the stage. Autodesk Inventor Modal Stress Analysis was used to evaluate the primary frequency of each axis for the stages.

Figure 91 shows an exaggerated visual representation of the expected deformation for the rectangular stage (Figure 90 (c)) at the resonant frequency in each drive axis. Furthermore, Figure 92 shows the primary numerical results for all three stages. Here, the four circular bolt holes have been constrained as fixed for the simulation further details of the simulation can be found in the appended media storage titled 'FEM simulation'.

(a) Drive Axis 1   (b) Drive Axis 2

3.6 mm

0 mm
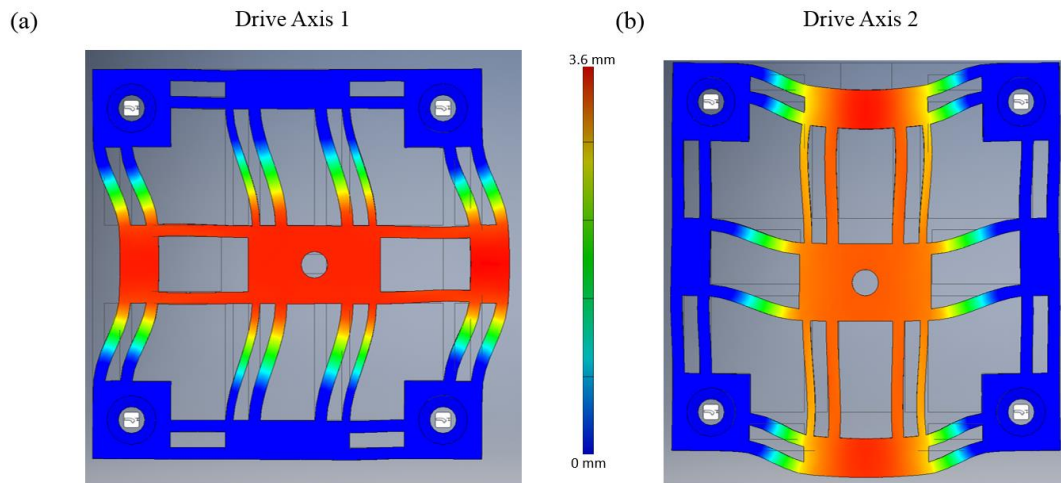
Figure 91: A visualisation of the deformation outputted by the modal stress analysis conducted with FEM in Autodesk Inventor of an ABS 'rectangular' parallel kinematic flexure stage and perturbation in (a) scan axis 1 (horizontal) and (b) scan axis 2 (vertical) for their primary resonant frequency.

	Asymmetric	Cross flexures	Rectangular
Primary Resonance axis 1	1.68 kHz	1.86 kHz	1.85 kHz
Primary Resonance axis 2	2.49 kHz	2.03 kHz	2.36 kHz
Relative Amplitude 1	1	1	1
Relative Amplitude 2	0.86	1	0.88

Figure 92: Table showing the summary FEM results calculated for the three stages.

From the numerical results, we see that the addition of flexures and flexure thickness (from Figure 90 (a) and Figure 90 (c)) have both the increase in resonant frequency (i.e. 2.49 kHz and 2.36 kHz) and reduction relative amplitude (i.e. 0.86 and 0.88) (Figure 92) compared to unmodified. The cross flexures (Figure 90 (b)) only affect the resonance of the second axis.

Subsequently, the designs were 3D-printed using a Formlabs (USA) Form 2 in standard black resin (version 2) with tensile modulus of 2.8 GPa and flexural modulus of 2.2 GPa. The 3D-printed stages were mounted in an aluminium housing. Stacked piezoelectric actuators (P-887.11, Physik Instrumente, Germany) with ruby hemisphere contacts were placed by the outside face of the stage footprint. Carbide locating pads (CPP-C-6, Newport Corporation, USA) were installed into the face of the stage, in each axis, to ensure consistent location of the ruby hemispheres and to reduce the amount

of deformation in the actuator-stage contact area. This configuration is the same as previously reported in literature with the aluminium, EDM-manufactured stage (2).

5.4.2 Optical pickup sensing of high-speed scanners

5.4.2.1 Overview

Given the compact and low-cost nature of the optical pickups they are well suited for integration into the monitoring of high-speed displacement stages for little additional cost or footprint. In order to evaluate the stage dynamics, the measurement location of the stage needs to reside within the calibrated linear range of the OPU. This sets the limit of the maximum range of the stage that can be measured from a fixed location of the OPU. The specifications for the Sanyo SF-HD65/850 OPU have a stated 'linear region' in the focus error s-curve with linear region 6 micrometres. However, due to the non-linear variation in the gradient within the 'linear region' (see Figure 11, Chapter 2), a smaller effective range is appropriate to use for displacement monitoring.

To do this a custom assembly was fabricated to hold the OPUs in the focal range of the external flexure stage face and firmly house the two piezo electric actuators. In addition, the piezo needed to be able to be repeatably located and tensioned onto the stages to minimise systematic errors. It was also designed with the appropriate non-permanent fixing so that many stages could be evaluated on the same assembly (see Figure 93 for more details).
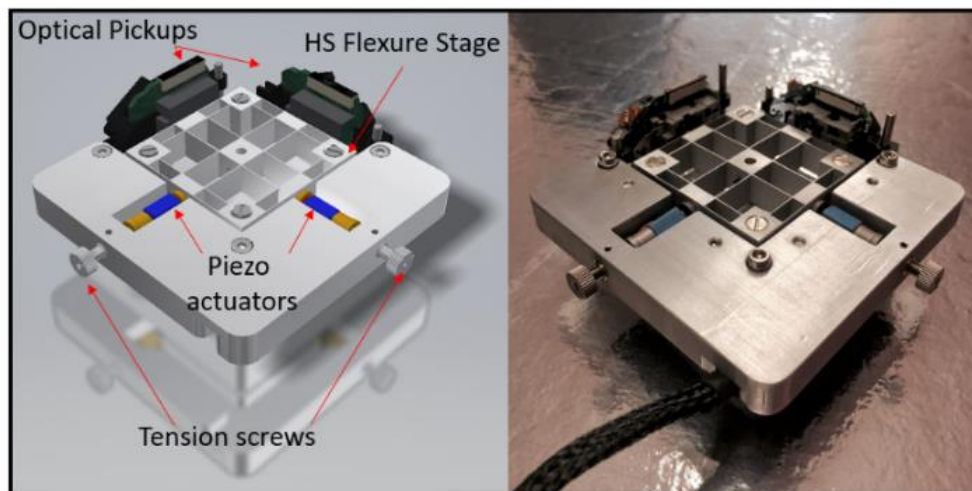
Figure 93: Bespoke assembly made to hold the high-speed flexure stage with two-axis OPU monitoring image correction or displacement modification.

5.4.2.2 Calibration

Initially without accurate calibration of the OPUs detection response, as described later in this section, the dual-axis OPU assembly could only be capable of analysing cross-axial motion for dual-axis flexure stages in the frequency domain in arbitrary units, by simply using astigmatic response curve (i.e. the NFE) as a proportional sensor over a micrometre wide region in the middle of the s-curve.

The OPUs used in the set-up described in Figure 93 are fixed onto vertical posts in each axis. To calibrate the OPU it is possible to use the stage itself and an interferometer Figure 94. By using the stage without a sample and setting the output drive signal to its maximum it is possible to achieve a range of motion that surpassed the linear range of the optical pickup (i.e. >6 µm). Looking at the measured displacement over a second, it can be seen how stable the resultant displacement is (Figure 95).

In order the operate the OPUs for correct monitoring of the flexure-stages, their focus error responses need to be calibrated. To do this, an experimental set-up was created that allowed for the Picoscale and optical pickup to be interchangeably used to monitor the same reference surface (i.e. silicon wafer) on the side of an EDM aluminium parallel flexure stage.
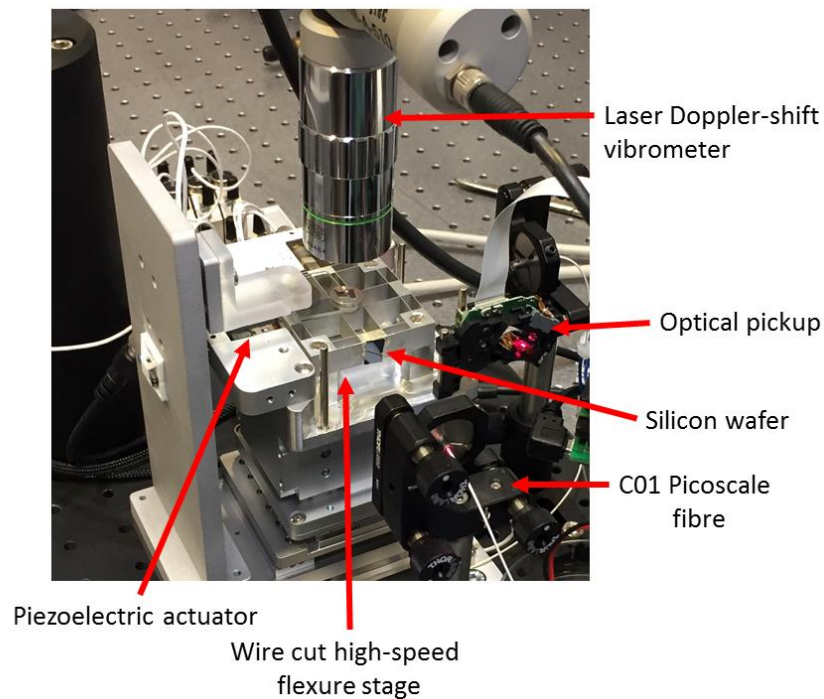
Figure 94: Experimental set-up used to evaluate a Sanyo HD-65's ability to monitor the high-speed flexure stage.
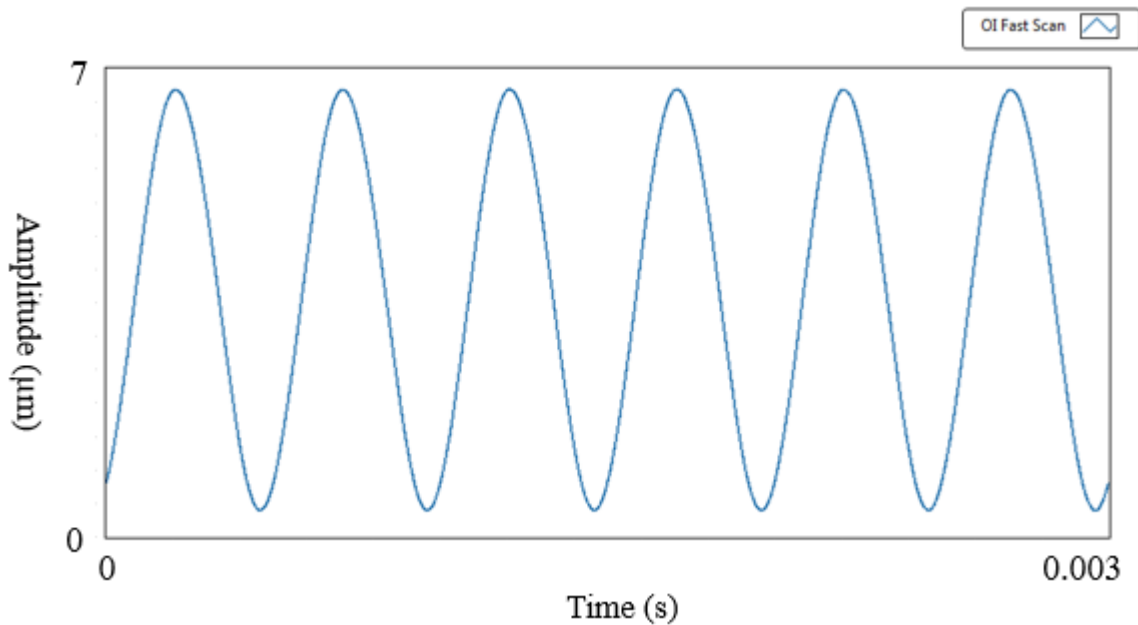
Figure 95: Snippet of the fast scan stage motion used for calibrating an OPU for high-speed position monitoring. The drive signal is a 2 kHz sinusoidal wave with a Picoscale interferometer measurement bandwidth of 2.5 megasamples per second.

Measuring the scan displacement with the Picoscale, it is possible to see that the displacement magnitude of the stage achieved here was 6.31 µm. By splitting the second-long sample into 2,000 repeat cycles it is possible to find a mean path and the standard error from that path at each mean location. Over the one second period, with 2,000 repeating sinusoidal cycles, the mean standard error from the mean sinusoid line was found to be 79.5 pm. This shows that the self-consistency of the path is well below the dimension of a typical pixel (i.e. >1 nm) as in the HS-AFM data presented in Chapter 3, Figure 40.

Subsequently, with the stage still oscillating with same motion seen in the Figure 95, the response from the Sanyo HD-65 was inspected. Here, we see that the 6.31 µm stage displacement amplitude exceeds the OPU peak-to-peak focus error range of 6 µm. This is seen periodically in the graph as double turning points (Figure 96). For this one second period the mean standard error for the OPU was found to be 4.14 picometres.
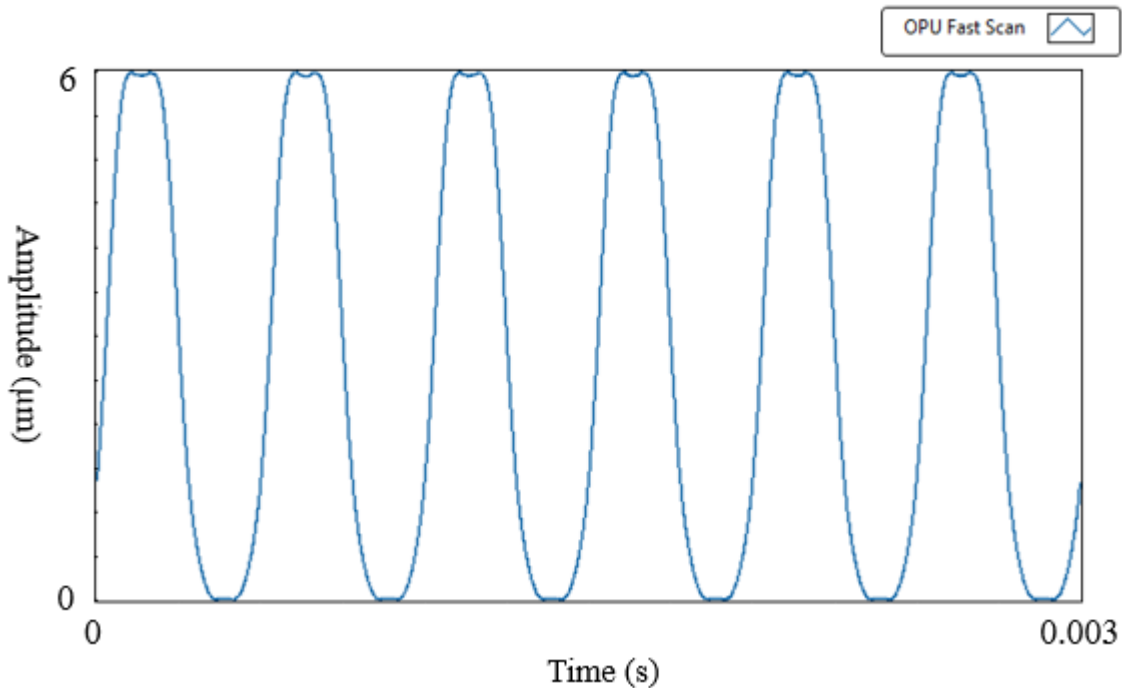
Figure 96: Snippet of the fast scan stage motion as measured by the OPU's focus error detection. The drive signal is 2 kHz sinusoidal wave with optical pickup measurement bandwidth of 2 megasamples per second.

Having phase-matched the Picoscale and optical pickup measurements, it is possible to plot the normalised focus error signal against Picoscale amplitude (Figure 97). This allows a calibration profile for the astigmatic detection system response to be calibrated against the traceable interferometer measurements and creates a calibration curve or small hysteresis loop for the 2,000 repeated cycles of the stage. It is then possible to fit a polynomial to these data to allow it to be saved in a more compact fashion than just the raw data itself. The polynomial coefficients can then be used to convert the normalised focus error signal back into a displacement in real-time whilst scanning.

HS-AFM images were constructed using the fibre interferometers and compared against the DVD OPUs to see if the hysteresis in the fast-scan direction could be accounted for in real-time using OPUs. In this section, we return to the EDM stage (2) used to assess if the calibrated OPUs can be implemented to monitor the scanner, in place of the fibre interferometers, to reduce imaging error when conducting HS-AFM on a sample. The real-time monitoring using the two systems for measurement were compared via imaging the same region of a sample with a modified HS-AFM, by placing the OPUs in the vertical posts labelled in Figure 94.
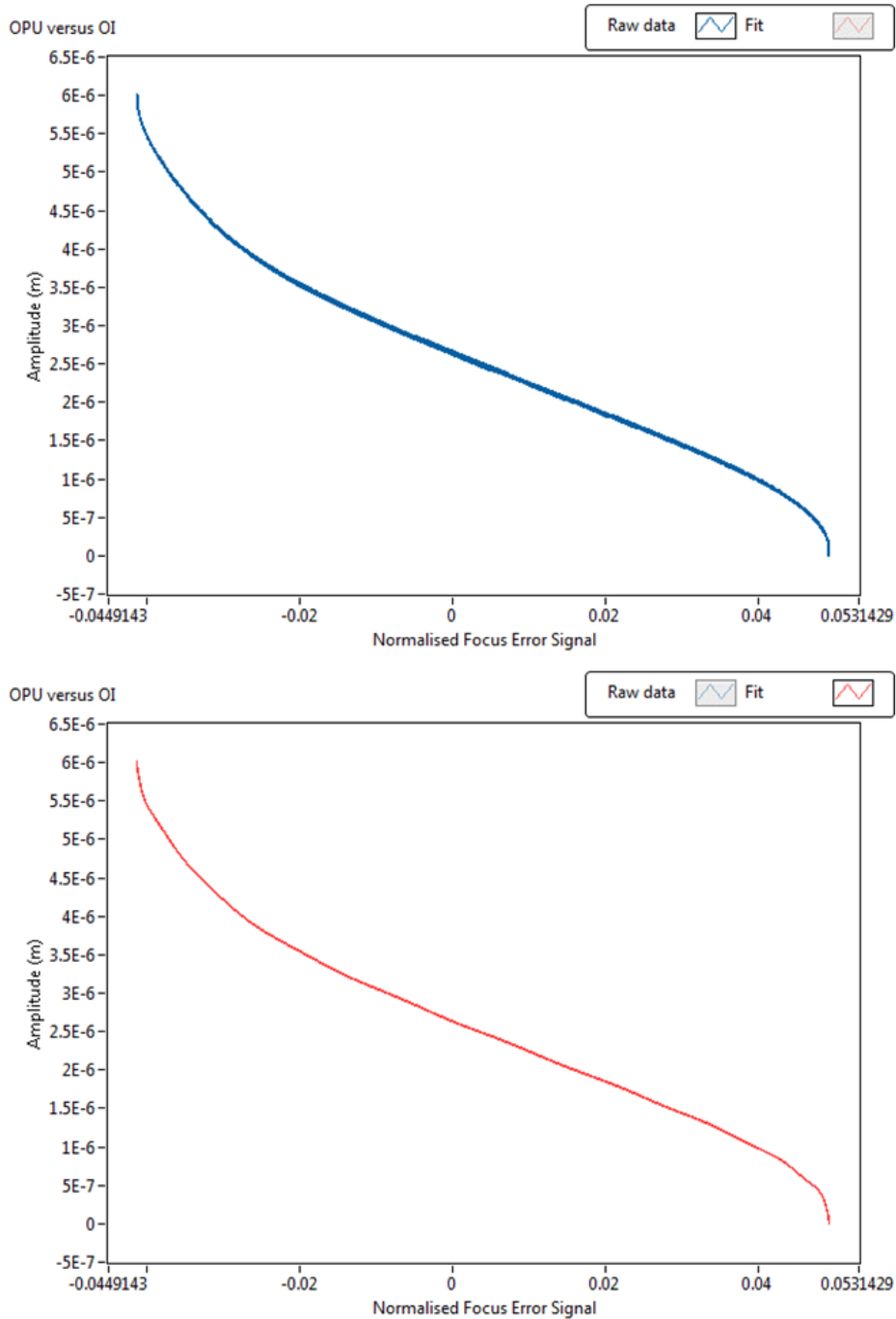
Figure 97: Normalised focus error signal from a Sanyo SF-HD65/850 against Picoscale optical interferometer displacement measurements (blue). A polynomial fit to the data can be used for live calibration of the normalised focus error signal.

Once the FES had been calibrated for both axes, each 3D-printed stage was measured in turn. A photo of the experimental set-up can be seen for each stage in Figure 98.
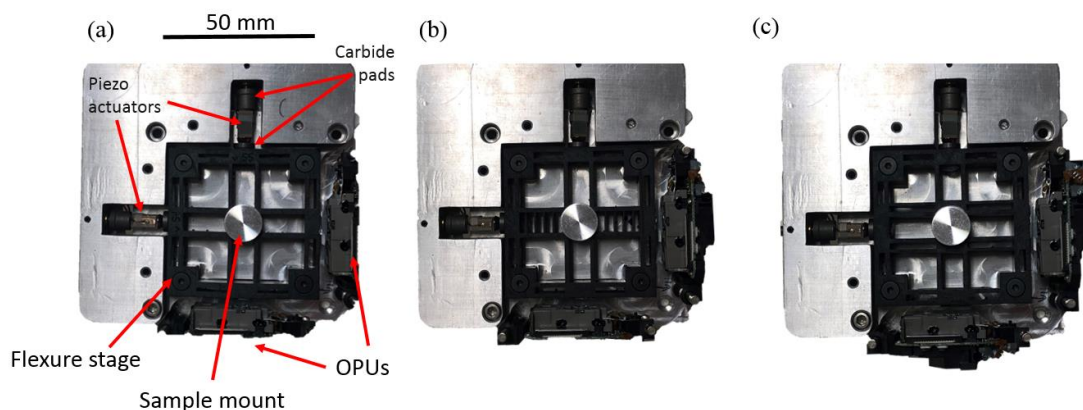
Figure 98: Experimental set-up used to monitor the fast- and slow-scan stage motion of the three stage design variations: (a) asymmetric (with components labelled); (b) cross flexures; and (c) rectangular.

5.4.2.3 One-dimensional evaluation of stage designs with OPUs

Firstly, the OPU-based evaluation platform (Figure 98) was used to evaluate each of the 3D-printed stage designs in turn, using a fast-scan frequency of 1 kHz and slow-scan frequency of 1 Hz (Figure 99), the typical frequencies to use when imaging a sample in HS-AFM. These values are typically used to move the sample in HS-AFM with scan amplitude of between 1-5 µm in order to obtain pixel sizes of ~ 5 x 5 nm (2).

For comparison, and to give further quantification of the stages' performance, the experiment was then repeated using twice the frequency in each axis (Figure 100), equivalent to increasing the frame rate of the instrument from two frames per second to four frames per second. These new drive frequencies are closer to modelled resonant frequencies of the stages and, as such, they exhibit greater amounts of cross axis coupling (i.e. as defined in Figure 71).

From these waveforms, it is possible to derive simplified metrics for the performance of each stage. These are tabulated in Figure 101. We see that the more performant of the two scan rate pairs investigated is that of 1 kHz and 1 Hz, with the rectangular stage (with additional flexures) and a crosstalk ratio (i.e. amplitude of fast-scan motion in the slow-scan axis divided by the amplitude of the slow-scan) of 1.6%. This is much less than for the aluminium stage which was found to have a crosstalk ratio of 3.6%.
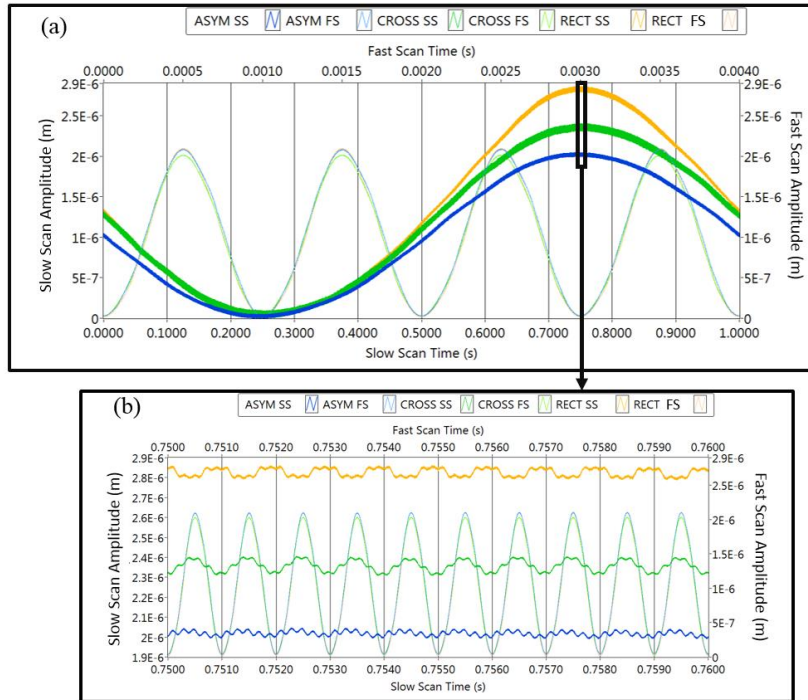
Figure 99: Displacement waveforms, as measured by the OPUs, in the fast (1 kHz) and slow (1 Hz) axes when driven with sinusoidal motion are shown in (a). The cross-axial coupling or crosstalk of the high frequency motion into the low frequency motion is measured using the optical pickup, seen more clearly in the zoom-in (b).
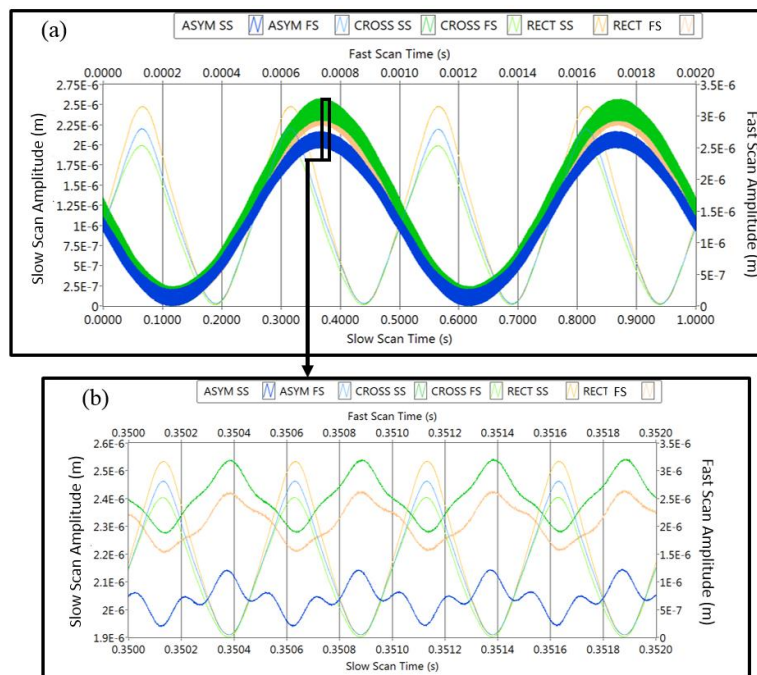
Figure 100: Displacement waveforms, as measured by the OPUs, in the fast (2 kHz) and slow (2 Hz) axes when driven with sinusoidal motion are shown in (a). The cross-axial coupling of the high frequency motion into the low frequency motion is measured using the optical pickup, seen more clearly in the zoom-in (b).

	Asymmetric		Cross flexures		Rectangular	
	1000*/1+ (Hz)	**2000*/2+ (Hz)**	**1000*/1+ (Hz)**	**2000*/2+ (Hz)**	**1000*/1+ (Hz)**	**2000*/2+ (Hz)**
FS Amplitude (m)	2.05E-06*	2.77E-06*	1.98E-06*	2.51E-06*	2.22E-06*	3.12E-06*
SS Amplitude (m)	2.04E-06+	2.17E-06+	2.40E-06+	2.58E-06+	2.35E-06+	2.47E-06+
Crosstalk Amplitude (m)	4.89E-08	2.05E-07	8.83E-08	2.68E-07	3.85E-08	2.21E-07
Crosstalk ratio	0.024	0.094	0.037	0.104	0.016	0.090

Figure 101: Evaluation metrics of the 3D-printed stages used in the OPU-based evaluation platform

By looking at the evaluation metrics table (Figure 101), measured via the calibrated OPUs it was possible to see that the stage with the greatest amplitude to cross-coupling ratio was the rectangular design (Figure 90 (c)).

5.4.2.4 Two-dimensional (xy) distortion map of scan stage with OPU monitoring

Subtle distortions in the measured waveforms at both low-frequency (due to hysteresis) and high-frequency (due to the fast-scan crosstalk) are seen in Figure 102 (b) and Figure 102 (c). To see how this motion leads to imaging error in two dimensions, we can simulate these effects on an idealised dataset such as a checkerboard pattern (Figure 102 (a)). Figure 102 (a) shows how the captured data would be displayed if ideal sinusoidal motion and interpolation of the data was carried out, whereas, Figure 102 (b) (FS trace) and Figure 102 (c) (FS retrace) show representations of the checkerboard (coloured brown and blue) of the true measured stage motion after a sinusoidal interpolation. As such, we see how these distortions contribute in two ways, firstly, by changing the aspect ratio of the unit areas in different parts of the image. In addition, pixels at the edge of the unit areas can be misallocated to neighbouring areas due to the higher frequency excitation in the stage seen in the zoom ins in Figure 102.

5.4.2.5 Three-dimensional performance of plastic stage design for HS-AFM

In order to integrate the 3D-printed stage into a HS-AFM, an existing instrument (67) at the University of Bristol was modified to accept the bespoke footprint of a stage with mounts for an optical pickup. The instrument was then operated in high-speed contact mode AFM using direct displacement measurement of the cantilever (MSNL-C, Bruker) from above, with an OFV-534 Laser Doppler Shift Vibrometer (LDV) and DD-900 displacement decoder card (Polytec GmbH, Germany). A collection of titanium dots, formed by evaporating titanium onto a flat silicon substrate (NIST, USA), was imaged using the system. This sample was chosen due to the combination of surface features, which includes large step heights, texture variation and spacing of features that could be placed within a typical scan amplitude up to 5 µm. The experimental set-up used for this can be seen in Figure 103.

141
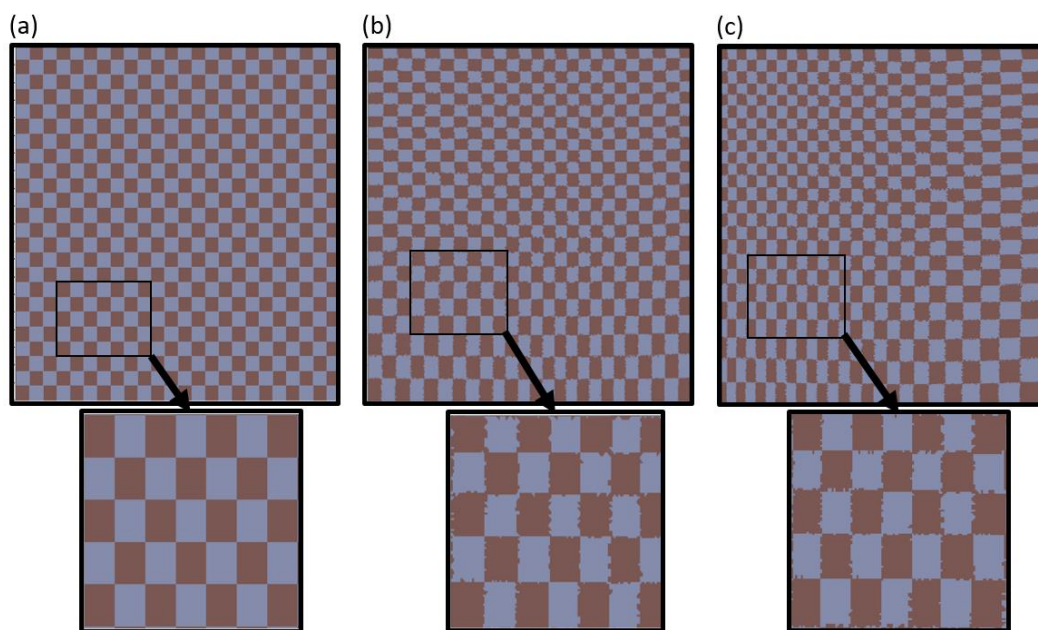
Figure 102: Spatial representation of the rectangular stage distortions using a checkerboard pattern of alternate colour. With perfect sinusoidal motion, each square should correspond to 20 by 20 pixels in a 1000 x 1000 pixel image. (a) A represents ideal checkerboard data, (b) represents distortions during the trace in the fast-scan (1 kHz) direction and (c) represent distortions in the retrace in the fast-scan (1 kHz) direction.
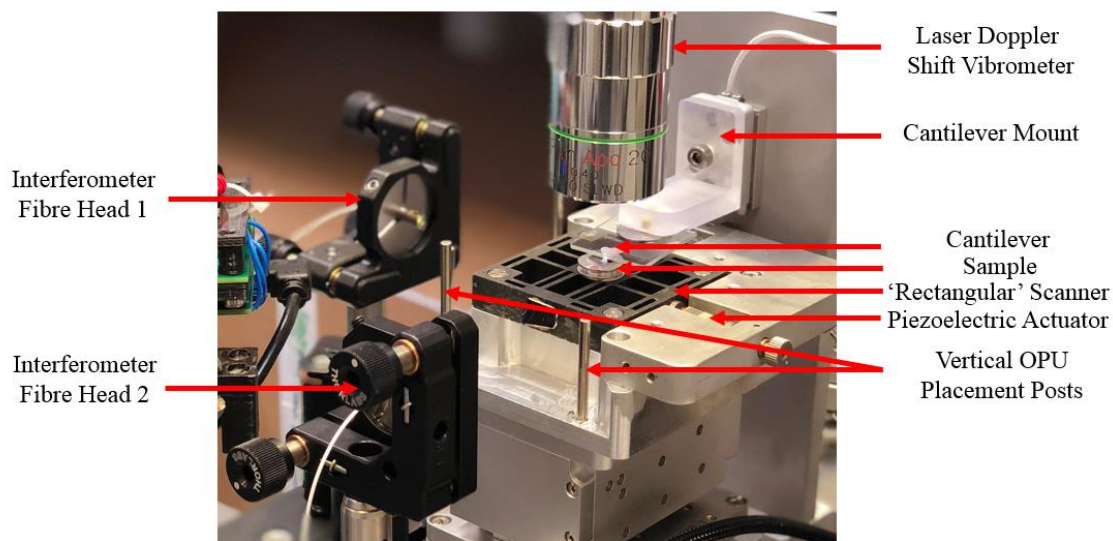
Figure 103: Evaluation of the 'rectangular' plastic stage with the fibre interferometer incident on a HS-AFM.

The real-time HS-AFM imaging results of the stage are displayed in Figure 104. Here, we see the benefits for real-time monitoring of the stage to correct for measured hysteresis in the system. This improvement is demonstrated in Figure 104 by identifying and measuring the minimum distance

between nine equidistant surface features, whilst using three separate ways of constructing the HS-AFM image from the height data. Figure 104 (a) shows the average of height data captured during the FS trace and retrace direction but built assuming ideal sinusoidal motion. The doubling of features highlights the presence of hysteresis between the FS trace and retrace. Figure 104 (b) shows an image constructed using the height data from both the trace and retrace direction but using the true position of the scanner, as measured by the Picoscale C02 fibre interferometer heads. In this image there is no apparent doubling of surface features, showing that the effect of hysteresis in the fast-scan direction has been accounted for.
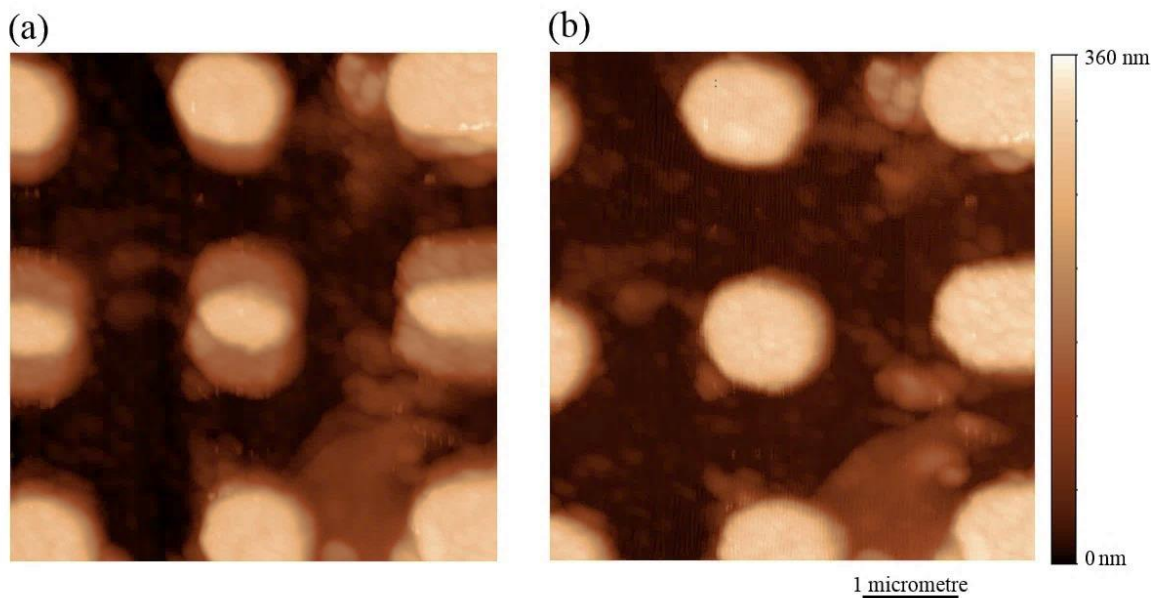
Figure 104: Two AFM images constructed using ideal sinusoidal motion (a) in the fast scan (FS) trace direction and the retrace (FS) direction, and then averaged ('ghosting' visible). (b) AFM image constructed using the fast- and slow-scan motion, as measured by the fibre interferometers.

The visible distortions can be quantified by measuring the edge-to-edge distance of the circular features. Using both the trace and retrace data (Figure 104 (a) and Figure 104 (b)) yielded the mean minimum distance between the nine surface features of 1.09 ± 0.16 µm, whereas for the interferometer-monitored image it is 1.06 ± 0.08 micrometre. The outcome of this demonstrates that real-time scanner monitoring with a fibre interferometer for these scanning conditions decreased the measurement uncertainty by 50%. Further demonstration of the plastic stage's performance at 30 different amplitudes can be seen in the supplementary video (see Digital Appendix folder: Plastic flexure-stage), visibly showing hysteresis occurs at different scan amplitudes on this sample. The effects of this hysteresis are not seen in the corrected data presented alongside.

5.4.2.5 Real-time image linearisation of HS-AFM scanner using OPUs

The initial results for these 3D printed stages showed they could all be operated with appropriate scan amplitudes, drive frequencies and repeatability within typical values used for HS-AFM imaging. From these results, it was decided to next integrate the most performant stage with the least amount of crosstalk (the rectangular design) into an HS-AFM to assess its performance for real-time scanning and contribution to imaging a sample.
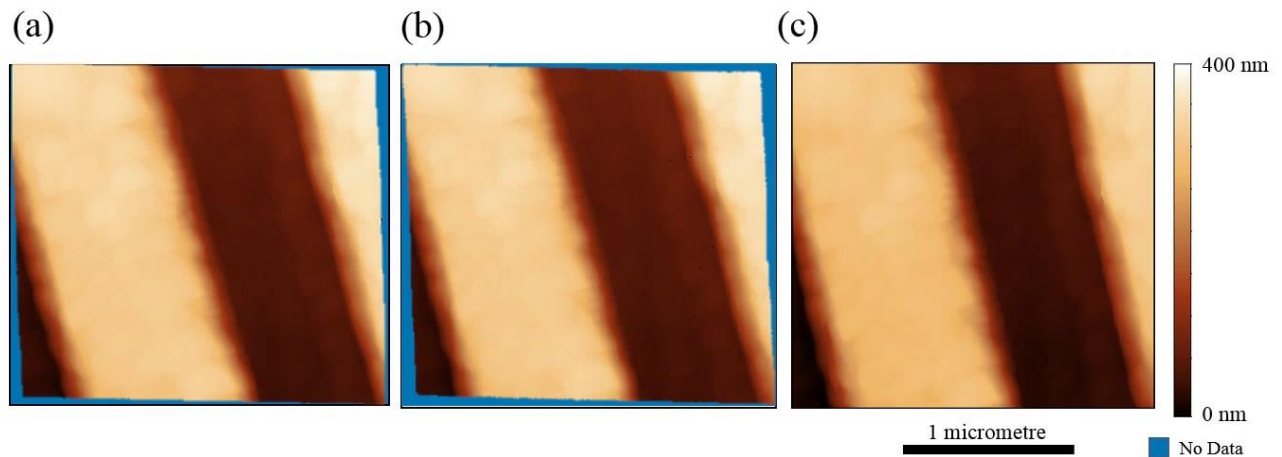
Figure 105: Comparison of HS-AFM images constructed using the monitored scan paths measured by the fibre interferometer (a) and the OPU (b) against assumed idealistic motion in the outgoing (trace) (c) and return (retrace) directions.

Here, we observed that there is less discrepancy between the fast-scan trace and retrace images than seen in Figure 105. We also observe that the corners of the corrected images in both the OPU and fibre interferometer corrected images have angles $\neq 90°$. In addition to Figure 105, we present a snapshot of the X and Y scanner positioning waveform (Figure 106), as measured by the OPU and fibre interferometer, to show in closer details the strong agreement observed in a waveform subsection measured dynamics between the systems.

For this image, the mean total error over one cycle between the fibre interferometer and OPU XY positions was found to be 1.4% (or 30.8 nm) in the fast-scan direction and 1.2% (28.2 nm) in the slow-scan direction when measured over one second of data. The path measured by the fibre interferometer shows that the stage dynamics overall deviate from ideal sinusoidal motion on average per cycle by 1.8% (or 39.6 nm) in the fast-scan direction and 2.0% (or 47 nm) in the slow scan direction. Therefore, the results show that the implementation of the OPU sensors to monitor the scanners resulted in a 9 nm per pixel (22.3%) reduction in percentage error in the fast-scan and a 19 nm per pixel (40%) reduction in percentage error in the slow-scan when compared to image formation using the assumption of ideal sinusoidal motion.

144
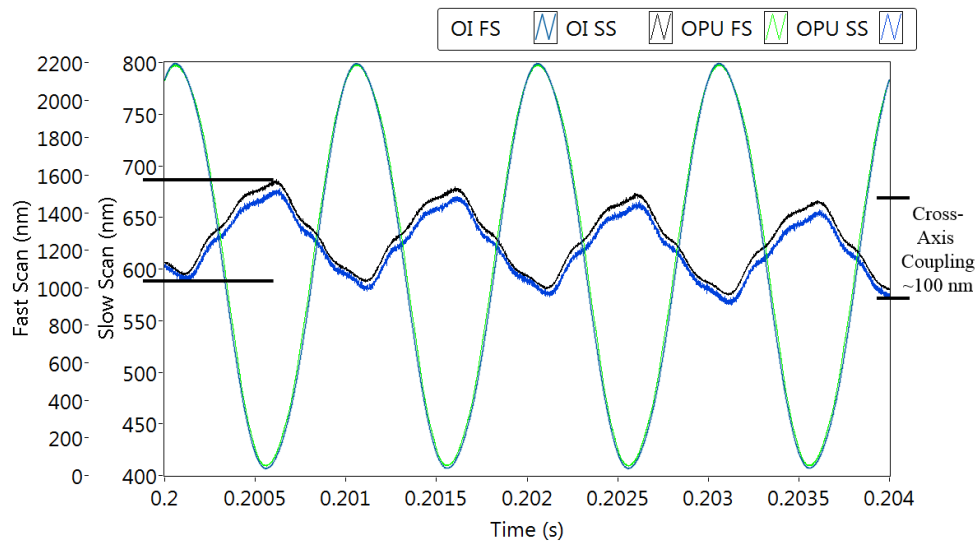
Figure 106: Snapshot of the displacement waveforms of the stage as measured by the fibre interferometer and the OPU in the fast-scan (FS) and the slow-scan (SS) axes.

5.4.3 Voice coil motor evaluation

To investigate the stability of the voice coil motors for the Sanyo SF-HD65/850 during operation the Picoscale fibre head interferometer was used to monitor the stability of the voice coil to maintain a fixed position, firstly whilst powered, then whilst powered with a damping medium (e.g. MS3 grease, Castrol, UK) applied to the actuator. Subsequently, the scanning performance of the voice coil motors was investigated. Due to the limited communication speeds of the Arduino Nano (i.e. via I2C), only ~ 3000 data points per second could be sent to the DAC driving the voice coils through a current amplifier. Therefore, an initial study using LTspice was carried out to assess the effects of driving the voice coils with a sparsely-populated (due to low temporal resolution of Arduino output) sine wave at high rates. Following this, a measurement of the true voice motion was performed using a Polytec laser Doppler vibrometer for a range of frequencies between 100 Hz and 200 Hz to evaluate the scanning performance of the objective lens capabilities for the high-speed scan axis for a number of applications, including for high-speed optical profilometry outlined in Chapter 4, Section 4.3.

5.4.3.1 Holding a fixed position

The primary investigation that was carried out was to assess the stability of the voice coil to remain in a fixed location when powered. It had been previously reported (151) that the implementation of a dampening medium around the voice coil motors can reduce unwanted electromechanical perturbations due to a number of environmental and electronic conditions. Therefore, a secondary evaluation of the stability was then carried out with the addition of a dampening medium lightly applied in between the voice coils and permanent magnets. A silicon wafer subsection (0.0262 g) was attached

145

to the OPU object lens and measured by the detection head (C01, Picoscale). The results are displayed in Figure 107.

Temperature: 17.2°C
Humidity: 46.1%
Pressure: 97750 Pa
σ: 24.5 nm

Temperature: 17.6°C
Humidity: 48.8%
Pressure: 97712 Pa
σ: 3.22 nm
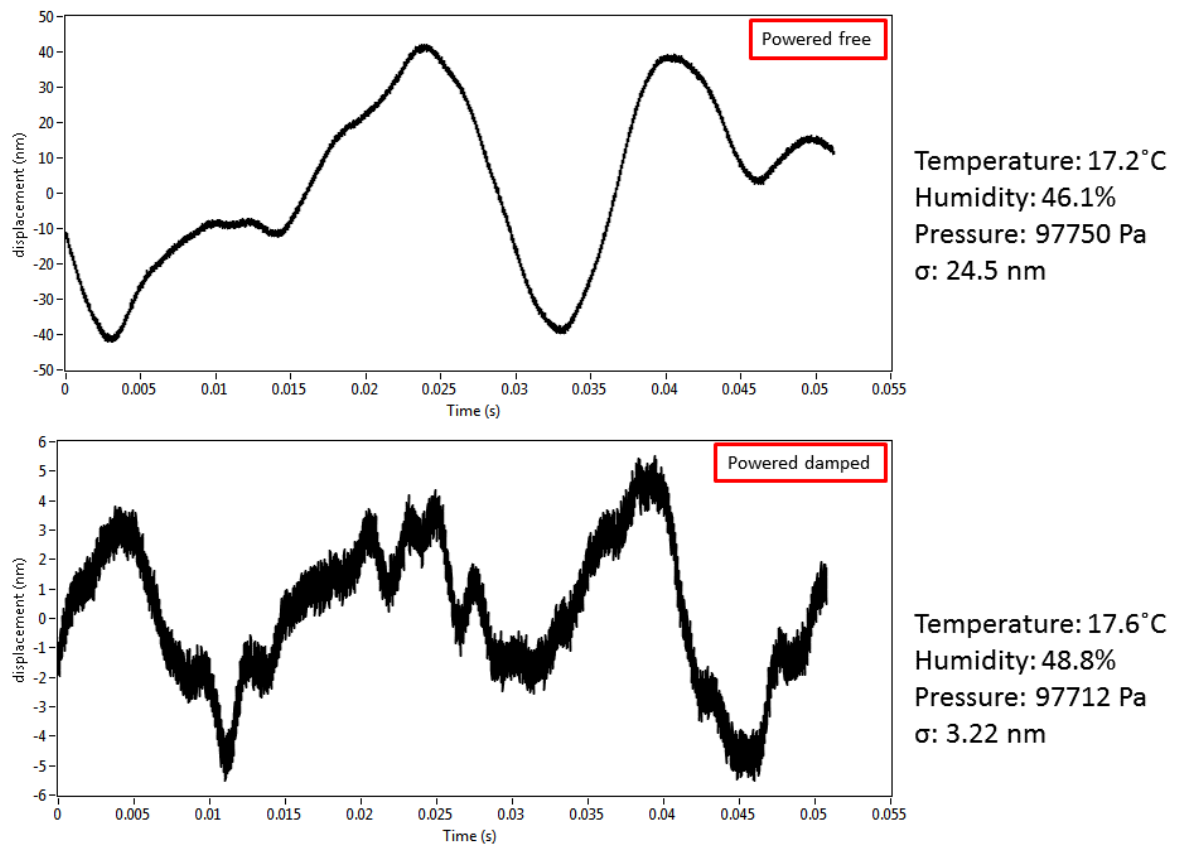
Figure 107: Displacement of the focussing actuator in a Sanyo HD-65/850 with and without a dampening medium collected at 1.25 MHz. The ambient conditions and the standard deviation are presented next to the graph.

Over a two second period the stability of the measurements of the free voice coil had a maximum standard deviation of 24.5 nm. The dampened voice coil had a standard deviation of 3.22 nm, showing a >7.5 times reduction in unwanted motion due to MS3 grease (Castrol, UK) being lightly applied to the lens housing.

5.4.3.2 Oscillating voice coils LTspice simulation

In this section, we look at a modified version of the previously-discussed control electronics for the OPU voice coils. Scan rates on the orders of 100s-1000 Hz were desired for real-time surface imaging.

A target of 200 line per second over a range of >25 µm was chosen to be suitable for the type of applications this actuator would be used for (such as optical profilometry). To understand how this can be achieved, we have to look further at the command electronics. The I2C protocol used to

communicate to the digital-to-analogue converter from the Arduino Nano board has a standard transfer mode of 100 Kbits per second. Therefore, the maximum number of bits to define each cycle of the 200 Hertz waveform is 500 bits, if a one-bit command is used to define turning points, such as in a Pulse waveform. However, for each point of the waveform communicated via I2C, the Arduino Nano must send the address (8-bit), command (8-bit) and desired voltage (16-bit), making the total package size 32 bits. Therefore, the maximum expected number of samples for a 200 Hertz waveform is 15.

To examine the effects of using sparsely sampled (or stepped) input waveforms with the amplifying electronics a generated waveform was passed through the LTspice simulation. The simulation revealed that the output analogue waveform may be susceptible to higher frequency oscillations due to the steps in the waveform. To reduce these effects, a low pass filter was applied at the DAC output and the results from this can be seen in Figure 108, where the cut-off frequency is set by the following:

$$RC = \frac{1}{2\pi f_c} \tag{25}$$

where the resistor (R) was 1 kΩ and capacitor (C) was 100 nF, making the cut-off frequency (f_c) of the low pass filter 1.6 kHz.
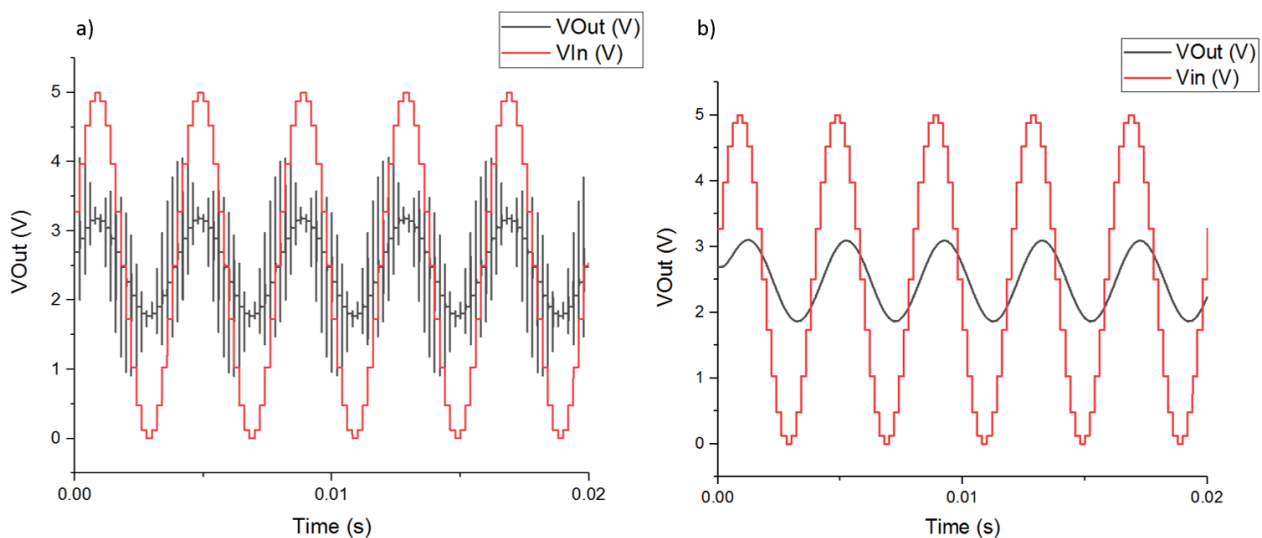
Figure 108: LTspice simulations of an input low resolution waveform and resultant output with (a) and without (b) a low pass filter, where VIn is sampled at the output of the DAC and VOut is sampled at the output of the op-amp.

5.4.3.3 Oscillating OPU voice coils evaluation with laser doppler vibrometer

The optical pickup voice coils and control electronics were then examined experimentally to ascertain if their scanning performance was suitable for high-speed imaging. To achieve high-speed scanning with the voice coil motors, the processing and communication rate of the Arduino approaches

its bandwidth limit, as discussed above. Furthermore, due to the poor clock stability onboard the Arduino the code had to be modified to act upon interrupts from an external clock source, provided by an NI USB-6366 DAQ output pulse waveform to avoid significant drift (several cycles per second), between drive and sensing electronics. The optical camera in the LDV without an objective lens was used to locate the laser spot onto the edge of the optical pickup objective lens casing (as seen in Figure 109 (b)) and the decoder card (DD-900, Polytec, Germany) was set to 10 µm.V⁻¹.
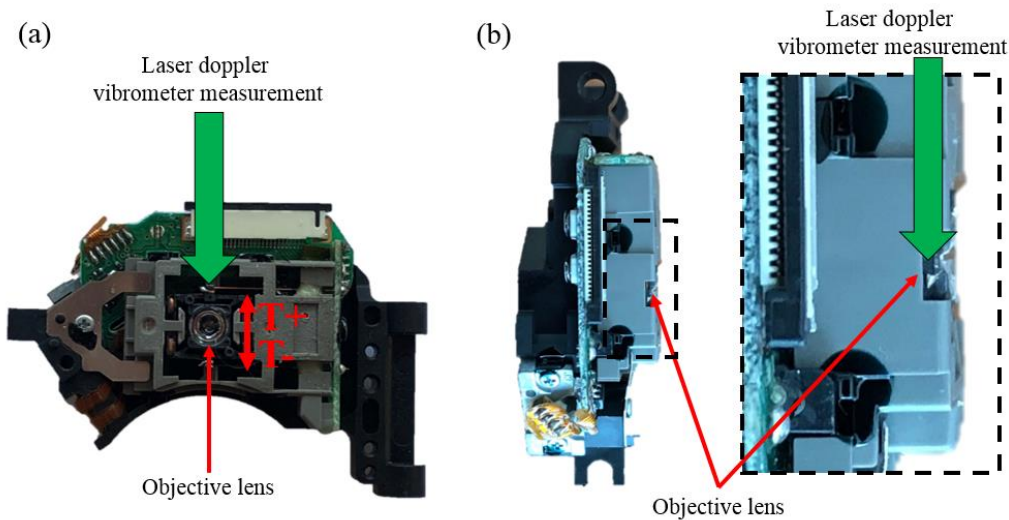
Figure 109: (a) Front view of Sanyo SF-HD65/850 with the tracking axis (T+ and T-), objective lens and laser Doppler measurement point labelled. (b) Top view of a Sanyo SF-HD65/850 showing the optical access to the objective lens that is used to monitor the motion of the tracking actuator.

Firstly, an inverse power relationship of voice coil amplitude with frequency was found for a fixed voltage (0.3 V pk-pk) output from the DAC, where the range of frequencies examined were in the range 100-200 Hz (Figure 110).

Looking in more detail at the measured displacement for the highest frequency (i.e. 200 Hertz) scanning amplitude (Figure 111 (a)), we see a smooth waveform without any visibly-apparent drift or scanning artefacts. By then looking at this positioning waveform over a 10 period, consisting of 2000 repeat cycles, it is possible to see that the measured scan path of the voice coils deviates about the mean measured scan path by as little as <0.1% (Figure 111 (b)), corresponding to a maximum displacement deviation of ±5.7 nm from the 4.73 µm scan amplitude.
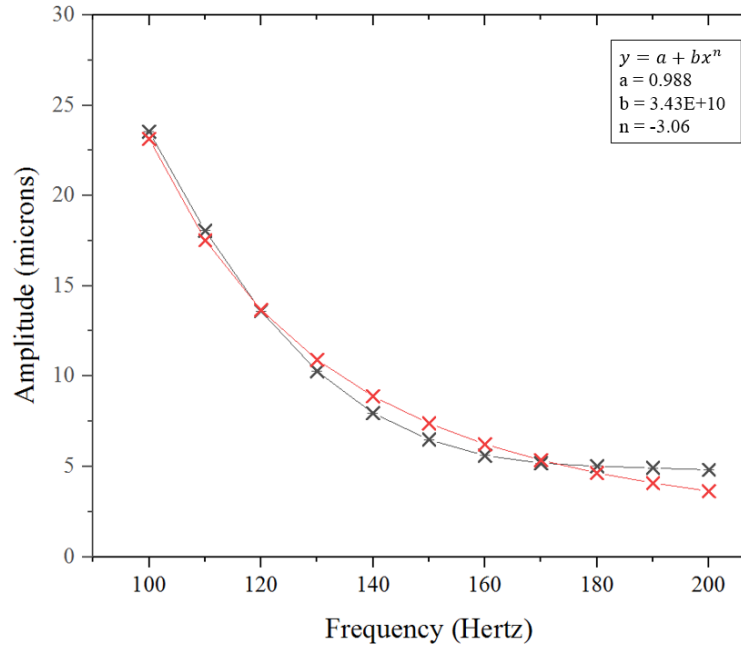
Figure 110: Frequency versus amplitude at a fixed voltage output (0.3 V pk-pk) for OPU voice coils. Measured displacement (black) and inverse power fit (red) with a χ^2 found to be 0.999.
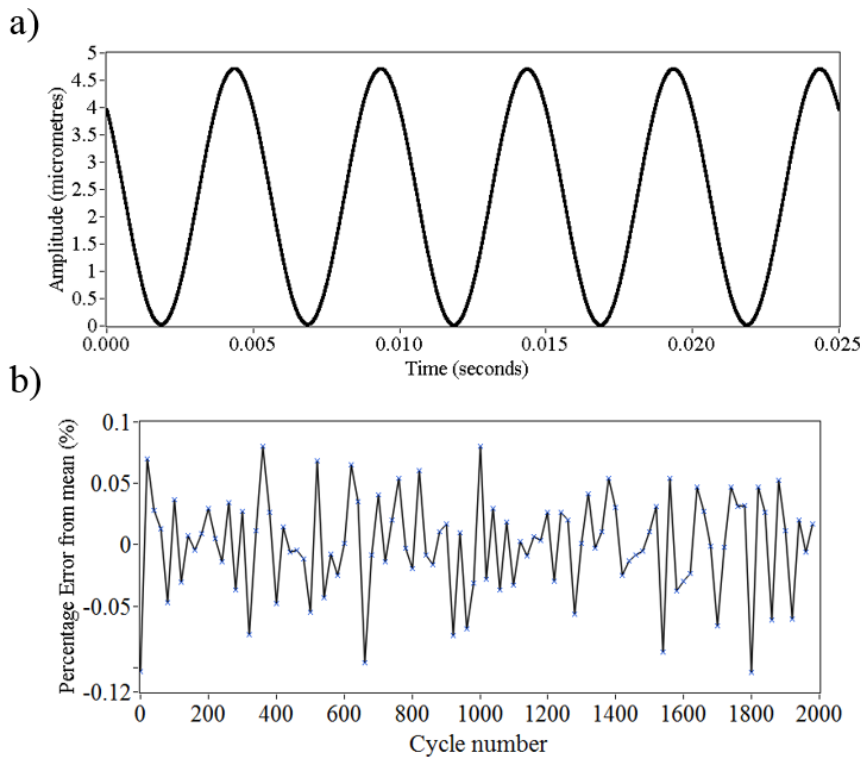
Figure 111: a) Waveform graph showing a snippet of a section of the measured displacement of the OPU tracking voice coil which was repeatably oscillated 2000 times and b) the repeatability as a percentage of the amplitude, 4.73 μm, for a scan frequency of 200 Hz.

Whilst a demonstration of highly-repeatable high-speed scanning with the tracking voice coil motor has been presented, the amplitude of this scan is much smaller than is well-suited for one of the proposed applications: high-speed optical profilometry. Therefore, a second study was undertaken to fix the scanning frequency, this time incrementally increasing the peak-to-peak voltage output of the DAC from 0.3 V to 1.2 V and with measurement of the resultant change in scan amplitude of the tracking axis voice coil motor. The results from this experiment, as presented in Figure 112, show a linear relationship, as predicted by the theory outlined in Section 5.3.2.

Equation	y = a + b*x
Intercept (a)	-0.735 ± 0.137
Slope (b)	46.2 ± 0.366
Pearson's r	0.99981
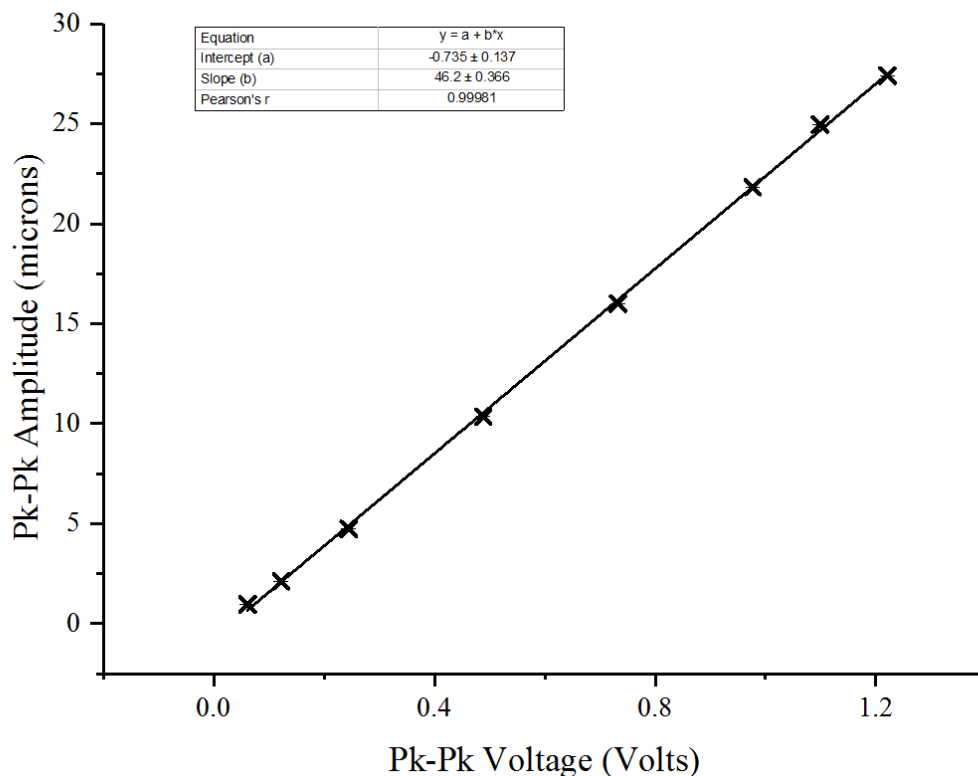
Figure 112: Graph showing the pk-pk voltage versus amplitude for OPU voice actuation at a frequency of 200 Hz.

5.4.3.4 Conclusion from the voice coil motor results

Results from using the Arduino-based custom electronics (detailed in Section 5.3.2.2) show that the voice coils benefit from using a light dampening grease (MS3, Castrol, UK) whilst powered and held at a fixed location, reducing the position noise by >7.5 times. It was also shown that the Arduino electronics can be triggered by an external clock to produce scanning in the frequency range 100-200 Hertz. It was shown that by fixing the peak-to-peak amplitude of the DAC output to the current driver and increasing the frequency resulted in an inverse power law relationship of displacement amplitude with frequency. It was then shown that a linear relationship between the peak-to-peak

amplitude of the DAC output and the displacement amplitude was found at a fixed frequency. Combining these two relationships, it was possible to achieve a peak-to-peak scan amplitude of 28 µm at a rate of 200 Hertz, further showing this scanning performance to be highly suitable for the application of high-speed optical profilometry as reported in Chapter 4.

5.4.4 Tuning fork actuator

In this section, a tuning fork with a resonant frequency of 100 kHz is evaluated for the function of providing an ultra-high-speed scan axis capable of rates 50-100 times greater than the fast-scan axis of the piezoelectric actuated dual-axis kinematic flexure stage outlined in Section 5.1. The purpose for evaluating this prototype scanner is to propose a route to make use of the higher measurement bandwidth in the optical pickup unit of up to several 100 mega-samples per second for HS-AFM. Historically, notable step changes in AFM imaging speed have been realised by L. Picco et. al. (19) by using quartz tuning fork actuators. In this case, detection mechanisms with lower achievable bandwidths than optical pickups were used.

To construct the prototype OPU-tuning-fork-based ultra-high-speed XYZ scanner, the quartz tuning fork was fixed onto the dual-axis voice coil motors suspending the objective lens of the Sanyo SF-HD65/850 evaluated in a previous section (Section 5.2), In this configuration, the scanner could be capable of line scan rates of ~100,000 lines per second in the fast-scan direction and 200 lines per second in the slow-scan direction.

5.4.4.1 Tuning fork actuator: evaluation with laser doppler vibrometer

To measure the displacement of the tuning fork, the same configuration was used as for analysing the voice coil motor in Section 5.4.3.3 using the LDV but with the decoder card (DD-900, Polytec, Germany) set to 1 µm.V^{-1}. In this instance, the optical image was used to place the laser spot from the side (i.e. in the direction of oscillation) and on a reflective part of the tuning fork tip 0.5 mm from the end (Figure 113 (b)) to measure the amplitude of motion.

The tuning fork was driven with an analogue function generator with an increment resolution of (0.001 Hz). A manual frequency sweep was conducted by hand until a maximum scan amplitude was achieved. This was found to be at the frequency of 99.65 ± 0.0005 kHz. The measured displacement waveform at this frequency can be in Figure 114 (a), with a zoom in of this waveform in Figure 114 (b) and detailed statistics of 10,000 cycles found in Figure 114 (c). The maximum peak-to-peak scan amplitude of this tuning fork driven at a frequency of 99.650 ± 0.005 Hz was found to be 7.24 ± 0.03 µm whilst driven by a 10 V peak-to-peak sine wave.
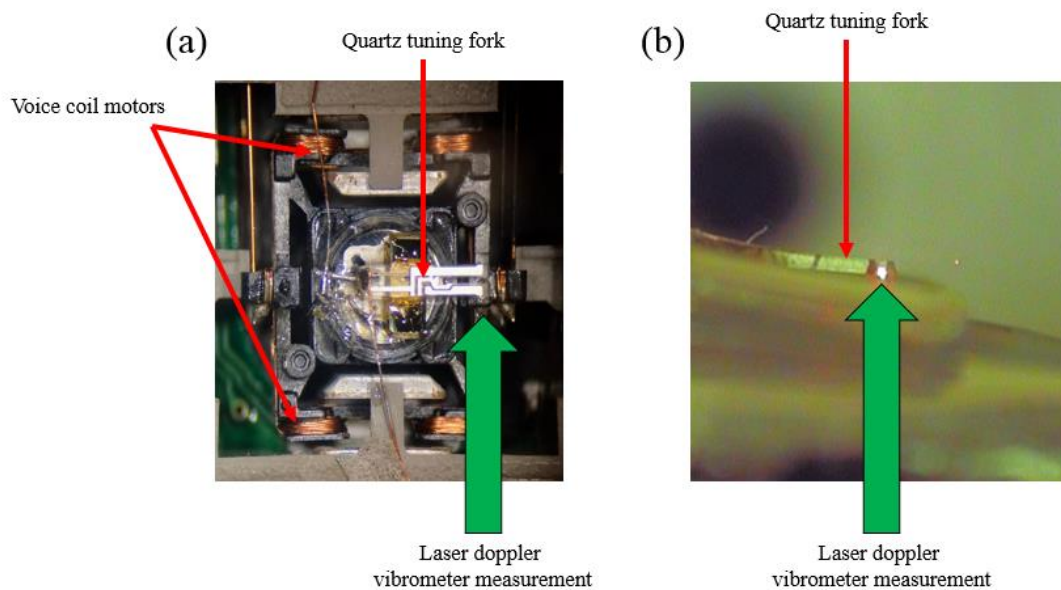
Figure 113: (a) Experimental set-up used for monitoring the oscillations of a quartz tuning fork using a laser doppler vibrometer. (b) Optical view through the laser doppler vibrometer.
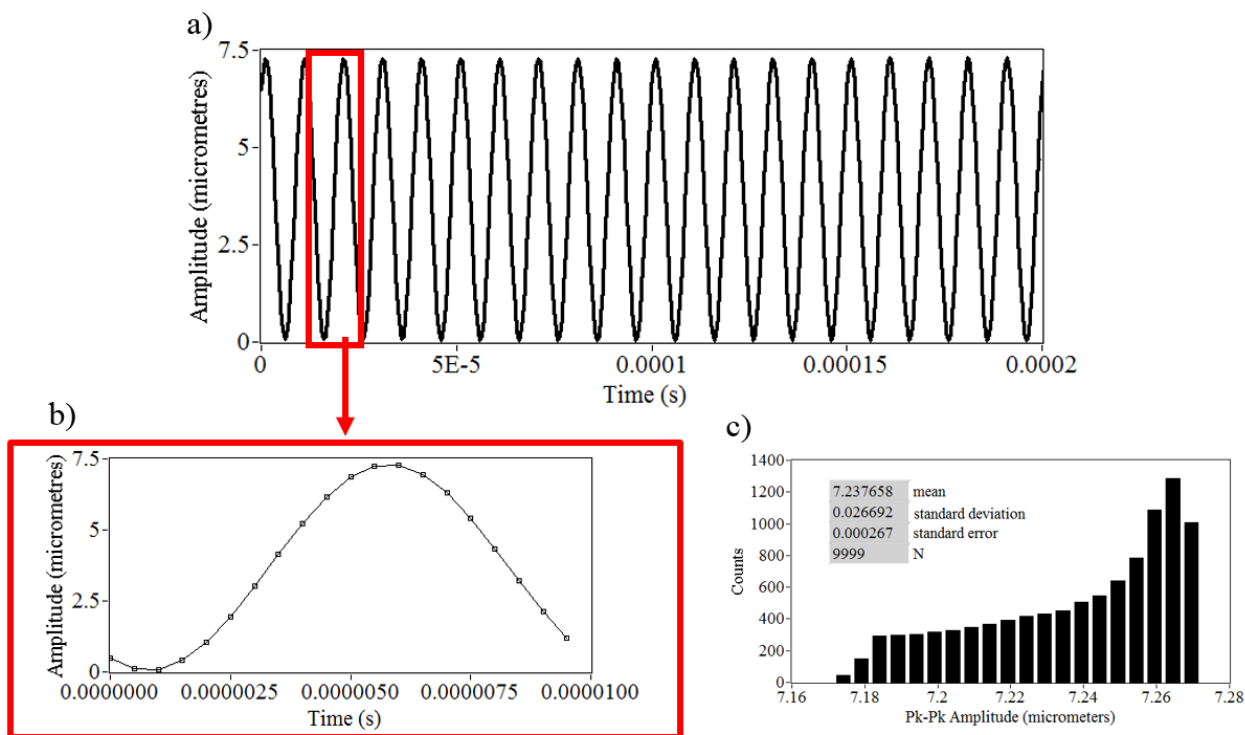
Figure 114: Evaluation of a quartz tuning fork for ultra-high-speed scanning whilst placed on a dual-axis voice coil motor from a Sanyo SF-HD65/850 optical pickup.

5.4.4.2 Tuning fork actuator: conclusions

The evaluation of the quartz tuning fork mounted to the Sanyo SF-HD65/850 optical pickup objective lens found it to be a performant ultra-fast-scan actuator within a prototype OPU-tuning-fork-based ultra-high-speed XYZ scanner. The stage achieved a fast-scan linear rate of 1.45 m.s^{-1} and from the results in Section 5.2.3 (i.e. 28 µm at 200 Hertz), a slow-scan linear rate 5.60 mm.s^{-1} is possible in the slow-scan axis. This proposed three-axis actuator gives tremendous potential to future developments of the research into HS-AFM carried out in Chapter 3, looking to make best use of the measurement bandwidth in both current and theoretically possible OPU-based AFM detection heads.

5.4.5 OPU-based lever reduction displacement sled

Inbuilt into most OPUs are two axes of motion for tracking and focusing via the voice coil surrounding the lens. However, for alignment of an object (such as a cantilever chip or sample) into the focus of the laser a third axis of motion is needed, perpendicular to the tracking actuator. Due to the 3 mm working distance of the objective lens, translating components in front of the OPU required a thin (~1 mm thick) translation armature. In addition, due to the sensitivity of the voice coil motors to electromagnetic interference, motors and magnets could not come into close proximity to the objective lens (e.g. <10 mm).

For this new axis of motion, a lever reduction displacement sled was constructed, as shown previously in Figure 83. The linear actuator within the cantilever sled consisted of a 50:1 micro-metal- geared motor, monitored via two optical encoders and a toothed flywheel on the rear shaft, with a fine pitch (pitch: 250 µm per revolution) Thorlabs screw (F3SS25) attached to the front drive shaft. A threaded bushing (F3SSN1P, Thorlabs, USA), with the corresponding pitch to the screw, was fixed inside a brass block, which had two guide rails passing through the block. The guide rails were also attached to the frame that was mounted to the front of the OPU.

5.4.5.1 Lever reduction displacement sled: method

The intention of the evaluation carried out in this subsection was to validate the optical encoders that monitor the back shaft of the geared motor against a calibrated displacement sensor, the LDV. The LDV was positioned on the side of the linear translation sled using the optical camera built into the instrument, without the use of a magnifying objective lens, to position the laser spot on a face perpendicular to the direction of travel. The DD-900 decoder card was set to 100 µm.V^{-1}.

The 50:1 geared motor was powered with a TB6612 1.2A DC motor driver (Adafruit, US), whilst the optical encoders and toothed wheel gave digital high/low events (with voltage 1-1.2V), which were captured by an Arduino ADC to inform the Arduino Nano of the angular speed of the motor. An Arduino sketch and LabVIEW VI (both found on the external media storage of this thesis) were written to control the motion of this motor. A basic protocol of motion control saw the LabVIEW VI instruct

the Arduino Nano, via serial communication, to drive the motor driver for some number of toothed wheel steps. The Arduino Nano was able to count via the sensor data from the onboard ADC that were connected to the optical encoders. The Arduino Nano could then instruct the motor driver to stop driving the motor once this number of steps counted by the Arduino had been reached.

Figure 115 shows a photograph of the measurement schema used to evaluate the determination of the motion of the brass block (labelled with the large vertical arrow) via the optical encoders by simultaneously monitoring the motion with the LDV. For the purposes of this evaluation, the optical encoder output was simultaneously digitised alongside the LDV signal on a NI USB-DAQ 6636 to ensure that there was no clock offset between the displacement measured by the LDV and the optical encoder events.
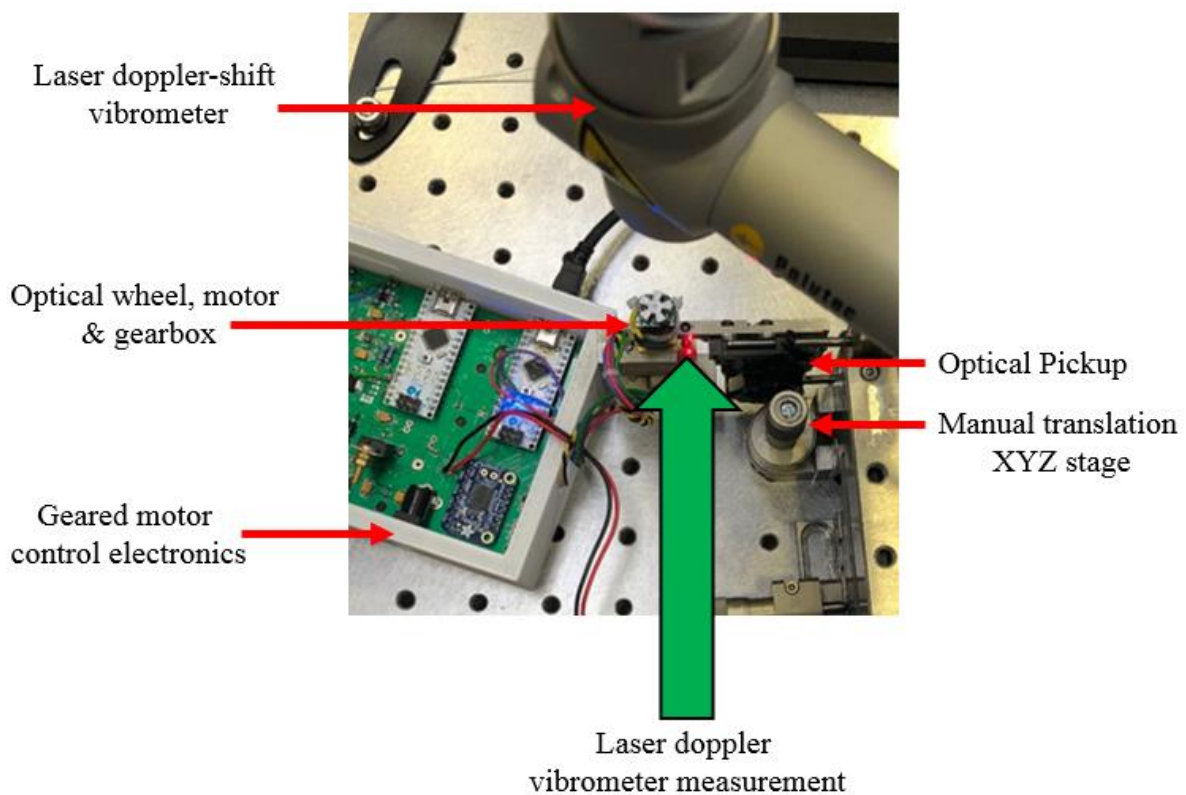
Figure 115: Evaluation of the geared motor and optical encoders for linear actuation in the cantilever sled.

5.4.5.2 Lever reduction displacement sled: evaluation

Firstly, the LabVIEW VI instructed the Arduino to move the geared motor until the Arduino registered one optical wheel event. This was repeated 15 times in the same direction (Figure 116 (a)) with a 200 ms pause inbetween each step. Looking at the outputs from the encoder (Figure 116 (b)), it can be seen that these 15 steps in fact resulted in 33 encoder events. By looking at Figure 116 (a), we see these extra events occur due to the true motion of the motor (as measured by the LDV) and occur due to the momentum of the moving motor taking some time to dissipate and slow down. As a

154

consequence of these 33 steps we see the linear sled has been displaced by 35 ± 0.5 µm showing us the one step of the linear sled is equivalent to 1.07 ± 0.535 µm.
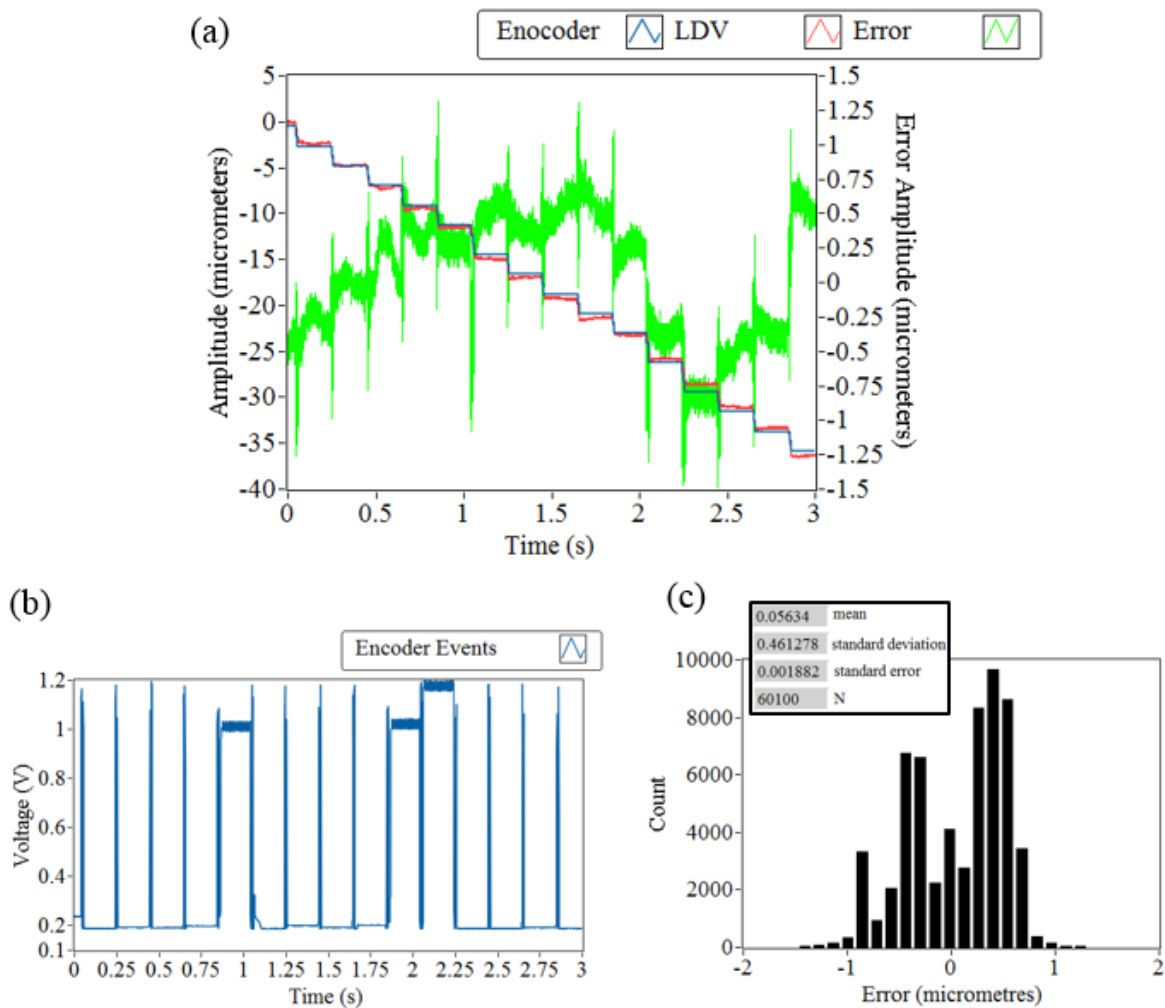
Figure 116: (a) Position of a linear sled that integrates a geared motor and a toothed flywheel monitored by optical encoders and comparing that determined by the encoders against a calibrated laser doppler vibrometer, where the error between them is plotted in green. The graph in (b) shows the digital pulse from the optical encoders in the system. (c) Detailed statistics of the error in (a) plotted in green.

To evaluate the motion of the geared-motor-based linear actuator in the cantilever sled, the system was then monitored whilst conducting bi-directional motion. The LabVIEW instructed the Arduino to move 50 steps forwards and then backwards, with a 500 ms dwell time between commands. A total of 673 encoder events were measured for nine repeats of the motion which was measured to be 75 ± 1 µm, resulting in one step in the linear sled being equal to 1.00 ± 0.5 µm, agreeing with the previous study.

Figure 117 (a) shows a graph of the position of the linear sled, as calculated by the optical encoders, compared with the LDV measurements of its actual position. Closer inspection of the

forwards and backward motion (Figure 117 (b) and Figure 117 (c)) showed than a linear velocity of 500 µm.s^{-1} was achieved. Combining these results with lever equation (Equation 24, p.125) the optical encoders can be used to determine the position of the linear sled and therefore the cantilever chip.
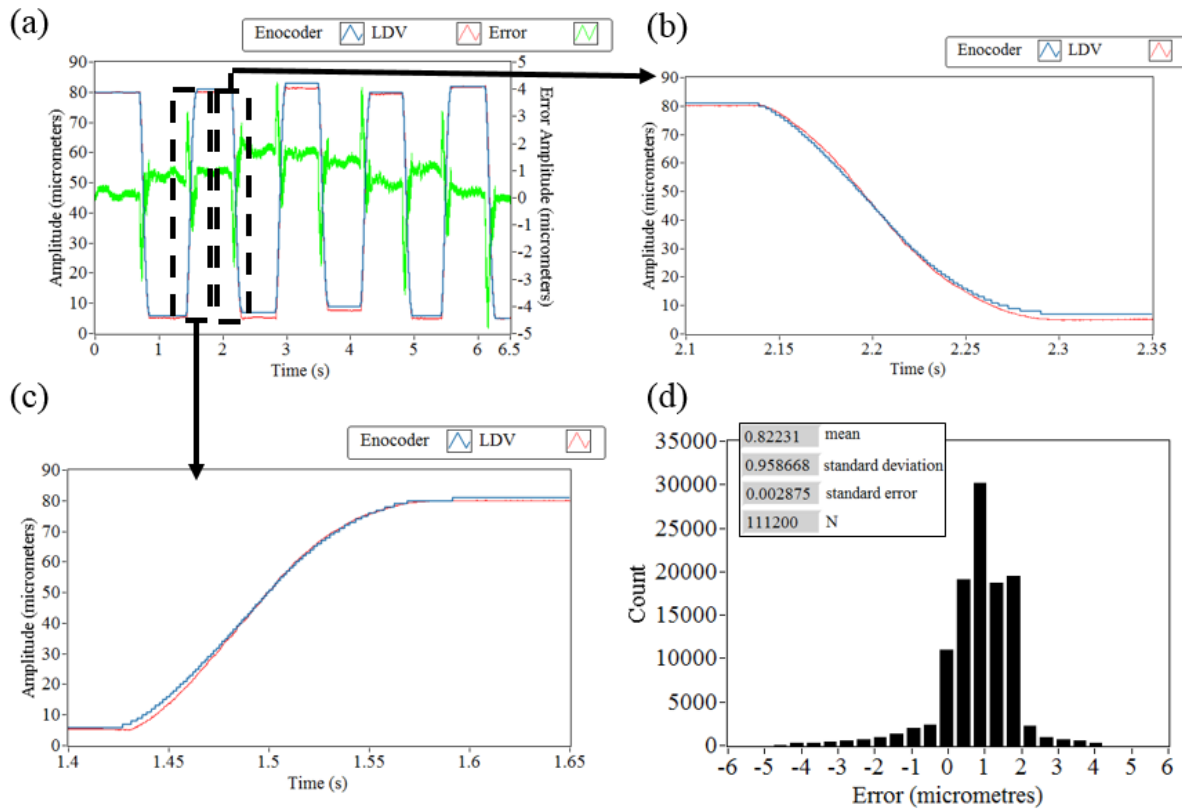
Figure 117: (a) Position of a linear sled, which integrates a geared motor, as determined by a toothed wheel monitored by optical encoders plotted by the position determined by a laser doppler shift vibrometer, where the error between them is plotted in green. (b) Closer preview of the returning motion, and (c) closer preview of the outgoing motion. (d) Detailed statistics of the error in (a) plotted in green.

5.4.5.3 Lever reduction displacement sled: discussion

Here, we see results from the optical encoders on the geared-motor-based linear sled to be in good agreement with the true motion as measured by the LDV, that is 1.0 ± 0.5 µm per step. Furthermore, if we compare this experimental result to what we would expect from the geared motor and optical wheel with the following configuration: a 5 toothed wheel, attached to the back shaft of a 50:1 geared motor, with a 250 µm per revolution fine pitch screw thread attached to the front drive shaft, as for 1 micrometre of linear travel would be expected per fifth of a rotation of the toothed wheel. Therefore, the experimental result is in full agreement with the expected results. As such, it has been

determined that the optical encoders are sufficiently accurate to be relied upon as a measure of the displacement of the linear stage within the geared motor-based cantilever sled.

5.5 Conclusions

In this chapter, an overview of the key actuation types, scan paths and external optical sensors has been discussed. A summary of the key motivation and role that nanopositioning plays in the enabling and ongoing development of HS-AFM was then outlined. Following this, the theory of four key actuator types used within the custom configurations evaluated in this chapter were described. Subsequently, the three optical sensors critical to the experimental work in the thesis were described and their measurement characteristic presented in simplified tables for comparison. Experiment work undertaken to evaluated each bespoke actuator configuration with external optical displacement sensors to validate their performance for their intended application in surface microscopy.

A highlight of this chapter has been the creation of a low-cost evaluation platform, using calibrated optical pickups to measure high-speed parallel kinematic flexure stages, has been shown to be suitable for developing 3D-printed nanoscale scanners for HS-AFM. The set-up was used to identify the most performant of three 3D-printed scanners. The suitability of the selected plastic scanner for HS-AFM was then evaluated by monitoring it in real-time using a fibre interferometer for generating high resolution topographical images in a bespoke HS-AFM. Results then obtained using a calibrated OPU-based sensing system, with an EDM aluminium stage, showed implementing OPUs in place of fibre interferometers could reduce HS-AFM spatial imaging error by up to 40%. These results both demonstrate the benefit of new additive manufacturing methods for the development of nanoscale scanners and implementation of OPUs for real-time XY monitoring. These outputs give exciting opportunities specifically for small batch, disposable or bespoke applications in AFM that might require atypical stage shapes or other custom requirements, such as embedded environmental cells.

The results, from using OPU sensors on the fast and slow scan axes also give scope for future work to implement higher-rate position control and scan path optimisation algorithms within the OPU-based HS-AFM outlined in Chapter 3. The measured prevalence of the inherent distortions (e.g. hysteresis and crosstalk) in the motion of the scanners covered in this work, further to previous work (86), highlight the requirement for high-speed and real-time monitoring of scanner positions to reduce spatial imaging error in HS-AFM. The results from the calibrated OPUs for scan stage monitoring show how they can be embedded into novel and low-cost evaluation platforms to assist in iterative HS-AFM scanner design using high-detailed 3D-printing.

Following this, a study into the scanning performance of the voice actuators with custom-built Arduino Nano control electronics was carried out. It was determined that the tracking axis voice coil present in the optical pickup could be used for scanning at rates of 200 Hz and with amplitudes of 28 µm. At this scan rate and amplitude, it was found that the voice coils showed a high level of

repeatability, with 2000 repeat cycles no more than a mean error of ±0.12% of the 4.73 µm scan amplitude (equivalent to ± 5.7 nm). The performance of the Arduino control electronics and resultant voice scanning showed it to be suitable for high-speed scanning, enabling techniques such as real-time optical profilometry, as outlined in Chapter 4.

For scanning at much high rates (i.e. 10s of kHz) than reported with the kinematic parallel flexure stage (i.e. 1-2 kHz), a prototype stage was built to show a custom configuration of an optical pickup combined with a tuning fork capable of providing a low cost three-axis ultra-high-speed scanner that could enable the scanning required for next generation of HS-AFM. Having previously shown the capability of the tracking actuator voice for scanning, the tuning fork was examined in a similar fashion. The tuning fork was shown to be capable of oscillating at a frequency of 99.65 kHz, with a maximum pk-pk oscillation amplitude of 7.24 ± 0.03 µm. Combined with the results from evaluating the tracking voice coil motor, the prototype stage shows it has the line scan rates and amplitudes to make use of the optical pickup heads capable of sensing up to 100s of MHz, such as those found in Blu-ray or HD-DVD.

Finally, the linear performance of a bespoke cantilever positioners for AFM that used an optical encoder micro-geared-motor was evaluated against a LDV. Here, the cantilever positioner was fastened to the front of the optical pickup and provided a translation axis perpendicular to the optical pickup tracking voice coil motor such that the cantilever could be positioned in the pathway of the emission laser from the optical pickup. In analysing the performance of the optical encoders, it was seen that there was a strong agreement with the position, as determined by the integrated optical encoder and the external LDV. Both optical systems revealed that an incremental step of the toothed wheel monitored by the optical encoders on the back of the geared motors corresponded to a displacement of 1.0 ± 0.5 micrometres – equivalent to the diameter of the DVD laser spot from the Sanyo SF-HD65/850.

Chapter 6: Traceable digital image processing for surface microscopy

6.1 Analysis and image processing

Image processing is used ubiquitously across disciplines and applied throughout scientific practices. Applications can be found in fields such as astronomy (152), medical imaging (153), particle physics (154), geological mapping (155), biological microscopy (156), photography (157) and many more. The contents of the images from each endeavour vary widely and can be formed from a vast range of different types of sensor inputs. The instruments used to capture the spatial information are diverse in their dimensionality and methodology of data capture. With each variation of sensor type or instrument configuration comes the requirement for specialised image processes to make best use of the physical information detected by the instrument. In general terms, with different types of physical interactions come different associated noise spectra, each of which can be filtered in various ways and to different degrees of success. As a result, we see some variation in the industry-standard software available to process images depending on the nature of the image formation. Such examples include lens flare for cameras and scar removal for SPM. Of all the tools available for image processing, there is a subset of these more specifically suitable to the processing of nano- and micro-scale topographical images and surface maps, like the ones reported in this thesis. These are found, for example, in an application called Gwyddion (45). It is common for advanced microscopes, such as a scanning electron microscopes, to incorporate dedicated software architecture, routines and workflow to capture and process images (158).

A very popular open source environment for image processing is 'GNU Image Manipulation Platform' (GIMP) (159), which is similar to 'Adobe Photoshop', both of which are versatile, with a diverse set of tools to manipulate images. By comparison, those are very different to an image processing suite specific to SPM, such as Gwyddion, that implements processes that are well-documented and explained to the user with a mathematical focus. At its heart, GIMP is intended to be a creative environment where images are modified to look visually appealing, well-blended and often exported from the environment as an exaggerated form of the original information imported into it, for the necessity of artistic preferences. In these processes, original information is actively modified and added with synthesised components. By contrast, it would be inappropriate in the post-processing of scientific images to add to or modify original data in a 'blind' or untracked way, where the underlying method of the modifying tools is not considered, for the effect of improving the aesthetics of the measured information. As such, this is a topic of concern within scientific and engineering communities (160) because this type of processing would result in a misrepresentation of the original measurements. For metrological considerations it is especially important that any path the data take through the

software is fully understood, so that any final outputs may be traceable back to the initial measurements and, therefore, any instrument calibration too. Therefore, it is always essential to explicitly define the steps taken in the processing of raw scientific measurements for the preservation of traceability.

In this work, there is a heavy focus on high-speed surface microscopy (2) in multiple forms, where frame rates can typically be in excess of 1 fps. Due to the real-time frame rates involved, it is important that essential image modifier tools can be implemented in real-time, such that they support the assayer in making live observations of a sample. Consequently, this too reduces the necessity for each video-rate frame to be developed by hand in post-processing. In turn, by integrating these tools into the control software it can reveal critical information about the surface that could otherwise be missed, and positively influence the decision-making underpinning the experimental undertaking, data collection and sample surface investigation. To enable real-time image processing, the image manipulation tools must be written into the instrument control code, which is written in LabVIEW in this case. In this chapter, the mathematical unpinning of the modifier tools that have been developed for real-time or embedded implementation is presented with principal demonstrations of the tools on sample or case study data. In some instances, pre-existing tools and libraries developed by National Instruments (161) are directly implemented, where the computation time and method are appropriate. In other cases, novel tools existing as subVIs or libraries using more fundamental building blocks in LabVIEW were built.

The initial part of this chapter details the key processes that were implemented in the control software (written in LabVIEW) to process the digital image data as it was captured by the sensors in the instruments. Firstly, a simplistic approach to remove any linear slope present in the image is explained, i.e. 'mean line levelling'. Thereafter, two methods of image averaging are described that seek to minimise the contributions of random noise to the final image and improve the detectable signal in the image. A further tool for removing image noise whilst preserving significant edges in the images, called an adaptive median filter, is also presented. Following a discussion of the implementation of these techniques for reducing sources of error in the image an evaluation of how surface microscopy data can be compressed is explored. A series of different imaging types are used to evaluate the success of this compression process.

Furthermore, this chapter goes on to describe the challenges involved in combining data taken from multiple sites on samples to create composite images (i.e. akin to a panoramic image taken on cameras created from a set of images taken with different spatial offsets). In a later section in the chapter, it is reported that relying on sensor data from an instrument's nanopositioners in surface microscopy instruments (e.g. HS-AFM) can lead to compound errors (e.g. due to backlash or overrun), when building these composite images over a long capture time. As 3D topographical maps generated by SPM or profiler techniques can be accurately displayed in 2D as height maps, tools developed in other

areas of digit image manipulation can be made use of. As such, a method was developed in this work that uses automated Normalised Cross-correlation (NCC) between such sections of overlapping images (161) to calculate how to best combine data to effectively improve the field of view of the instruments. The success of this method is then evaluated using optical profilometry data collected using an OPU-based optical profilometer, HS-AFM data and, finally, greyscale aerial photography with a variety of to features akin to surface microscopy, with a synthesised uniform noise spectrum added to the images to evaluate the noise-dependant performance of the NCC method.

Where techniques for image processing have been presented, it is not possible to exhaustively test each method to its breaking point or, indeed, prove how it can be successful in every case, due to the extensive variation of possible images. Therefore, the sample data or case studies have been selected as they represent a typical dataset in the surface microscopy techniques developed in this work, where the image modifying tools can be used to improve the outcome of the scientific study or the dataset offers the opportunity to represent a diverse selection of use cases within a single dataset.

Whereas in Chapter 5 (Section 5.2.4) imaging artefacts were discussed, such as hysteresis, crosstalk or drift, due to distortion in the actuator performances, this chapter instead focusses on correction to the 'z-channel' or sensor data. As a comparison, in photography the origin of these 'z-channel' noise sources may be shot noise on the image sensor or salt and pepper noise due to the sensor operating in a high-flux of gamma radiation (162). In the optical pickups-based configuration used in this work, such noise (in the 'z-channel') may come from thermal fluctuations in the voice coil motors or electronic interference of the analogue outputs from the quadrant photodiodes. Due to the high sensitivity of the instruments used in this work, imaging is also sensitive to mechanical vibrations from physical impulses or acoustic excitation too.

This chapter firstly looks at simplistic methods, that were implemented into the instrumentation software for the instruments described in Chapters 3 and 4, to correct for common surface microscopy imaging artefacts such as sample slope and low signal-to-noise datasets. Following this, an outline of a method for compressing surface microscopy data, with little compromise to the integrity of surface data, is evaluated for several real HS-AFM case studies. In the final part of this chapter, an investigation into the combining of images from multiple sites on a sample is carried out for both optical profilometry and HS-AFM showing that relying on the coordinates of stacked actuators can be prone to error in composite image formation. The development of an algorithm to create large composite images, from smaller overlapping images, without the need for actuator coordinates is subsequently carried out using a method based on normalised cross-correlation. In turn, this is evaluated using a control image with varying levels of uniform z-channel noise added to it.

6.2 Mean line levelling

This image modifier is used as a simple method to account for linear slopes in the data and is often essential in real-time imaging. Mean line levelling is a simplistic technique and can be misused if applied to the wrong type of data (*e.g.* where levelling requires a non-linear correction). To prevent unwanted height distortion to the image, it should only be used on a certain type of data, such as where significant 'step changes' (i.e. greater than a threshold gradient) in the surface are not expected. A single pass of this process only acts in one direction across the image (*e.g.* up-to-down, left-to-right or vice versa). Therefore, it often needs to be applied twice to a 2D image. More intensive levelling procedures can be implemented to account for surface undulation, using more advanced fits to the region under examination rather than just a linear fit. Examples of these fits are polynomial fits, median of difference and modulus(45). The purposes of levelling the data with mean line levelling include to account for linear sensor drift or for large linear sample slopes, especially if the height of textured features is much less than the even a gradual sample slope. To perform this in both directions on an image the following must be carried out.

A linear line of best fit must be calculated in each direction:

$$MLL(n) = mn + c_n, \ MLL(p) = mp + c_p \tag{26}$$

where mean levelling line (MLL) is a fitted line through the mean of *n* rows ($\overline{z_n}$) and *p* columns ($\overline{z_p}$):

$$\left\{ \overline{z_n} = \frac{1}{N_n} \sum_{n=0}^{n=N_n} z_n \right\} \text{ for p=0 to p=N}_p, \quad \left\{ \overline{z_p} = \frac{1}{N_p} \sum_{p=0}^{p=N_p} z_p \right\} \text{ for n=0 to n=N}_n \tag{27}$$

then subtracted from the original array:

$$\bar{I}_{\text{MLL}}(z) = \left[\bar{I}_n(z) - MLL(n) \right]_{n=0}^{n=N_n}, \qquad \bar{I}_{\text{MLL}}(z) = \left[\bar{I}_p(z) - MLL(p) \right]_{p=0}^{p=N_p} \tag{28}$$

where $\bar{I}_{\text{MLL}}(z)$ is the flattening image, $I_n(z)$ is the row of the image at index n, $I_p(z)$ is the column of the image at index p, MML(n) is the mean line levelling fit in the row direction and MLL(p) is the mean line levelling fit in the column direction, for a total number of pixels in the row direction N_n and column direct N_p.

6.2.1 Mean line flattening case study

To demonstrate the benefit of real-time mean-line flattening the images, taken using method described in Section 3.5.1 with the OPU based HS-AFM, of CRISP-Cas9 labelled RNA on a mica surface is presented without flattening Figure 118 (a) and with mean line flattening Figure 118 (b). Here, we see the demonstration for mean-line flattening revealing surface features (2-3 nm) that are equivalent or smaller than sources of noise (e.g. ringing >10 nm) in the image and smaller than the unlevelled sample slope (~40 nm).
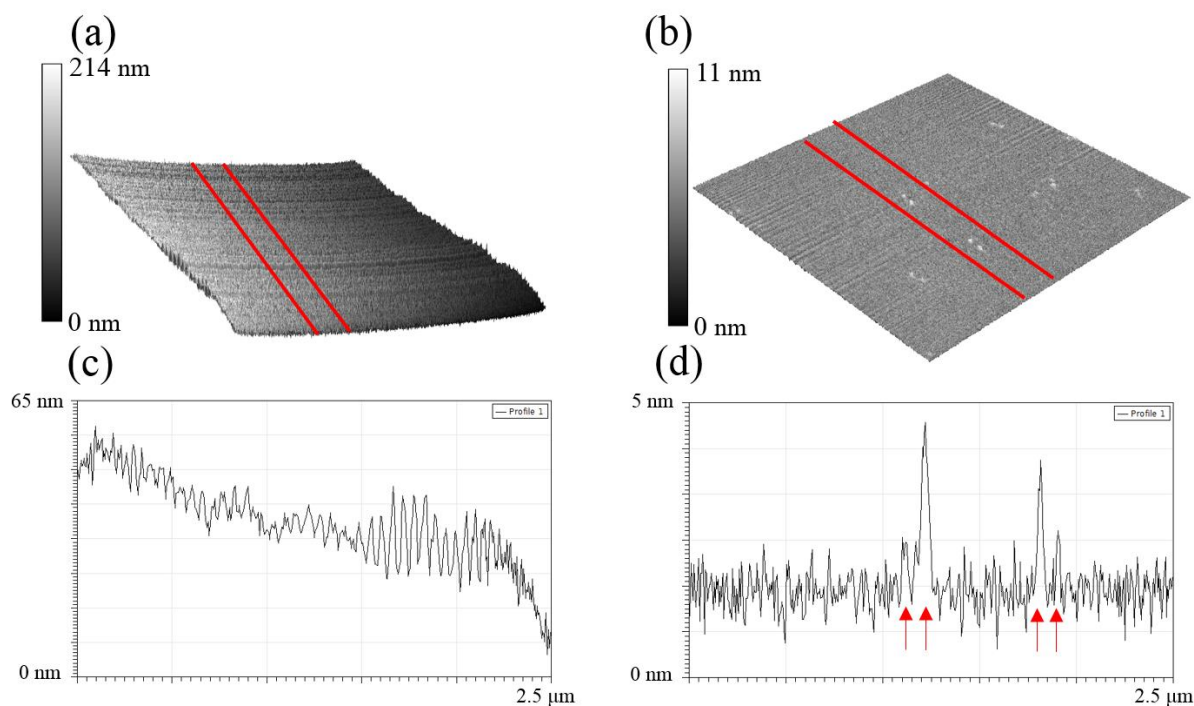
Figure 118: Demonstration of mean line flattening on an 3D surface plot of the raw HS-AFM data of CRISPR-Cas9 labelled RNA strands on a mica surface (a) (averaged over 10 seconds, therefore 10 trace frames) to produce a mean line levelled 3D surface plot which reveals the molecules under investigation (b). Subsequently, 10-pixel-wide line-profile were taken from the two surface and plotted below for comparison (c & d).

The side-by-side comparison of this dataset demonstrates that without the implementation of mean line levelling these subtle surface features of CRISPR Cas-9 (Figure 118 (d), red arrows) would be missed.

6.3 Tools for denoising images

In this section, a description of the tools used to filter out noise in the underlying raw data in an image captured from the instruments described in Chapters 3 and 4 are presented. Many of the techniques explorable here can also be applied to other forms of topographical height maps and are in some instances, extendable to techniques such as optical microscopy if they are sufficiently free of non-orthographic projections. The type of noise present in an image can take several forms. These variants are typically named after the type of distributions that can be fitted to noise histograms or appearance including: Impulse, Gaussian, Rayleigh, Gamma, Exponential, Uniform; and Salt and Pepper (163–165). The type of noise spectra present have typical (but not exclusive) associations with sources of origin. The origins of these noise spectra are the product of the 'natural world' around us combining with the sensitivity of the sensors and environmental fluctuations.

6.3.1 Image averaging: stacking

In AFM, as with other microscopy techniques, the instruments are often required to achieve nanoscale to sub-nanometre resolution and, therefore, the resultant signals can be very small (e.g. an atomic spacing $\sim 10^{-10}$ m), approaching the physical measurement limits of sensors. As a result we can have poor signal-to noise ratios (SNR) (e.g. the SNR nearing 1).

$$SNR = \frac{power\ of\ the\ signal}{power\ of\ the\ noise} \tag{29}$$

To improve the SNR of the final image, it is possible to take repeat measurements at the same location on the sample. A statistical argument can then be used to improve the relative contrast of underlying features or 'signal' compared to the randomly measured noise given that there is no significant height drift (e.g. > than 5% of the underlying signal) in the system. To do this the following mean averaging operation can be carried out:

For each height element in the array $z_{x,y}$

$$\bar{I}(z) = \begin{bmatrix} Z_{(x_{n=0},y_{p=N_P})} & \cdots & Z_{(x_{n=N_n},y_{p=N_p})} \\ Z_{(x_{n=0},y_{p=0})} & \cdots & Z_{(x_{n=N_n},y_{n=0})} \end{bmatrix} = \frac{1}{M}\sum_{m=0}^{m=M} \begin{bmatrix} Z_{(x_0,y_0)} & \cdots & Z_{(x_{N_n},y_{N_P})} \\ Z_{(x_0,y_{N_p})} & \cdots & Z_{(x_{N_n},y_0)} \end{bmatrix}_m \tag{30}$$

where M is the total number of arrays, m is the array index, n is the row dimension index of the array, p is the column index of the array, for an N_n by N_p element array, and $z_{x,y}$ is the height (as a function of positions (x,y)) at element index n and p.

6.3.1.1 Example Process and Conclusion

In Figure 119 it is possible to see the advantages of implementing Equation 30 in real-time as the calculated SNR (from Equation 29) improves with time. Here, the noise is calculated by the pk amplitude of the signal on the atomically flat mica and the signal is calculated by the pk amplitude of the molecular clusters being measured. In these data, short strands of RNA (approx. 0.6 nm tall) labelled with CRISP-Cas9 (approx. 3 nm tall), corresponding to the TERT gene measured for breast cancer detection, are imaged on a flat mica surface (1). Here, the formation of a frame takes 0.25 and repeated every second and contains 500,000 pixels taken using an OPU HS-AFM (Version 1.0, Chapter 4, Section 3.5.1). A simple mean line flattening algorithm (Section 6.2) is also performed on the data to account for sample slope.
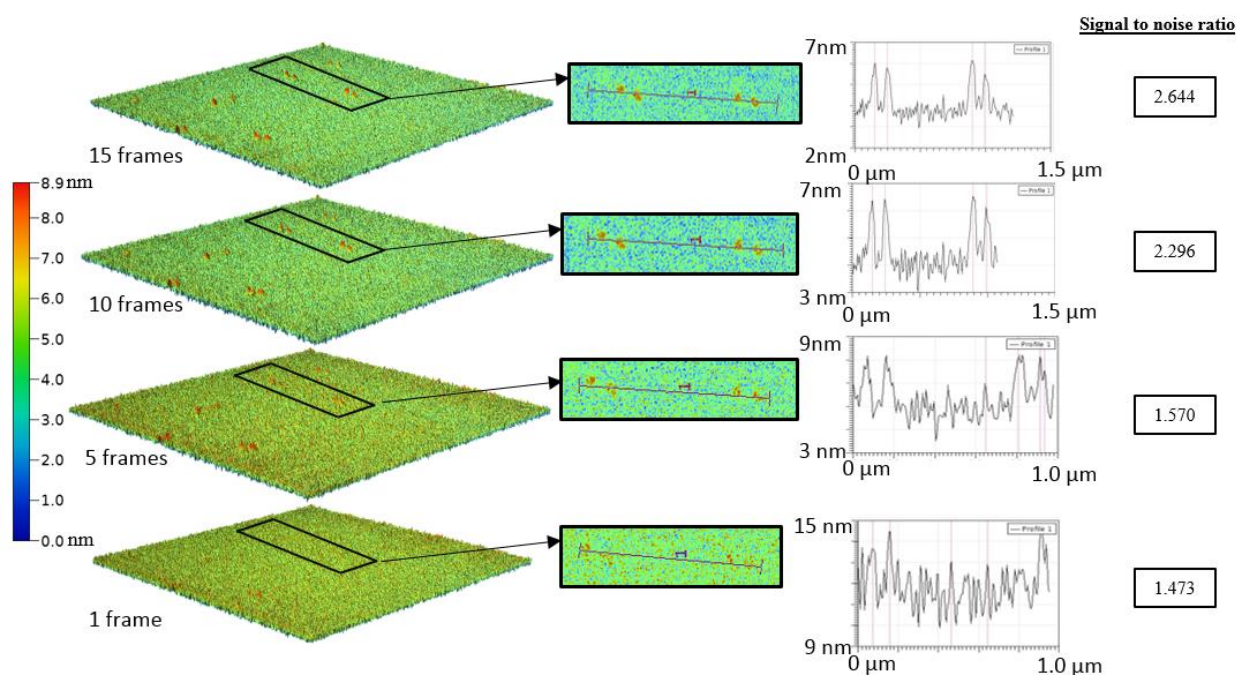
Figure 119: Demonstration of image averaging via stacking for identification of CRISPR-Cas9 particles present on an SNR-limited image taken on a mica surface. A lift-out with a line profile is also shown from Gwydion and used to calculate a signal-to-noise ratio (i.e. the mean mica surface to peak amplitude of the CRISPR-Cas9 divided by the mean mica surface to the peak amplitude of the noise on the mica surface) displayed on the right-hand side of the image.

Image averaging is an essential process for the identification of low-contrast surface features, i.e. where feature sizes are comparable to measurement noise levels as averaging helps to reduce statistical noise. Therefore, it can be critical to scientific study of atomic scale surfaces that it is carried out in real-time during imaging static low-contrast surface features to avoid an assayer missing the opportunity to capture critical sample information.

Improvement in the SNR via this method comes at a time cost (as it requires longer exposure) and will not improve the quality of the image infinitum as other components, such as scan stability (e.g. high-speed optical profilometry: 0.62 nm/s, Chapter 4, Section 4.6.2) or thermal drift, become larger than the gains established from repeat measurements. This is due to a number of reasons, including: scanner repeatability error; low frequency drift due to thermal expansion in the components; tip shape change due to surface contaminants (i.e. 'tip wear' affecting spatial resolution); and mobile material on the surface. There are a number of variants to this method, which could perform different statistics on the 'stacked' $z_{x,y}$ elements, such as different averaging methods (e.g. median or mode), to arrive at the final averaged frame.

A significant advantage of this method over others is that it uses repeat measurements (i.e. an extended dataset) to improve the signal-to-noise rather than a mathematical procedure based on a set of assumptions (i.e. a re-interpretation of the existing dataset). Another key benefit is that the number of x and y pixels in a frame remain constant over time, regardless of the number of iterations used. As such it does not degrade the high pixel density established in the instruments nor smooth or blur the spatial information – given sufficient stability and repeatability. For example, maintaining consistent pixel dimension is highly important for a later section regarding stitching images (see Section 6.5) as once the pixels are spatially calibrated to physical units, all pixels in frames taken across the sample have consistent spatial dimensions, allowing images to be compatible to tessellate across larger areas and improve the field-of-view in the study.

6.3.2 Image averaging: moving block average

For dynamic events of changing surface conditions, it is not possible to use repeat images to improve SNR in the way mentioned in the previous section. In such instances, making use of the high pixel density of the image, where it is available, can be an alternative way to improve the SNR. This process aims to reduce measurement noise by assuming they exist evenly around the mean value in a local region, thus the positive (e.g. above the mean) noise components cancels with the negative (e.g. below the mean) noise components. In the case of optical profilometry or HS-AFM, the 2D image has to be formed from a 1D waveform. Conducting a local mean once a 2D image is formed of a surface can give a more representative 'spatial mean' of the surface, than performing a moving average on the 1D waveform. As the pixels neighbouring were all taken with different time offsets, they are less susceptible to contributions such as impulse noise artefacts which a discrete time constant associated with them.

For this method, the algorithm operates internally within a single array, using a moving 'window' or 'subsection' that may be translated throughout a given frame. By sampling subsections of the array and finding the mean of this window, the centre of the subsection can be uniformly replaced with the mean.

$$I'(z) = \begin{bmatrix} Z_{\left(x_{n=0},y_{p=N_P}\right)} & \cdots & Z_{\left(x_{n=N_n},y_{p=N_p}\right)} \\ Z_{(x_{n=0},y_{p=0})} & \cdots & Z_{(x_{n=N_n},y_{n=0})} \end{bmatrix}' = \begin{vmatrix} Z_{(x_n,y_{p+\alpha})} & \cdots & Z_{(x_{n+\alpha},y_{p+\alpha})} \\ \cdots & & \cdots \\ Z_{(x_n,y_p)} & \cdots & Z_{(x_{n+\alpha},y_p)} \end{vmatrix}_{n=0,p=0}^{n=N_n-\alpha, \ p=N_p-\alpha} \tag{31}$$

where α is the dimension of the square subsection or window size, n is the row index of the element in the image array and p is the column index of the array, with again the image made from N_n by N_p pixels and $z_{x,y}$ being the height at position (x,y) in image I(z).

6.3.2.1 Case study of moving block image averaging

As a demonstration of moving block averaging, the data from the same sample as in the previous section is used, taken with the OPU HS-AFM (Version 1.0, Chapter 3, Section 3.3.3). Here we take the final image in Figure 119 (i.e. having dwelled at the same location for 15 frames over 15 seconds) and in Figure 120 show how the SNR can be further improved with $\alpha = (1,2,3,4)$ by sacrificing spatial resolution.
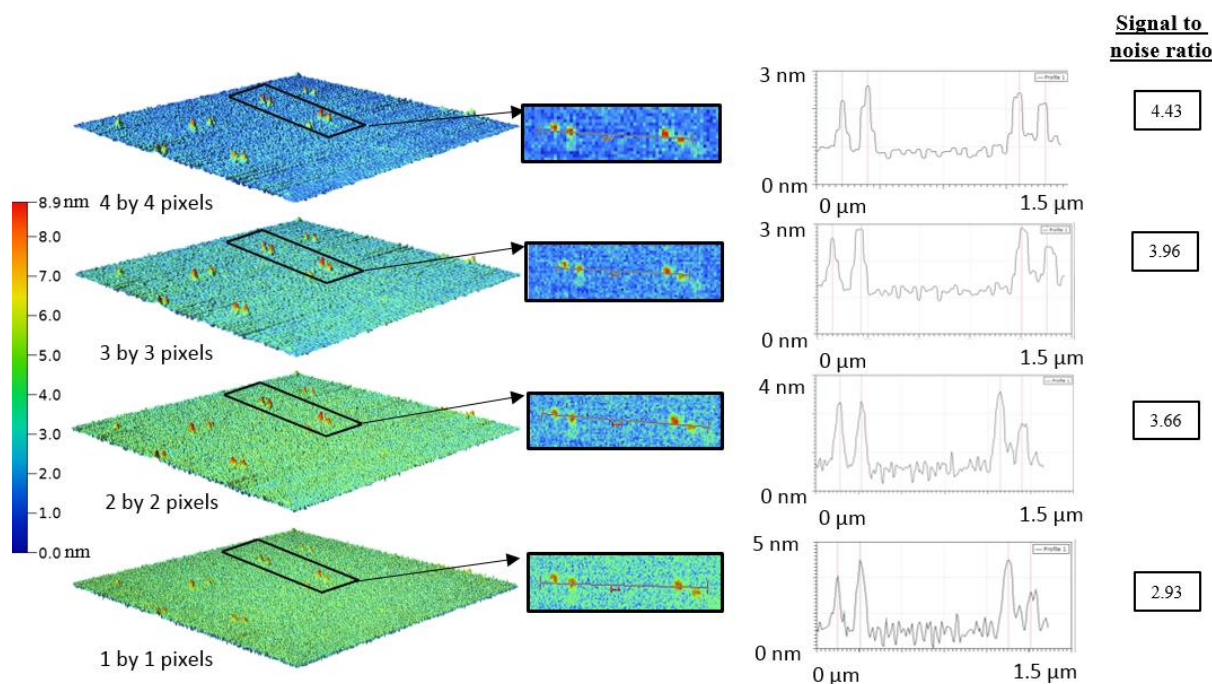
Figure 120: Demonstration of image averaging with a moving block average for further improvements of identification of CRISPR-Cas9 particles, present on a mica surface. A lift-out with a line profile is also shown from Gwydion and used to calculate a signal-to-noise ratio displayed on the right-hand side of the image.

As this method acts upon the array internally, it doesn't require any further repeat measurements at the same location on the sample and can be implemented in post-processing. However, it instead acts to improve the SNR to the detriment of the spatial (x,y) resolution (i.e. the effectively unique number of pixels) of the image. This can be an essential tool in an SNR-limited frame where the loss of spatial (x,y) resolution, is justified, if it enables a measurement not possible otherwise. Due to the dependency of the final image resolution on the moving length of window size (α) it makes this method less versatile where images collected across the surface may have a widely-varying SNR. However, a successful hybrid of this method with 'image stacking' could help to reach the desirable SNR sooner and prevent additional imaging time being needed.

In the presented example, this method can be shown to have a positive effect on the data. However, in circumstances where fine surface features occur (e.g. corresponding < 5 pixels) this process

would lead to sufficient loss of resolution (e.g. blurring of surface features) to preclude the measurement of surface features. Several variants to this method can be implemented, which have modification to the movement of the subsection, in terms of how it is translated, whether the subsections overlap and its shape. Increased layers of complexity can be added to make the subarray selection and processing of the data 'adaptive', as is seen in the next section where the Adaptive Median Filter is introduced. The adaptive nature of these image modifiers permits a decision process to exist within the filter that can be informed by localised surface features. By using information contained within the subarray such as statistical metrics, the filter can be instructed to perform tasks such as increasing the window size or altering the usage of the raw sampled data (e.g. with different methods for averaging).

This moving block average, otherwise known as 'mean' filter, is just one of the basic smoothing spatial filters, as outlined in Chapter 4 of the Gwyddion user guide (45). It is discussed here due to its simplicity to implement, quick computation time and observable improvements to SNR. Related filters include Gaussian smoothing (166), minimum (45) or adaptive median filter (167) (as discussed in the next section). In cases where the image needs to be down-sampled to smaller pixel dimensions, this is one way in which it can be done whilst making use of local pixels to reduce noise.

6.3.3 Adaptive median filtering

Adaptive median filtering (AMF) is a widely-used (167,168) tool which seeks to remove different noise sources from images while also being reported to maintain the underlying contrast in the image, rather than smoothing noise into surrounding pixels. Median filters are generally well-known for removing high abundance of noise (169) and fall under the classification of non-linear filters.

A non-linear filter acts such that for a number (n) of inputs (f_n)

e.g. inputs: $f_0(x,y) + f_1(x,y) + \ldots + f_n(x,y)$

gives output f'_n,

where if the inputs were acted upon by unique constants, (κ_n),

e.g. if κ_0 were to act on example inputs: $\kappa_0 f_0(x,y) + \ldots + \kappa_n f_n(x,y)$

then filtered the outputs are not always equal to a linear combination of the unique constants multiplied by the original filter outputs (f'_n)

e.g. it is **not** necessarily the case that: $\kappa_0 f'_n = (\kappa_0 f'_0(x,y) + \ldots + \kappa_n f'_n(x,y))$.

The functionality of the adaptive median filter is as follows: the AMF samples an image, I(z), made up of height values ($z_{x,y}$), with a window ($w_{\alpha_1, \alpha_2}(x,y)$) of width ($\alpha_1$) and height ($\alpha_2$) at pixel locations (x,y), where a maximum window size ($\alpha_{1,max}, \alpha_{2,max}$) can be set. For each window, the

170

following are calculated: maximum value z_{max}; minimum value z_{min}; and median value z_{med}. Subsequently, the data are taken through the following two-layered process:

Layer 1:

If $z_{min} < z_{med} < z_{max}$: Go to layer 2

Otherwise,

If $(\alpha_1, \alpha_2) \leq (\alpha_{1,max}, \alpha_{2,max})$: $w_{\alpha1, \alpha2}(x,y)$ ++ (make window bigger) and repeat layer 1

If $(\alpha_1, \alpha_2) > (\alpha_{1,max}, \alpha_{2,max})$: The filter outputs $z_{x,y}$

Layer 2:

If $z_{min} < z_{x,y} < z_{max}$: filter outputs $z_{x,y}$

Otherwise,

The filter outputs z_{med}.

The filter, therefore, starts by checking that the maximum, median and minimum values in the window are not equal to each other. If this isn't the case, it expands its sampling window, unless that has already reached its maximum. Thereafter, it either repeats layer 1 or will progress to layer 2, where a decision process is made to choose whether the original data $z_{x,y}$ should be outputted or z_{med}. If $z_{x,y}$ lies inbetween z_{max} and z_{min} then it is outputted; otherwise z_{med} is outputted. The number of changes the AMF makes to data are tremendously varied and dependant on the signal and noise present in the image.

6.3.3.1 Example Process and Conclusions

The evaluation of the AMF is done here in two parts, firstly using HS-AFM data of 2D phosphorene nanoribbon (PNR) on highly oriented pyrolytic graphite (HOPG) (24) with synthesised uniform impulse noise added to different strengths. This dataset allows for comparison of the output from the filter against the original reference image to quantify the success of removing the noise, a popular evaluation method found in literature (167). The selected HS-AFM frame has nine 'terraces' of height representing integer numbers of atomic step heights (i.e. of HOPG and of a PNR). This image was chosen for the varying degrees of subtle height changes, whilst having characteristic edges allowing us to observe if these edges are preserved throughout the process. Secondly, a HS-AFM dataset of ZIRLO (Westinghouse, 1% Nb, Non-Optimised) used for nuclear fuel cladding (170), was used to show the capability of the AMF to reduce the prevalence of noise in the image. Subsequently, a second dataset captured using HS-AFM was explored, built using XYZ data. Here, we see how the AMF can help to remove the presence of digital noise in the image, making the surface look much more akin to the realistic surface.

In the initial evaluation, uniform noise was synthesised and added to the image in the following way. Firstly, each pixel of the image was indexed and in turn, at each coordinate, a random integer (Rnd_1) was selected from a random distribution generated between 0 and 100 using LabVIEW's random number generator. To set the abundance of noise, a divisor (div) could then be selected. Then the first (between 0-100) random integer was divided by the divisor (Rnd_1/div). If the remainder (rem_{div}) was equal to zero, a second random number (Rnd_2) was generated. This second random number was generated in the same range as the data (i.e. between z_{min} and z_{max}) in the image and combined at a ratio of 1:1 with the data at that pixel index (i.e. the average of the measurement pixel and synthesised impulse). For evaluation purposes, 10 AFM images with synthesised noise were generated, where the divisor was set incrementally from 2 to 11. The consequence of adding this synthesised noise can be seen in Figure 121(a), where the original data are presented alongside datasets with divisors 2, 6 and 11. Furthermore, the deviation from the original data is plotted in Figure 121(b) (blue crosses), showing the resultant mean deviation in nanometres that the noise corresponded to in height for each dataset. Also, presented in the figure is a demonstration of the advantage of repeat uses of the AMF for low signal-to-noise images. Dataset 10 is presented with repeat runs (up to four) of the AMF filter that in turn corresponded to a ~6 times decrease in error.

As a study into the AMF's ability to remove measurement noise, an HS-AFM 'XYZ' image (i.e. using interferometer sensing on the X and Y axis) taken with using the method outlined in Chapter 5, section 5.1.6 of a ZIRLO sample, is filtered with a varying number of 'passes'. The primary results look to show what visual effects the AMF has on the image and displays characteristics of the adaptive window size, and how that varies in size with repeat passes.
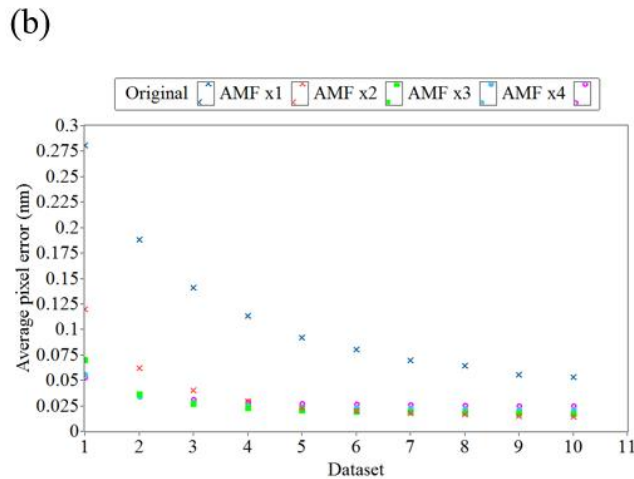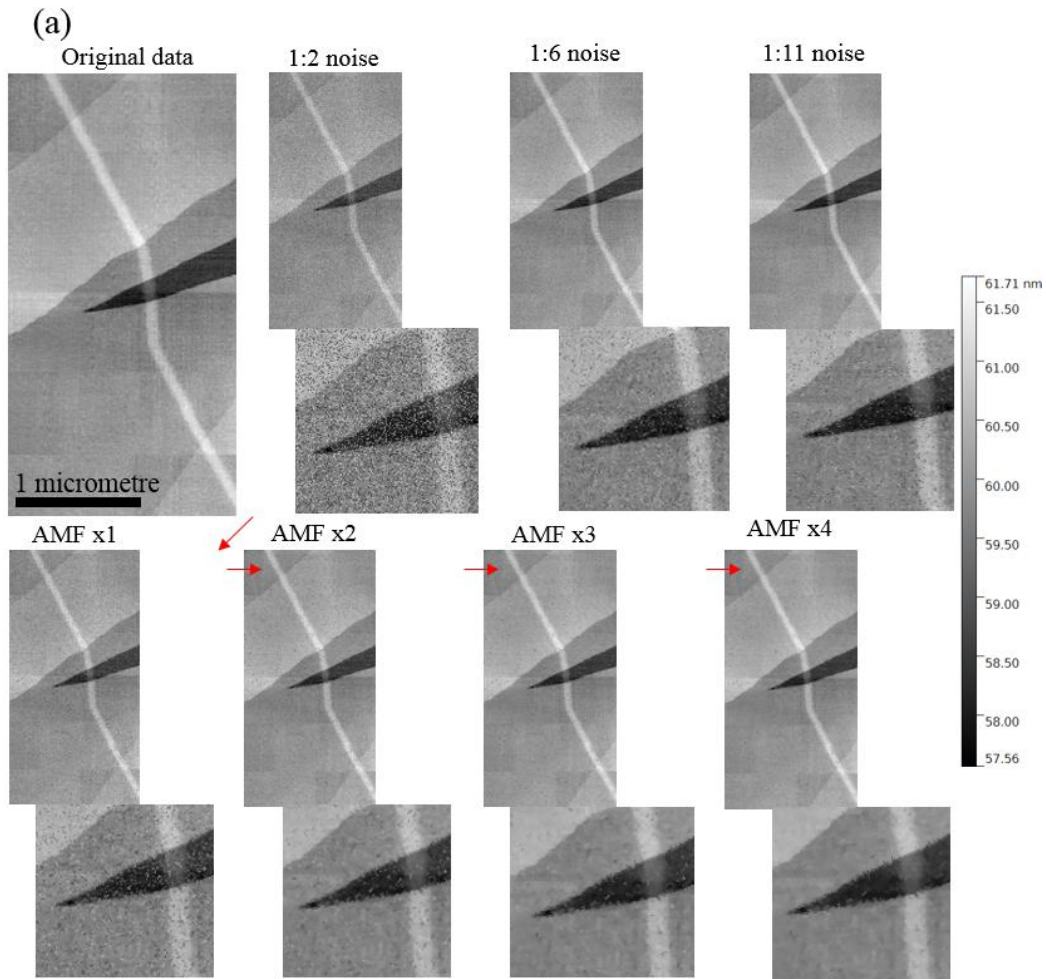
Figure 121: An adaptive median filtering case study with HS-AFM data of a phosphorene nanoribbon on HOPG with varying simulated noise. in (a) Original data, with previews for datasets 1,5,10 and again dataset 10 with 1-4 passes of AMF also shown on the second, resulting in the changes of average pixel error in each datset (b) and a table of how each of the 10 datasets mapped to spatial noise ratio (c).
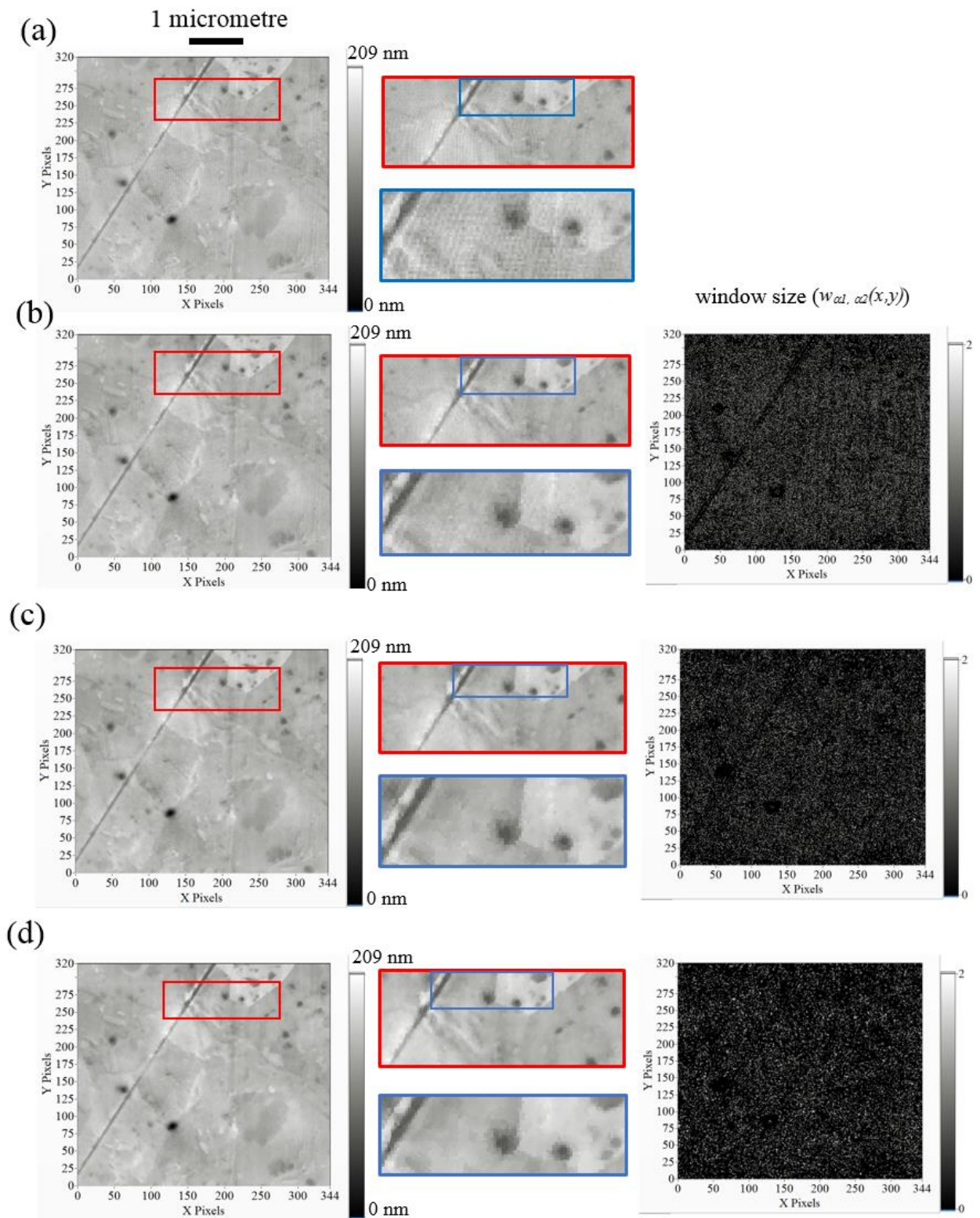
Figure 122: A 'xyz' HS-AFM image taken of a Zirlo (Zircaloy) sample with zoom-in with 0 passes (a), one pass (b), two passes (c) and three passes (d) of the AMF, are presented with zoom-ins (red and blue) and a map of the AMF changes to the data and the window size that was used, represented in the greyscale channel in each case.
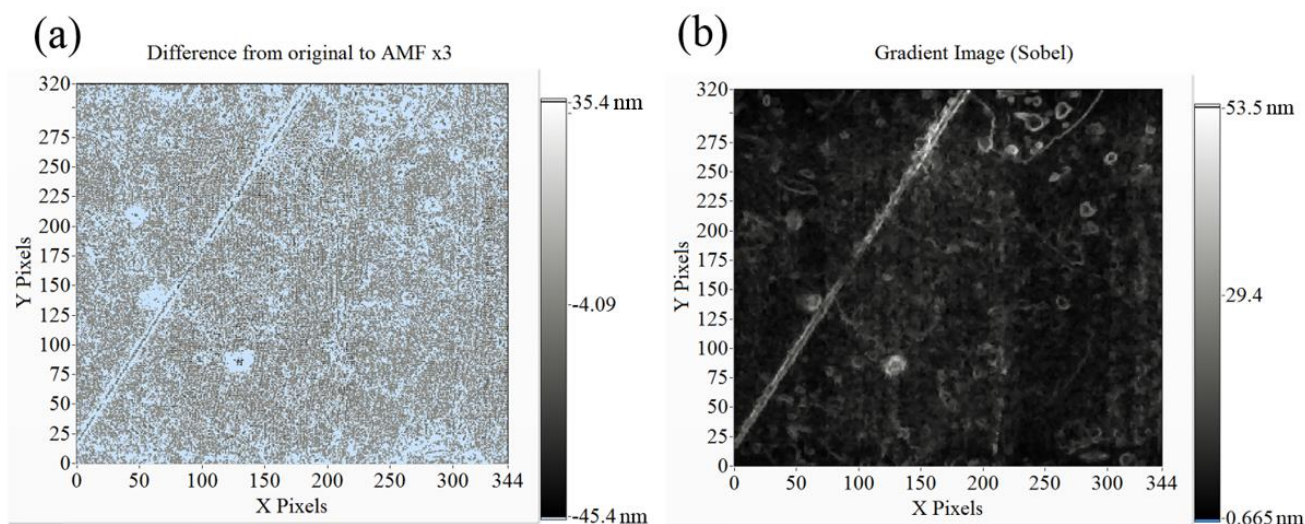
Figure 123: An image representing the differences (a) between the original data and the final dataset (AMF x3) presented alongside a gradient image (b) calculated via the Sobel method.

From the difference image in Figure 123 (a) we can see that many of the 'zero' changes occur around the feature edges, thus, as hoped, preserving the edges in the image from being smoothed out even after repeat runs. The Sobel gradient image (171) is presented side-by-side for comparison to reveal the regions of most change in height compared to the original image. Such removal of noise from low SNR images, whilst preserving edges, can be essential for successfully performing normalised cross-correlation functions as is later explained in Section 6.5.3.

6.4 Adaptive difference compression algorithm

A large amount of raw data is transferred to the computer per second in OPU HS-AFM and for faster OPUs (with bandwidths of up to 400 MHz). Therefore it is necessary to have consideration for data transfer and storage on the computer. The sensor data captured by the HS-AFM, consisting of a waveform of height (from either LDV or OPU) and XY displacement (from either OI or OPU) to form an XYZ HS-AFM image, gets collected at ≥ 2 MS/s per channel with 16-bit resolution per channel. The data have 16-bit bit depth to allow for high sensitivity of sub-nanometre displacement over several micrometres (e.g. ~0.1 nm resolution of ~6.5 µm). Therefore, the total raw data input into the computer is 12 MB per second per channel, i.e. one gigabyte in less than 90 seconds.

There are a long list of general purpose image compression algorithms that are commonly used, such as JPEG (172), Lempel-Ziv-Welch algorithm (173) and Freeman chain code (174) to mention but a few. Of these, there are two main types of approach: lossy; and lossless. This terminology refers to how much of the original data is preserved. Compression algorithms are deployed in several ways and are, in some instances, immediately implemented as sensor information is captured, such as within the architecture of digital cameras (175). Challenges faced in digital camera compression are, in many

ways, similar to the surface microscopy instruments developed in this work in terms of the digital throughput of multi-megapixel 2D arrays or images.

Considering the imaging stability (Chapter 5, Section 5.4.2) of the OPU HS-AFM as typically <5%, whilst used in general operation imaging a static surface it does not seem necessary to continually capture data at full 16-bit resolution (or 'shooting in RAW' as it is referred in filmography). Therefore, it can be considered possible to use a lower bit depth (e.g. 8-bit) to quantify the differential changes frame-by-frame, given that there are no significant changes in surface features that require a large proportion of the dynamic range of the sensor to be used and therefore stored as a 16-bit number. It is also preferable that this compression is done without considerable loss of measurement quality or an increase in measurement error (e.g. without inaccuracies becoming greater than the inherent uncertainty in the instrument). Additionally, the compression results in a considerable saving of total data stored (e.g. a reduction in file size of a significant fraction).

The proposed route for the compression process developed in this work targeted image properties specific to surface microscopy techniques. Where the surfaces are typically flat (e.g. atomically flat plateau in HS-AFM) and, therefore, are unlikely to change significantly from frame to frame. To demonstrate the methodology, a sample dataset taken on the OPU HS-AFM is used from the same location. For the evaluation of the compression three different types of AFM dataset were used; static; dynamic; and roaming. These are presented and the algorithm's error performance in each case is calculated.

6.4.1 Example process and application

The first step of the algorithm, the difference step, is to calculate the changes between the previous or 'key' frame (K) and the current $(K+c_k)$ frame. For the high-fidelity spatial data found in OPU HS-AFM, most of these changes fall into a Gaussian distribution where the sample is mainly flat, as is typical in OPU surface measurements due to the limit range of the FES linear range. This distribution of changes can now be stored as a lower bit depth (e.g. 8-bit) 2D array of values instead of the original 16-bit raw values. The second step, the adaptive step, selects how much of the distribution should be stored as a function of some number (n_σ) of standard deviations (σ_{k+ck}) from the mean (μ_{k+ck}). The setting of 'n_σ' is very much dependant on the percentage change in the dataset being compressed, as is demonstrated later for the three types of data. The changes, in the case of an array of 8-bit integers, are then stored between -127 to 127 with a max and min value being stored too, such that the 8-bit 2D array of changes can be scaled when uncompressing the data to represent the magnitudes of the original changes. In Figure 124 we see five sequential frames taken with the OPU HS-AFM, the four plots of percentage change below and the four 8-bit adaptive binning of these changes for $n_\sigma = 4$.
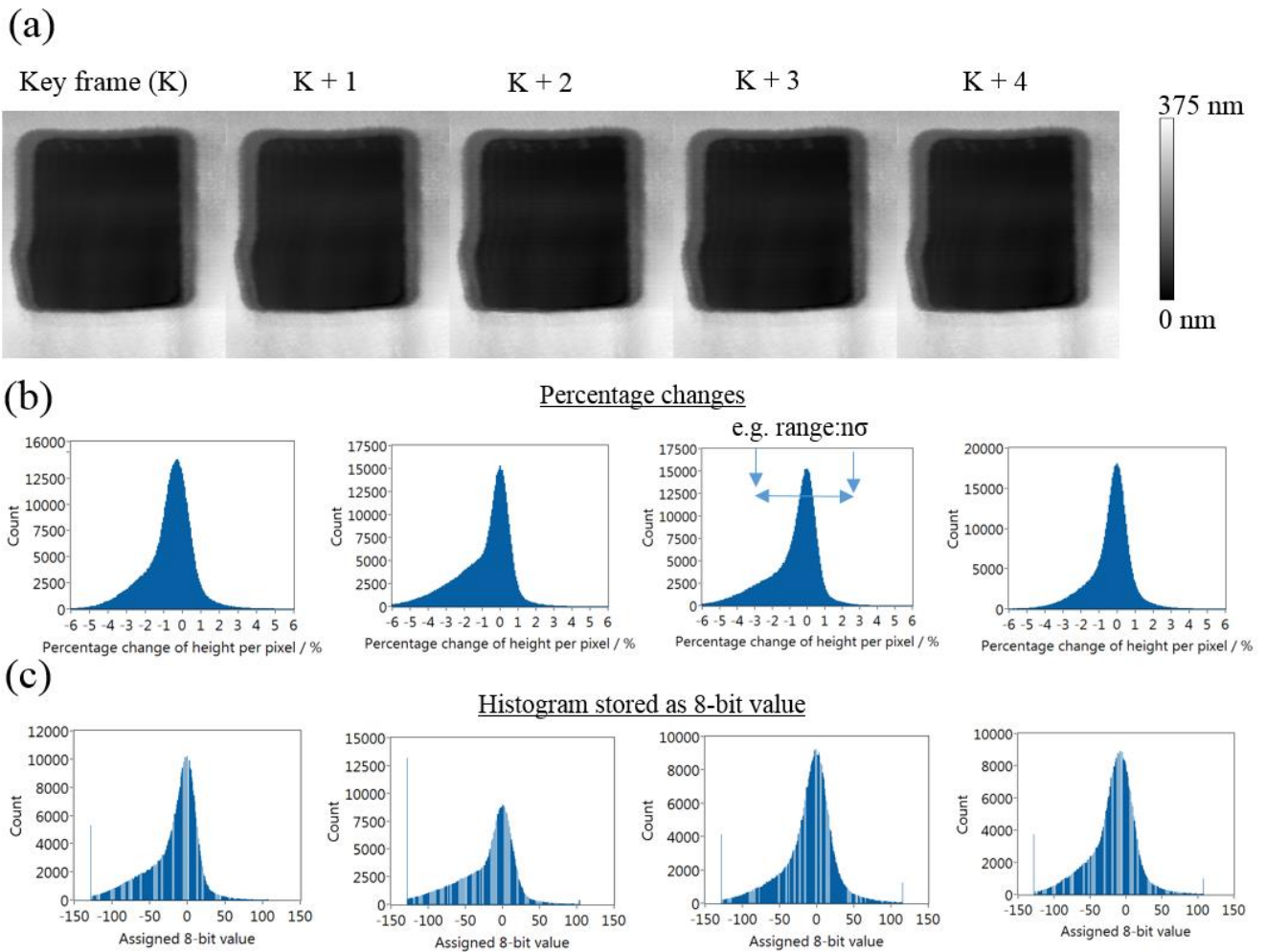
Figure 124: Overview of the basic steps that can be taken for compression of static OPU HS-AFM data to reduce the amount of memory used to store data for a static surface, where (a) shows five frames of data, (b) shows the percentage change between each frame and (c) shows how these are allocated to an 8-bit value between -127 and 127.

Taking this static dataset forward and demonstrating the algorithm's performance for different values of 'n_σ', it is shown, by calculating the mean percentage error over time, which value of n_σ is best suited for this static dataset.
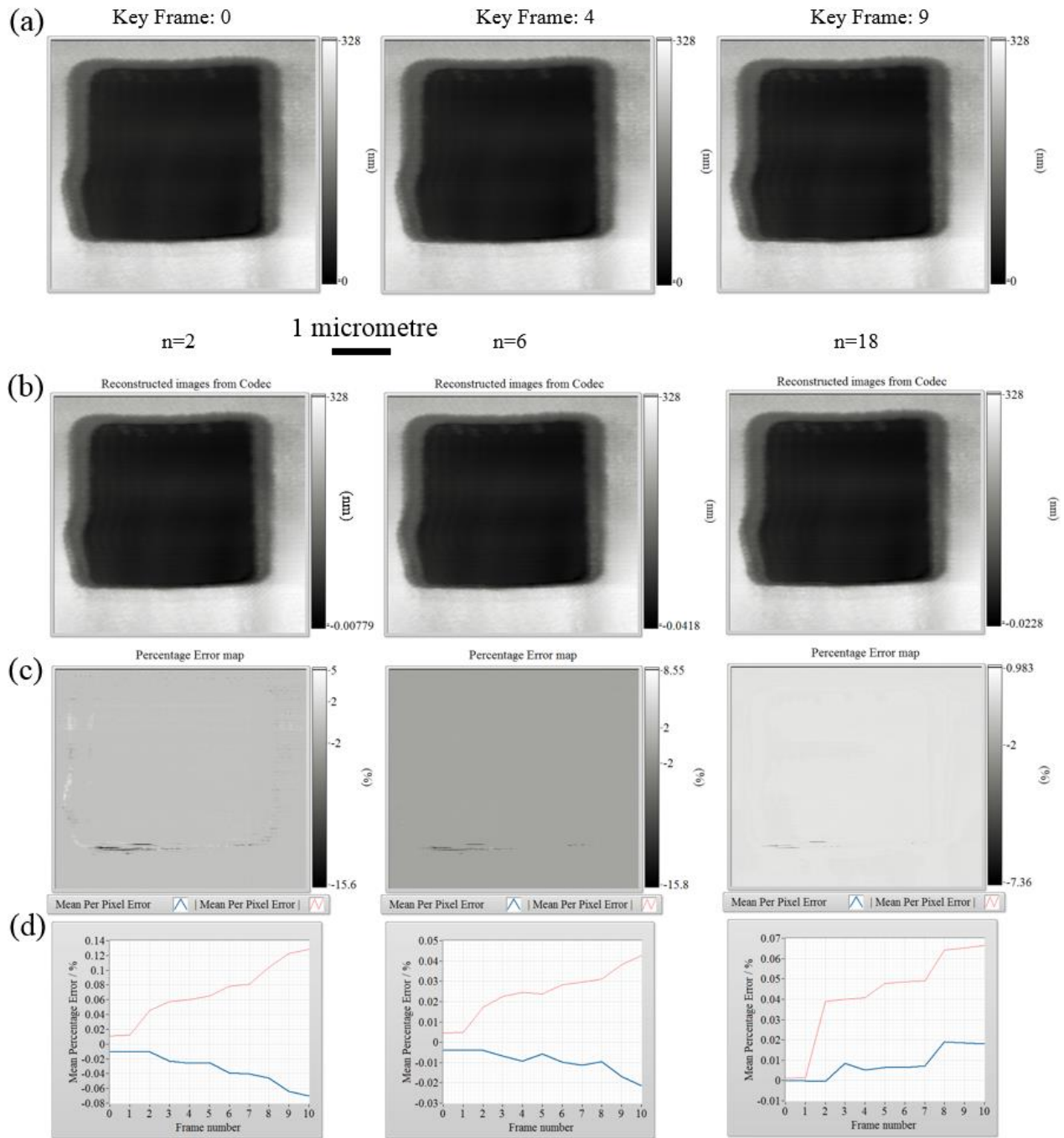
Figure 125: Grid of images where (a) shows some of the arbitrarily-chosen key frames (as numbered), (b) shows the images reconstructed from the 8-bit histograms of changes, (c) shows the percentage error of the reconstructed image compared to the original (each column represents the number of standard deviations (n)) and the three graphs in (d) show how the percentage error (blue) and modulus of percentage error (red) compare with the raw data changes with frame number for each value of n.. The data were captured whilst looking at a square pit on an Si Ti sample with an OPU HS-AFM by F. S. Russell-Pavier.

Here, it is seen that a value of $n_\sigma = 18$ yielded the smallest value percentage error, of -0.125% or 0.41 nm, after 10 consecutive frames for a static dataset. For most cases this level of measurement error is acceptable for the saving of 37.5% of memory. However, this is only one type of data (i.e. static) that may be typical in surface microscopy techniques and, therefore, this value of n standard deviations is unlikely to hold for other types of data. In the next evaluation a new dataset is introduced that images a dynamic event captured by O. D. Payton on the LDV-based HS-AFM (Bristol Nanodynamics, UK) situated in B23, H H Wills Physics Laboratory, Bristol of phosphorous nanoribbons (PNR) prepared by Watts et al. (24) (UCL, London). In this next dataset, a dynamic event is observed on the surface in which a PNR is moved across the surface of highly orientated pyrolytic graphene (HOPG). Here there are five primary plateau of height, with one of them changing its position spatially (i.e. in the x- and y-axis) in the image with time. This dynamic event is captured over 152 consecutive frames (Figure 126).

For the dataset that captured an object (PNR) moving on a static sample (HOPG) shown in Figure 126, a large value for n (n=18) yields the best preservation (mean percentage error: 0.82% or 0.068 nm) of the data with compression. This is due to the change in the distribution of changes as compared with the previous static dataset. In this instance, as well as an approximate gaussian distribution of changes to the static features, such as that shown in Figure 124 (b), the dynamic surface features change pixels by a much greater amount and, therefore, reside as outliers in the distribution of changes.

A subsequent case that is used to evaluate the compression algorithm contains data captured from 'free-roaming' around an AISI304 stainless steel sample by S. Moore and F. S. Russell-Pavier using a LDV and Picoscale based HS-AFM. This dataset represents yet another way in which the real-time capability of HS-AFM is used to explored surface features. Here these features are made up of an inclusion (i.e. whiteish polygon), an unstructured distribution of surface corrosion products (i.e light dots across the surface) and a triple point grain boundary (i.e. three dark lines meeting at a point). For every new location that the sample is moved to, every pixel should undergo a more significant change than for an equivalent pixel associated to static surface features in the previous two datasets. This is because every feature on the surface moves, as the sample moves resulting in many more types of changes occur at any given pixel index through the capture time of this experiment. Due to the diverse range of features and the ubiquitous abundance of changes at every pixel index, this dataset is a more complex dataset to test the compression algorithm than previously discussed. For this evaluation, 60 frames were taken as the assayers roamed around the sample. The mean error from the raw data is calculated for the three presented values of n over one minute (60 frames) of compression of HS-AFM data.
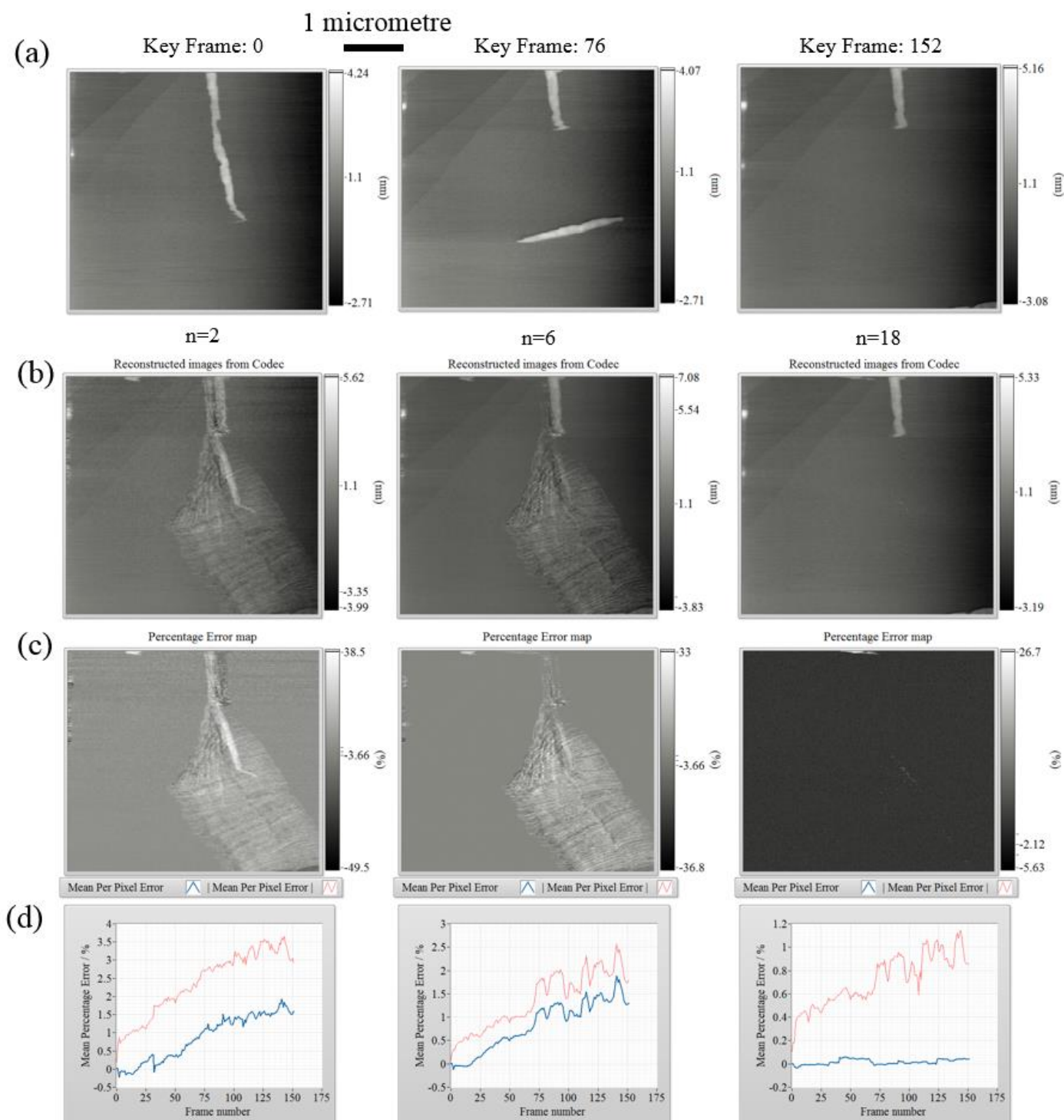
Figure 126: (a) Selection of arbitrarily-chosen key frames (as numbered), (b) Images reconstructed from the 8-bit histograms of changes, (c) percentage error of the reconstructed image compared to the original and each column represents the number of standard deviations. The three graphs in (d) show how the percentage error (blue) and modulus of percentage error (red) compare with the raw data changes with frame number for each value of n. The data are captured whilst looking at a dynamic event of a PNR moving across the HOPG captured with an LDV based HS-AFM by Dr. O. D. Payton.
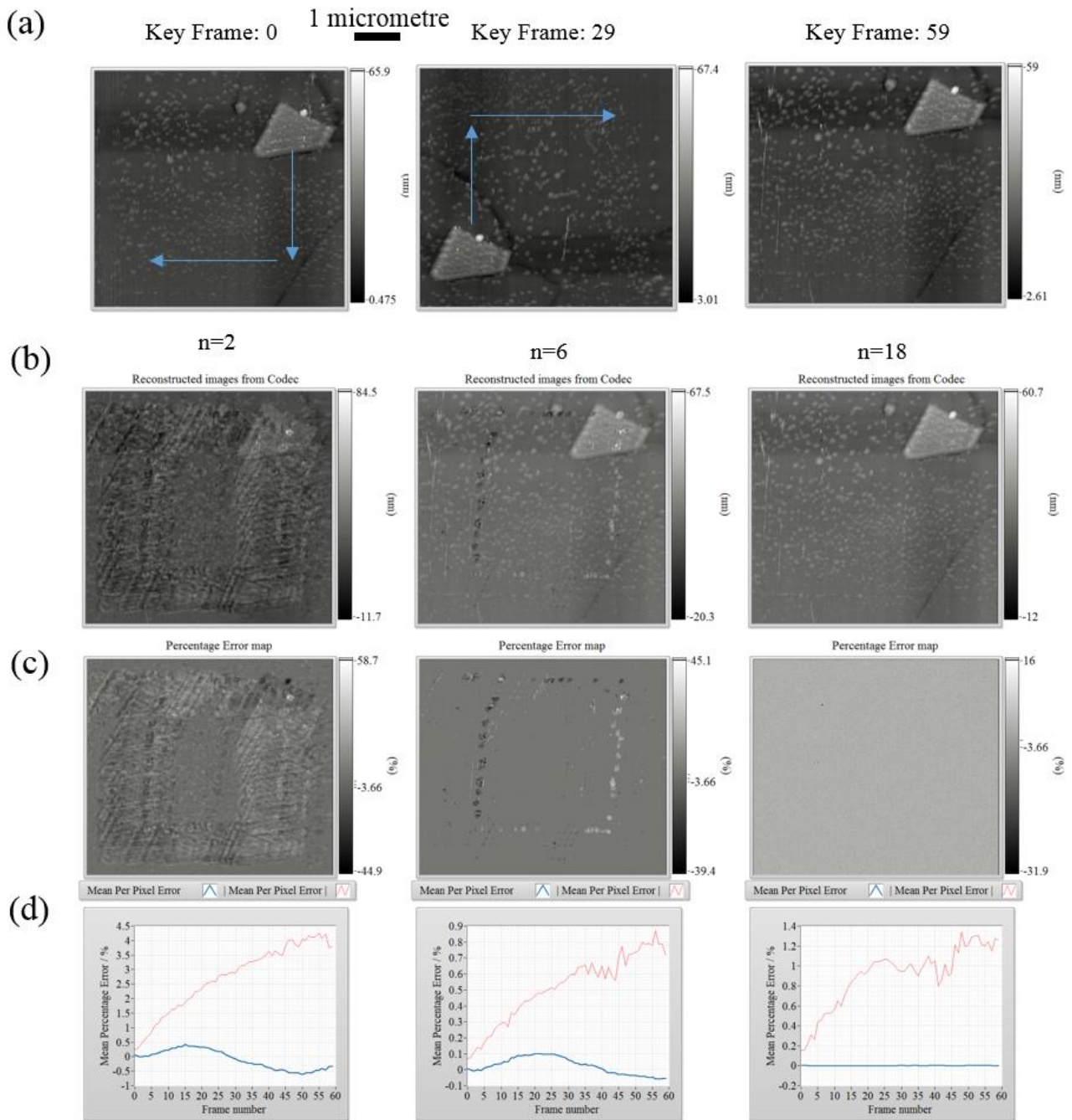
Figure 127: (a) Selection of arbitrarily-chosen key frames (as numbered), (b) images reconstructed from the 8-bit histograms of changes, (c) percentage error of the reconstructed image compared to the original (each column represents the number of standard deviations). The three graphs in (d) show how the percentage error (blue) and modulus of percentage error (red) compare with the raw data changes with frame number for each value of n. The data were captured by S. Moore and F. S. Russell-Pavier whilst moving an inclusion found on stainless steel around using the LDV and Picoscale based HS-AFM.

In Figure 127, it is shown that once again, for a surface with a greater range of surface feature changes selecting a mid-value of 'n' (n=6) permits for the smallest reduction of mean percentage error (0.6% or 0.34 nm).

6.4.2 Tuning the compression algorithm

Looking in more details at the three cases presented of Si Ti stationary, PNR dynamic and steel roaming, it is possible to see how varying the number of standard deviations used in the compression algorithm varies the mean error (and the absolute mean error) per pixel.
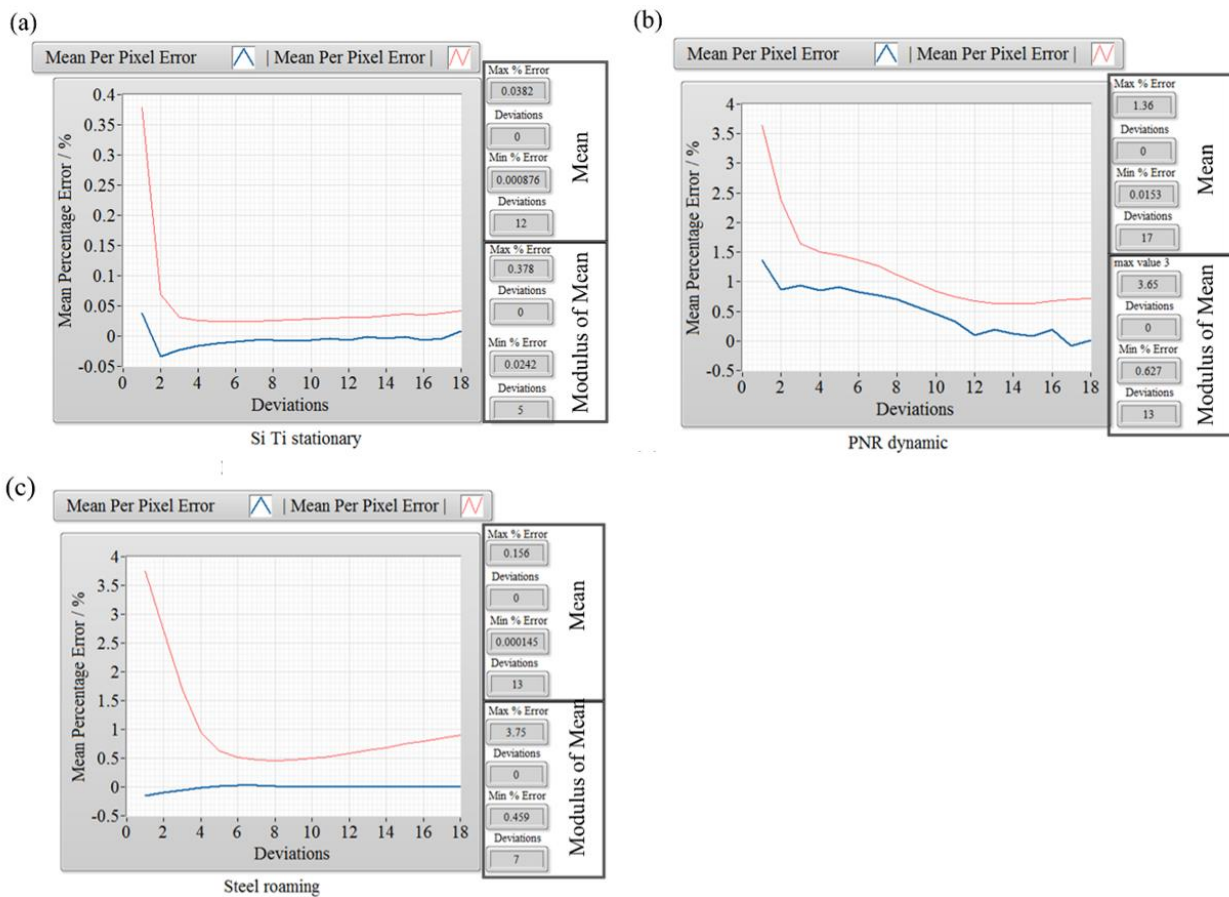
Figure 128: Absolute and modulus of the percentage error calculated over time for the static Si Ti (a), dynamic PNR (b) and roaming steel (c) datasets when the adaptive difference compression algorithm is applied to the data.

Figure 128 shows us that in the three cases a different parameter sweep for values of n_σ results in a different quantity of error for each case and for each number of standard deviations. For the Si Ti (static) sample little reduction in error is observed when $n_\sigma > 7$. For the PNR (dynamic), the optimal n is $n_\sigma = 18$ and for the steel (roaming) $n_\sigma > 5$ results in little change to the percentage error.

For the real-time application of the adaptive difference compression algorithm, the evaluation of the best value to select for n_σ can be done by calculating this minimum on a frame-by-frame basis.

An extension to this that has not been implemented here would be to scale the bit depth of the number depending on how many standard deviations are required. For the static Si Ti 'n_σ' is less than 1/3 of the equivalent value for the PNR.

In conclusion, it has been shown how a simple compression algorithm for surface microscopy data instead of saving raw sensor data (e.g. at 16-bit resolution) between consecutive frames taken by a HS-AFM it saves the difference between frames using a value with a lower bit depth (e.g. 8-bit) for each pixel. To improve the success of the algorithm, a step is implemented to adapt the scaling of the 8-bit values to match some number of standard deviations of a distribution of differences between consecutive frames. By using three distinct types of HS-AFM datasets (i.e. static, dynamic and roaming) it has been shown that the number of standard deviations required to achieve the minimum error varies according to what is being imaged. As such, it is recommended that an evaluation of the best number of standard deviation is calculate whilst compressing the data to establish the optimal mapping of the changes to the 8-bit values. It was shown that a significant saving of up to 50% could be achieved using this method without resulting in a >1 % error.

6.5 Image combination from multiple sites of sample

Image combination or 'stitching' (176) is a process found in many imaging techniques (177–179), where multiple sequential images are taken with a spatial or angular offset and then later combined to create a larger composite image, increasing the field-of-view of the instrument compared to one image. This process gives rise to the popular tools to create 'panoramic' images on smartphones (180) or digital cameras (181). This requirement is also commonly found in scientific fields that use instruments such as telescopes (182), microscopes (46) and aerial photography (183). In general, it arises where high fidelity measurements possible in a single image with a limited field-of-view are required over a larger area than is possible with a single image or capture event. The field-of-view of one image, at the desired lateral resolution, is typically limited by the number of unique measurements that can be taken per image capture. In the case of photography this is the number of pixels on your image sensor and the properties of the lenses used to resolve a virtual image incident on the sensor. In SPM the spatial unique measurements are limited by the unique measurement area (e.g. tip surface interaction area in HS-AFM ~10 nm) and the full range of the scanner's motion (e.g. up to 6.31 µm, Chapter 5, Section 5.4.2). Therefore, to extend this lateral resolution to a greater field-of-view (e.g. 0.5 mm by 0.5 mm) or larger area than for one image (e.g. >64 by 64 µm), multiple images with physical offsets must be taken.

In the field of photography, there are several well-known tools that are used such as Photoshop's industry standard Photomerge (184) or Image Composite Editor (ICE, Microsoft) based on the techniques reported in (185). These tools, tuned for photography, often must consider distortions

typically encountered due to the focussing optics resolving a 3D environment onto a 2D sensor (e.g. spherical aberration, radial distortion or defocus aberration) (178). Moreover, for large composites which aren't taken in a grid-like structure, ICE expects the data to be projected onto one of several 3D projection mappings, a step that is not suitable for the types of data described here (i.e. in surface microscopy involving planar motion only). It is not possible to avoid this step whilst processing these data with this software.

The distortions in SPM or scanning laser optical profilometry using the method described in Chapter 5, Section 5.2.4 (e.g. spatial hysteresis and crosstalk) are rarely common to those found in photography. This is because in the case of SPM the displacement changes of a mechanical beam are used to determine subtle contrasts in height on a relatively flat surface. Therefore, the distortions can come instead as a product of significant excitation of the probe (arising to erroneous decaying oscillations in the data or 'ringing') (21) or scan path distortions (86) (see section Chapter 5, Section 5.2.4). Other distortions, include the change of the measurement probe contact area due to contamination or tip wear (131).

6.5.1 Terminology and construction overview

For the purposes of the explanations in the coming sections we shall consider the *canvas* as being a 2D array or corresponding image that is initiated with a uniform value (e.g. zero or an arbitrary minimum number such as -∞) and of a user-defined fixed dimension (e.g. 3000 by 3000 pixels). Once the canvas is established, we look to add data to it as we build an understanding of the spatial relationship (e.g. either by eye or calculated) between the subsequent images. Typically, the initial or *zeroeth image* will be placed at the origin in the canvas. Every subsequent image will be compared to at least one other image before being placed in the canvas. During this comparison process the image that has a known location in the canvas shall be referred to as the *template* and the new image with an unknown location referred to as the *frame*. In the automated image process a *frame* is often subdivided into several image subsections and here the subsections are referred to as *tiles*. Once two or more images have been add to the canvas, with a known spatial relation, and combined (merged or 'stitched') a *composite image* is made by cropping the canvas to the area that is populated by the frames. The initial uniform value can be set to be a uniform colour or transparent in the alpha channel and exported to common image formats (i.e. .png, .jpg or .tiffs).

6.5.2 Basic calibration and simplistic image formation with positioner data

In order to build a composite image where the pixels are calibrated to physical distances, as in a SPM topographical map, there are two key approaches used in this thesis: calibrated frames; or calibrated frame offsets. On the one hand, calibrated frames are formulated using methods using

external sensors (such as those described in Chapter 5, Section 5.4.2), where each frame is built using interferometer data and, therefore, the physical dimension of each pixel (e.g. ~2 nm) is known to some measurement uncertainty (e.g. ± 0.5 nm). In other forms of imaging, where the high-speed scanners are operated in open-loop mode, instead the low-speed long-range positioners (e.g. Attocube ECSx3030, Germany) that are operated in closed-loop are responsible for calibration of the images (OPU HS-AFM V1.0, Chapter 3). For the closed-loop positioners, it is possible to obtain the (x,y) actuator positions for every site on the sample where a surface image has been collected. By making a small motion (e.g. 0.25 × frame size > the magnitude of the translation vector < 0.75 × frame size) diagonally across the sample surface (i.e. a translation in both axes) between two overlapping sites, ensuring that there is a common identifiable feature in both frames and by identifying the translation of the prominent feature in pixels and dividing that by the translation measured by the close-loop positioners, the physical dimensions of the pixels can be set. As an example, the system layout for the standard mode optical profiler is displayed in Figure 129.
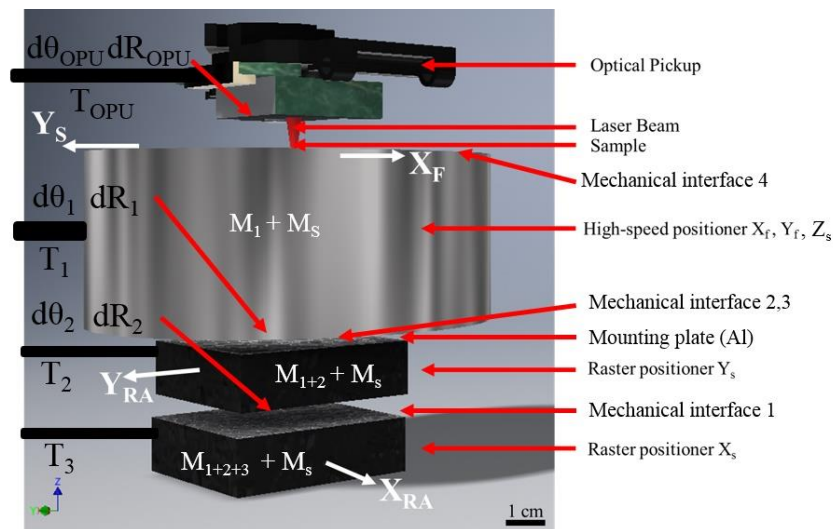
Figure 129: System layout schematic of the OPU-based standard mode optical profiler used to image features on a leaf surface. Here we see how two single-axis long-range 'Raster positioners' (ECS3030, Attocube) are responsible for low-frequency raster path positioning (X_s and Y_s) to translate the location of each collected frame, are placed underneath the nPoint XY60Z20 stage, which is responsible for higher-speed scanning (X_f, Y_f and Z_s) to create a single frame. The mass being moved by each actuator is also labelled, denoted by '$M_{component}$'. Also labelled in the schematic are external forces incident on each of the actuators due the cabling, denoted by '$T_{component}$'. Another cause for error that is labelled in the system is angular offset of the actuators and sensor coordinate systems, labelled as '$d\theta_{component}$' in each instance, where $d\theta$ is a function of the rotation about each axis ($d\theta_x$, $d\theta_y$ and $d\theta_z$). The translational equivalent vector is also labelled '$dR_{component}$' and is a function of spatial offsets in each axis (dx, dy and dz).

To give an example, in Figure 130 three overlapping frames taken with OPU optical profilometry and their corresponding positioner coordinates are presented. A prominent feature found in each of the three frames is highlighted with an arrow in each frame.
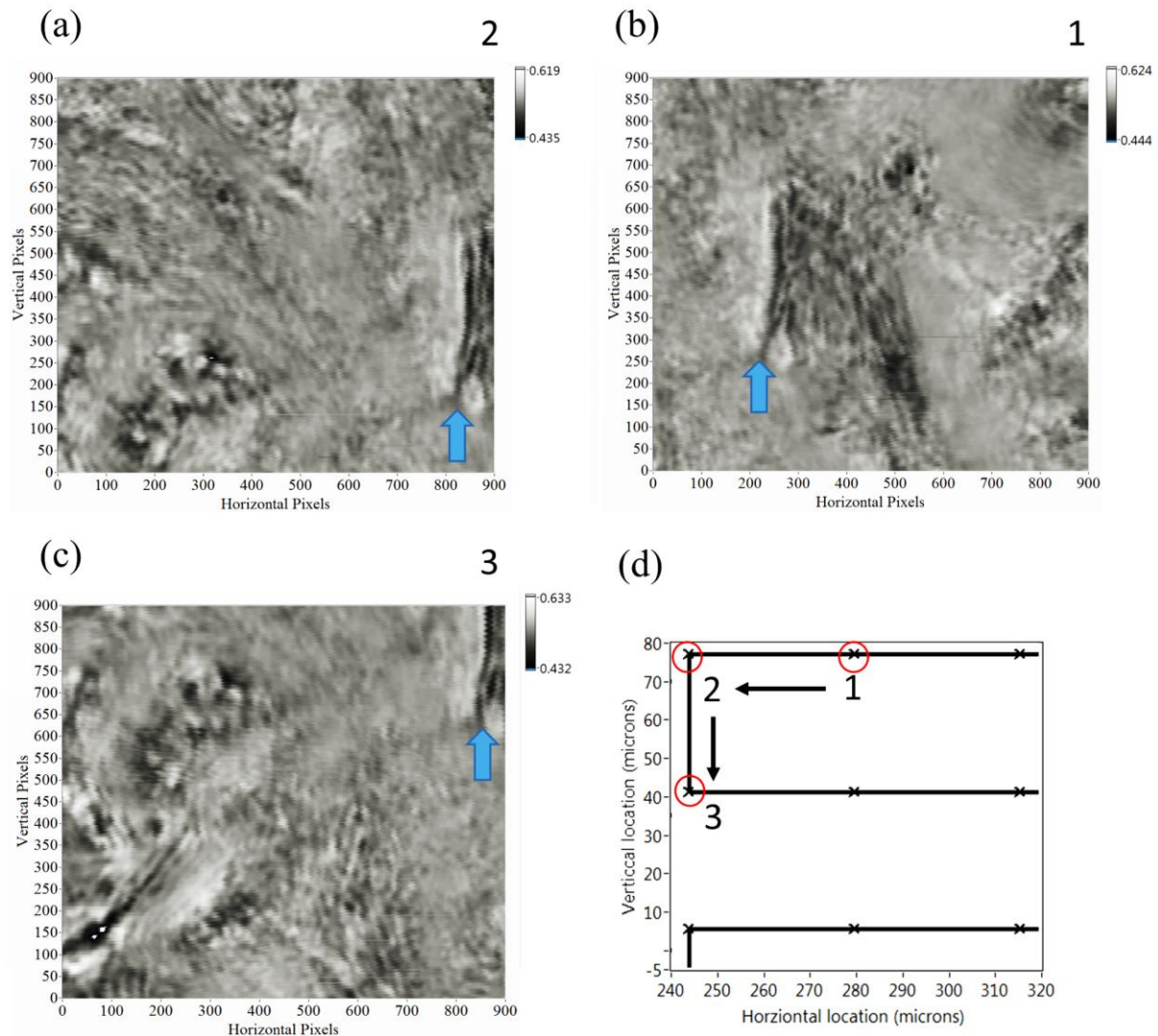
Figure 130: Selection of sample optical profilometry frames (a-c) with the prominent feature indicate with a blue arrow. The corresponding actuator coordinates are displayed in (d), where we can see a subsection of a serpentine raster path.

Subsequently, Figure 131 shows that when we align the frames described in the previous figure, then the angle between the two vectors is not equal to 90º as expected, showing that there is some cross-axial motion, in this case between the two Attocube ECS3030 stacked positioners in this configuration (Figure 129). In practice, the process of adjoining images using sensor coordinates can appear to be successful, but this typically only holds for a few frames (e.g. fewer than five) and often only when moving in a single direction due to compound errors. There are several possible disruptions to this simplistic approach that prove difficult to engineer against. For example, a collection of error sources arises from stacking linear actuators on top of each other - an approach commonly found in the

186

techniques reported in this thesis. These error terms can arise in different ways depending on the configuration and number of actuators. A small amount of inevitable mechanical play or backlash can be induced into the system with every mechanical conjunction. This can result in small erroneous offsets when switching the direction of motion of the stacked positioners. Furthermore, as the number of stacked positioners increases so does the height of the sample platform from the lowest actuator and the number of conjunction interfaces. As the distance between the sample and the furthest positioner increases it promotes the likelihood for greater Abbe error. Other factors may occur due to external forces on the stages, including such as tension in cabling, gravity or magnetic coupling.
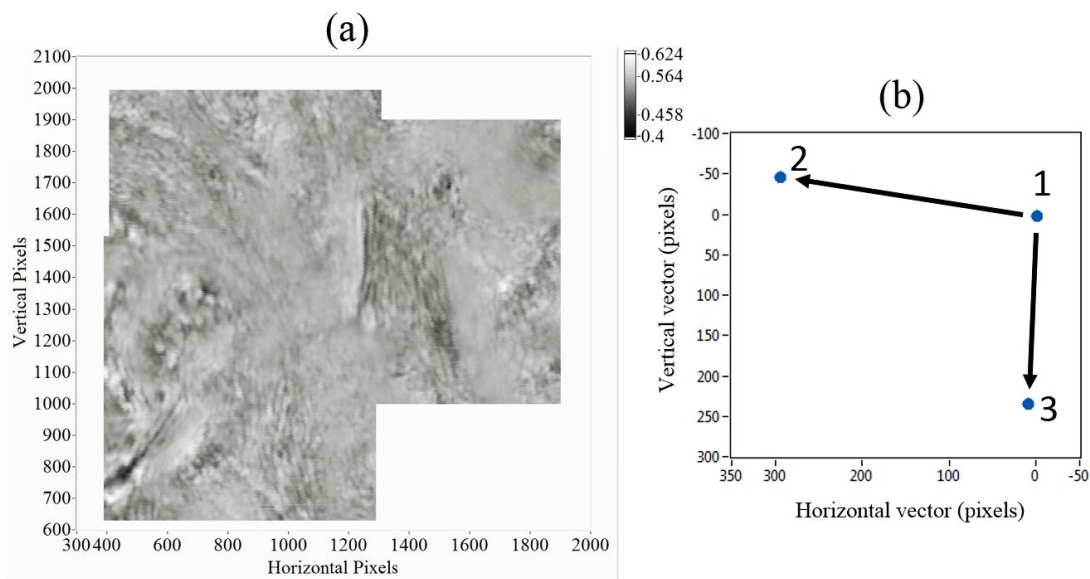
Figure 131: Example canvas with three frames inserted, with the prominent feature aligned by eye (a) and the vectors corresponding to the displacement between them (b), equal to (10,233) and (296,-48) pixels where the original physical translations were request to be (0 µm, 35 µm) and (35 µm, 0 µm), respectively.

In addition to the introduction of mechanical play, consider the time taken to image a single frame in surface microscopy. For the techniques reported in this chapter it is typically: 1 s for HS-AFM (typical area of 4 by 4 µm) (2); 120 s for standard optical profilometry (area 50 by 50 µm, Chapter 4: Section 4.2); and 1 s for HS optical profilometry (with typical area 35 by 50 µm, Chapter 4: Section 4.3). When extending this to many frames to cover a typical large area image of 250 by 250 µm area, including a 50% overlap, the time taken to image this equates to 8.7 hours, 3.7 hours and 0.08 hours, respectively. Over these timeframes, for a typical lab environment, with one or more users and several fan-cooled instrument control boxes within a few metres of the instrument, we can hypothesise that the local room temperature could to vary by $>\pm1°C$ without significant temperature regulation. From this, we can inspect how thermal contributions would lead to offsets of the sample compared to the coordinates reported by closed-loop nanopositioners even in a single aluminium mounting plate such

as that found in the OP HS-AFM (2). By taking the linear coefficient of thermal expansion of aluminium (α: 23 μm.m^{-1}.C^{-1}) we can calculate that a 10 cm bar of aluminium would change dimension by 2.3 μm .C^{-1} per degree Celsius. Extending this for an instrument, which operates in two dimensions, an aluminium scanner mounting plate a possible temperature dependant offset of up to 3.25 μm.C^{-1}. In addition, the instrument is typically made of many components of several materials, each with the potential to contribute to temperature dependant expansion and compression offsets.

To reduce the effect of any low frequency (<1 Hz) height sensor (i.e. in the z-channel) drift or error, due to thermal factors, sensor drift accumulation or vertical actuator motion, a *median overlap correction* can be implemented. To apply this correction, the *placement vectors* (V_f) (Figure 132 (b)) of an overlapping *template* and *frame* can be used to identify the intersecting area between the two images, where common surface features can be found. The median value of these intersecting areas (A_n), i.e. m_{A1} and m_{A2} in Figure 132 (c) below, is then found in both the *template* and *frame* before the difference between the two is calculated (i.e. m_{A1}-m_{A2}). This difference can then be subtracted from the most recent image (i.e. *frame)* before finally placing it in the *canvas*.
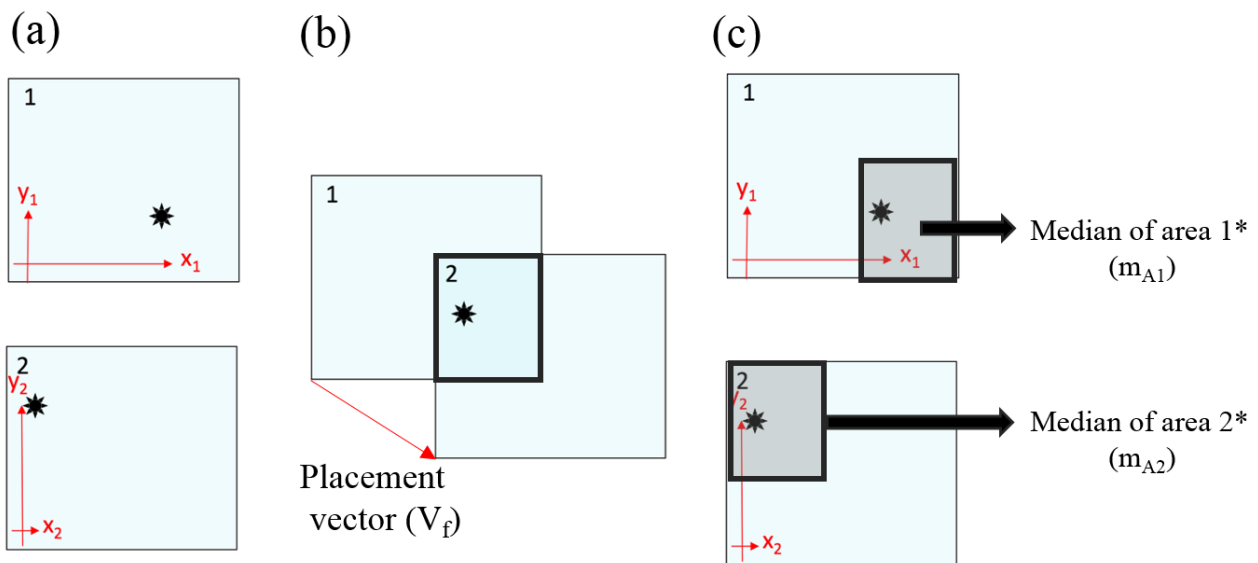
Figure 132: Schematic showing the process by which the median value in overlapping regions can be used to account for low frequency drift in height sensor measurements. Here, (a) shows template (1) and a frame (2), (b) shows a prominent feature common to both images and the placement vector (V_f) between 1 and 2 and (c) shows the regions in each image where the median values of the overlapping regions (m_{A1} and m_{A2}) are taken from.

This process is underpinned by the assumption that the surface hasn't changed in height of its own accord but that any differences in the median value of the intersecting areas between the two sequential images has arisen due to the aforementioned factors in height sensor measurement.

6.5.2.1 The limitations of stacked actuator coordinates for combining images (e.g. > 10)

Using the calibration shown in Figure 131, the calibrated pixels and the reported physical coordinates from the actuators can be used to work out the corresponding pixel coordinates where each image should be placed in the canvas. By extending this basic approach to a dataset of 100 frames, that have been collected by performing a serpentine raster pattern (Figure 133 (c)), we can see how the data combines to produce the composite image in Figure 133 (a). An initial observation of this composite image, by eye, shows some distinguishable long-range order across the sample texture. However, closer inspection (Figure 133 (a) and (b)) shows prominent vertical and horizontal stitching lines, and a decrease in clarity compared with the data presented in Figure 133 (d). These stitching artefacts are a typical indication that the positions of the frames, in this case due to the unreliable actuator coordinates, are incorrect. In turn, this results in the median overlap correction to incorrectly offset the frames with respect to one another, as the median values will be falsely calculated by the difference in features present in the two areas. This causes poor combination of the surface data and visual confusion in the local topography. Though these typically look like digital artefacts and are ordered, and can be observed to be unrepresentative of the natural topography of the surface.

A clearer representation of the surface data is shown in Figure 133 (d). Looking at an equivalent subsection of the composite, we see that data clarity can be preserved in this combination process. The coordinates used to generate this composite image (Figure 133 (f)) are notably different to those in the previous composite. By eye, there is good vertical alignment of coordinates (in Figure 133 (f)), as the vertical lines joining the coordinates run approximately parallel to one another. However, when looking at the horizontal lines joining the coordinates we see that they are not parallel in Figure 133 (f) and not perpendicular to the vertical lines as expected from Figure 133 (c).

By looking in more detail at positions displayed in Figure 133 (f) to create the composite image (Figure 133 (d)), we can examine the repeatability of the translation vectors over the 100 frames (Figure 134) and identify if there was a greater deviation from the serpentine raster pattern than reported by the actuators. This explains why Figure 133 (a) was a poor representation of the surface, as the performed vectors vary from the magnitude of the expected vectors, which should have a magnitude of either 292 pixels or 0 pixels corresponding to the 0 μm and 35 μm steps that made up the raster that was used. Instead, in Figure 134, we see that there is a moderate spread in the three distinct groupings of vectors, with the average spread on the mean in the vertical direction found to be 53.6 pixels, and 3.37 pixels in the horizontal direction.
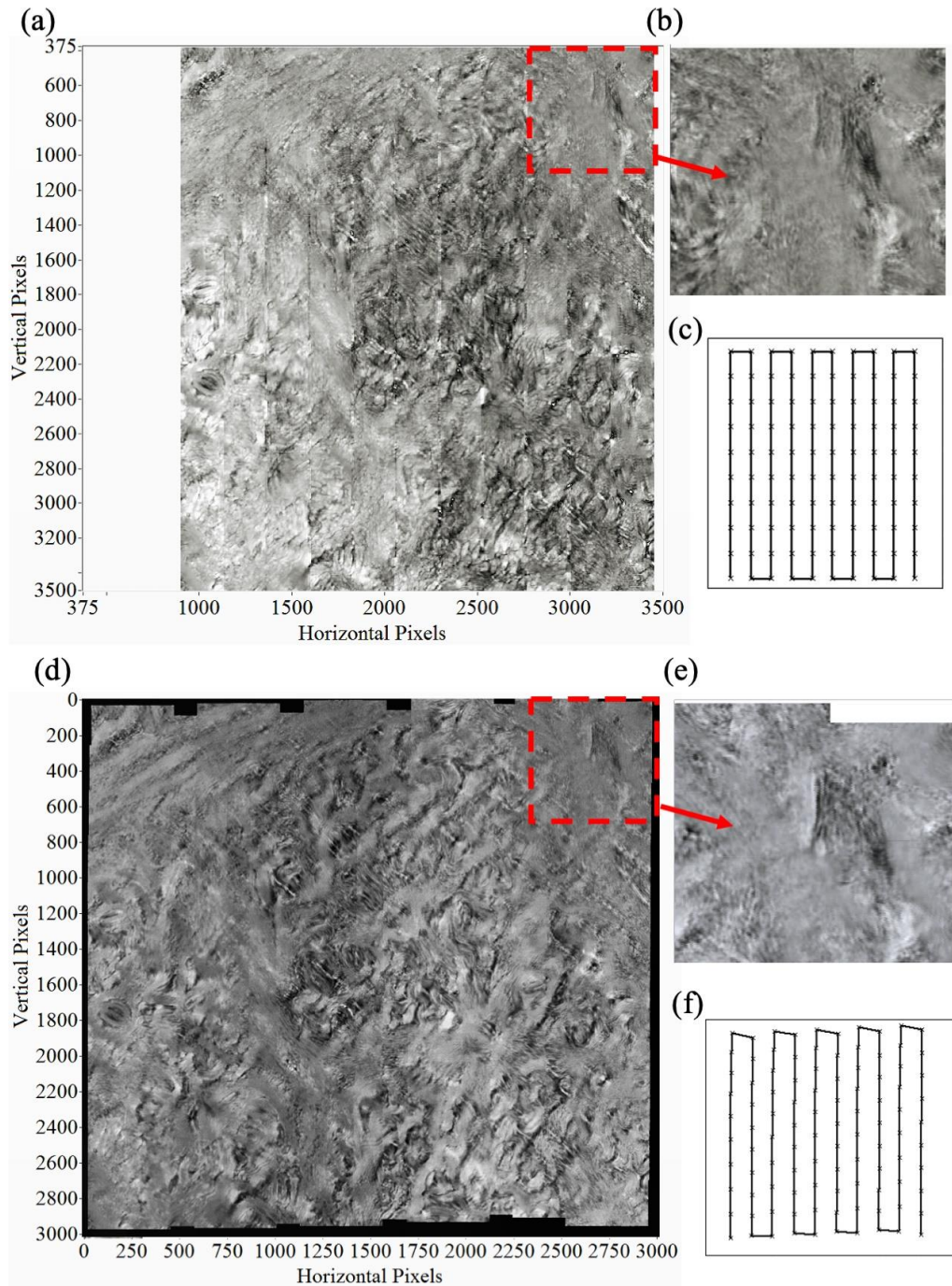
Figure 133: Composite image formation: (a) is a composite image, with a zoom-in region (b), formed using the physical reported actuator positions (c) to combine the frames in (a), (d) shows an improved version of this composite image with zoom-in (e), formed using the vectors calculated by automated feature recognition with normalised-cross-correlation to combine frames for (d).
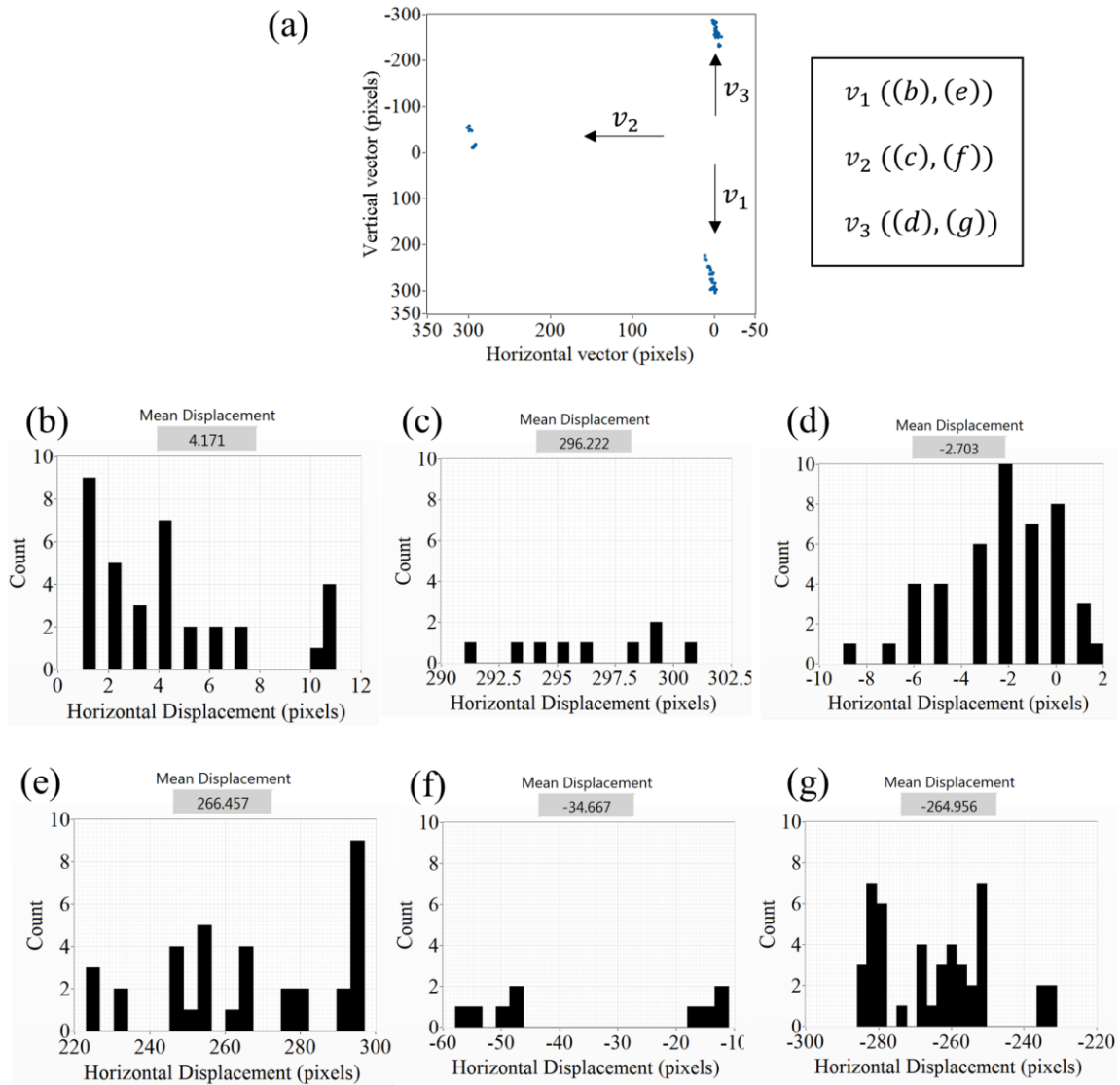
Figure 134: Summary statistics of the vectors used to create the composite in Figure 133 (d) where (a) shows a plot of the data in vector space and the three main types of vectors present (v₁-v₃) and labels how the vector components correspond to the vector component histograms in ((b)-(g)) below.

In Figure 135 we see two composite images of the data previously displayed in Figure 133, where one uses the stitching process outlined in this thesis and the after uses a commercially-available software environment called Image Composite Editor (ICE).
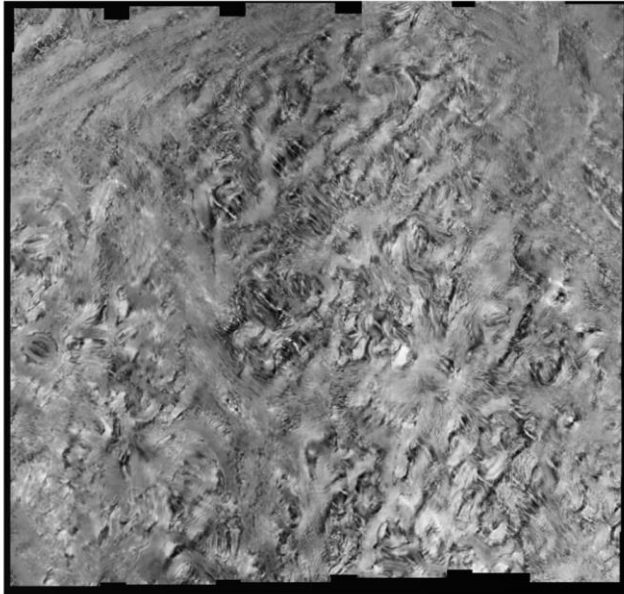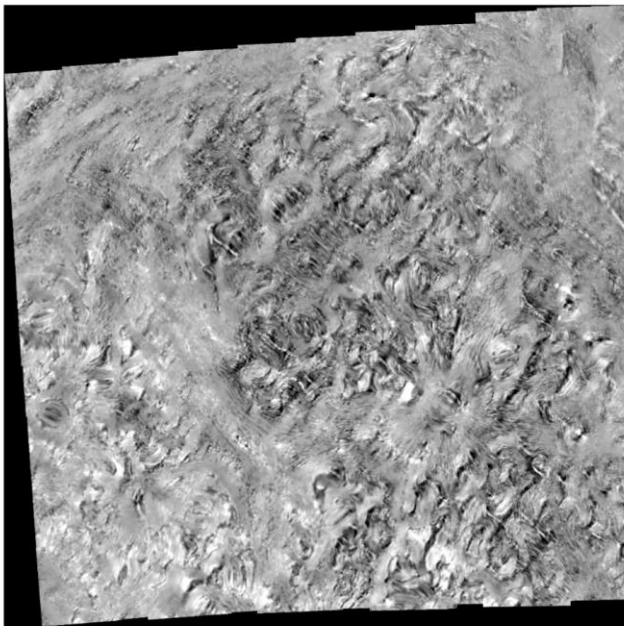
Figure 135: (a) Composite image of optical profilometry data of a surface impression of a leaf (species: arabidopsis) formed using the NCC-based automatic stitching algorithm explained in this chapter. (b) Composite image formed using Microsoft's Image Composite Editor with the same input data as (a).

Comparing Figure 135 (a) and Figure 135 (b), we see that the two images have very similar levels of clarity and persistence of surface features, much better than seen in Figure 133 (a) constructed from a raster pattern of locations. However, from knowing how the optical profilometer is constructed

and how it took these images is constructed, it makes the construction of Figure 135 (b) seem highly unlikely to be correct for a number of reasons. Firstly, it can be seen in Figure 135 (b) that the left-hand vertical edge of the composite is both significantly shorter than the right vertical edge and at an angle of 4º to vertical. This is also true when comparing the top horizontal and bottom horizontal lines. These factors combined would imply that either the imaging window size or step length has changed, and that the actuators are rotating significantly, with micrometres of translation. Given that the instrument has each of the two ECS3030 (Attocube, Germany) actuators bolted in four places to the actuator below and each actuator runs along a pair of rails with specified yaw, pitch and roll angles of < 0.1 mrad over 10 mm of travel according, to the manufacturers, this amount of angle change is unlikely to be a true motion. Furthermore, the scan window is being monitored by a pair of closed-loop sensors, which did not report a change in scan window. The step lengths are also reported by closed-loop sensors in each axis, with neither registering this change in step size.

With this in mind, it gives strong motivation for developing a program or image composition environment tailored to the instruments developed in this work (Chapter 3 and Chapter 4), where constraints specific to each instrument used can be implemented, which can be different to those commonplace in photography. The following section looks to detail the method that was created as part of the work done in this thesis and successfully implemented to combine images taken from multiple overlapping locations in surface microscopy.

6.5.3 Automatic feature recognition for scalable image combination

As seen in the previous section (6.5.2), combining many images (i.e. >10) collected using a raster with a serpentine pattern poses several challenges due to significant uncertainty in the reporting of stacked actuator positions (e.g. Figure 134). In turn, a method using automatic feature recognition was developed to offer an alternative approach that can work in conjunction with or independently of the actuator positions where required. A key highlight of this algorithm is that it does not require knowledge of the underlying translation of the sample in order to combine sequential images, although they do need to overlap. As a result, this process can be used universally with datasets which adhere to the feature properties with appropriate SNR (described later in Section 6.5.3.4).

6.5.3.1 Method for automatically combining overlapping images

To find the 'best position' to combine two sequentially-captured overlapping images (i.e. a *template* and a *frame*), we could imagine trying to align them by eye in a single process, by comparing the two images and attempting to find the position that results in the least amount of blurring in the overlapping area. However, this single process would leave us with a single 'best position', telling us a single solution for the best location to combine the two images. From everyday experiences of

attempting to match shapes (e.g. checking two signatures) or building images together (e.g. tiling assembly) together by eye we know that it is easy to be 'fooled' by similar features or colours. This problem is typically made harder if there are degrees of symmetry in the shapes of interest or there are multiple repeats of the same shapes. A common way in which we may encounter a similar but subtly different challenge by eye in everyday life is in jigsaw puzzles for entertainment.

As an aside to give this work some general context imagine if there was a prominent feature (e.g. bold line or distinctive symmetrical shape) in a jigsaw image running across several pieces. To construct the region where the prominent feature is expected from the image preview on the box we would likely first find several pieces with snippets of this prominent feature. On a first pass, many in this selection of pieces may interchangeably look like they fit more than one region of the area containing the prominent feature in the jigsaw puzzle as we know very little about their final orientation or positions. If the prominent feature is quite uniform, over a range greater than a few pieces and with few surrounding additional features, it becomes even more challenging. In the fields of mathematics and computer vision an object of this sort is referred to as self-similar (186). When looking closer at the remaining pieces, additional information can be gained by ignoring the prominent features and looking for any others such as shading, specific textures or less-prominent features. It is this subtler information that is most useful to differentiate between pieces that look similar. To aid with solving this, jigsaw puzzles have the added constraint that each piece is uniquely shaped. In practice, this property can be used to isolate the more probable solutions (187). This case draws some parallels with the challenge of combining two overlapping microscopy images, where we may find many apparent 'good' solutions to overlay one image over the other in many places along prominent features. This is made more challenging if there are repeat structures or shapes with a high degree of symmetry, making it harder to identify the best results.

The method that has been developed in this work can be divided up into the following principal parts: *de-noise*; *initialising*; *comparison*; *statistical evaluation;* and *merge*. For each of these parts there are method variations that could be substituted, replaced or added to, to achieve the best outcome of the algorithm. However, for the purposes of this work the algorithm has been tailored for combining the data produced in real-time and to be applicable for a wide variety of sample types for the surface microscopy techniques outlined in this thesis.
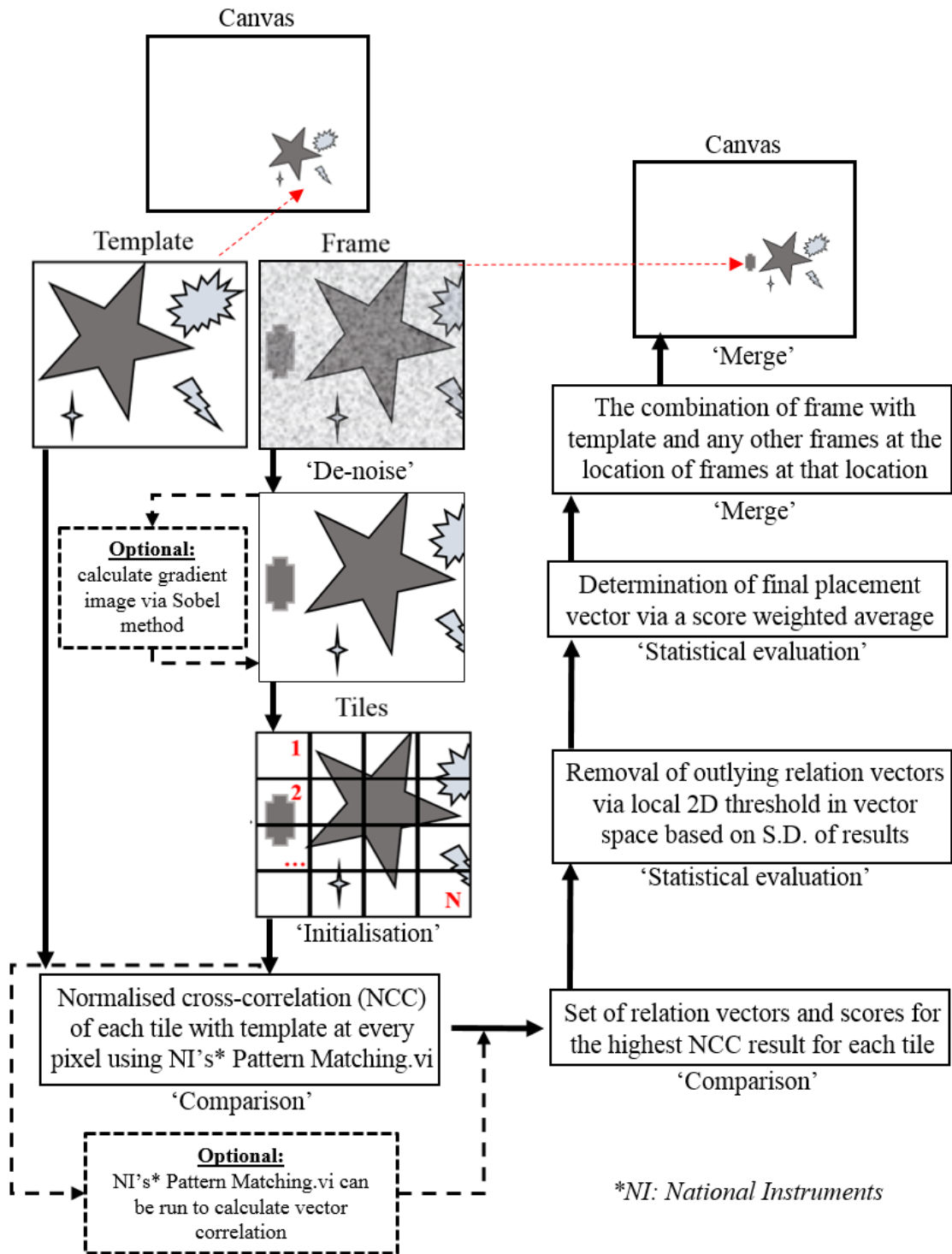
Figure 136: Overview of principal processes done in an automatic image stitching algorithm represented as a flow diagram summarising the five stages of processes: *de-noise, initialisation; comparison; statistical evaluation;* **and** *merge*.

'De-noise':

In this part of the algorithm, the new image or *frame* can be acted upon in an attempt to remove any sources of uniform noise, impulse noise, scars or image slope that might be present in the data. The methods for doing this include the tools described previously in this chapter (section 6.3).

'Initialisation':

One way to sub-divide these challenges is to divide each image into many sub-images or *tiles,* so as to break apart the contributions of any prominent features. Each *tile* can then in turn, contribute individually to the final matching of the offset between two frames. From these considerations, it is probable to think that uniform features can lead to more mistakes in matching features and, therefore, greater uncertainty in the outcome of identifying commonality inbetween two or more images. To manage the introduction of this uncertainty, a *frame* can be sub-divided into several sub-images or *tiles* (n_t) and then each compared to the *template*. The preferred number of tiles used in this stage of the process is a user preference. Selecting the appropriate number of tiles is dependent on factors such as the number of pixels per image, required processing time and image features. Once the tiles have been extracted they can be sent to the comparison section.

In turn, we can find a number (n_v) of relation vectors that will point from common features in the template to common features in the frame. By performing a comparison many times, rather than just once, the contributions from each instance of commonality found can be isolated. Later, statistical evaluation of these results can be used to discount outliers and mismatches. By knowing where each of the *tiles* have been taken from in the *frame*, we can subtract their original *tile position* from their calculated *placement position* calculated in the comparison step to give a set of *placement vectors*. Figure 136 shows a simple step-by-step schematic of the steps taken to allocate a set of tiles from a template and frame pair.

'Comparison':

There are many forms of the 'comparison' process which can be used to recognise features common between a tile and a frame. Indeed, within the software architecture developed in this work many of the variants of this process is available for immediate implementation. A range of the tools typically used in the comparison of two images are available in the 'Machine Vision' library that comes in LabVIEW's (National Instruments, USA) Vision package. In this work, the Pattern Matching tool has been selected for further evaluation as it implements Normalised Cross-Correlation (NCC), which is a popular and well-proven method for quantitative measurement between images in microscopy (188) and other image processing. The key benefits of NCC include its tolerance to variations in contrast, blur, noise and geometric distortions, all of which are commonplace in microscopy and the images processed in this thesis.

196

In order to calculate the NCC between a tile, $t(x, y)$, of size d_x^t by d_y^t pixels and an image, $T(x, y)$, of size d_x^T by d_y^T pixels, where $d_x^t \leq d_x^T$ and $d_y^t \leq d_y^T$ we must first consider the correlation, $C(i, j)$, to be calculated:

$$C(i, j) = \sum_{x=0}^{d_x^t - 1} \sum_{y=0}^{d_y^t - 1} t(x, y) \, T(x + i, y + j) \tag{32}$$

where $i = 0, 1, \ldots, d_x^T - 1$, $j = 0, 1, \ldots, d_y^T - 1$

It then follows that the normalised cross-correlation, NCC(i,j), is:

$$NCC(i, j) = \frac{\sum_{x=0}^{d_x^t - 1} \sum_{y=0}^{d_y^t - 1} (t(x,y) - \bar{t})(T(x+i, y+j) - \bar{T}(i,j))}{\left[\sum_{x=0}^{d_x^t - 1} \sum_{y=0}^{d_y^t - 1} (t(x,y) - \bar{t})^2\right]^{0.5} \left[\sum_{x=0}^{d_x^t - 1} \sum_{y=0}^{d_y^t - 1} (T(x+i, y+j) - \bar{T}(i,j))^2\right]^{0.5}} \tag{33}$$

The computed NCC is in the range from -1 to 1. By looking at all the NCC results from the positions (i, j) in the template $T(x, y)$ with the tile $t(t, y)$, we can also obtain a 'score' (s_{NCC}) that assesses how highly correlated a tile is across an template and fined a maximum. This score can be used to identify the best location of feature coincidence for each of the *tiles* with the *template*. Later, the score is used in the statistical evaluation by combining the score and the best position results from each tile to establish a weighted average and to find the final placement vector describing the best location for the frame to be placed in relation to the template.

When implementing the NCC as part of the Pattern Matching tool (National Instruments, USA), other options are available to improve processing time and versatility. The first of these is the 'Pyramidal matching' which first scales both the tile and frame to be sampled to lower resolutions using Gaussian pyramids (189,190). This process can help improve computation time by working with smaller images. The algorithm then initially goes through a learning phase, where it computes the maximum pyramid level for a tile under inspection. Here, the user can set bounds for the detection of features to be searched for over a range of geometric transformation, such as scale or angle invariance. These can be set to reduced ranges or turned off (e.g. where these transformations are unlikely) in order to save computation time.

Furthermore, the Pyramidal matching in this software can be operated in two modes as elected by the user, either greyscale or gradient image (177) via the Sobel method (171). The greyscale method is suitable for general use and is more useful when there is a high density of features or predominantly surface textures. The gradient method can be more useful in the cases when an image is dominated by strong edges, high resolution and lines. Whilst the gradient method is not evaluated in this work, it is possible to set the user preference in the developed software and can be used where samples may require it.

Now, by returning to the example dataset presented in Figure 136, each of the 16 tiles selected in the template can be passed through the Pattern Matching tool to generate a set of relation vectors (n_v) highlighting how the features in the template correlate to features found in the frame. Looking in Figure 137, we see how an example tile, tile N = 16, has been matched in the frame using the Greyscale Pyramidal method. Figure 137 (c) then shows the results from the 16 tiles, nine have found matches (red crosses). Having then subtracted the original position of each tile in the template it is possible to see the set of placement vectors (Figure 137 (d)) that inform us of the vector between the centres of the template and frame.
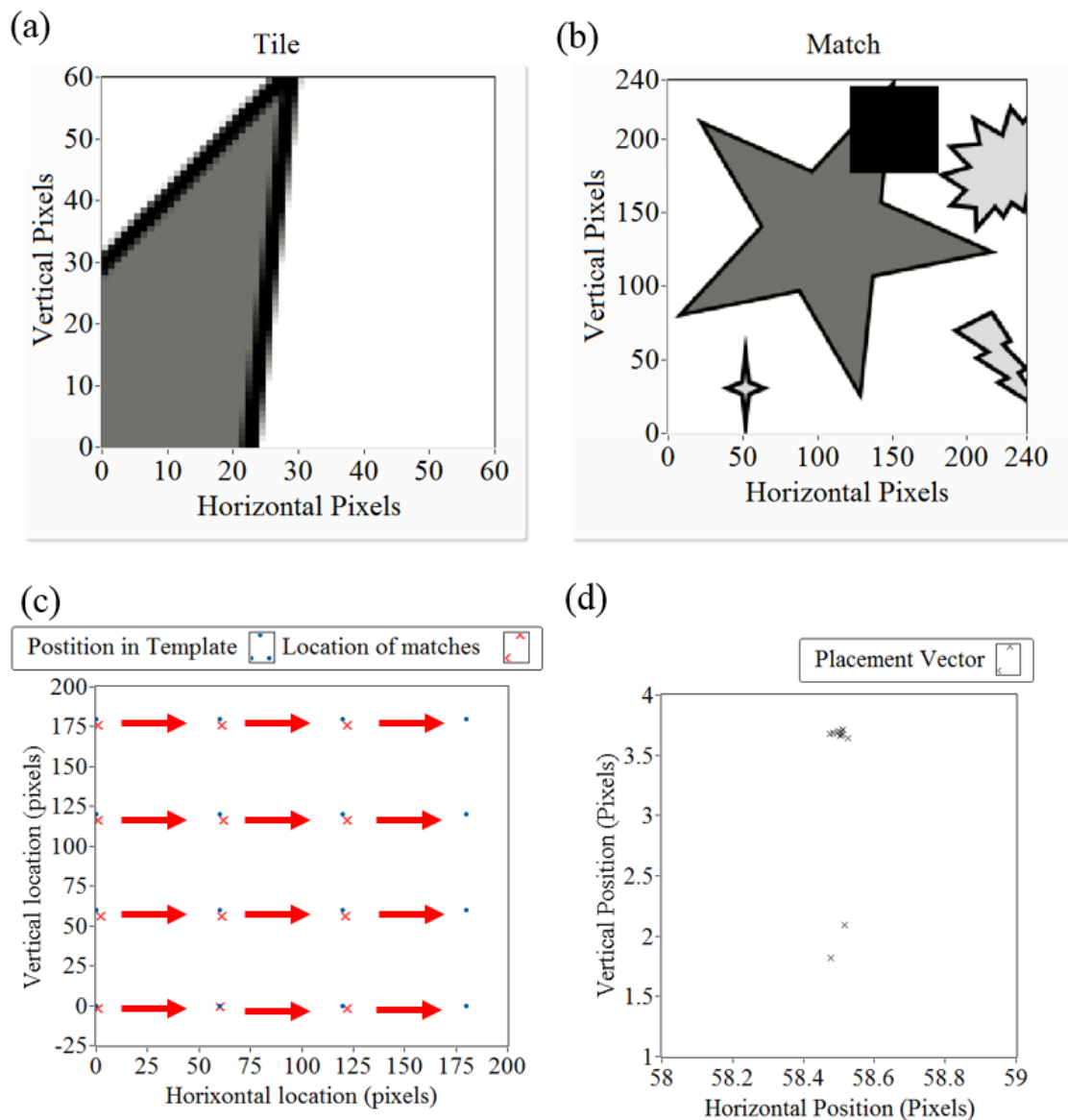
Figure 137: Example tile (a) being found in a frame (b) accompanied by the locations of the tiles in the template (blue) and the matches found (red crosses) in the frame and their corresponding relation vectors (c) leading to a set of placement vectors being calculated in (d).

In the next stage of the process we can choose how to interpret the set of placement vectors that has been calculated. From the experimental results as seen in Figure 137 (c) and our intuition of the likelihood of mismatching results, we see that there is a reasonable spread in the possible vector matches. This is because there is a chance that multiple areas of a frame correlate well with a tile. As we compare the tile with the any location in the frame, there is the possibility for a large mismatch (i.e. several tile widths away from the correct match). However, because we are looking for the best match calculated via NCC, the weak matches (i.e. below a threshold) are discounted. For good signal-to-noise samples we expect the set of placement vectors, for any give tile, to have a majority of matches close to the correct match and perhaps a few outliers.

It is expected that we have a typical sample size of between 9-64 vectors, depending on how many tiles the user chooses. For lower sample sizes, the mismatches or outliers in the set of placement vectors will cause a significant contribution in erroneously offsetting the mean. To mediate against the outliers having this affect, we can first look at some simple statistics behind the set of placement vectors. For all placement vectors we can find the mean vector (μ_v) and standard deviation of the vectors (σ_v). The standard deviation can be used to set a threshold radius, around the mean in 2D vector space, where the number of outliers (n_{out}) outside this radius will be discounted. A radius of less that one standard deviation is typically used. For example, during the work carried out in this chapter it was set to 0.6 of one standard deviation.

Once we have removed the outliers, we can use the normalised scores ($\hat{s}_{NCC}$) calculated earlier in the NCC, and then normalised to run between 0 to 1, to calculate a weighted average of the remaining datapoints to obtain our final placement vector (V_F). This is done by finding the average score-weighted distance away from the unweighted mean placement vector ($\bar{V}_p$) for all remaining placement vectors ($n_v - n_{out}$) and adding this to $\bar{V}_p$, as in equation (34):

$$V_F(x,y) = \bar{V}_p + \frac{1}{n_v - n_{out}} \sum_{K=0}^{K=n_v-n_{out}} (V_p(x,y) - \bar{V}_p)\, \hat{s}_{NCC} \qquad (34)$$

Once the final placement vector has been established, this can then be used to merge the frame into the canvas in the merging stage.

'Merging':

This part of the process looks to make use of the final placement vector (V_f) as shown in Equation 34 and combine it with any image data that have already been placed in the canvas. As many frames may overlap in the canvas due to either raster paths or free roaming motion across the sample, a record of the number of frame pixels that have been placed into the canvas at every location is kept. This array is called the pixel stack canvas. In a similar way, an array summing the greyscale values

from any overlapping frames at the same location (the pixel sum canvas) is built. A composite image can then be calculated by finding the mean at every pixel by dividing the pixel sum canvas by the pixel stack canvas. For some applications, where the end state of the sample at each location is more relevant, the most recently placed value could be used instead of the average when creating the composite.

At this step of the process, there are a number of additional layers of processing that could be developed in the future, as described in literature. These processes look to improve the 'smoothness' of the stitching interfaces in the composite image, including calculating a minimal error boundary and implementing Poisson or pyramid blending. Other beneficial post-processing that can be done in post-processing includes using Gwyddion's 2D FFT filter (45) to diminish stitching interface lines. As the images are square or rectangular, many of the stitching artefacts are highly aligned along the up, down, left and right directions and are of high contrast. Filtering out the high-frequency components in the 2D FFT along the horizontal and vertical axes can help to remove these components.

6.5.3.2 Summary of method

In summary, a process for combining surface microscopy images from locations with overlapping fields of view to create a larger composite image has been described here. The process has five distinct phrases of operation. These phases aim to respectively: reduce 'z-channel' noise on the data; segment the newest image into sub-images or 'tiles'; perform a comparison of each of the tiles with the other image; statistically evaluate the results from the comparison; and then, once the best guess of the optimal place to combine the two images has been found, merge them together before placing them in a pre-allocated canvas.

There are limitations to the approach of this method for all use cases in surface microscopy. For instance, this method is not compatible with sparsely-taken data, where there is not an overlap between frames. Equally the technique can be more prone to error by any loss of quality of image clarity during translation (e.g. due to mechanical excitation or blurring) and will perform poorly if the surface is constantly evolving (e.g surface corrosion or sweeping of loose material). Equally, this form of the method can be susceptible to compound error as each image is only compared to one other, even when several may in fact overlap. An extension to this method would, therefore, involve using a second pass of the comparison and final placement vector calculation once an initial composite image has been formed to show which images overlap.

In the following sections, captured images are used to further evaluate the performance of this approach for combining images. Using an HS-AFM dataset, a comparison of the placement coordinates, as calculated via the method described in this section, and the placement coordinate reported by the instrument's actuators is carried out. In addition, a control dataset, consisting of a large image divided into smaller images from known locations, is used to evaluate the performance of reconstructing the

original images from the smaller images. In turn, 'z-channel' noise is added to the small image and the success of the automatic combination of images is tested at various signal-to-noise levels.

6.5.3.3 HS-AFM case study of AISI type 304 stainless steel

In this section the automatic feature recognition method described in the previous section is applied to a real 'free-roaming' AFM dataset. The dataset was taken with a user guided free-roaming path over a sample following a grain boundary on the surface of thermally-sensitised stainless steel (AISI type 304), prepared and imaged by S. Moore using an HS-AFM with an LDV (Polytec GmbH, Germany) detection head and 3 axis sample actuation stack (SmarAct GmbH, Germany) (1). In the actuator stack, the positioners are specified to have sensor resolution of: x=1 nm; y=1 nm; and z=1 nm. This stack was also specified to have a repeatability of up to x: $\pm$ 60 nm, y: $\pm$ 50 nm and z: $\pm$ 100 nm, as detailed by the manufacturers. Here, the height range of the images is of the order of tens of nanometres, with three primary types of surface features. The three surface features are made up of a prominent grain boundary (a prominent self-similar feature), surface corrosion products (e.g. salt), offering a unique surface texture, and a number of polishing impressions as is typical of this type of sample (105). Over a time period of 6 minutes 40 seconds, 200 AFM images were taken at both repeat and unique locations across the sample at two frames per second. Due to the free-roaming nature of the dataset, there is at least one vector populating each quadrant of the vector space (i.e. (+x,+y), (+x,-y), (-x,-y), (-x,+y)) between images. Also, the motion vectors used to explore the sample vary greatly in magnitude throughout the dataset from frame to frame. Therefore, a much more diverse dataset than exhibited in Figure 138 (a) as is common for the serpentine raster path.

In Figure 138 a composite image (Figure 138 (a)) is combined using the actuator coordinates (Figure 138 (b)) for all 200 AFM images. Here we see multiple repeats of the grain boundary when combining the images, even though this feature cannot be seen in any individual frame in isolation, showing it is formed by error. There is some evidence of long-range order in this composite image as a persistent grain boundary is visible across the image, although convoluted with false-placed frames, and a triple point can be identified where three grain boundaries intersect. As such, it can be deduced that the actuator position can inform us as to the direction that the user has moved over the sample. However, the actuator sensors do not appear to be known to enough certainty for direct image stitching as there is a lack of coincidence of common features in the composite image, as can be seen in the repeat features highlighted with blue arrows in Figure 138 (a).
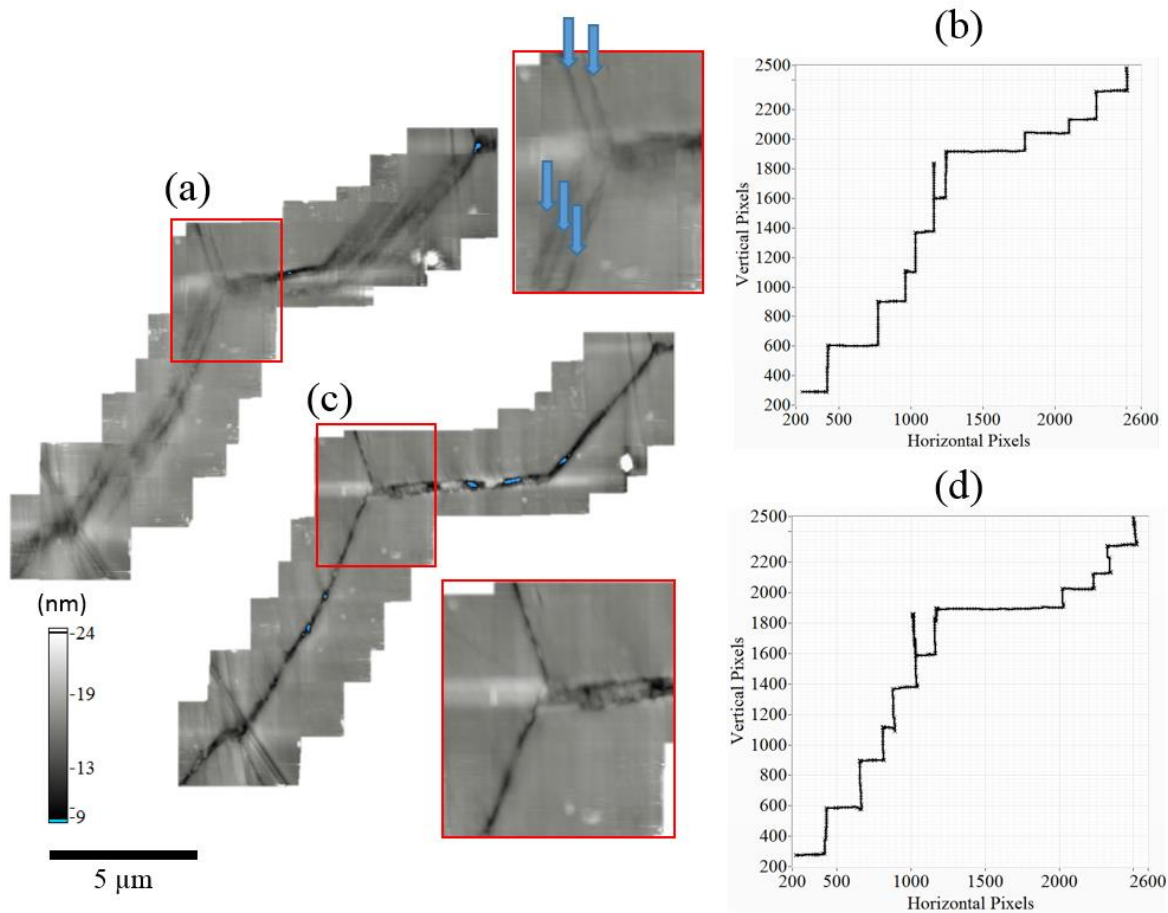
Figure 138: (a) Composite image made from 200 HS-AFM frames (6 nm per pixel) of a grain boundary formed using actuator determination of position (b). (c) Composite image formed with the coordinates found using the automated feature recognition algorithm described in the previous section.

In contrast, Figure 138 (c) shows a composite image formed using coordinates found via automatic feature recognition as in Figure 138 (d). In this process, the actuator positions were not provided to the algorithm at all and instead the placement vectors were calculated using normalised cross-correlation, with tile dimensions of 50 by 50 pixels from a 300 by 300 pixel frame with the 300 by 300 pixel template, of features implementing the method mentioned above. By inspecting and comparing Figure 138 (b) and Figure 138 (d), we see that the number and direction of the motions across the sample are the same but that there appear to be discrepancies in the length and straightness of the constituent parts of the overall path. In the composite image Figure 138 (c) there is no visible evidence of multiple repeats of image features and the image contrast is higher. Furthermore, the clarity of the composite image is much more akin to a single frame, indicating that the stitching process has resulted in little compromise to the integrity of the data to correctly represent the surface.

In Figure 139, the translations between sites on the sample are plotted in vector space (see Figure 139 (a)) for both the actuators, and the results from automatic feature recognition and the

discrepancies between the sets of vectors are plotted in Figure 138 (b). From this we can see that the differences are dominated by errors highly aligned to the vertical and horizontal axes.

(a)   (b)
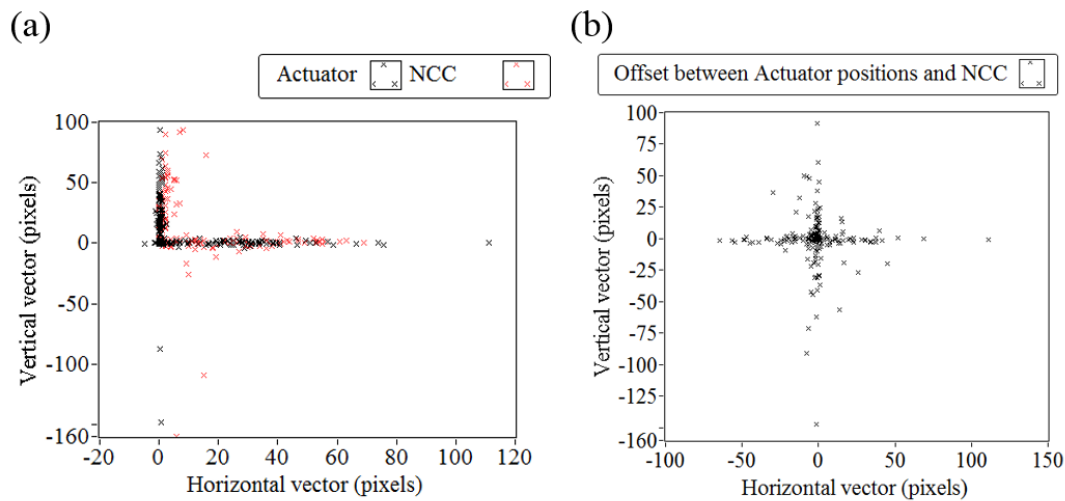
Figure 139: (a) Showing the placement vectors calculated for the actuator measured path (black) while using an HS-AFM to follow a grain boundary. In the same plot are a second set of vectors which were calculated with automatic feature recognition using normalised cross-correlation (red). (b) Plot of the difference between these two sets of vectors.

Figure 139 (b) shows that the offset data points are centred around an (x,y) mean of (0,1) pixels, with standard deviation of (20, 25) pixels. Furthermore, looking at Figure 139 (b) we see a strong tendency for the errors to align with the orthogonal axes of motion, showing that most of the errors likely come from such effects as axis backlash or actuator position overrun.

6.5.3.4 Evaluation of automated stitching algorithm for varied signal-to-noise ratio

Both composite images so far (Figure 133 (a) and Figure 139 (c)) have shown successful implementation of the NCC algorithm, however it has not yet been established how the accuracy of the final placement vectors of the algorithm varies according to known positions or varying signal-to-noise ratio of the data. As the signal-to-noise ratio varies across different techniques (e.g. HS-AFM or optical profilometry), across a single sample and from sample to sample can vary so it is important to establish where it is necessary to highlight the limitations of this approach. To evaluate this a new dataset is introduced with a variety of spatial features; it is known where each of the frames have been taken from. In turn, a varied amount of randomly-generated synthesised noise is added in the height axis, to attempt to establish a relationship between signal-to-noise and automated stitching algorithm error.

As discussed earlier composite image formation is a very broad topic as an image may refer to any form of data that can be represented as a 2D array of values. The surface features and textures are different from sample to sample with deviations in their repeatability, degrees of symmetry, spatial feature density and height variation to mention but a few key properties. Therefore, for evaluation

purposes a sample image has been selected for its variety of spatial feature properties (Figure 140). The four key types of features found in the image chosen include: 1. Organic fractal structures (191) (e.g. crack propagation, crystal growth, leaf veins and rivers); 2. Flat surfaces with a small amount of surface roughness (e.g. 2D materials, silicon wafers, highly polished surfaces and aerial photography's of bodies of liquid) (192); 3. Ordered synthesised structure (e.g. calibration patterns, grid pattern of wells, ordered material properties and other human-made structures) (2); and 4. Bi-modal distributions of terraces (e.g. 2D materials on substrate, polished duplex steel, lithographic calibration patterns and aerial photographs of clouds over water) (22).
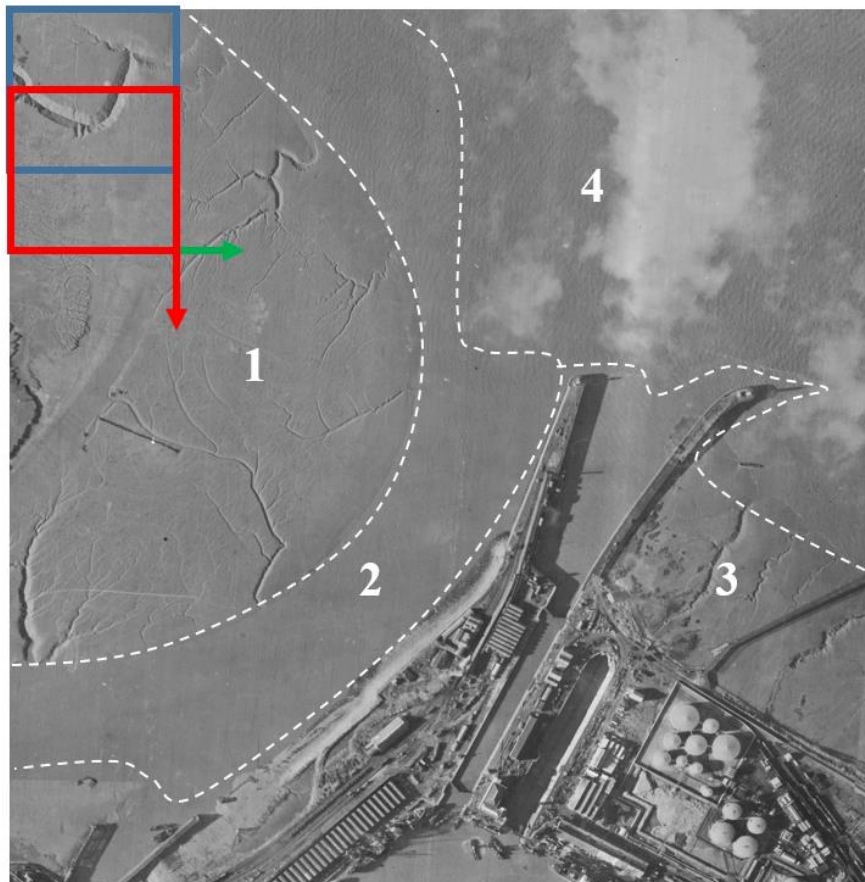
Figure 140: An aerial photograph from 1946 of the mouth of the River Avon as it enters the Bristol Channel at Avonmouth. This image (1920 by 2080 pixels) was chosen for evaluating an automated image combination algorithm due to its similarity in variety of surface features to those found in typical surface microscopy (labelled 1-4). The blue and red boxes show the area size (320 by 320 pixel) that the image was sub-sampled by using a 10 by 11 serpentine raster pattern with 50% overlap between sequential frames, where the red arrow indicates the primary translation direction and the green arrow represents the secondary translation direction of the serpentine raster pattern used. (Source: 1946 aerial imagery, English Heritage).

To make the image more akin to a property commonly found in surface microscopy, a moderate linear sample slope (at a ratio of 1:24) was added to the data (running downhill from top to bottom). A total of 110 subsections, equivalent to HS-AFM or optical profilometry frames in this instance, were then extracted from the image in Figure 140, with a serpentine raster pattern path (10 by 11) and 50% overlap between frames. This serpentine path starts in the top left and translates downwards first, and then right. Each of the subsections or simulated frames had dimensions 320 by 320 pixels. By knowing precisely which the pixels (x,y) where each of the 110 frames was originally sampled from in the image, the success of the coordinates found via the NCC method (outlined in Section 6.5.3.2) can be evaluated against these correct locations.

The results from the first attempt to combine these subsections using the method outlined in Section 6.5.3.2, without the addition of synthesised noise, can be found in Figure 141. The subsections were selected via a serpentine raster pattern akin to the path seen in Figure 133, so as expected the final placement vectors are found to fall into three distinct groupings in vector space. Due to the 50% overlap these are expected to be equal to (0,160), (-160,0) and (0,-160) pixels. The mean of these vectors was found to be correct to within ±1 pixel, with a standard deviation on each vector ≤1 pixel. Some more descriptive summary statistics on these principal vectors can be found in a table beneath the composite image in Figure 141 (b).

(a)

(b)

	Vector group 1 mean | stdev (pixels)		Vector group 2 mean | stdev (pixels)		Vector group 3 mean | stdev (pixels)	
Horizontal	0.82	0.98	-160	0.73	1.1	0.34
Vertical	160	0.42	1.00	0.00	-160	0.84

Figure 141: Recombination of the image subsections sample from an archive image (Source: 1946 aerial imagery, English Heritage) split up via a 10 by 11 serpentine raster pattern (a), the summary statistics of the final placement vectors used to do this (b) and a summary table of vector statistics. The magnitudes of the vector components were expected to be 0 or 160 in the respective directions.

Subsequently, this study looks to evaluate how the success of the algorithm, with fixed variables for tile size (40 by 40 pixels) and NCC threshold, changes with increased synthesised uniform noise in the system. From any comparison made by the automated process there are three chosen categorisations of outcomes: true match (within 5% or 8 pixels of the correct translation vector (magnitude 160) where they were taken from originally); false match (not within 5% or 8 pixels of the correct vector); and zero

match (no results found above the NCC threshold). Figure 142 shows the original frame (Figure 142 (a)) and then three additional versions of the same image with synthesised noise in contrast or the z channel were added, with corresponding ratios of 1:9, 1:3 and 1:1 as compared to the original image subsections.
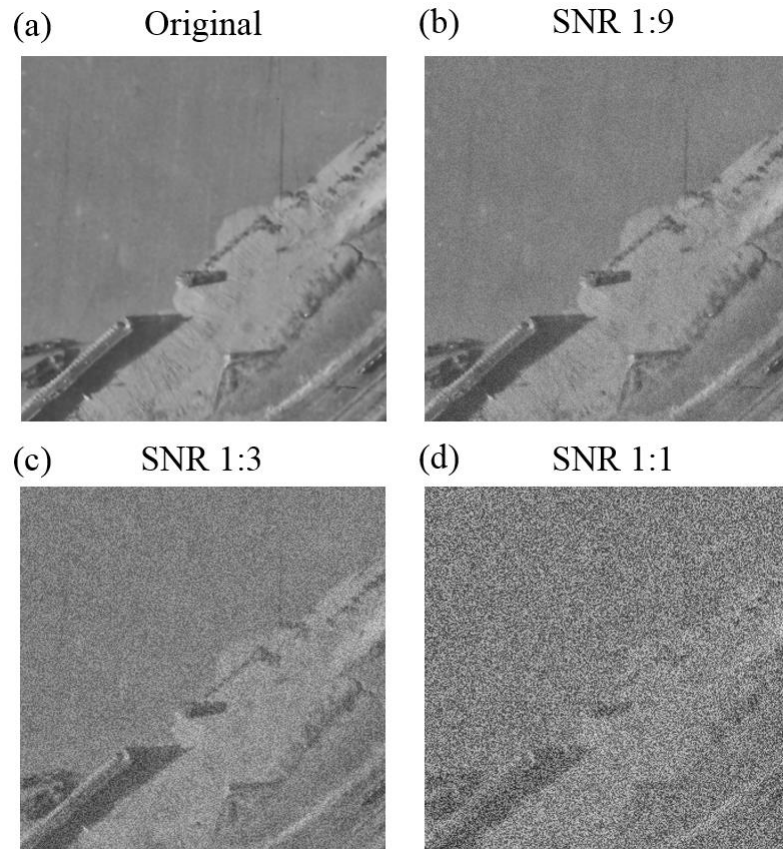
Figure 142: Images (a-d) showing examples of additional noise being added to frame 11 from Figure 140 for the purpose of evaluating the automated NCC stitching algorithm.

The process of recombining the 110 images was then repeated for nine different datasets with SNRs 1:99, 1:49, 1:19, 1:9, 1:5, 1:4, 1:3, 1:2 and 1:1. The success of the matches for every image was then put into one of the three categories (mentioned above) and plotted in Figure 143 (b) according to the dataset number. The number of correct matches from datasets 1-9 for any given frame are plotted in Figure 143 (c). These are represented spatially by overlaying the number of matches as a colour (Figure 143 (d)) over the image in the locations where each of the frames was taken from.
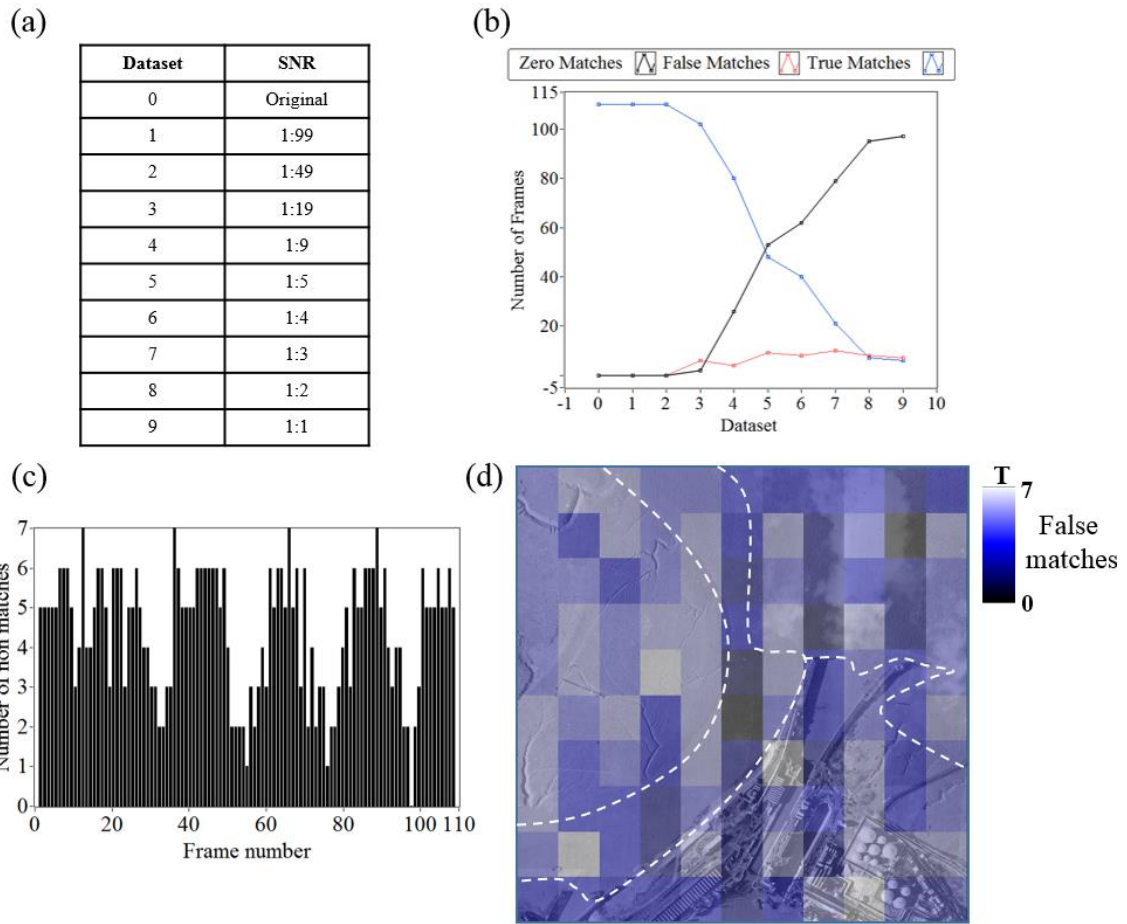
Figure 143: Key results from evaluation of the automated stitching algorithm using datasets with different SNR (a). The success of the algorithm to output several zero matches, false matches and true matches for each dataset are plotted in (b). A histogram of the number of non (i.e. zero + false) matches according to frame number are plotted in (c). These are then converted into a 2D histogram and overlaid on the original image showing the total number of non-matches in the spatial regions of the image (d).

From looking at Figure 143 (d), it can be seen how the mismatches can be mapped across the image. By calculating the total number of frames in each of the four dashed regions with different feature types and the number of mismatches in each of those areas, it is possible to generate a score for the mean number of mismatches per subsection in each dashed area. These were found to be: Region 1 (fractals): 5.17; Region 2 (flat): 4.29; Region 3 (ordered): 4.27 and Region 4 (bi-modal) 3.75.

The results show that the dashed region with the least amount of error over all SNR ratios is Region 4, made up of a bimodal distribution of high contrast areas with diffuse features which have very little self-similarity, whilst also having consistently varying texture across the image. Meanwhile, Regions 1 and 3 exhibit 37.8% & 14.4% more error respectively whilst still having many high-contrast features. In these regions, as well are the high contrast there is also a large number of repeat structures

and much self-similarity which tends to lead to high correlation in mismatching locations. Region 2 exhibits approximately the same mean number of non-matches as Region 3 although the appearance of the region is very different. In Region 2 there is a lack of high-contrast surface features. However, there is a moderate amount of persistent non-self-similar surface texture.

Whilst it was seen in some cases that automatic feature correlation using NCC proved to be very effective, for example in Figure 133 (leaf) and Figure 138 (steel), it was later shown in lower signal-to-noise images (Figure 143) how this approach can prove less effective with images with decreasing signal-to-noise ratios. Here, we saw the number of true matches fall to 50% as SNR increased to 1:4 – 1:5. As such, it is important that further user input be used to accompany the two previously-outlined methods. Therefore, a final location may be found using either actuator positions, normalised cross-correlation or user input, or indeed a weighted combination of all three.

6.5.4 Further user input

The user input can be valuable contribution in the construction of image composition, as a pair of human eyes is well-equipped to detect in- and out-of-focus images. For the image stitching described in this chapter, it is a condition of the data that any two sequential images will have an overlapping region. It is in this region that the human eye can be very useful in confirming the alignment of the images. An interactive way of integrating the users input thus embedding the resourcefulness of the human eye, was developed in the stitching environment developed in this work. A combination of tools for increasing the contrast in the image and 'jiggling' the frames from left-to-right, up-to-down or both and at the same time allowed the user to gain confidence in image alignment and feed into the outcome of the algorithm where necessary. The user can then choose to update the central location of the 'jiggle' motion such that if it was aligned correctly then the overlapping area should go in and out of focus symmetrically left-to-right and up-to-down. If this is observed by the user then they can confirm the final placement vector. Furthermore, both a speed and amplitude of the jiggling motion may also be set to the user's preference. Figure 144 shows an example of this, demonstrating the observable effect of moving the images about a location with a strong NCC result. The interface by which the user does this is outlined in Figure 145 (b).

With enough additional monitoring of translation stages and sample motion such as has been reported earlier in this thesis (Chapter 5, Section 5.4.2), the inclusion of optical interferometers can reduce the need for an automated image combination and a more thorough traceable link to the data can be established. However, due to such effects as environmental fluctuation or instrumentation drift in the interferometers it is possible that for different scan amplitudes, imaging timeframes or sample

dimensions these automated techniques can be used in post-processing to address small discrepancies between measured position and surface consistency.
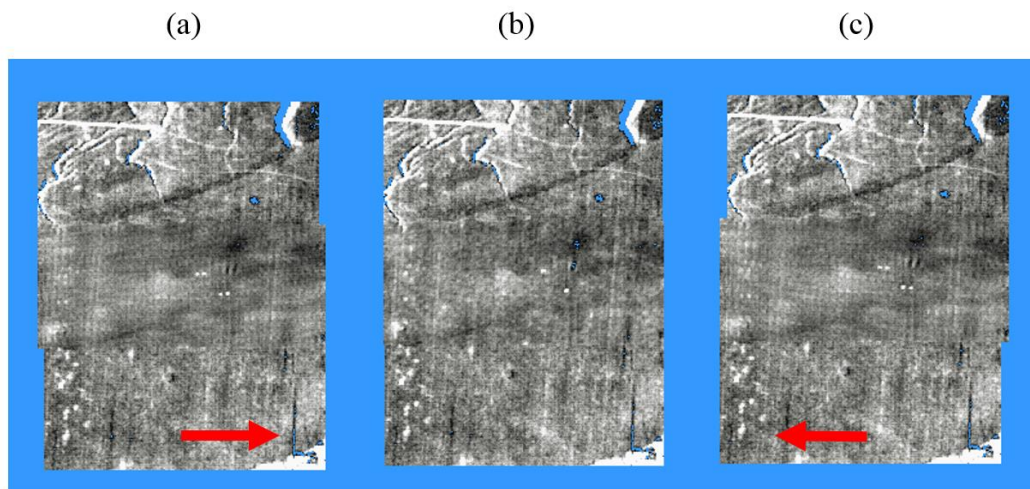
Figure 144: An example of the 'jiggle' motion used to aid user input into the image stitching environment where (a) shows the maximum right horizontal jiggle position, (b) shows the mid-point and (c) shows the maximum left jiggle position.

6.5.5 Software Outputs from Research

Embodying all the developments outlined in Section 6.5, an installer and two executables (.exe) were produced, which can be found in the external media storage link to this thesis for evaluation purposes. A summary of the primary user interaction panels of the software are summarised in Figure 145. The software works in two halves. First, there is the read-in of the images, which includes functionality to manually select from a folder of images and apply a calibration, filters, cropping, MLL, AMF and for a replacement of outliers in the image with spatial noise. This executable has been named Tiff-2-Canvas (T2C) (Figure 145). The second executable, named Vector-2-Canvas (V2C) (Figure 146) allows presentation of the final placement vectors to be plotted, these vectors to be used in tandem with another version of the set of images (e.g. such as the raw instrumentation data or further-modified data). Allowing for another version of the set of images can prove resourceful where the frames have had to be highly filtered, changed to gradient images or had outliers replaced in the image for effective NCC in the T2C .exe. Once there is good confidence in the x and y locations found from the T2C, other routes to constructing the composite can be explored in V2C, such as a pre-allocated change in canvas size or manual adjustment of final placement vectors.
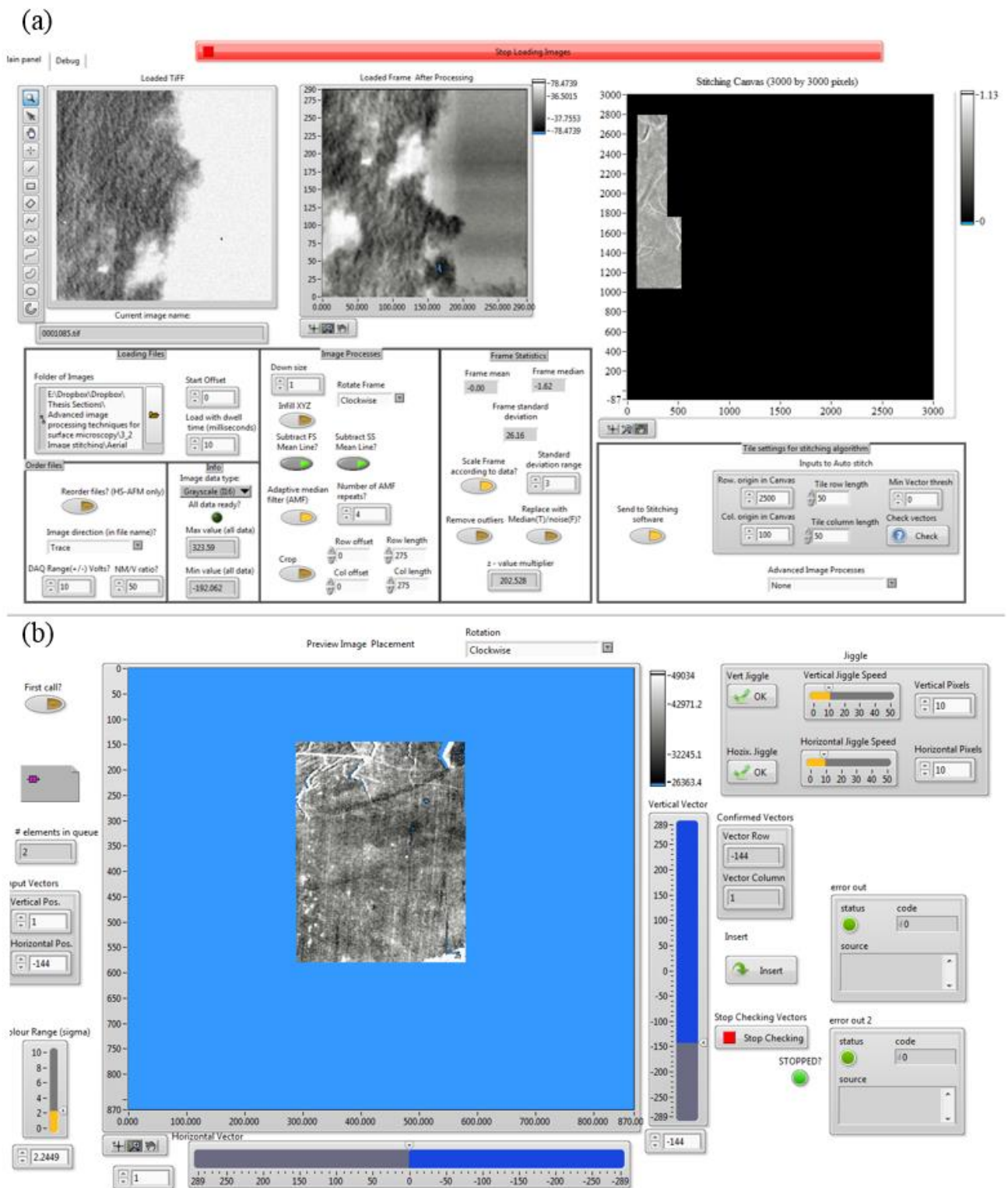
Figure 145: Screenshot of the image stitching environment (a) main page and (b) the user input panel.
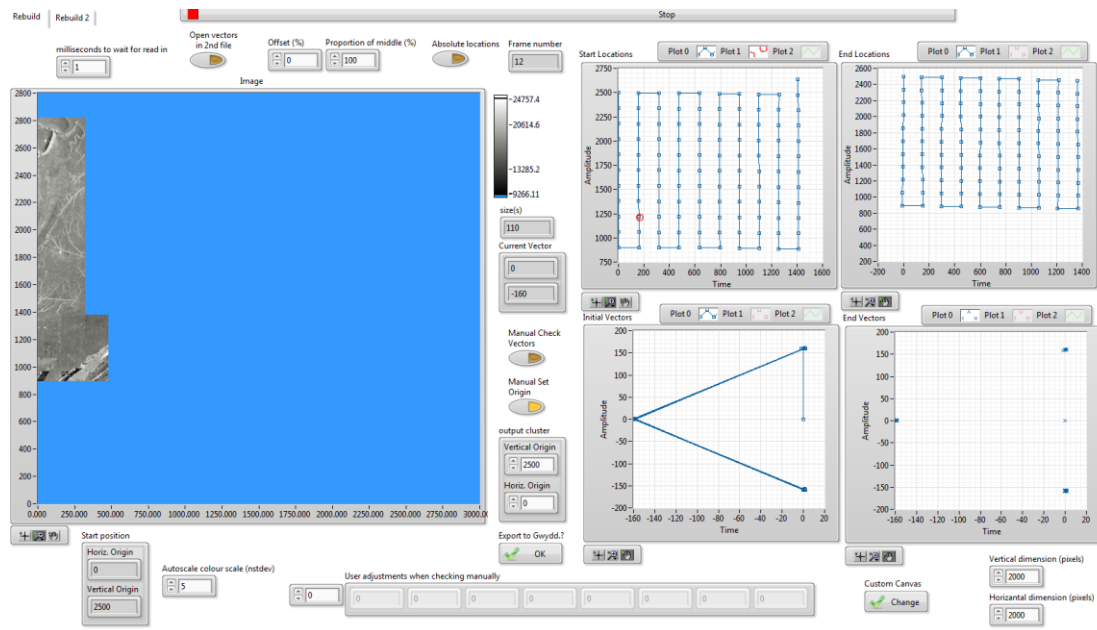
Figure 146: User interface of the Vector-2-canvas executable used to read back the outcomes from the automated stitching algorithm.

6.5.6 Conclusions

The integration of a few key image modifier techniques into the instrument control code explored in this work, including image averaging, mean-line flattening and adaptive median filtering, have been described. These modifiers have been shown to be very useful for real-time observation in scanning microscopy images of sample surfaces and in each instance, case-studies have been presented demonstrating how their implementation can be vital to the success of scientific studies of sample features, as has been experience in the experimental work carried out in this work.

Subsequently, one of the key methods to support the scalability of micro- and nanoscale surface microscopy instruments has been broached in this chapter: multi-image combination or image stitching. To overcome the challenges presented in attempting this, a software environment was developed integrating the tools available from National Instruments Vision Software and others specifically created for this research. Consequently, bespoke executables that could be used to expand the field-of-view, of the instruments developed in this work were produced. As well as presenting successful case studies, the success of the algorithm has been further evaluated for a mixed dataset representing four categories of feature types that are typical to surface microscopy. This mixed dataset was then combined with different ratios of synthesised uniform height noise to assess the algorithm's dependency between erroneous outcomes and signal-to-noise ratios.

Further work in the area of image combination could be explored, both more advanced blending and levelling. Another key advancement would be to not only use final placement vectors from

sequential images but also use normalised cross-correlation or vector correlation with neighbouring images in the canvas.

Chapter 7: Summary and Conclusions

Much of the work presented in this thesis builds upon the success of the mass-produced technologies found in OPUs, developed for reading and writing to optical media discs. Custom electronics developed in this work have made use of the onboard systems in OPUs, capable of performing nanoscale-to-millimetre scale optical displacement sensing and actuation. Once a sufficient utilisation of the OPU toolset were ascertained and characterised in this, the technology was found to be instrumental to a number of surface microscopy techniques including high-speed atomic force microscopy, optical profilometry and nanoscale positioning.

Multiscale correlative microscopy is an evolving area of instrumentation development that continually supports discoveries in material science, medicine and other scientific study. One emerging microscopy technique is HS-AFM, which is uniquely placed with its ability to capture real-time topographical maps with sub-atomic height resolution and lateral ranges that can be extended over several orders of magnitude. However, the instrumentation used to carry out this technique is typically costly and has much fewer pixels (i.e. < 1 megapixel) per image than many other current imaging techniques.

In this work, it has been shown how the optical pickup technology has been translated to make advances in HS-AFM. Firstly, a CD/DVD OPU (SF-HD850/65, Sanyo) was incorporated as the principle cantilever detection head, in a contact mode high-speed atomic force microscope. This instrument is shown to have high operational imaging rates, in excess of most commercial AFMs, allowing for real-time imaging of nanoscale surface topography. This work goes on to cover a side-by-side comparison of the new OPU-based HS-AFM, with a commercial laser-doppler-shift vibrometer based HS-AFM to show the advantages and disadvantages associated with each of the detection schemes. It was seen whilst the LDV has a higher measurement resolution of ±15 picometres on a single measurement (i.e. a single pixel) the optical pickup provided more measurement stability across a single image of dimension 5 µm × 5 µm, which was taken in 0.25 seconds at 0.25 megapixels.

It is then shown how the OPU based HS-AFM is capable of sub-nanometre sensitivity and imaging multiple frames per second via the mapping of CRISP Cas-9 labelled DNA on a mica surface. Such measurements by this instrument have been shown to assist a newly discovered method for the identification of short lengths (e.g. 100-1000s of base pairs) of CRISP Cas9 labelled DNA. Here, we've shown that the combination of the OPU HS-AFM and DNA mapping technique can be used to identify two CRISPR Cas-9 labelled DNA sequences as the HER2 and the TERT gene. Where measuring the expression ratio of these two particular genes are commonly used in breast cancer detection. This application of the OPU-based HS-AFM would benefit from a lower measurement noise floor in the focus error detection system and faster sample scanning to make use of the high bandwidth sensing

onboard OPUs to increase the throughput of the labelled molecule identification and sample wide abundancy counting.

Further work reports how the OPU based HS-AFM can also be used for the mapping of carbide inclusions in thermally sensitized AISI 304 stainless steel. Such a study gives unique insight into the nano-to-microscale processes of corrosion and transition of the localized material properties, which in turn can lead to the increased likelihood of component failure, for example due to stress corrosion cracking. Future work could build upon this, to make use of the real-time imaging in the OPU HS-AFM to observe the transition in material properties as they happen. In addition, without modification this method could be used for other studies in metallurgy, for example linking grain orientation to corrosion or growth rates under varied environmental conditions.

The second principle microscopy application of OPU technology reported in this thesis made use of the astigmatic focus error detection system and voice coil motors for developing optical profilometry instrumentation. It is shown that the OPU can be used directly on the sample surface (i.e. without a cantilever as in HS-AFM) for a non-contact surface microscopy technique. Initially the OPU is used with a closed-loop, 3-axis, nanopositioning stage to measure a large area of a UO_2 thin film and map out 10s of grains over a 90000 μm^2 area. Regions of this UO_2 sample are compared with SEM images to show equivalent UO_2 grains, grain boundaries and a fiducial marker are visible at the same magnification. It is then shown how the full focus error response (i.e. s-curve) can be collected at several locations across the image and further information extracted link to reflectivity and height of the sample features. This same instrument is also shown to be able to image the surface of a leaf and reveal stomata structures on the surface akin to data reported in literature and taken on SEMs.

The investigations into optical profilometers go on to show how the OPUs can be combined in low cost easy-to-construct configurations that are able to perform real-time optical profilometry, allowing for dynamic processes to be observed. One of these configurations, entirely consisting of two OPUs, shows that the voice coils around the objective lens can provide fast and slow scan displacements for optical profilometry, whilst also being able to provide 'DC' offsets of the imaging window (e.g. in a serpentine raster pattern), extending the field of view of the instrument via composite imaging. Whilst performing optical profilometry with scanning voice coils it was found that there was a good level of internal imaging linearity with the errors (i.e. 200 nm) falling below the measurement laser spot size (i.e. 1 μm). There was also shown to be a low level of actuation drift in the dual-axis voice coil scanning arrangement, when continually performing open-loop scanning. When the instrument was left imaging in the same location for 180 minutes the features were found to have moved by 6.8 μm corresponding to a very small drift rate of 0.62 nm/s.

It was then shown how optical profilometry could be used with the MSNL cantilever chip used for HS-AFM placed on a simple, geared motor driven, angular sled to image and locate the cantilever. It is proposed that embedding optical profilometry into the OPU based HS-AFM, described in Chapter 3, would give add a two-fold benefit to the HS-AFM. Firstly, the scanning of the cantilever would allow for more accurate positioning of the laser onto the measurement location on the topside of the cantilever. Secondly, it would allow for a large-area (100s of micrometers), non-contact, image to be constructed prior to imaging with contact mode HS-AFM. A wider field of view could then be used to identify regions of interest or fiducial markers. This preliminary step would allow for the identification of areas unsuitable for contact mode imaging due to the presence of roughness or debris, preventing damage to the cantilever tip when scanning.

The third major translation of optical pickup technology into real-time surface microscopy, investigated in this thesis, focused on using the optical pickups as real-time sensors in a nanoscanners used in HS-AFM. Here a pair of OPUs were used to successfully evaluate three distinct parallel flexure stage designs, manufactured using stereolithography 3D printing, and determine which of the stage design exhibited the least amount of scanning error. Once identified, the most performant stage was embedded into an LDV-based HS-AFM and used to image a sample surface so that the performance of the stage could be measured when operating in open-loop. When measuring the scanning motion of the stage with the optical interferometer and optical pickup, non-linearities and an erroneous cross-axial motion gave rise to an average deviation from ideal motion of 21 nm per pixel. Building the images using this showed in fact the previous uncorrected images are in fact trapezoidal. However, the 3D printed stages were found to have appropriate scanning performance for use in an HS-AFM.

In Chapter 6, the attention of the thesis turns to the traceable processing of the images created by the instruments developed in this work. Here, we detail core image processing techniques that were implemented at runtime in the OPU-based instruments to enhance the signal-to-noise and image quality in the microscopes The processes included: mean-line flattening, averaging (stacking and moving window) and adaptive median filtering. It is further demonstrated how high-speed OPU based scanning profilers could benefit from a simple difference compression algorithm that is shown to save up to 50% of stored data. By dynamically saving the changes between frames at a lower bit-depth, it is possible to maintain image data integrity with a small resultant error from the uncompressed image, of less than 1%. It is therefore proposed that this is an important consideration when trying to perform surface microscopy at the high fidelity and measurement bandwidths plausibly achieved using the photodiodes in optical pickup detection heads.

Another method developed for processing the data from the OPU-based microscopes, permitted images from multiple sites to be combined creating composite images to increase the field of view to greater orders of magnitude. In this thesis, a description is given of the image stitching environment,

217

created using LabVIEW, that implements machine learning to calculate the maximum normalized cross correlation between overlapping frames and produce a set of vectors to recommend how two images should be combined. The results from using this image stitching algorithm show composite images can be built better than when relying on nanoscale actuators, which are shown to have a number of on-axis errors most likely due to mechanical play in the stacked actuator arrangements used in the microscopes in this study. To show the benefits of using the method developed in this work a dataset, consisting of multiple images taken across a leaf impression sample using the OPU-based optical profilometer, were built into a composite image using actuator coordinates, Image Composite Editor (ICE) and the method developed here. Subsequent evaluation of the image stitching method was carried out by taking a large test image that was divided into 120 sub-images and then re-combined with recommended locations compared to true locations. The large test image was also modified, i.e. via the addition of a sample slope and varying amounts of synthesized white noise, the stitching processes carried out again and evaluated. It was shown how the success of the method diminished with additional noise.

Collectively the chapters reported within, build upon a range of previous works reported in literature over several decades, to demonstrate how optical pickup detection heads found in CD, DVD and Blu-ray players have tremendous potential and application in real-time surface microscopy, sensing and positioning. The low-cost OPU detection heads can be used in conjunction with inexpensive open-source microcontrollers, 3D printed parts and readily available computer coding environments to create powerful tools for displacement measurements across at least 6 orders of magnitude (i.e. 10^{-10}-10^{-3} metres) at very high sensing rates of 10s-to-100s of megasamples per second. A particular highlight of this research include demonstrating the potential of the technology embedded into a high-speed atomic force microscopy and applying it for genomic studies of DNA. Future work could look to further push the measurement resolution of the given OPU used in these applications and embed multiple microscopy techniques into a single unified instrument.

References

1. Mikheikin A, Olsen A, Leslie K, Russell-Pavier F, Yacoot A, Picco L, et al. DNA nanomapping using CRISPR-Cas9 as a programmable nanoparticle. Nat Commun [Internet]. 2017 Dec 21 [cited 2017 Nov 23];8(1):1665. Available from: http://www.nature.com/articles/s41467-017-01891-9

2. Russell-Pavier FS, Picco L, Day JCCC, Shatil NR, Yacoot A, Payton OD. 'Hi-Fi AFM': high-speed contact mode atomic force microscopy with optical pickups. Meas Sci Technol [Internet]. 2018 Oct 1 [cited 2018 Oct 12];29(10):105902. Available from: http://stacks.iop.org/0957-0233/29/i=10/a=105902?key=crossref.8bcadd95949d60b90fa26090f29ef689

3. James Russell. US3501586A - Analog to digital to optical photographic recording and playback system - Google Patents [Internet]. US3501586, 1966 [cited 2019 Oct 7]. Available from: https://patents.google.com/patent/US3501586A/en?oq=US3501586

4. News B. Compact disc hits 25th birthday. BBC News [Internet]. 2007 Aug 17;Online. Available from: http://news.bbc.co.uk/1/hi/technology/6950845.stm

5. Kim K-S, Lee S-H, Choo Chung C. A Survey of Control Issues in Optical Data Storage Systems. IFAC Proc. 2011;44(1):854–68.

6. Quercioli F, Tiribilli B, Ascoli C, Baschieri P, Frediani C. Monitoring of an atomic force microscope cantilever with a compact disk pickup. Rev Sci Instrum [Internet]. 1999 [cited 2017 Sep 29];70(9):3620–4. Available from: http://dx.doi.org/10.1063/1.1149969

7. Quercioli F, Tiribilli B, Bartoli a. Interferometry with optical pickups. Opt Lett. 1999;24(10):670–2.

8. Quercioli F, Mannoni A, Tiribilli B. Laser Doppler velocimetry with a compact disc pickup. Appl Opt. 1998;37(25):5932.

9. Bartoli A, Poggi P, Quercioli F, Tiribilli B. Fast one-dimensional profilometer with a compact disc pickup. 2001;

10. Hwu EE-T, Boisen A. Hacking CD/DVD/Blu-ray for Biosensing. ACS Sensors [Internet]. 2018 Jul 27 [cited 2019 Aug 12];3(7):1222–32. Available from: http://pubs.acs.org/doi/10.1021/acssensors.8b00340

11. Molesini G, Pedrini G, Poggi P, Quercioli F. Focus-wavelength encoded optical profilometer. Opt Commun [Internet]. 1984 Mar 15 [cited 2019 Apr 17];49(4):229–33. Available from: https://www.sciencedirect.com/science/article/pii/0030401884901792

12. Hwu E-T, Illers H, Jusko L, Danzebrink H-U. A hybrid scanning probe microscope (SPM) module based on a DVD optical head. Meas Sci Technol [Internet]. 2009 Aug 1 [cited 2019 Apr 3];20(8):084005–8. Available from: http://stacks.iop.org/0957-0233/20/i=8/a=084005?key=crossref.5c24146be14c6a39ab60926fa7983269

13. Ehrmann K, Ho A, Schindhelm K. A 3D optical profilometer using a compact disc reading head. Meas Sci Technol. 1998;9:1259–65.

14. Feynman R. There's plenty of room at the bottom. In: Feynman and Computation. CRC Press; 2018. p. 63–76.

15. Binnig G, Quate CF. Atomic Force Microscope. Phys Rev Lett [Internet]. 1986 Mar [cited 2014 Oct 12];56(9):930–3. Available from: https://journals.aps.org/prl/pdf/10.1103/PhysRevLett.56.930

16. Piner RD, Zhu J, Xu F, Hong SH, Mirkin CA. "Dip-pen" nanolithography. Science (80-)

[Internet]. 1999;283(5402):661–3. Available from: http://www.cheric.org/article/260827%5Cnhttp://www.sciencemag.org/content/283/5402/661

17. Russell, Phil, Dale Batchelor and JT. SEM and AFM: complementary techniques for high resolution surface investigations. Veeco Instruments Inc,. 2001;(AN46, Rev A 1).

18. Humphris ADL, Miles MJ, Hobbs JK. A mechanical microscope: High-speed atomic force microscopy. Appl Phys Lett [Internet]. 2005 Jan 17 [cited 2014 May 3];86(3):034106. Available from: http://aip.scitation.org/doi/10.1063/1.1855407

19. Picco L, Bozec L, Ulcinas A, Engledew DJ, Antognozzi M, Horton M, et al. Breaking the speed limit with atomic force microscopy. Nanotechnology [Internet]. 2007 Jan 31 [cited 2014 May 16];18(4):044030–4. Available from: http://stacks.iop.org/0957-4484/18/i=4/a=044030?key=crossref.a4d936335737fdd09823901aa50219ef

20. James PJ, Antognozzi M, Tamayo J, Mcmaster TJ, Newton JM, Miles MJ, et al. Interpretation of Contrast in Tapping Mode AFM and Shear Force Microscopy. A Study of Nafion. Langmuir. 2001;73(17):349–60.

21. Payton OD, Picco L, Robert D, Raman A, Homer ME, Champneys AR, et al. High-speed atomic force microscopy in slow motion—understanding cantilever behaviour at high scan velocities. Nanotechnology. 2012;23(20):205704–6.

22. Cullen PL, Cox KM, Subhan MK Bin, Picco L, Payton OD, Buckley DJ, et al. Ionic solutions of two-dimensional materials. Nat Chem [Internet]. 2016 Nov 21;9(3):244–9. Available from: http://dx.doi.org/10.1038/nchem.2650

23. Miller TS, Suter TM, Telford AM, Picco L, Payton OD, Russell-Pavier F, et al. Single crystal, luminescent carbon nitride nanosheets formed by spontaneous dissolution. Nano Lett [Internet]. 2017;acs.nanolett.7b01353. Available from: http://pubs.acs.org/doi/abs/10.1021/acs.nanolett.7b01353

24. Watts MC, Picco L, Russell-Pavier FS, Cullen PL, Miller TS, Bartuś SP, et al. Production of phosphorene nanoribbons. Nature [Internet]. 2019 Apr 10 [cited 2019 Apr 25];568(7751):216. Available from: http://www.nature.com/articles/s41586-019-1074-x

25. Hwu E-T, Hung S-K, Yang C-W, Hwang I-S, Huang K-Y. Simultaneous detection of translational and angular displacements of micromachined elements. Appl Phys Lett [Internet]. 2007 [cited 2014 May 3];91(22):221908. Available from: http://scitation.aip.org/content/aip/journal/apl/91/22/10.1063/1.2817750

26. Bosco FG, Hwu ET, Keller S, Greve A, Boisen A. Self-aligned cantilever positioning for on-substrate measurements using DVD pickup head. Microelectron Eng [Internet]. 2010 May [cited 2014 May 3];87(5–8):708–11. Available from: http://linkinghub.elsevier.com/retrieve/pii/S0167931709009071

27. Unger S, Ito S, Kohl D, Schitter G. Development of a compact atomic force microscope based on an optical pickup head. IFAC-PapersOnLine [Internet]. 2016;49(21):629–35. Available from: http://dx.doi.org/10.1016/j.ifacol.2016.10.671

28. Fan X, Xu P, Zhou D, Sun Y, Li YC, Nguyen MAT, et al. Fast and E ffi cient Preparation of Exfoliated 2H MoS 2 Nanosheets by Sonication-Assisted Lithium Intercalation and Infrared Laser-Induced 1T to 2H Phase Reversion. Nano Lett. 2015;5956–60.

29. Sang Heon Lee. Probe-rotating atomic force microscopy for determining material properties. Rev Sci Instrum [Internet]. 2014 [cited 2019 Aug 5];85(3):033708. Available from: https://doi.org/10.1063/1.4869474

30. Lee SH. High precision deflection measurement of microcantilever in an optical pickup head based atomic force microscopy. Rev Sci Instrum [Internet]. 2012 Nov [cited 2014 May

28];83(11):113703–4. Available from: http://www.ncbi.nlm.nih.gov/pubmed/23206067

31. Ulčinas A, Vaitekonis S. Rotational scanning atomic force microscopy. Nanotechnology. 2017;28(10).

32. Donolato M, Antunes P, Zardán Gómez de la Torre T, Hwu E-T, Chen C-H, Burger R, et al. Quantification of rolling circle amplified DNA using magnetic nanobeads and a Blu-ray optical pick-up unit. Biosens Bioelectron [Internet]. 2015 [cited 2017 Sep 29];67:649–55. Available from: https://ac.els-cdn.com/S0956566314007854/1-s2.0-S0956566314007854-main.pdf?_tid=6340855e-a4f9-11e7-919b-00000aab0f02&acdnat=1506677848_c5dc90924e8b9f3e20f2c9a865c42fe0

33. Liao H-S, Huang K-Y, Hwang I-S, Chang T-J, Hsiao WW, Lin H-H, et al. Operation of astigmatic-detection atomic force microscopy in liquid environments. Rev Sci Instrum [Internet]. 2013 Oct [cited 2014 May 28];84(10):103709–7. Available from: http://www.ncbi.nlm.nih.gov/pubmed/24182121

34. Wu EH, Uang KH, Ung SH, Ã IHW. Measurement of Cantilever Displacement Using a Compact Disk / Digital Versatile Disk Pickup Head Measurement of Cantilever Displacement Using a Compact Disk / Digital Versatile Disk Pickup Head. Jpn J Appl Phys. 2006;45:2368.

35. Hwu E-T, Hung S-K, Yang C-W, Braunsmann C, Schäffer TE, Hwang I-S, et al. Low-voltage and high-performance buzzer-scanner. Nanotechnology [Internet]. 2013 [cited 2017 Mar 7];24:455503. Available from: http://iopscience.iop.org/0957-4484/24/45/455503

36. Ricci D, Braga PC. Recognizing and Avoiding Artifacts in AFM Imaging. In: Atomic Force Microscopy [Internet]. New Jersey: Humana Press; 2004 [cited 2019 Oct 7]. p. 25–38. Available from: http://link.springer.com/10.1385/1-59259-647-9:25

37. Tuma T. The Four Pillars of Nanopositioning for Scanning Probe Microscopy. Charles University in Prague; 2013.

38. Ramachandraiah H, Amasia M, Cole J, Sheard P, Pickhaver S, Walker C, et al. Lab-on-DVD: standard DVD drives as a novel laser scanning microscope for image based point of care diagnostics. Lab Chip [Internet]. 2013 Mar 19 [cited 2019 Aug 5];13(8):1578. Available from: http://xlink.rsc.org/?DOI=c3lc41360h

39. La Clair JJ, Burkart MD. Molecular screening on a compact disc. Org Biomol Chem. 2003;1(18):3244–9.

40. Fan K-C, Chu C-L, Liao J-L, Mou J-I. Development of a high-precision straightness measuring system with DVD pick-up head. Meas Sci Technol. 2002;14:47–54.

41. Liu C-H, Lin B-H. Development of a nanometer resolution flatness measurement system for the ceramic surface by using Blue-ray optical pickup. Microsyst Technol [Internet]. 2013 Apr 20 [cited 2014 May 3];19(11):1817–21. Available from: http://link.springer.com/10.1007/s00542-013-1805-0

42. Edwin Hwu. Fundamentals of an Atomic Force Microscope Based on a Digital Versatile Disk Optical Pick-up Unit. Google Books. 2007;114–8.

43. Lee SH. Note: Compact and light displacement sensor for a precision measurement system in large motion. Rev Sci Instrum [Internet]. 2015 Aug 10 [cited 2019 Aug 5];86(8):086103. Available from: http://aip.scitation.org/doi/10.1063/1.4928528

44. Kim J, Liu GL, Lee LP. Lens-scanning Raman microspectroscopy system using compact disc optical pickup technology. Opt Express. 2005;13(12):4780–5.

45. Klapetek P, Nečas D, Anderson C. Gwyddion user guide. http://gwyddion.net/download/user-guide/gwyddion-user-guide-en.pdf {Accessed: 11/JUNE/2019} [Internet]. 2004 [cited 2017 Sep

29]; Available from: http://gwyddion.net/download/user-guide/gwyddion-user-guide-en.pdf

46. Abramoff MD, Magalhães PJ, Ram SJ. Image processing with ImageJ. Biophotonics Int [Internet]. 2004 [cited 2019 Mar 26];11(7):36–42. Available from: https://dspace.library.uu.nl/handle/1874/204900

47. Fantner GE, Barbero RJ, Gray DS, Belcher AM. Kinetics of antimicrobial peptide activity measured on individual bacterial cells using high-speed atomic force microscopy. Nat Nanotechnol [Internet]. 2010 Apr 14 [cited 2019 Aug 5];5(4):280–5. Available from: http://www.nature.com/articles/nnano.2010.29

48. Russell J. Analog to digital to optical photographic recording and playback system. US; US3501586A, 1970.

49. Immink KA. The Compact Disc Story. J Audio Eng Soc [Internet]. 1998 May 1 [cited 2019 Jul 15];46(5):458–65. Available from: http://www.aes.org/e-lib/browse.cfm?elib=12144

50. Institution of Electronic and Radio Engineers. KAS, Gross U. Optimization of low-frequency properties of eight-to-fourteen modulation [Internet]. Vol. 53, Radio and Electronic Engineer. Institution of Electronic and Radio Engineers; 1983 [cited 2019 Jul 1]. 63–66 p. Available from: https://digital-library.theiet.org/content/journals/10.1049/ree.1983.0017

51. Sarid D, Schechtman BH. A Roadmap for Optical Data Storage Applications. Opt Photonics News 18. 2007;(5):32–7.

52. Cope JA. The physics of the compact disc. Phys Educ [Internet]. 1993 Jan [cited 2019 Jul 15];28(1):15–21. Available from: http://stacks.iop.org/0031-9120/28/i=1/a=003?key=crossref.143fad888ae3eaf98d18e466180fd2e2

53. Jacobus P. J. Heemskerk HRAJS. Optical focussing-error detection system [Internet]. US; US4358200A, 1980 [cited 2019 Jul 15]. Available from: https://patents.google.com/patent/US4358200A/en

54. Hideaki Hirai HA. Optical element, optical pickup unit, and optical disk drive unit [Internet]. US7050380B2, 2002 [cited 2019 Jul 15]. p. Fig. 3. Available from: https://patents.google.com/patent/US7050380B2/en

55. Shih H, Lu W, Chang J. Design of single-path optical pickup head with three wavelengths using integrated optical unit. IEEE Trans Magn [Internet]. 2009 May;45(5):2202–5. Available from: http://ieeexplore.ieee.org/lpdocs/epic03/wrapper.htm?arnumber=4815993

56. Yi-Lin Lai SW. Method and circuit for generating a tracking error signal using differential phase detection [Internet]. Taiwan, US; US7161877B2, 2007. Available from: https://patents.google.com/patent/US7161877

57. TC31 ETC. Standard ECMA-267: 120 mm DVD - Read-Only Disk. 2001.

58. Moore S, Burrows R, Picco L, Martin TL, Greenwell SJ, Scott TB, et al. A study of dynamic nanoscale corrosion initiation events using HS-AFM. Faraday Discuss. 2018;210:409–28.

59. Chu C-L, Chiu C-Y. Development of a low-cost nanoscale touch trigger probe based on two commercial DVD pick-up heads. Meas Sci Technol [Internet]. 2007;18(7):1831–42. Available from: http://stacks.iop.org/0957-0233/18/i=7/a=006?key=crossref.92913ec26fd68def6041ad3819210ddf

60. Liao H-SH-S, Chen Y-HY-H, Ding R-FR-F, Huang H-FH-F, Wang W-MW-M, Hwu E-TE-T, et al. High-speed atomic force microscope based on an astigmatic detection system. Rev Sci Instrum [Internet]. 2014 Oct [cited 2015 Jan 8];85(10):103710–7. Available from: http://dx.doi.org/10.1063/1.4898019

61. Bosco FG, Hwu E-T, Chen C-H, Keller S, Bache M, Jakobsen MH, et al. High throughput label-

free platform for statistical bio-molecular sensing. Lab Chip [Internet]. 2011 Jul 21 [cited 2014 May 3];11(14):2411–6. Available from: http://www.ncbi.nlm.nih.gov/pubmed/21623438

62. Binnig G, Quate ' ' CF, Gi EL, Gerber C. Atomic Force Microscope. [cited 2018 Feb 26]; Available from: https://journals.aps.org/prl/pdf/10.1103/PhysRevLett.56.930

63. Meyer G, Amer NM. Novel optical approach to atomic force microscopy. Appl Phys Lett [Internet]. 1988 [cited 2014 May 3];53(12):1045–7. Available from: http://ieeexplore.ieee.org/xpls/abs_all.jsp?arnumber=4857553%5Cnpapers3://publication/uuid/676DBE73-A7D4-4C42-9D7B-B7B63206C761

64. Hansma PK, Cleveland JP, Radmacher M, Walters DA, Hillner PE, Bezanilla M, et al. Tapping mode atomic force microscopy in liquids. Appl Phys Lett [Internet]. 1994 Mar 28 [cited 2015 Jul 3];64(13):1738–40. Available from: http://link.aip.org/link/?APPLAB/64/1738/1%5Cnhttp://scitation.aip.org/content/aip/journal/apl/64/13/10.1063/1.111795

65. Giessibl FJ. Atomic resolution on Si(111)-(7×7) by noncontact atomic force microscopy with a force sensor based on a quartz tuning fork. Appl Phys Lett [Internet]. 2000 Mar 13 [cited 2015 Oct 12];76(11):1470–2. Available from: http://scitation.aip.org/content/aip/journal/apl/76/11/10.1063/1.126067

66. Ando T. High-speed atomic force microscopy. Microscopy [Internet]. 2013 Feb [cited 2014 Nov 17];62(1):81–93. Available from: http://www.ncbi.nlm.nih.gov/pubmed/23291302

67. Payton OD, Picco L, Scott TB. High-speed atomic force microscopy for materials science. Int Mater Rev [Internet]. 2016 [cited 2016 Jul 15];61(8):473–94. Available from: http://www.tandfonline.com/doi/abs/10.1080/09506608.2016.1156301?journalCode=yimr20

68. Payton OD, Picco L, Champneys AR, Homer ME, Miles MJ, Raman A. Experimental observation of contact mode cantilever dynamics with nanosecond resolution. Rev Sci Instrum. 2011;82(4):043704–5.

69. Schitter G, Allgöwer F, Stemmer a. A new control strategy for high-speed atomic force miciroscopy. Nanotechnology. 2004 Jan 1;15(1):108–14.

70. Ando T. Control techniques in high-speed atomic force microscopy. Proc Am Control Conf [Internet]. 2008;(4586984):3194–200. Available from: http://ieeexplore.ieee.org/xpls/abs_all.jsp?arnumber=4586984

71. Fantner GE, Schitter G, Kindt JH, Ivanov T, Ivanova K, Patel R, et al. Components for high speed atomic force microscopy. Ultramicroscopy [Internet]. 2006 Jun 1 [cited 2014 May 3];106(8–9):881–7. Available from: https://www.sciencedirect.com/science/article/pii/S0304399106000593

72. Bozchalooi IS, Youcef-Toumi K, Burns DJ, Fantner GE. Compensator design for improved counterbalancing in high speed atomic force microscopy. Rev Sci Instrum. 2011;82(11):1–12.

73. Ando T, Uchihashi T, Fukuma T. High-speed atomic force microscopy for nano-visualization of dynamic biomolecular processes. Prog Surf Sci [Internet]. 2008 Nov [cited 2014 Apr 29];83(7–9):337–437. Available from: http://linkinghub.elsevier.com/retrieve/pii/S0079681608000464

74. Ando T, Uchihashi T, Kodera N, Yamamoto D, Taniguchi M, Miyagi A, et al. High-speed atomic force microscopy for observing dynamic biomolecular processes. J Mol Recognit. 2007;20(September):448–58.

75. Pyne A, Marks W, Picco L, Dunton P, Ulcinas A, Barbour M, et al. High-speed atomic force microscopy of dental enamel dissolution in citric acid. Arch Histol Cytol. 2009;72(4–5):209–15.

223

76. Casuso I, Rico F, Scheuring S. High-speed atomic force microscopy: Structure and dynamics of single proteins. Curr Opin Chem Biol. 2011 Oct;15(5):704–9.

77. Bosco FG, Chen CH, Hwu ET, Bache M, Keller S, Boisen A. High-throughput automated system for statistical biosensing employing microcantilever arrays. 2011 IEEE 24th Int Conf Micro Electro Mech Syst. 2011;877–80.

78. Morais S, Tamarit-López J, Carrascosa J, Puchades R, Maquieira A. Analytical prospect of compact disk technology in immunosensing. Anal Bioanal Chem [Internet]. 2008 Aug [cited 2014 May 3];391(8):2837–44. Available from: http://www.ncbi.nlm.nih.gov/pubmed/18597081

79. Hwu E-T, Liao H-S, Bosco FG, Chen C-H, Keller SS, Boisen A, et al. An Astigmatic Detection System for Polymeric Cantilever-Based Sensors. J Sensors [Internet]. 2012 [cited 2014 May 3];2012:1–7. Available from: http://www.hindawi.com/journals/js/2012/580939/

80. Hwu E-T, Huang K-Y, Hung S-K, Hwang I-S. Measurement of cantilever displacement using a compact disk/digital versatile disk pickup head. Jpn J Appl Phys [Internet]. 2006 Mar 27 [cited 2014 May 3];45(3B):2368–71. Available from: http://stacks.iop.org/1347-4065/45/2368

81. Stark RW, Drobek T, Heckl WM. Thermomechanical noise of a free v-shaped cantilever for atomic-force microscopy. Ultramicroscopy [Internet]. 2001 Jan [cited 2017 Sep 29];86(1–2):207–15. Available from: http://www.ncbi.nlm.nih.gov/pubmed/11215624

82. Bruker. MSNL Probes Product Description, Bruker. http://www.brukerafmprobes.com/p-3710-msnl-10.aspx {Accessed: 11/JUNE/2019} [Internet]. 2019; Available from: http://www.brukerafmprobes.com/p-3710-msnl-10.aspx

83. Mikheikin A, Olsen A, Picco L, Payton O, Mishra B, Gimzewski JK, et al. High-Speed Atomic Force Microscopy Revealing Contamination in DNA Purification Systems. Anal Chem. 2016;88(5):2527–32.

84. Mikheikin A, Olsen A, Leslie K, Mishra B, Gimzewski JK, Reed J. Atomic force microscopic detection enabling multiplexed low-cycle-number quantitative polymerase chain reaction for biomarker assays. Anal Chem [Internet]. 2014 Jul 1 [cited 2014 Jul 11];86(13):6180–3. Available from: http://dx.doi.org/10.1021/ac500896k

85. Reed J, Hsueh C, Lam M, Kjolby R, Sundstrom A, Mishra B. Identifying individual DNA species in a complex mixture by precisely measuring the spacing between nicking restriction enzymes with atomic force microscope. J R Soc Interface. 2012;9:2341–50.

86. Klapetek P, Picco L, Payton O, Yacoot A, Miles M. Error mapping of high-speed AFM systems. Meas Sci Technol [Internet]. 2013 Feb 1 [cited 2014 May 3];24(2):25006. Available from: http://stacks.iop.org/0957-0233/24/i=2/a=025006

87. Krivonosova EA, Krivonosova EA. A review of stress corrosion cracking of welded stainless steels. OALib [Internet]. 2018 May 4 [cited 2019 Jun 11];5(5):1–41. Available from: http://www.oalib.com/paper/pdf/5293654

88. Brandão P, Infante V, Deus AM, Martinez-Ubeda AI, Griffiths I, Karunaratne SA, et al. Thermo-mechanical modeling of a high pressure turbine blade of an airplane gas turbine engine Influence of nominal composition variation on phase evolution and creep life of Type 316H austenitic stainless steel components. Procedia Struct Integr [Internet]. 2016 [cited 2019 May 9];2:958–65. Available from: www.sciencedirect.comAvailableonlineatwww.sciencedirect.comwww.sciencedirect.com

89. Trillo EA, Murr LE. A TEM investigation of M 23 C 6 carbide precipitation behaviour on varying grain boundary misorientations in 304 stainless steels. J Mater Sci [Internet]. 1998 [cited 2019 May 9];33(5):1263–71. Available from: https://link.springer.com/content/pdf/10.1023%2FA%3A1004390029071.pdf

90. Tarasenko L V, Heat D, Tarasenko L V. Rules of formation of the chemical composition of M23C6 multicomponent carbide in high-temperature steels. Met Sci Heat Treat [Internet]. 2000 [cited 2019 Jun 11];42(1):7–12. Available from: http://dx.doi.org/10.1007/BF02471348

91. Warren, A. D., Martinez-Ubeda, A. I., Payton, O. D., Picco, L., & Scott TB. A method for the preparation of stainless steels surfaces for scanning probe microscopy techniques. Micros Today. 2016;24(3):52–5.

92. Ando T, Bhamidimarri SP, Brending N, Colin-York H, Collinson L, De Jonge N, et al. The 2018 correlative microscopy techniques roadmap. J Phys D Appl Phys [Internet]. 2018 Nov 7 [cited 2019 May 14];51(44):443001. Available from: http://stacks.iop.org/0022-3727/51/i=44/a=443001?key=crossref.b474b90d6c0d4a0eb2e9c52c29cc7a55

93. Warren AD, Martinez-Ubeda A, Griffiths I, Flewitt PEJ. The implications of fabrication and cast-to-cast variability on thermal aging in the creep range for aisi type 316h stainless steel components. Metall Mater Trans A [Internet]. 2019 [cited 2019 Jun 12];50(2):987–96. Available from: http://www.bristol.ac.uk/pure/about/ebr-terms

94. Shatil NR, Homer ME, Picco L, Martin PG, Payton OD. A calibration method for the higher modes of a micro-mechanical cantilever. Appl Phys Lett. 2017;110(22):223101.

95. Kohno T, Ozawa N, Miyamoto K, Musha T. High precision optical surface sensor. Appl Opt. 1988;27(1):103–8.

96. Verma V, Kumar R, Hsu S. 3D building detection and modeling from aerial LIDAR data. In: 2006 IEEE Computer Society Conference on Computer Vision and Pattern Recognition - Volume 2 (CVPR'06) [Internet]. IEEE; 2006 [cited 2019 Apr 17]. p. 2213–20. Available from: http://ieeexplore.ieee.org/document/1641024/

97. Perera RW, Kohn SD, Bemanian S. Comparison of road profilers. Transp Res Rec J Transp Res Board [Internet]. 1996 Jan 1 [cited 2019 Apr 17];1536(1):117–24. Available from: http://journals.sagepub.com/doi/10.1177/0361198196153600117

98. Wang C-C, Lin J-Y, Lee C-H. Membrane ripples of a living cell measured by non-interferometric widefield optical profilometry. Opt Express [Internet]. 2005 Dec 26 [cited 2019 Apr 17];13(26):10665. Available from: https://www.osapublishing.org/abstract.cfm?URI=oe-13-26-10665

99. Wang Z, Guo W, Li L, Luk'yanchuk B, Khan A, Liu Z, et al. Optical virtual imaging at 50 nm lateral resolution with a white-light nanoscope. Nat Commun [Internet]. 2011 Sep 1 [cited 2019 Apr 17];2(1):218. Available from: http://www.nature.com/articles/ncomms1211

100. Caber PJ. Interferometric profiler for rough surfaces. Appl Opt [Internet]. 1993 Jul 1 [cited 2019 Apr 17];32(19):3438. Available from: https://www.osapublishing.org/abstract.cfm?URI=ao-32-19-3438

101. Geng J. Structured-light 3D surface imaging: a tutorial. Adv Opt Photonics [Internet]. 2011 Jun 30 [cited 2019 Apr 17];3(2):128. Available from: https://www.osapublishing.org/abstract.cfm?URI=aop-3-2-128

102. Bartoli A, Poggi P, Quercioli F, Tiribilli B, Vassalli M. Optical profilometer with a standalone scanning sensor head. Opt Eng [Internet]. 2001 Dec 1 [cited 2014 May 3];40(12):2852. Available from: http://opticalengineering.spiedigitallibrary.org/article.aspx?doi=10.1117/1.1417494

103. Liao H-S, Yang C-W, Ko H-C, Hwu E-T, Hwang I-S. Imaging initial formation processes of nanobubbles at the graphite–water interface through high-speed atomic force microscopy. Appl Surf Sci [Internet]. 2018 Mar 15 [cited 2018 Jan 29];434:913–7. Available from: https://www.sciencedirect.com/science/article/pii/S0169433217332828

104.   Liao HS, Huang GT, Tu H Da, Lin TH, Hwu E Te. A novel method for quantitative height measurement based on an astigmatic optical profilometer. Meas Sci Technol [Internet]. 2018 Sep 14 [cited 2019 Apr 1];29(10):107002. Available from: https://iopscience.iop.org/article/10.1088/1361-6501/aadc49

105.   Warren AD, Martinez-Ubeda AI, Payton OD, Picco L, Scott TB. Preparation of stainless steel surfaces for scanning probe microscopy. Micros Today. 2016;24(3):52–5.

106.   Thorén P-A, de Wijn AS, Borgani R, Forchheimer D, Haviland DB. Imaging high-speed friction at the nanometer scale. Nat Commun [Internet]. 2016 Dec 13 [cited 2019 Apr 17];7(1):13836. Available from: http://www.nature.com/articles/ncomms13836

107.   Dürig U, Pohl DW, Rohner F. Near-field optical-scanning microscopy. J Appl Phys [Internet]. 1986 May 15 [cited 2015 Sep 15];59(10):3318–27. Available from: http://scitation.aip.org/content/aip/journal/jap/59/10/10.1063/1.336848

108.   Fecht H-J, Werner M. The nano-micro interface [Internet]. Weinheim, FRG: Wiley Online; 2004 [cited 2019 Apr 16]. 327 p. Available from: http://doi.wiley.com/10.1002/3527604111

109.   Kumaran Mani S, Durairajan R, Barford P, Sommers J. An Architecture for IoT Clock Synchronization. In: Proceedings of the 8th International Conference on the Internet of Things [Internet]. 2018 [cited 2019 Jul 30]. p. 17. Available from: https://doi.org/10.1145/3277593.3277606

110.   Kuk Y, Silverman PJ. Scanning tunneling microscope instrumentation. Rev Sci Instrum [Internet]. 1989 Feb 4 [cited 2019 Apr 17];60(2):165–80. Available from: http://aip.scitation.org/doi/10.1063/1.1140457

111.   Schnurr J, Shockey J, Browse J. The acyl-CoA synthetase encoded by LACS2 is essential for normal cuticle development in Arabidopsis. Plant Cell [Internet]. 2004 Mar [cited 2019 Apr 16];16(3):629–42. Available from: http://www.ncbi.nlm.nih.gov/pubmed/14973169

112.   Gitz DC, Baker JT. Methods for creating stomatal impressions directly onto archivable slides. Agron J. 2009 Jan;101(1):232–6.

113.   Gates DM, Keegan HJ, Schleter JC, Weidner VR. Spectral Properties of Plants. Appl Opt [Internet]. 1965 [cited 2019 Jul 30];4(1):11–20. Available from: https://www.osapublishing.org/DirectPDFAccess/97D84E05-0D47-7A08-73BEA5656245DBD5_13623/ao-4-1-11.pdf?da=1&id=13623&seq=0&mobile=no

114.   Maier B, Frankel GS. Pitting Corrosion of Bare Stainless Steel 304 under Chloride Solution Droplets. J Electrochem Soc [Internet]. 2010 Oct 1 [cited 2019 Apr 17];157(10):C302. Available from: http://jes.ecsdl.org/cgi/doi/10.1149/1.3467850

115.   Taguchi A, Miyoshi T, Takaya Y, Takahashi S. Optical 3D profilometer for in-process measurement of microsurface based on phase retrieval technique. Precis Eng [Internet]. 2004 Apr 1 [cited 2019 Jul 30];28(2):152–63. Available from: https://www.sciencedirect.com/science/article/pii/S0141635903000849?via%3Dihub

116.   Kenton BJ. Design, Characterization, and Control of a High-Bandwidth Serial-Kinematic Nanopositioning Stage for Scanning Probe Microscopy Applications [Internet]. University of Nevada; 2010 [cited 2018 Mar 19]. Available from: http://www.kam.k.leang.com/academics/pubs/BJKentonThesis2010.pdf

117.   Yong YK, Moheimani SOR, Kenton BJ, Leang KK. Invited review article: high-speed flexure-guided nanopositioning: mechanical design and control issues. Rev Sci Instrum [Internet]. 2012 Dec [cited 2014 May 2];83(12):121101–22. Available from: http://www.ncbi.nlm.nih.gov/pubmed/23277965

118.   Ziegler D, Meyer TR, Farnham R. Gwyscan : a library to support non-equidistant scanning probe

microscope measurements. Meas Sci Technol. 2017;28(3):034015.

119. Bazaei A, Yong YK, Moheimani SOR. High-speed Lissajous-scan atomic force microscopy: scan pattern planning and control design issues. Rev Sci Instrum [Internet]. 2012 Jun [cited 2015 Jan 23];83(6):063701–10. Available from: http://www.ncbi.nlm.nih.gov/pubmed/22755628

120. Mahmood I a, Moheimani SOR. Fast spiral-scan atomic force microscopy. Nanotechnology. 2009;20(36):365503.

121. Yong YK, Moheimani SOR, Petersen IR. High-speed cycloid-scan atomic force microscopy. Nanotechnology. 2010;21(36):365503.

122. Gao W, Aoki J, Ju B-F, Kiyono S. Surface profile measurement of a sinusoidal grid using an atomic force microscope on a diamond turning machine. Precis Eng [Internet]. 2007 Jul 1 [cited 2019 Jun 20];31(3):304–9. Available from: https://www.sciencedirect.com/science/article/pii/S0141635907000335

123. Chang S, Wang CS, Xiong CY, Fang J. Nanoscale in-plane displacement evaluation by AFM scanning and digital image correlation processing. Nanotechnology [Internet]. 2005 Apr 1 [cited 2014 May 3];16(4):344–9. Available from: http://stacks.iop.org/0957-4484/16/i=4/a=002?key=crossref.cae85e63cc532a2a1d593660037d2e8a

124. Yacoot A, Koenders L. Recent developments in dimensional nanometrology using AFMs. Meas Sci Technol [Internet]. 2011 Dec 1 [cited 2014 Jul 1];22(12):122001. Available from: http://iopscience.iop.org/0957-0233/22/12/122001

125. Schitter G, Åström KJ, Demartini BE, Thurner PJ, Turner KL, Hansma PK. Design and Modeling of a High-Speed AFM-Scanner. 2007;15(5):906–15.

126. Ando T, Kodera N, Naito Y, Kinoshita T, Furuta K, Toyoshima YY, et al. A High-speed Atomic Force Microscope for Studying Biological Macromolecules in Action. ChemPhysChem. 2003;4(11):1196–202.

127. Kodera N, Yamamoto D, Ishikawa R, Ando T. Video imaging of walking myosin V by high-speed atomic force microscopy. Nature [Internet]. 2010;468(7320):72–6. Available from: http://dx.doi.org/10.1038/nature09450

128. Shibata M, Nishimasu H, Kodera N, Hirano S, Ando T, Uchihashi T, et al. Real-space and real-time dynamics of CRISPR-Cas9 visualized by high-speed atomic force microscopy. Nat Commun [Internet]. 2017 Dec 10 [cited 2018 Oct 15];8(1):1430. Available from: http://www.nature.com/articles/s41467-017-01466-8

129. Wang J-Y, Mullin N, Hobbs JK. High-speed large area atomic force microscopy using a quartz resonator. Nanotechnology [Internet]. 2018 Aug 17 [cited 2018 Oct 15];29(33):335502. Available from: http://stacks.iop.org/0957-4484/29/i=33/a=335502?key=crossref.c7ee4ddb6df55eaac87993033bca8016

130. Klapetek P, Valtr M, Nečas D, Salyk O, Dzik P. Atomic force microscopy analysis of nanoparticles in non-ideal conditions. Nanoscale Res Lett [Internet]. 2011 Jan [cited 2014 May 3];6(1):514–9. Available from: http://www.pubmedcentral.nih.gov/articlerender.fcgi?artid=3212053&tool=pmcentrez&rendertype=abstract

131. Klapetek P, Valtr M, Picco L, Payton OD, Martinek J, Yacoot A, et al. Large area high-speed metrology SPM system. Nanotechnology [Internet]. 2015 Jan 19 [cited 2015 Jan 20];26(6):65501. Available from: http://stacks.iop.org/0957-4484/26/i=6/a=065501

132. Schitter G, Astrom KJ, DeMartini B, Fantner GE, Turner K, Thurner PJ, et al. Design and modeling of a high-speed scanner for atomic force microscopy. 2006 Am Control Conf [Internet]. 2006 [cited 2018 Oct 15];15(5):906–15. Available from:

http://ieeexplore.ieee.org/document/1655406/

133.   Gao P, Swei S-M, Yuan Z. A new piezodriven precision micropositioning stage utilizing flexure hinges. Nanotechnology [Internet]. 1999 Dec 1 [cited 2018 Oct 17];10(4):394–8. Available from: http://stacks.iop.org/0957-4484/10/i=4/a=306?key=crossref.da11226a49c1ad3806a3c9d21ffe99c7

134.   Li Y, Yin B, Liu J, Jin P. Optimal Design of Micro/Nano Positioning Stage with Wide Range and High Speed Based on Flexure Structures. IOP Conf Ser Mater Sci Eng [Internet]. 2017 Dec [cited   2018   Oct   17];274(1):012055.   Available   from: http://stacks.iop.org/1757-899X/274/i=1/a=012055?key=crossref.9de0ba86b832c601950fd8a21af2e4b9

135.   Alsharif N, Burkatovsky A, Lissandrello C, Jones KM, White AE, Brown KA. Design and Realization of 3D Printed AFM Probes. Small [Internet]. 2018 May 1 [cited 2018 Oct 16];14(19):1800162. Available from: http://doi.wiley.com/10.1002/smll.201800162

136.   Yacoot A, Klapetek P, Valtr M, Grolich P, Dongmo H, Lazzerini GM, et al. Design and performance of a test rig for evaluation of nanopositioning stages. Meas Sci Technol [Internet]. 2019 Mar 1 [cited 2019 Mar 14];30(3):035002. Available from: http://stacks.iop.org/0957-0233/30/i=3/a=035002?key=crossref.fccd29ba4507597135fab19974c9527e

137.   Gautsch S. Development of An Atomic Force Microscope and Measurement Concepts for Characterizing Martian Dust and Soil Particles [Internet]. University of Neuchâtel; 2002 [cited 2018   Feb   21].   Available   from: http://citeseerx.ist.psu.edu/viewdoc/download?doi=10.1.1.133.403&rep=rep1&type=pdf

138.   Parrat D, Gautsch S, Akiyama T, Howald L, Brändlin-Müller D, Tonin A, et al. The FAMARS instrument: an atomic force microscope for the phoenix mission. [cited 2018 Feb 19]; Available from: https://www.lpi.usra.edu/meetings/polar2006/pdf/8047.pdf

139.   Herfst R, Dekker B, Witvoet G, Crowcombe W, de Lange D, Sadeghian H. A miniaturized, high frequency mechanical scanner for high speed atomic force microscope using suspension on dynamically determined points. Rev Sci Instrum [Internet]. 2015 Nov 16 [cited 2018 Oct 15];86(11):113703. Available from: http://aip.scitation.org/doi/10.1063/1.4935584

140.   Schitter G, Rost M. Scanning probe microscopy at video-rate. Mater Today [Internet]. 2008 [cited   2014   May   3];11:40–8.   Available   from: http://linkinghub.elsevier.com/retrieve/pii/S1369702109700069

141.   Liu Y, Shan J, Gabbert U, Qi N. Hysteresis compensation and trajectory preshaping for piezoactuators in scanning applications. Smart Mater Struct [Internet]. 2014 Jan 1 [cited 2019 Feb   7];23(1):015015.   Available   from: http://stacks.iop.org/0964-1726/23/i=1/a=015015?key=crossref.aecf7c29d06810e1f90db180607fb5cf

142.   Williams WS, Breger L. Piezoelectricity in tendon and bone. J Biomech [Internet]. 1975 Jan 1 [cited   2018   Feb   26];8(6):407–13.   Available   from: https://www.sciencedirect.com/science/article/pii/0021929075900767

143.   Goldfarb M, Celanovic N. Modeling piezoelectric stack actuators for control of micromanipulation. IEEE Control Syst [Internet]. 1997 Jun [cited 2018 Feb 26];17(3):69–79. Available from: http://ieeexplore.ieee.org/document/588158/

144.   Janocha H, Kuhnen K. Real-time compensation of hysteresis and creep in piezoelectric actuators. Sensors Actuators A Phys [Internet]. 2000 Feb 1 [cited 2018 Feb 26];79(2):83–9. Available   from: https://www.sciencedirect.com/science/article/pii/S0924424799002150?via%3Dihub

145.   Kuhnen K, Krejci P. Inverse control of systems with hysteresis and creep. IEE Proc - Control Theory Appl [Internet]. 2001 May 1 [cited 2018 Feb 26];148(3):185–92. Available from:

http://digital-library.theiet.org/content/journals/10.1049/ip-cta_20010375

146.   Friedt J-M, Carry É. Introduction to the quartz tuning fork. Am J Phys [Internet]. 2007 [cited 2019 Jan 7];75(5):415–22. Available from: http://aapt.org/ajp

147.   Abbott BP. Observation of Gravitational Waves from a Binary Black Hole Merger. Phys Rev Lett [Internet]. 2016 [cited 2018 Feb 27];116(6):061102. Available from: https://physics.aps.org/featured-article-pdf/10.1103/PhysRevLett.116.061102

148.   Yacoot A, Downs MJ. The use of x-ray interferometry to investigate the linearity of the NPL Differential Plane Mirror Optical Interferometer. Meas Sci Technol [Internet]. 2000;11(8):1126. Available from: http://stacks.iop.org/0957-0233/11/i=8/a=305

149.   Yacoot A, Koenders L, Wolff H. An atomic force microscope for the study of the effects of tip–sample interactions on dimensional metrology. Meas Sci Technol [Internet]. 2007;18(2):350–9. Available from: http://stacks.iop.org/0957-0233/18/i=2/a=S05?key=crossref.c78de9952db8f8fe5655a6d1541c6ce5

150.   Leach RK, Claverley J, Giusca C, Jones CW, Nimishakavi L, Sun W, et al. Advances in engineering nanometrology at the National Physical Laboratory. Meas Sci Technol. 2012;23(7):074002.

151.   Hwu E-T, Illers H, Wang W-M, Hwang I-S, Jusko L, Danzebrink H-U. Anti-drift and auto-alignment mechanism for an astigmatic atomic force microscope system based on a digital versatile disk optical head. Rev Sci Instrum [Internet]. 2012 Jan [cited 2014 May 3];83(1):013703. Available from: http://www.ncbi.nlm.nih.gov/pubmed/22299958

152.   Collins KA, Kielkopf JF, Stassun KG, Hessman F V. ASTROIMAGEJ: image processing and photometric extraction for ultra-precise astronomical light curves. Astron J [Internet]. 2017 Jan 25 [cited 2019 Mar 25];153(2):77. Available from: http://stacks.iop.org/1538-3881/153/i=2/a=77?key=crossref.9b1fe1c5500702184feaf7262d7607cd

153.   Ganguly D, Chakraborty S, Balitanas M, Kim T. Medical Imaging: A Review. In Springer, Berlin, Heidelberg; 2010 [cited 2019 Mar 25]. p. 504–16. Available from: http://link.springer.com/10.1007/978-3-642-16444-6_63

154.   Bock RK. Techniques of image processing in high-energy physics [Internet]. Cern; 1996 [cited 2019 Mar 25]. Available from: https://cds.cern.ch/record/323781/files/p181.pdf

155.   Saadi NM, Watanabe K. Assessing image processing techniques for geological mapping: a case study in Eljufra, Libya. Geocarto Int [Internet]. 2009 Jun [cited 2019 Mar 25];24(3):241–53. Available from: http://www.tandfonline.com/doi/abs/10.1080/10106040802556199

156.   Uchida S. Image processing and recognition for biological images. Dev Growth Differ [Internet]. 2013 May [cited 2019 Mar 25];55(4):523–49. Available from: http://www.ncbi.nlm.nih.gov/pubmed/23560739

157.   Fried O. Photo manipulation, the easy way [Internet]. University of Princeton; 2017 [cited 2019 Mar 25]. Available from: https://search.proquest.com/docview/1928888635?pq-origsite=gscholar

158.   Tafti AP, Kirkpatrick AB, Alavi Z, Owen HA, Yu Z. Recent advances in 3D SEM surface reconstruction. Micron [Internet]. 2015 Nov [cited 2019 Mar 25];78:54–66. Available from: https://linkinghub.elsevier.com/retrieve/pii/S0968432815300226

159.   Solomon RW. Free and Open Source Software for the Manipulation of Digital Images. Am J Roentgenol [Internet]. 2009 Jun 23 [cited 2019 Mar 25];192(6):W330–4. Available from: http://www.ajronline.org/doi/10.2214/AJR.08.2190

160.   Parrish D, Noonan B. Image Manipulation as Research Misconduct. Sci Eng Ethics [Internet].

2009 Jun 6 [cited 2019 Mar 25];15(2):161–7. Available from: http://link.springer.com/10.1007/s11948-008-9108-z

161. Kwon KS, Ready S. Practical Guide to Machine Vision Software: An Introduction with LabVIEW [Internet]. Wiley and Sons; 2014. Available from: https://books.google.co.uk/books?id=kl6FBQAAQBAJ

162. F. Russell-Pavier. Testing radiation using frozen fluid laden with energy sensors (TRUFFLES) [Internet]. University of Bristol; 2015 [cited 2019 Aug 12]. Available from: https://www.researchgate.net/publication/328642345_Testing_radiation_using_frozen_fluid_laden_with_energy_sensors_TRUFFLES

163. Peng L. Adaptive Median Filtering [Internet]. Proceedings of Machine Vision: Digital Image Processing. 2004. p. 1677–1682. Available from: http://www.massey.ac.nz/~mjjohnso/notes/59731/presentations/Adaptive Median Filtering.doc.

164. Jha AK, Agarwal P, Schaefer G, Zaz Y. A novel image detail preserving impulse noise removal algorithm. In: 2016 5th International Conference on Multimedia Computing and Systems (ICMCS) [Internet]. IEEE; 2016 [cited 2019 Feb 8]. p. 137–40. Available from: http://ieeexplore.ieee.org/document/7905630/

165. Kumar Boyat A, Kumar Joshi B. Noise models in digital image processing. An Int J [Internet]. 2015 [cited 2019 Feb 8];6(2):63–75. Available from: https://arxiv.org/ftp/arxiv/papers/1505/1505.03489.pdf

166. Snyder WE, Qi H. Machine vision. Machine Vision. Cambridge University Press; 2004.

167. Hwang H, Haddad RA. Adaptive median filters: new algorithms and results. IEEE Trans Image Process [Internet]. 1995 Apr [cited 2019 Mar 25];4(4):499–502. Available from: http://ieeexplore.ieee.org/document/370679/

168. Zhao Y, Li D, Li Z. Performance enhancement and analysis of an adaptive median filter. In: 2007 Second International Conference on Communications and Networking in China [Internet]. IEEE; 2007 [cited 2019 Feb 14]. p. 651–3. Available from: http://ieeexplore.ieee.org/document/4469475/

169. Hamza A Ben, Luque-Escamilla PL. Removing Noise and Preserving Details with Relaxed Median Filters. J Math Imaging Vis [Internet]. 1999 [cited 2019 Feb 15];11(2):161–77. Available from: https://link.springer.com/content/pdf/10.1023%2FA%3A1008395514426.pdf

170. Sabol GP, Comstock RJ, Weiner RA, Larouere P, Stanutz RN. In-Reactor Corrosion Performance of ZIRLO and Zircaloy-4. Zircon Nucl Ind Tenth Int Symp ASTM Int [Internet]. 1994 [cited 2019 Mar 26]; Available from: www.astm.org

171. Vincent O, Folorunso O. A Descriptive Algorithm for Sobel Image Edge Detection. Proc 2009 InSITE Conf. 2017;40(1):97–107.

172. Wallace GK. The JPEG still picture compression standard. IEEE Trans Consum Electron [Internet]. 1992 [cited 2019 Feb 26];38(1):xviii–xxxiv. Available from: http://ieeexplore.ieee.org/document/125072/

173. Welch. A Technique for High-Performance Data Compression. Computer (Long Beach Calif) [Internet]. 1984 Jun [cited 2019 Feb 26];17(6):8–19. Available from: http://ieeexplore.ieee.org/document/1659158/

174. Freeman H. On the Encoding of Arbitrary Geometric Configurations. IEEE Trans Electron Comput [Internet]. 1961 Jun [cited 2019 Feb 26];EC-10(2):260–8. Available from: http://ieeexplore.ieee.org/document/5219197/

175. Tsai YT. Color image compression for single-chip cameras. IEEE Trans Electron Devices

[Internet]. 1991 May [cited 2019 Mar 26];38(5):1226–32. Available from: http://ieeexplore.ieee.org/document/78401/

176. Szeliski R. Image Alignment and Stitching: A Tutorial. Found Trends R Comput Graph Vis [Internet]. 2006 [cited 2019 Mar 26];2(1):1–104. Available from: http://www.cs.toronto.edu/~kyros/courses/2530/papers/Lecture-14/Szeliski2006.pdf

177. Levin A, Zomet A, Peleg S, Weiss Y. Seamless Image Stitching in the Gradient Domain. In Springer, Berlin, Heidelberg; 2004 [cited 2019 Mar 26]. p. 377–89. Available from: http://link.springer.com/10.1007/978-3-540-24673-2_31

178. Brown M, Lowe DG. Automatic Panoramic Image Stitching using Invariant Features. Int J Comput Vis [Internet]. 2007 [cited 2019 Mar 26];74(1):59–73. Available from: http://www.realviz.com

179. Buckman J. SEM image stitching S13 Use of automated image acquisition and stitching in scanning electron microscopy: Imaging of large scale areas of materials at high resolution. Microsc Anal [Internet]. 2014 [cited 2019 Mar 26];28(1):13–5. Available from: https://microscopy-analysis.com/sites/default/files/2014_Janaury_Buckman.pdf

180. Pulli K, Tico M, Xiong Y. Mobile panoramic imaging system. In: 2010 IEEE Computer Society Conference on Computer Vision and Pattern Recognition - Workshops [Internet]. IEEE; 2010 [cited 2019 Mar 26]. p. 108–15. Available from: http://ieeexplore.ieee.org/document/5543792/

181. May M, Parulski K, Rinas E, Van Sprewenburg B, Vermillion C, Dunsmore C. Producing panoramic digital images by digital camera systems [Internet]. United States Patent; US6714249B2, 1998 [cited 2019 Mar 26]. p. 1–16. Available from: https://patents.google.com/patent/US6714249B2/en

182. Agarwal D, Cheah Y-W, Fay D, Fay J, Guo D, Hey T, et al. Data-intensive science: The Terapixel and MODISAzure projects. [cited 2019 Mar 26]; Available from: http://www.world

183. Li J, Yang T, Yu J, Lu Z, Lu P, Jia X, et al. Fast Aerial Video Stitching. Int J Adv Robot Syst [Internet]. 2014 Oct 30 [cited 2019 Mar 26];11(10):167. Available from: http://journals.sagepub.com/doi/10.5772/59029

184. Andrews P. Adobe Photoshop Elements 6. In: Adobe Photoshop Elements 6: A Visual Introduction to Digital Photography [Internet]. 1st Edition. New York: Routledge; 2009 [cited 2019 Mar 26]. p. 22. Available from: https://www.taylorfrancis.com/books/9780080569031

185. Winder S, Hua G, Brown M. Picking the best DAISY. In: 2009 IEEE Conference on Computer Vision and Pattern Recognition [Internet]. IEEE; 2009 [cited 2019 Mar 26]. p. 178–85. Available from: http://ieeexplore.ieee.org/document/5206839/

186. Kaplan LM, Kuo C-CJ. An improved method for 2-D self-similar image synthesis. IEEE Trans Image Process [Internet]. 1996 May [cited 2019 Mar 27];5(5):754–61. Available from: http://ieeexplore.ieee.org/document/495958/

187. Hoff DJ, Olver PJ. Automatic Solution of Jigsaw Puzzles. J Math Imaging Vis [Internet]. 2014 [cited 2019 Mar 12];49(1):234–50. Available from: http://www.math.umn.edu/~olver

188. Emmenlauer M, Ronneberger O, Ponti A, Schwarb P, Griffa A, Filippi A, et al. XuvTools: free, fast and reliable stitching of large 3D datasets. J Microsc [Internet]. 2009 Jan 1 [cited 2019 Jan 17];233(1):42–60. Available from: http://doi.wiley.com/10.1111/j.1365-2818.2008.03094.x

189. Grauman K, Darrell T. The Pyramid Match Kernel: Efficient Learning with Sets of Features. J Mach Learn Res [Internet]. 2007 [cited 2019 Jan 17];8(4):725–60. Available from: http://jmlr.csail.mit.edu/papers/volume8/grauman07a/grauman07a.pdf

190. Grauman K, Darrell T. The pyramid match kernel: Discriminative classification with sets of

image features. In: Proceedings of the IEEE International Conference on Computer Vision. 2005.

191. Zhao Q, Qian J, Gui Z, An Q, Zhu M. Interfacial self-assembly of cellulose-based polyelectrolyte complexes: pattern formation of fractal "trees." Soft Matter [Internet]. 2010 Mar 9 [cited 2019 Mar 26];6(6):1129. Available from: http://xlink.rsc.org/?DOI=b918529a

192. Soylemez E, de Boer MP, Sae-Ueng U, Evilevitch A, Stewart TA, Nyman M. Photocatalytic Degradation of Bacteriophages Evidenced by Atomic Force Microscopy. Gan Y, editor. PLoS One [Internet]. 2013 Jan 3 [cited 2019 Mar 26];8(1):e53601. Available from: http://dx.plos.org/10.1371/journal.pone.0053601

Appendix

A digital appendix is available either via a DVD at the back of this thesis or online. For access to the online appendices please email: freddie.russell-pavier@bristol.ac.uk